NTNU

Norwegian University of
Science and Technology

Platinum Group Elements in the Reinfjord Ultramafic Complex

Even Nikolaisen

Geology
Submission date: May 2016
Supervisor: Rune Berg-Edland Larsen, IGB
Co-supervisor: Thomas Grant, IGB
Bjørn Eske Sørensen, IGB

Norwegian University of Science and Technology
Department of Geology and Mineral Resources Engineering

Abstract

Fifty km W - NW of the Norwegian city of Alta in Troms fylke, is the Reinfjord ultramafic complex (RUC), which is composed of three intrusive events with an age of approximately 560 - 570 Ma. Drill core RF-1 from 2011 show two peaks of economic elements, one Cu-Ni reef low in PGE at a depth of 86-93m and a PGE reef low in Cu-Ni at 107-113m.

The PGE spike in RF-1 is concentrated in a 6m thick section dominated by an orthopyroxene pegmatite and dunite. This section shows a total amount of 0.79 ppm Pt+Pd+Au+Os. The $\delta^{34}S$ signature of the PGE reef is -0.40 and the Cu-Ni reef -4.56, a significant difference within 20m. This clearly indicates that the sulfur has different sources with low country rock contamination.

This thesis presents a detailed study of the PGE's and their mineral assembly, with the aim of identifying the process(es) that could form this kind of a deposit. Detailed thin section microscopy, BSD imaging, EDS mapping and EPMA identified 61 grains with noble metals in four thin sections. The PGM's are mainly PGE-tellurides situated in both dunite and pegmatite and can be subdivided into three main categories: Pt-dominant (moncheite), Pd-dominant (merenskyite) and Pt-Pd-dominant (mix of the two). These minerals are hosted by base metal sulfides (BMS), indicating that the deposit was generated by magmatic processes.

The PGE reef in the RUC display very different ore forming relation when compared with the massive deposits of Norilsk and Bushveld. The parental melts are thought to derive from a mantle source that intruded into the lower crust at 6-9 kbar, where the RUC represents as an open and active part of a conduit system. The intrusive magmas were either gradually enriched in situ or already enriched in a deeper magma chamber prior to entering the RUC. The reef position in the stratigraphically upper third of the intrusion is very rare for layered intrusions. The magmatic environment does represents the typical models to form a PGE deposit, but strong enrichments of tellurides have only been described at two locations, the Platreef and Merensky reef in Bushveld. A gravimetric model of the reef represents a slightly dipping open bowl, which could suggest that the late arriving, denser PGE enriched melt started to flow/slide parallel to the layering and carved a channel in the underlying cumulates.

Based on all the results in this thesis, it is clear that despite a sub-economical grade, the RUC provide a valuable insight in to the ore forming potential for deep-seated layered intrusions.

Sammendrag

Femti km V – NV for Alta i Troms, finnes Reinfjord ultramafiske kompleks (RUK) som består av 3 separate pulser av ultramafiske magma, datert til ca 560 – 570 Ma. Borrekjerne RF-1 fra 2011 påviste to anomalier for økonomiske mineraler, en Cu-Ni rik sone fra 86 – 93m og en PGE rik sone fra 107 -113m.

PGE anomalien er konsentrert i en 6m tykk sone som domineres av en pegmatittisk pyroksenitt sammen med intrusjonenes dunittiske hovedbergart. Denne seksjonen viser til sammen en anrikelse på 0.76 ppm Pt+Pd+Au+Os. Svovel isotop an lyser viser ÷0.40 PGE revet og ÷4.56 for Cu-Ni revet, noe som er en signifikant endring over kun 20m. Dette indikerer at svovelen for de to revene stammer fra forskjellige kilder med svært liten forurensing fra sidebergartene.

Denne masteroppgaven presenterer en detaljert studie av edelmetallene og deres sammensetning, med et mål om å identifisere prosessen(e) som kan danne en slik type forekomst som PGE revet i RUK. Detaljert tynnslip mikroskopering, BSD kartlegging, EDS analyser og EPMA analyser har identifisert totalt 61 korn som inneholder edelmetaller. Hovedsakelig opptrer alle PGM'ene som tellurider, som igjen kan deles inn i tre hovedgrupper: Pt-rik (moncheite), Pd-rik (merenskyite) og en Pt-Pd-rik (miks av både moncheit og merenskyite)

Ved å sammenligner PGE revet i RUK med større forekomster i Norilsk og Bushveld, så er det noen vesentlige forskjeller. Magmaen som dannet RUK har en mantel signatur og er kalkulert til størkne ved 6-9 kbar, i et miljø som er et åpent og aktivt magmatisk system. Magma ble enten anriket på PGE i RUK eller intruderte allerede rik på edelmetaller fra et større og dypere magmakammer. Revets posisjon er i den øverste tredjedelen av intrusjonen, som er svært sjelden for PGE rev i lagdelte intrusjoner. Det magmatiske miljøet i RUK passer godt med modeller for dannelse av PGE forekomster, men en sterk anrikelse av tellurider er kun funnet to plasser i lokale deler av Platreef og Merensky reef i Bushveld. En gravimetrisk modell av forekomsten i RUK, viser at anrikningen er formet som en slakt NØ hellende åpen skål. Dette kan tyde på en PGE anriket, tyngre smelte som intruderte i RIK ved et senere stadie. Denne smelten akkumulerer på eksisterende kumulater, for så å skli/strømme med lagdelingen og dermed grave ut en kanal/dal i underliggende kumulater.

Selv om forekomsten i RUK foreløpig ikke er økonomisk drivverdig, så gir denne lokaliteten verdifull innsikt i malmdannende prosesser som forekommer i dype lagdelte intrusjoner.

Acknowledgements

This thesis is a part of my Master of Science degree in Bedrock and Resource Geology at the Department of Geology and Mineral Resources Engineering, Norwegian University of Science and Technology (NTNU). It has been funded by NORDMIN, IGB (NTNU), EU-ITN and Nordic Mining, as a part of the Platinum project, run by Prof. Rune Berg-Edland Larsen at NTNU.

First, I must thank my supervisor Prof. Rune Berg-Edland Larsen for giving me the opportunity to work on such an inspiring project. Despite being a very busy man, you have always made yourself available, with great positivity and constructive feedback in every discussion and for that, I am grateful. Together with Rune, I would also thank my co supervisors, Thomas Grant and Bjørn Eske Sørensen for the incredible inspiring enthusiasm, supervisions and the extensive knowledge. I have learned so much, thanks to all of you.

Thanks to the EM lab at NTNU, especially Morten Peder Raanes for doing the fine detailed work of analyzing the tiny PGM's on the EPMA and to Yingda Yu for the teaching and supervisions that was necessary for endless hours on the SEM.

I would like to express my gratitude to the small village of Reinfjord and especially Oddmund Hansen, without whom the field trip would not have been possible.

Kim Grannes, who endured my presence in the field. I am grateful for all the discussions that have helped me to better evaluate data and hypotheses regarding my thesis. Together we are dynamite.

To my fellow students who have made these five years fly by. I am grateful for the work ethic you have all showed and inspired to always achieve better results. It have been a painful pleasure in joining the frequently occurring coffee breaks for one who don't drink coffee, but it always lifted the mood whenever it was needed. Thanks to Ina Cathrine Sagen for corrections and providing constructive feedback.

Finally yet importantly a big thank to my parents who have helped with corrections, support and positivity. Despite that you have little knowledge regarding the content, the discussions and explanations have truly helped me gain a better understanding and ability to constructively share my observations more efficiently.

Table of content

List of figures

List of tables

Abbreviations

NTNU - Norwegian University of Science and Technology
LLS - Lower Layered Series
ULS - Upper Layered Series
MZ - Marginal zone
CS - Central Series
RUC - Reinfjord Ultramafic Complex
SIP - Seiland Intrusive Province
PGE - Platinum Group Elements
Pt - Platinum
Pd - Palladium
Os - Osmium
Au - Gold
Cu - Copper
Ni - Nickel
Fe - Iron
SEM - Scanning Electron Microscope
BSD - Back Scatter Detection
EDS - Energy-Dispersive X-ray Spectroscopy
EPMA - Electron Probe Micro Analyzer
Fld - Feldspar
Bt - Biotite
Opx - Orthopyroxene
Cpx - Clinopyroxene
Ol - Olivine
Dol - Dolomite
Rut - Rutile
Ccp - Chalcopyrite
Pn - Pentlandite
Po - Pyrrhotite
Ppl - Plane polarized light
Xpl - Cross polarized light
SCSS - Sulfide concentration at sulfur saturation
Cbn - Cubanite
Pb - Lead
Te - Tellurium
Se - Selenium
MSS - Monosulfide solution
BMS - Base Metal Sulfides

1 Introduction

1.1 Aims of study

After reading an old thesis (Hansen, 1971), Prof. Rune Berg-Edland Larsen proposed that the Reinfjord Ultramafic Complex (RUC) could host a Cu-Ni ore deposit and possibly also PGE's. With the collaboration of Nordic Mining ASA, fieldwork studies were sufficiently promising to justify helicopter-flown geophysics (skyTEM) of the intrusive complex. This survey indicated a shallow conductor that was drilled in 2012 and analyzed by geological consultant Markku Iljina (Iljina, 2013). The drilling successfully intersected two horizons with elevated sub-economical content of Cu, Ni, PGE and Au. One Cu-Ni enriched zone at 86-93m and one PGE enriched zone at 107-113m below the surface. The PGE bulk composition shows an enrichment in platinum, palladium, osmium and gold, with a total PGE + gold of 0.76 ppm (table 1.1). The discovery of PGE is not entirely new to the province since it was already known at Lokkarfjord. Assessed in 2008 by the Norwegian Geological Survey (NGU), the Lokkarfjord hornblendite contained 0.8 ppm PGE.

This thesis specifically addresses the distribution and speciation of the PGE's in RUC. PGM's here, were not previously identified or studied hence i.e. the first task was to find and identify the different PGM's and to describe their mineral compositions using BSD, EDS and EPMA. When the minerals are found and identified, the second task is to describe the textures and the hosting mineral assemblages.

Finally, with this knowledge at hand, the aim is to approach a genetic model for the formation of the PGE-Cu-Ni deposits in the RUC

Table 1.1: PGE anomaly and its location in RF-1

Depth (m)		Au (ppb)	Pd (ppb)	Pt (ppb)	3PM (ppb)
From	To				
103	105	64	215	166	445
105	107	<5	16	17	33
107	107.75	<5	8	10	18
107.75	109.45	22	297	271	590
109.45	110.20	213	730	419	1362
110.20	110.60	47	117	69	233
110.60	111	135	116	96	347
111	113	129	243	180	552
113	115	32	63	47	142

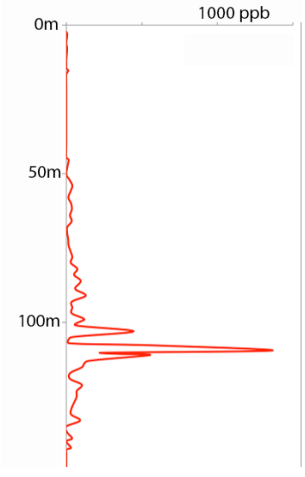

1.2 Previous work

Geologically, the RUC is part of the SIP covering Seiland, Stjernøya and the Øksfjord peninsula in Troms and Finnmark municipalities. The province was first mapped by Pettersen (1875) and later described in more details by Barth (1927) and Barth (1952). It covers 5400 km^2, dated between 560-570Ma (Roberts, 2007), made up by 35% ultramafic, 50% gabbro, 10% felsic (monzonite, diorite and granitoid) and 5% alkaline (nepheline syenite, syenite, alkaline gneiss and minor amount of carbonatite) (Roberts, Corfu, Torsvik, Ashwal, & Ramsay, 2006). The general model represents SIP as magmatic cumulates associate with a mantle plume (Bennett, Emblin, Robins, & Yeo, 1986; Griffin, Sturt, O'Neill, Kirkland, & O'Reilly, 2013; Robins & Gardner, 1975), forming during continental rifting or back arc spreading (Andréasson, Svenningsen, & Albrecht, 1998; Daly, Aitcheson, Cliff, Gayer, & Rice, 1991; Elvevold, Reginiussen, Krogh, & Bjørklund, 1994; Roberts, 2007; Roberts et al., 2006; Roberts, Corfu, Torsvik, Hetherington, & Ashwal, 2010) at the marginal segments of Rodinia (Kirkland, Daly, & Whitehouse, 2007; Roberts, 2007). Barometric calculations (Emblin, 1985; Grant et al., 2016; Reginiussen, 1996) suggest a pressure of 6-9 kbar, which correlates to an emplacement in the middle crust and under ductile conditions. Then the SIP transported to its current position during the closing of the Iapetus Ocean, 420Ma as a part of the Kalak Nappe Complex (Roberts et al., 2010).

The ultramafic cumulates in the SIP was described in details by Oosterom (1963) and have been debated for a long time, regarding the parental melt. Bennett et al. (1986) described the parental melt to be "*probably picritic, with up to c. 20 wt% MgO and emplaced at temperatures of c. 1450°C*". Calculations by Grant et al. (2016) resulted in the highest estimates to be 1120°C. While Griffin et al. (2013) studied the Nordre Bumandsfjord intrusion and suggested, *"The primary magma of the Nordre Bumandsfjord pluton was a relatively iron-rich (Fo78–80) dunite, with minor cpx and spinel. It intruded near the base of the crust at high T (≥1,700 C) in a highly fluid state, and in an extensional environment."*

The interest for economic resources started when NGU was prospecting Nepheline pegmatites in 1952. As a part of this project, the Lokkarfjord area was mapped and prospected in 1954 by Knauskopf, eventually leading to the discovery of PGE's here that in 2008 was assessed by Sollie and Schiellerup, on behalf of NGU.

Reinfjord is located 50km West of Alta (figure 1.1). Most of RUC is located on a plateau (lake district, figure 5.7) 600m – 1100m above the Reinfjord village, south of Langfjordjøkelen glacier, exposing 25 km^2 of ultramafic rock and 100 km^2 of gabbro (Emblin, 1985).

Even after being subjected to extensive collision during the formation of the Caledonian mountain range, the RUC is barely effected by the metamorphic events. Oriented the right way up and with layering that dips 10-30° towards northeast. Some tectonic events are visible as faults, within or in close approximation to the intrusion. Several were mapped (Emblin, 1985), but none of them are dated or interpreted to a satisfying tectonic context.

Publications by Bennett (1971), Hansen (1971) and Hooper (1971) is the first recorded studies of the RUC that described the lithologies and their relation. Emblin (1985) updated the interpretation and mapped the area in greater details, to show the six main lithologies. Revisions of Emblins map was done by Øen and Rasch in 2013 and by Grannes and Nikolaisen in 2015, introducing GPS and computer precision to the lithology boundaries.

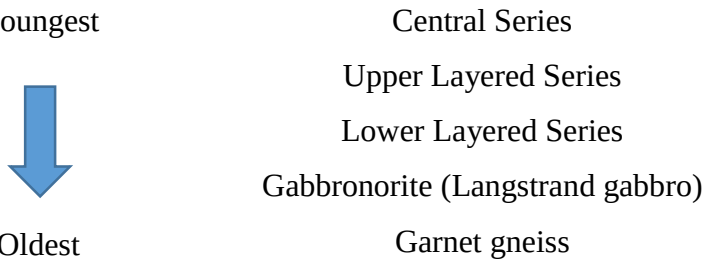

Øen's study of the sulfur isotopes suggest the sulfur that forms the ore deposits have a mantle origin, with low crustal contamination. Rasch's research of the silicate composition from surface samples, describes the RUC to form due to crystal fractionation. This is evident by the transition from Mg-olivine to Fe-olivine upward in the chamber stratigraphy.

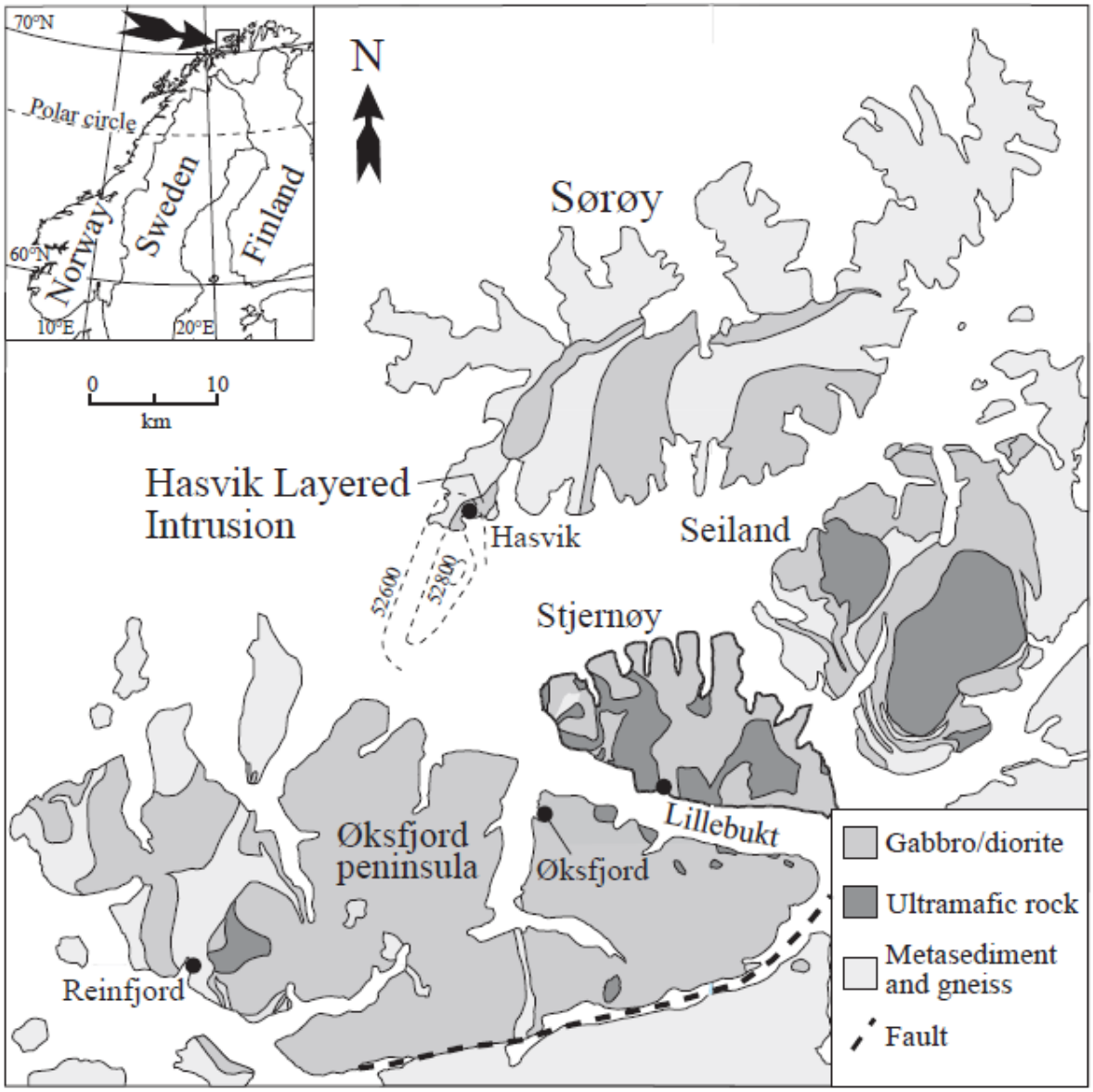

Figure 1.1: Geologic map of Øksfjord-Seiland (Tegner, Robins, Reginiussen, & Grundvig, 1990). The dotted lines at Hasvik show the Bouguer anomaly, thought to represent a deeper and larger magma chamber that fed the SIP with magmas (Brooks, 1969)

2 Regional geology

2.1 Garnet gneiss

The host rock for the RUC is an upper amphibole facies garnet gneiss (Bennett, 1971, 1974; Hooper, 1971) dated to the Neoproterozoic Era (1000 – 541Ma) (Hooper, 1971; Roberts et al., 2010), that is exposed west and southwest of the RUC. Because of the later intruding Langstrandsgabbro and the ultramafic sequence, a 2-3km wide thermal aureole have formed within the garnet gneiss (Bennett, 1974). This thermal metamorphism has locally changed the mineral assemblage and introduced sillimanite and kyanite. Indicating a pressure of 5-6 kbar at the time of crystallization (Bennett, Emblin, Robins, & Yeo, 1985).

Emblin (1985) observed that kyanite was cut by sillimanite needles and therefore concluded that kyanite was the stable Al_2SiO_5 polymorph during regional metamorphism. The main minerals identified is plagioclase (An_{25-36}), biotite and bright red to pink translucent almandine garnets (figure 2.1A) (Emblin, 1985). Garnets, sillimanite, kyanite, biotite and muscovite are observed, but only locally within the planes of schistosity.

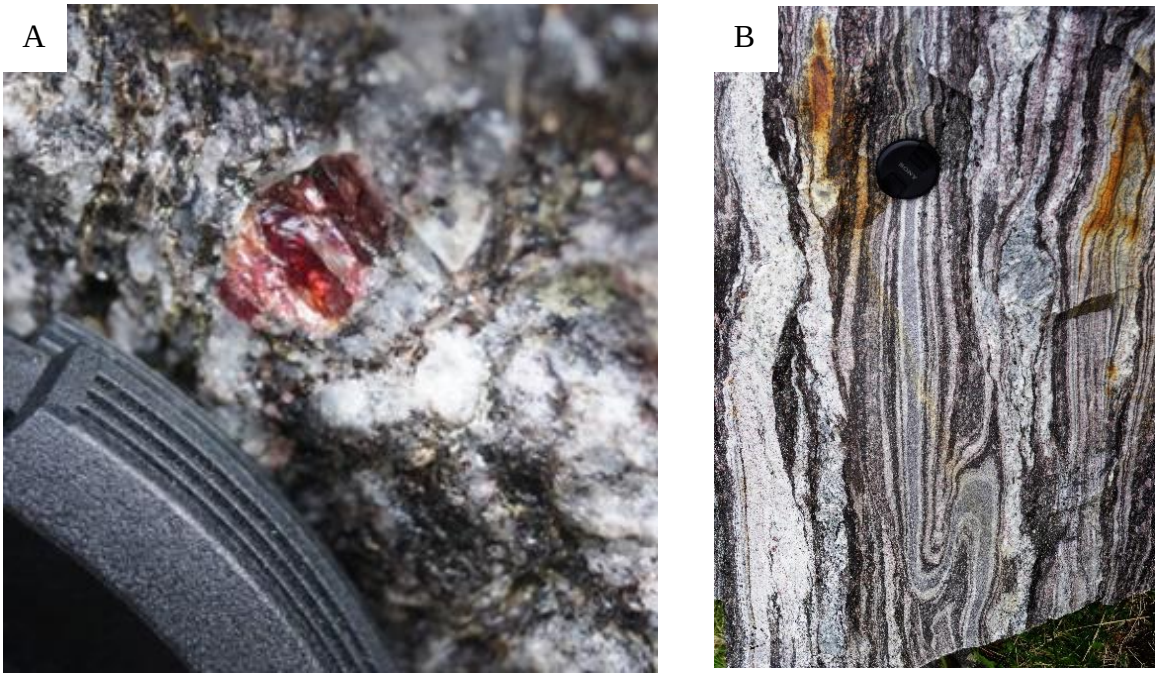

Figure 2.1: A) Almandine garnet. B) Gneiss folding with plagioclase porphyroclasts.

2.2 Langstrand gabbronorite

The 100-km^2 Langstrand gabbronorite is a large layered mafic pluton that intruded into the country rock (Bennett, 1971, 1974; Grant et al., 2016), that is mainly composed of plagioclase-clinopyroxene-olivine cumulates (Bennett et al., 1986). Together with the gneiss, this form the host rock, which the later ultramafic melts intruded. The internal layering of the gabbronorite dips 10-30° and some of these layers show mineralization (figure 2.3), but concluded in the report by Iljina (2013) to have no economic interest.

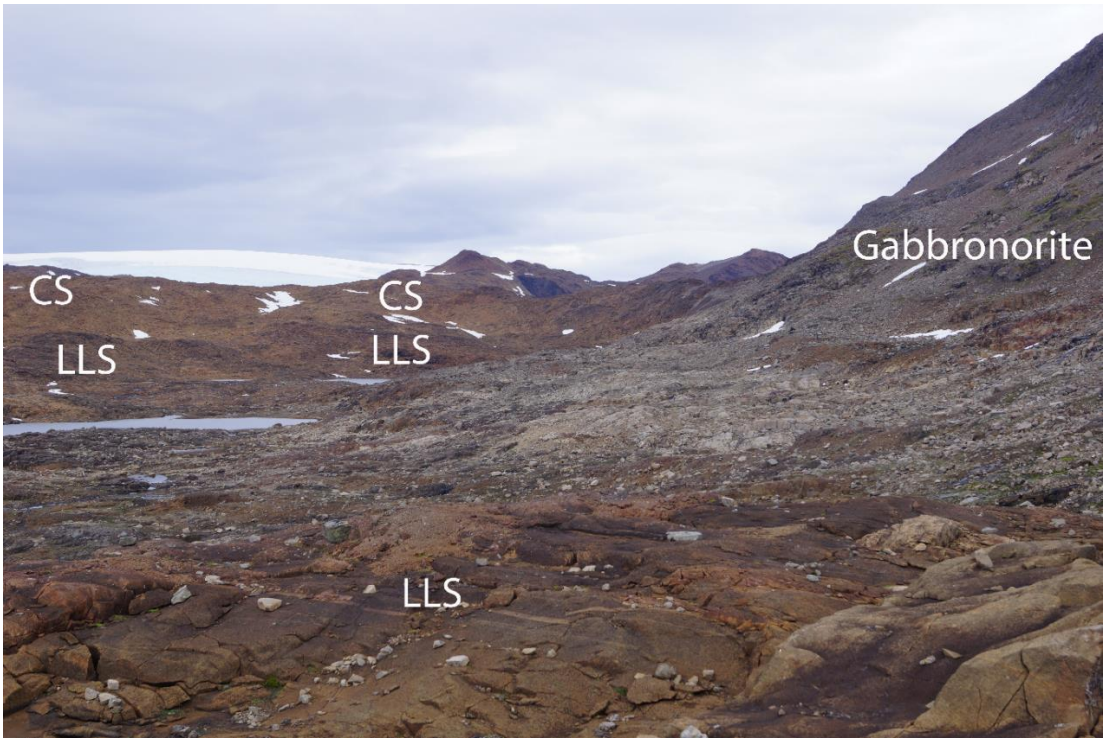

Figure 2.2: The eastern contact between gabbronorite and LLS. Photo taken from the southern end of LLS, towards N.

Figure 2.3: Mineralized layer in gabbro, dipping 30° NE. Photo taken towards E, with Kim as scale.

2.3 Lower layered series

The lower layered series (LLS) (Emblin, 1985) is stratigraphically the lowest part of the ultramafic cumulates and is underlying a gabbro screen, separating it from the other ultramafic lithologies. It is ca. 300 m thick, dipping 31° east and may be divided into four main layers (Emblin, 1985), that are comprising of lherzolite and wehrlite, and olivine clinopyroxenite. A contact sulphide deposit occur in the MZ, where it comes in contact with the gneiss. Isolated mineralized sulphide disseminations with pentlandite, chalcopyrite and pyrrhotite are also common throughout the intrusion.

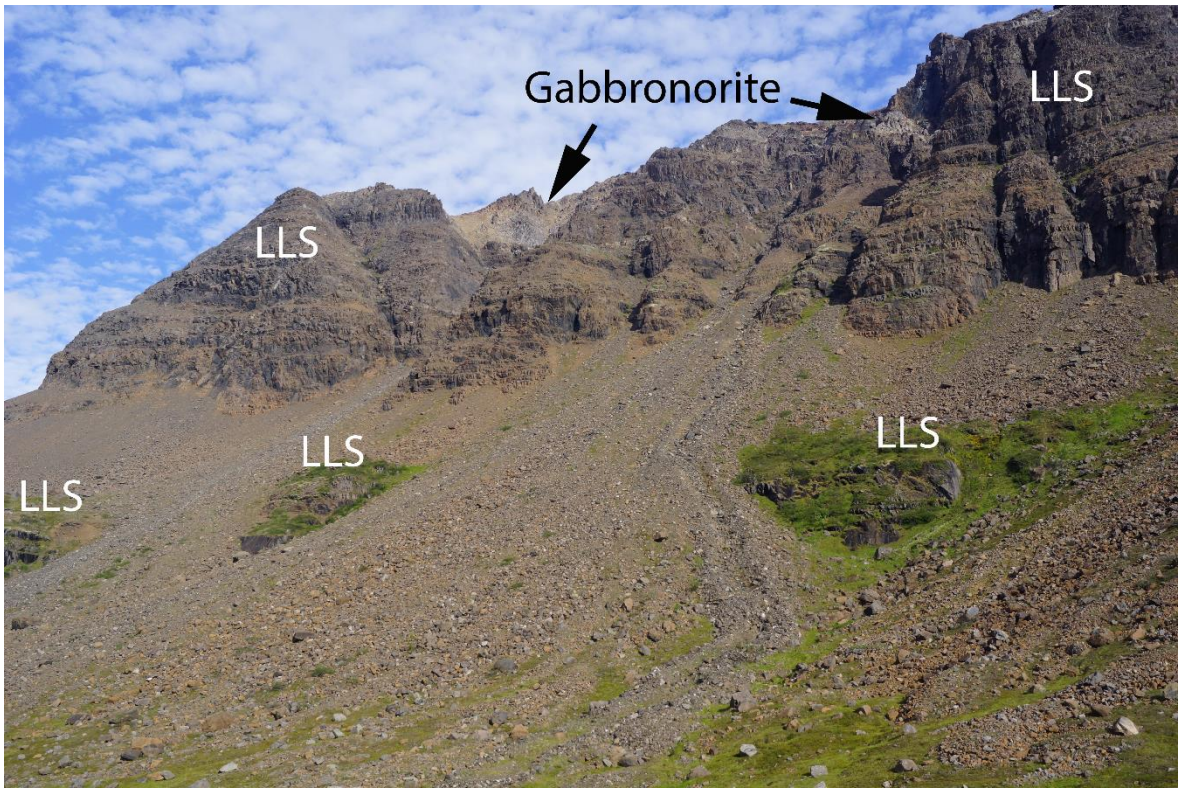

Figure 2.4: The LLS situated under the Gabbro screen. Located in the cliff face parallel to Storvannet river. Photo taken toward N

2.4 Upper layered series

The upper layered series (ULS) is most accessible at the eastern contact (gabbro-ultramafic) on the plateau and in Storvannet valley. It is composed of seven cyclic units visible by the distinct macro rhythmic layering exposed in on the plateau and in Bonvik dalen (Emblin, 1985). ¾ th of the lowest units are dunitic in composition with poicilitic clinypyroxenes, which upwards evolve into olivine-clinopyroxene cumulate rocks. The layering have a large variation

in thickness from centimeters to meters and can be mapped in a 250m continuous stratigraphic section (Emblin, 1985). When observing the upper olivine clinopyroxenite, the appearance changes to show a rhythmic layering between wehrlite and olivine clinopyroxenites. Wehrlite layers are typically 1-10 cm thick. Clinopyroxene is less abundant here and typically create cm-thick layers, while olivine cumulates typically are 1-5 cm thick (Emblin, 1985) (figure 2.5).

Presence of slumping (figure 2.7), crossbedding (figure 2.6) and load structures gives good indicators for lateral and horizontal flow movements or shear between cumulates as they consolidated.

Figure 2.5: mm-cm scale layering in ULS at the eastern contact. Photo taken towards E.

Figure 2.6: Crossbedding in ULS, created by movement and interaction between magma in the magma chamber. Photo taken towards NE.

Figure 2.7: Slumping of pyroxene cumulates into underlying olivine cumulates (ULS).

2.5 Central Series

The central series (CS) comprises the central 50% of the RUC where it consists of dunite and poicilitic wehrlite (figure 2.8) (Emblin, 1985). The intrusive contact between the CS and older lithologies indicates that it formed as the last major intrusive event. Modal layering are much more subtle than in the ULS. Emblin (1985) describes the poicilitic clinopyroxene to not

form any cumulus phase and therefore does not give a clear rhythmic variation as seen in the ULS. However, cryptic variations and the evidence that spinel and clinopyroxene forms at the base level of each layer does gives an indication that a modal layering is present (Grant et al., 2016). Drilling in 2012 showed that the CS is hosting two mineralized reefs (Schanche, Iljina, & Larsen, 2012).

Figure 2.8: Poicilitic texture in CS with cpx oikocryst.

Figure 2.9: Dunite (CS) above the 2014 campsite. Photo taken towards S.

2.6 Marginal Zone

The marginal zones (MZ) appears in the RUC where the ultramafic cumulates are in contact with either metasediments or gabbronorite and comprises hybrid rocks that formed during assimilation of the host rock. Between the garnet gneiss and the LLS, the MZ comprises olivine websterite and websterites with large bronzite oikocrysts (Emblin, 1985). When in contact with gabbronorite, marginal series shows distinct features of poikilitic plagioclase and plagioclase veins. Pegmatitic pyroxene with interstitial plagioclase is also present at several locations where the marginal zone forms in contact with gabbro. For more detailed description of the marginal series, see section 5.1 (remapping of the RUC).

3 Methods

3.1 Field work

Fieldwork lasted two seasons in 2014 and 2015, with a duration of two weeks at the end of August to the beginning of September, which increased the probability for good weather. Since the RUC is located in such a remote and isolated area, the camp and its participants were flown in by helicopter and stayed in personal tents. The main field objective for this thesis was to obtain samples that could possibly indicate ore forming processes and to remap the intrusion, to gain a better overall understanding of the lithological units.

In 2014, the south and the eastern contact of the intrusion was revised and one possible outcrop of the PGE-Cu-Ni reef in the south was sampled and marked with GPS location. This was an expected find, based on the reefs depth in RF-1 and the general dip of the CS. I also assisted Kim Rune B. Grannes in sampling profiles, necessary for him to obtain the chemical results needed to assess the RUC's cryptic variations. These samples were oriented and marked, so they can be used for multiple purposes (geologically and geophysically).

Main focus of the 2015 field season was to complete the new map and to sample the pegmatite exposed near RF-1. The NE end of the intrusion was mapped in detail, resulting in a major revision of this area. We also spend the first days mapping and sampling for geologically and geophysically purposes in Isdalen and Storvannet valley. The mapping from both field seasons resulted in a totally revised map, shown figure 5.7. For details, see the master thesis of Grannes (2016) (in prep). The pyroxene pegmatite near RF-1 was sampled and marked with GPS.

3.2 Lab work

Samples from both field seasons were cut with a diamond blade into 1cm thick slices for thin sections, while the rest of the material was jaw-crushed. To minimize Fe-pollution, we used tungsten carbide jaws. Before each sample, the crusher was washed with ethanol and dried with compressed air. Samples were split into bags of ca. 50g before packed and shipped to CHEMEX (Sweden) for further chemical analyses.

Representative areas on the 1cm thick slice was marked (28x48mm) and made into a polished thin section, for SEM and EPMA analyzes. Thin sections are prepared by gluing a

piece of rock to a glass plate, then slice and polish it down to 30 µm thickness. All thin sections were prepared by the thin section lab at NTNU.

3.3 NGU's drill core storage (Løkken)

NGU's facility at Løkken, Norway stores the drill cores from 2011 and 2014, which we had the ability to study and log. Drill cores RF-3 and RF-4 were split and logged in detail during spring of 2015. Afterwards, the cores were sampled in interval of 5m and shipped to Sweden for chemical analysis

In the interest of this thesis, we decided to revise RF-1 where the highest spike in PGE are located. The PGE reef was resampled for thin section preparation to gain a better understanding of the interaction between the dunite and pegmatite.

3.4 Thin section scanning

The thin sections were all scanned in both plane polarized light (ppl) (figure 3.1) and cross polarized light (xpl) (figure 3.2) using Epson v600 photo scanner with polarizing film. These scans were used as reference and maps when working with optical and electron microscope.

Figure 3.1: Plane polarized light scan of thin section 109.55.

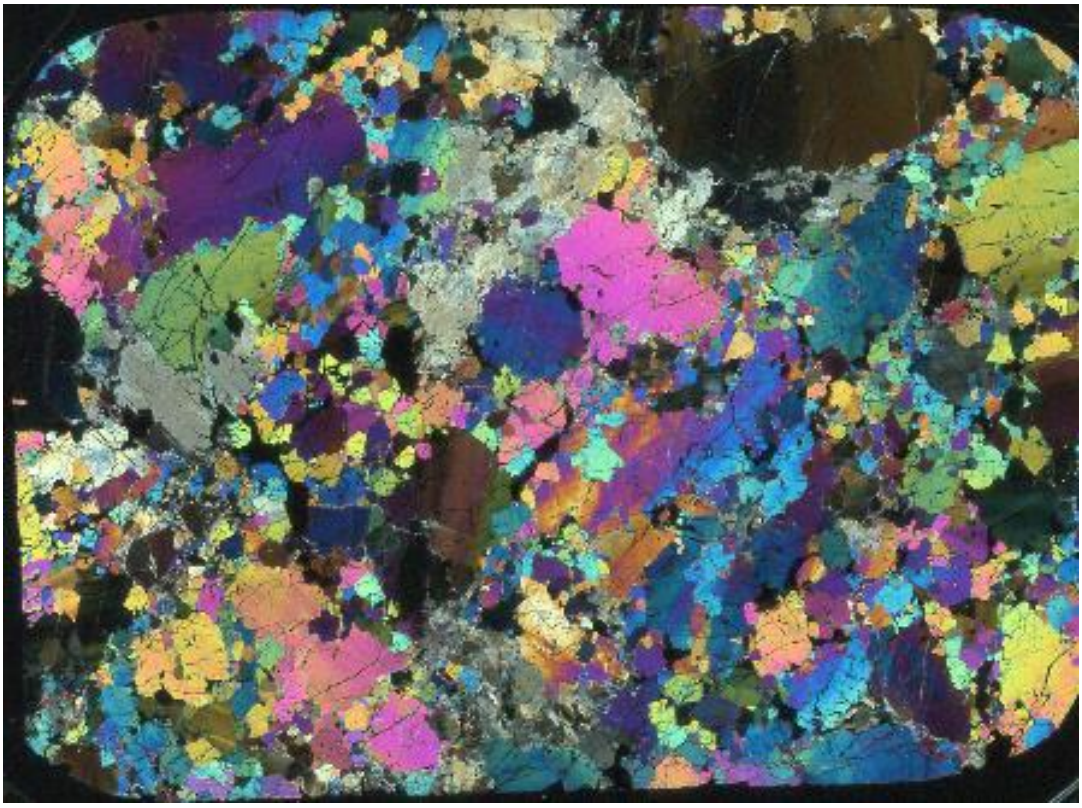

Figure 3.2: Cross polarized light scan of thin section 109.55.

3.5 Optical microscopy

In optical microscopy, plane polarized light (ppl) is filtered and oriented in one direction before it enters the thin section. When passing through, the light is scattered in all directions according to the optical properties of the mineral. As shown in figure 3.1 (ppl), white light is dominant followed by opaque minerals that blocks light. Some minerals may have distinct colors and show changes in color brightness in ppl, known as pleochroism. This is an effect of the minerals ability to absorb more or less wavelengths based on its crystallographic orientation. When applying a second polarized filter, also referred to as an analyzer, the colorization of each mineral changes and viewed as cross polarized light (xpl). The analyzer is oriented perpendicular to the first filter and will only transmit wavelengths in a certain direction after passing through a mineral, referenced as interference colors seen in figure 3.2 (xpl). These colors are divided into an interference color chart (figure 3.3) that can be used when identifying xpl colors for all anisotropic minerals.

Relief can also be used as an optical identifying reference, observed as a mineral appears to stick out from the background, created by the minerals refraction index.

Based on the identification criteria's above, each thin section were mapped using an optical microscope to identify the silicate assembly and the petrographic evolution during crystallization. These results can indicate the ore forming processes at the time of PGE-Cu-Ni reef development.

Reflected light microscopy is used to observe opaque minerals. In this relation chalcopyrite, pyrrhotite, pentlandite and spinel is the most abundant opaque minerals present in these thin sections. Each of the minerals are identified by the amount of light they reflect, their color and the way they relates to neighboring minerals.

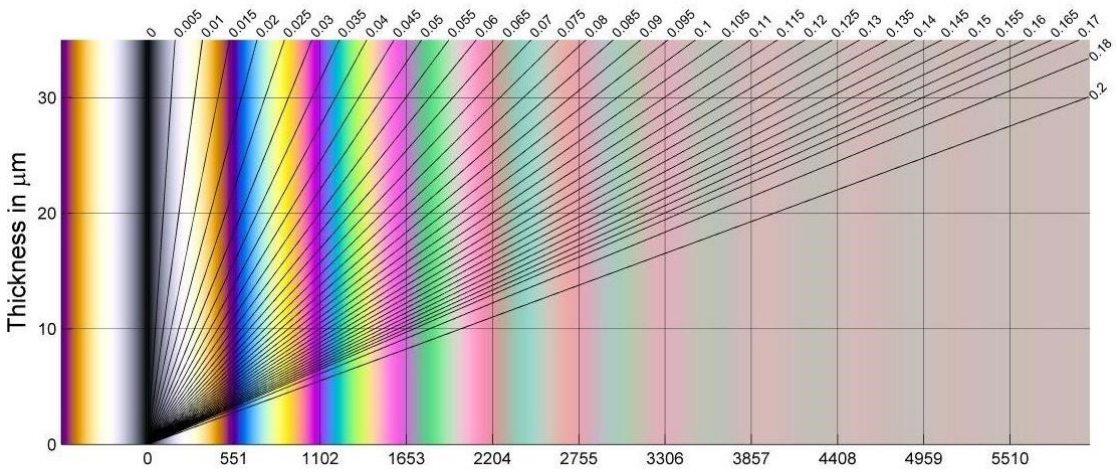

Figure 3.3: Interference chart (Sørensen, 2013).

3.6 Scanning Electron Microscope

A necessary tool for working on the scale needed for this thesis, since most of the precious metal grains are < 5µm. The Scanning Electron Microscope (SEM) machine used is the Zeiss Ultra, 55 limited edition with Backscatter Detection (BSD) and Electron Dispersive Spectroscopy (EDS). The following description is based on the book "Scanning Electron Microscopy and X-Ray Microanalysis" by Lawes (1987).

Scanning Electron Microscope works when applying a current of electrons that scans over a surface. The big difference between optical and electron microscopy is the ability to achieve a much higher resolution on an electron microscope, limited by the beam diameter. Optical microscopy is limited to our eyes ability to distinguish between wavelengths. We can only detect the visible light at wavelengths between 390 - 700 nm. The SEM operates differently by not relying on visible light, but rather on the invisible beam of electrons. It can only achieve focus for one point if all the electrons have the same energy, therefore the acceleration voltage must be very stable so there is no electrons of different wavelength. To form an image of a specimen, SEM operates by letting the electron beam systematically swipe over a surface, scanning it one line of a 1000 points at the time and collecting the returning electronic signal. This signal is interpreted by a computer and displayed as an image.

Backscattered Detection is used when analyzing further into the material and not only scanning the surface. BSD makes the electron beam penetrate into the material and reflecting of the nucleus of an atom. Minerals with larger atoms will show up brighter, because of the greater numbers of electrons that bounces of the nucleus (Krinsley, Pye, Boggs Jr, & Tovey, 2005). This is useful for this thesis, because of the larger nucleus of PGE and gold. Since the PGE are small and incorporated into sulfides that are much denser than the silicate matrix, they would be difficult to find without working on a SEM with BSD. The method I used when searching for these minerals, was to lower the brightness to the point that all sulfides were almost invisible and then to apply a high current (subjecting the material for more electrons, increasing the ability to view even the smallest grains) and searching with a view field of 200 µm. The thin section was manually scanned systematically from end to end. Even at this magnification, I had to use higher magnification (100µm view) in areas with more sulfides.

Electron dispersive spectroscopy (EDS) gives an element assembly for a given area or point. The method embraces the concept that each element has a distinct atom configuration of electrons in shells surrounding a nucleus. Emitting x-rays towards an element, causes electrons in an inner shell to be knocked out of orbit, leaving an empty position that an electron from an

outer shell can fill. The energy released when an electron fills this empty position is measured in KeV (Kilo electron Volt) and counted how many times the same energy peak is being registered (Lawes, 1987). These results are shown in a diagram with KeV on the x-axis and count-rate on y-axis (figure 3.4). Each element has its own emitted energy and this method can therefore be used for element identification. When applied for geological purposes, this method can be useful in indicating which mineral is present in a point or area. Minerals have a specific element composition that can be analyzed for their identification. By comparing the known element assemblage of a mineral with the measured element spectra, it is possible to get an indication of which mineral is present. The EDS only gives a bulk composition and can therefore only be valued as a semi quantitative analysis. When analyzing an area two results will be detected and displayed: Characteristic x-rays and continuum x-rays (Kα, Lα, Mα, etc.) (Theisen, 2013). The characteristic x-ray is the result when electrons are ejected from the inner shell of an atom. Continuum x-rays are those creating the "background noise". They are formed by continuous interaction between the beam electron and the nucleus of an atom. The reaction causes the electron to loose energy that is picked up by the detector and displayed as the background in figure 3.4 (Hafner, 2006).

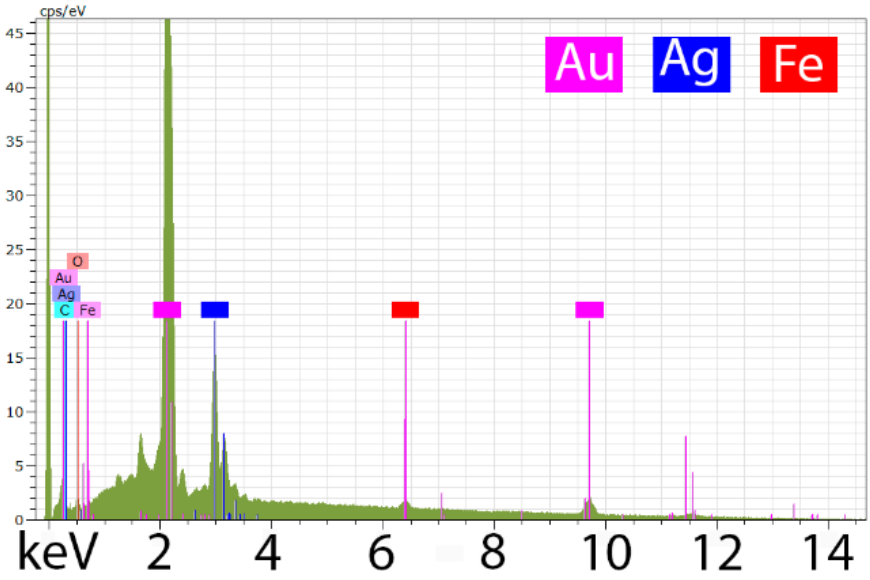

Figure 3.4: EDS spectra of Au-81. Showing the strong x-ray peak of Au.

All SEM raw data of the PGE's have been interpreted and are shown as false color charts. Figure 3.5 show the end result of such an interpretation, where the raw data is presented in the top picture. The lower color map is created to better observe the sulfide and silicate relationship.

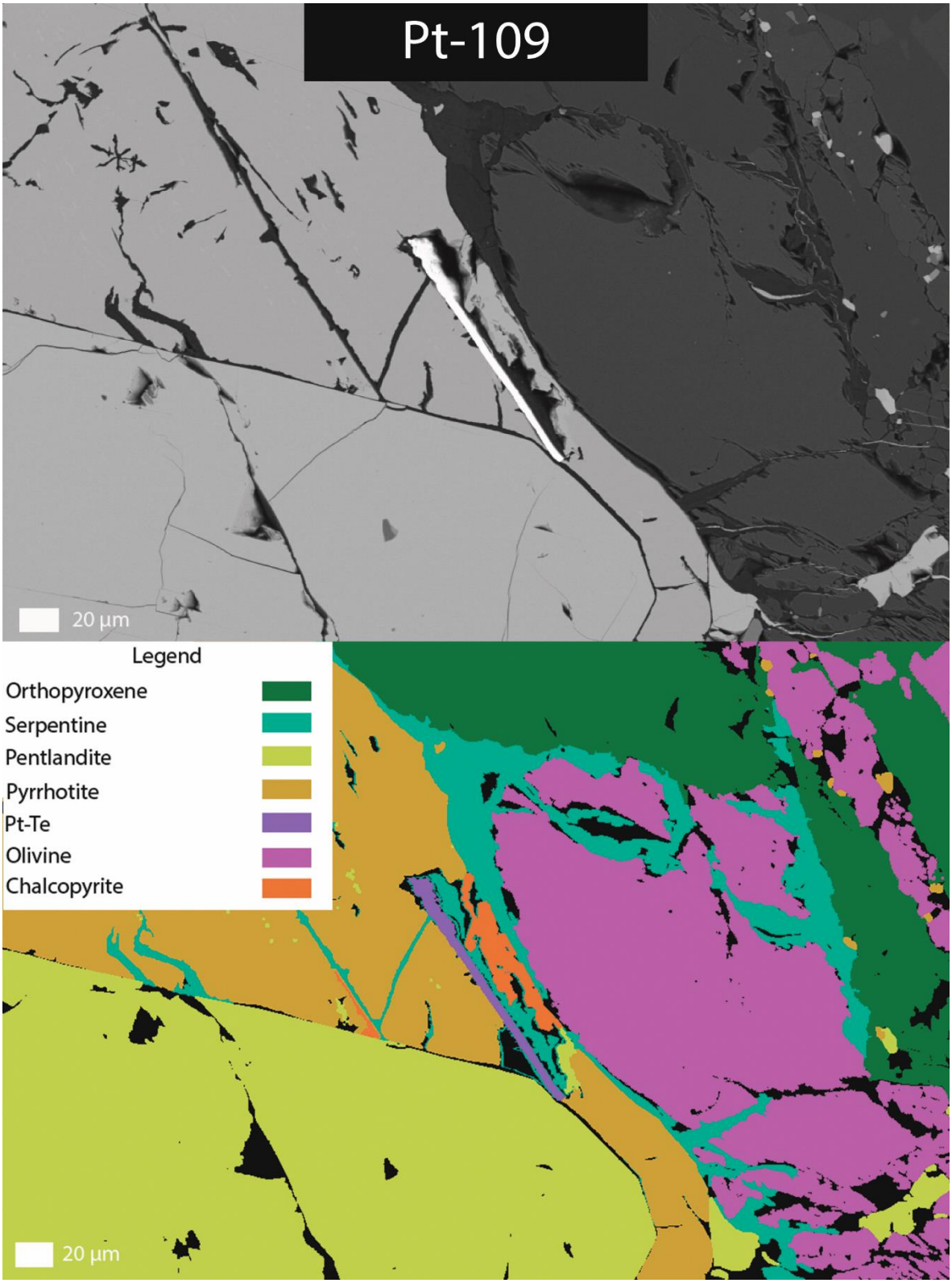

Figure 3.5: False color chart of Pt-109.

3.7 Electron Probe Micro-Analysis (EPMA)

The machine used is the JEOL JXA-8500F, located at NTNU. This is basically a SEM. and operates on the same concept as EDS. A beam of electrons analyzes the sample and the emitted x-rays mixture is then separated by a diffracting crystal to an x-ray detector. The separation isolates the characteristic x-ray peak for the selected element by adjusting the angle of the diffracting crystal. The crystal then reflects only the characteristic x-rays and thereby eliminating the continuum x-rays. This results in a clean x-ray peak that can be used as a quantitative analysis (Theisen, 2013).

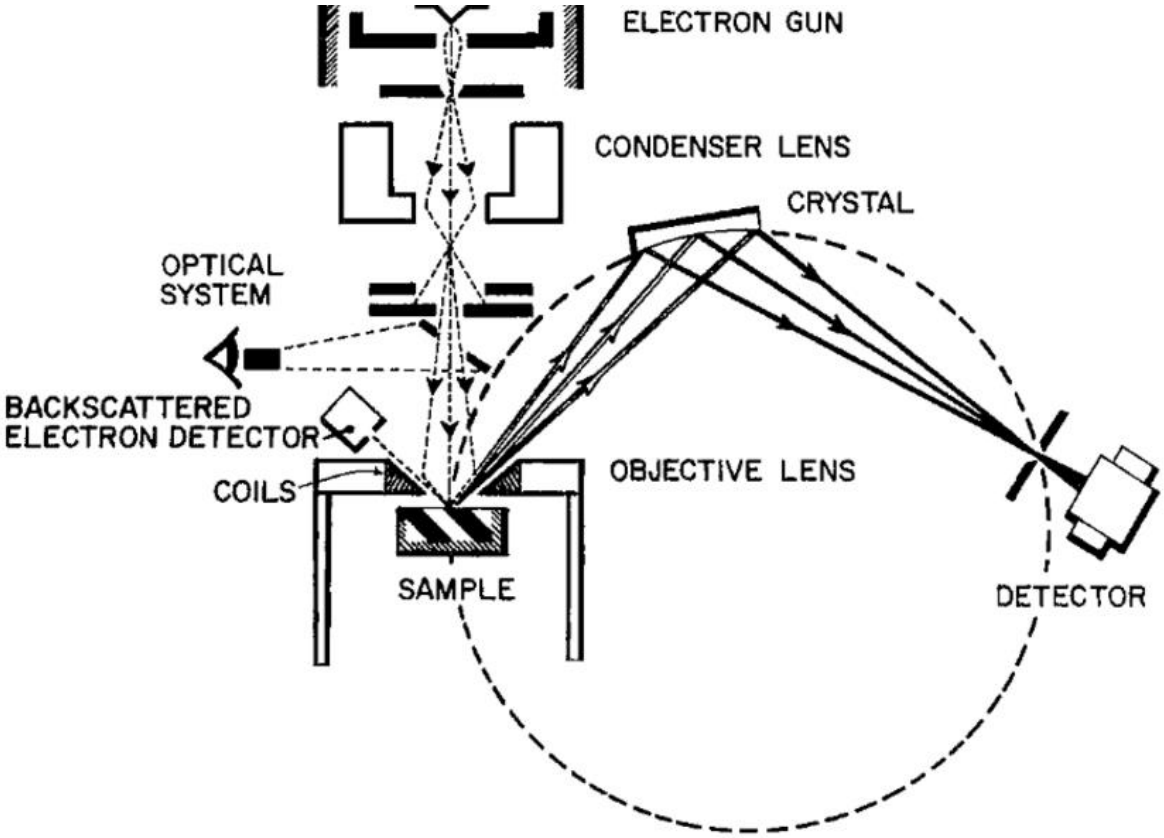

Figure 3.6: Basic components of an Electron Microprobe Analyzer (Cescas, Tyner, & Gray, 1968).

All samples were analyzed with a beam current of 20nA and 15 KeV acceleration voltage. For the PGE analyses, the machine was first calibrated using metal standards with results representing total weight percent of an element within the analyzed area. Due to the size, all points was spot analyzed, with a beam diameter of 1 µm.

For silicates the analyses was calculated as weight percent of oxides, based on calibration (appendix figure F 12) standards from Astimex MINM25-53 with natural standards

(Astimex). Since each mineral occurred in very variable sizes, some points were possible to conduct analyzes with a wider beam than others.

Table 3.1: Beam diameter for analysis of silicates.

Olivine	5 µm
Orthopyroxene	2 µm
Plagioclase	5 µm
Amphibole	2 µm
Carbonates	10 µm

For the carbonates, it was necessary to increase the element measuring time to account for evaporation under the intensity of the electron beam. Sodium was analyzed for 10 seconds, aluminum and silicon for 20 seconds and magnesium, calcium, manganese and iron for 40 seconds.

One issue with this system that is important for this thesis is the machines beam width of 1 µm. Since the majority of PGM's are < 1 µm wide, there will be some contamination.

4 Theory

The following chapter summarizes processes that form mineralized sulfide deposits known to host PGE. These processes are well documented to form due to igneous processes in mafic – ultramafic magmatic systems.

4.1 Igneous rock classification

An igneous rock is mostly formed by partially melting the mantle or the crust. They can be classified by their mineral assemblage in ternary diagrams and categorized into two main groups: Felsic or Mafic. These two can further be divided into numerous subgroup, that when analyzed can give further information about temperature, pressure regimes and chemical composition of the parental melt.

Figure 4.1 shows the ternary classification system for rocks in the felsic regime, generated by Streckeisen (1974) for the International Union for Geological Science (IUGS).

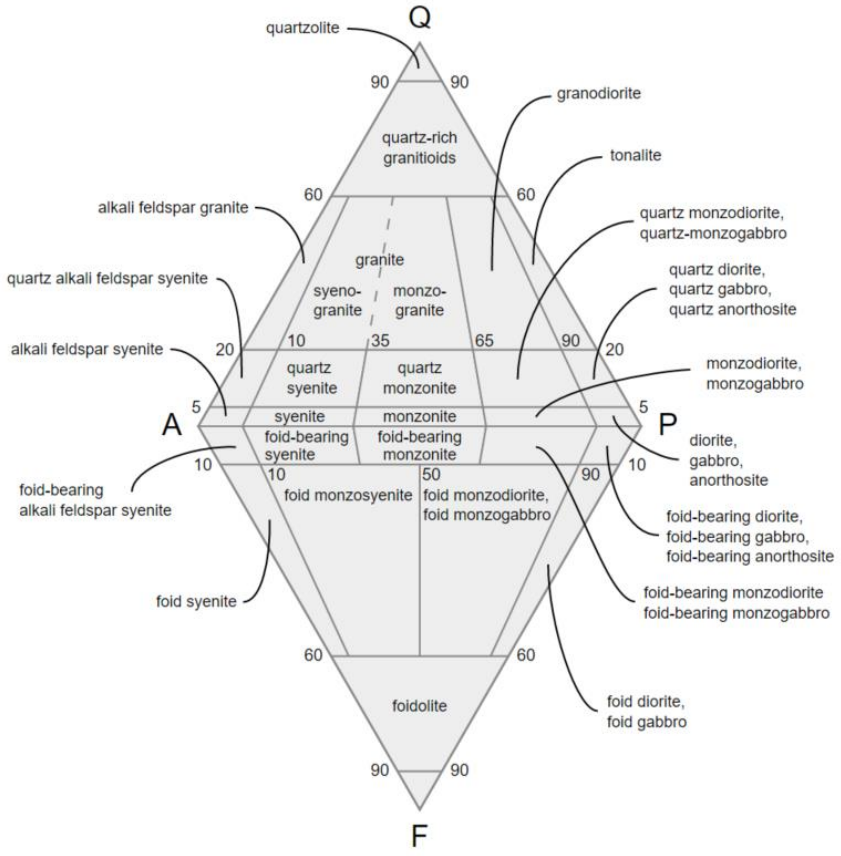

Figure 4.1: QPAF (quartz, plagioclase, alkali feldspar and feldspathoid) diagram (Streckeisen, 1974).

If a rock sample contains little or no quartz and alkali feldspar, but do contain plagioclase, it will indicate that the rock is of mafic to ultramafic in composition and formed from igneous melts that had relative low concentrations of SiO_2. To classify these rocks, different ternary diagrams are required, ones that include mafic and ultramafic minerals to determine the rocks identity. This relationship is shown in figure 4.2, where the mafic minerals orthopyroxene and clinopyroxene is included in the same ternary diagram as plagioclase. This chemical composition is what identifies most mafic rocks that form within plutons, such as gabbro (plagioclase and clinopyroxene) and norite (plagioclase and orthopyroxene).

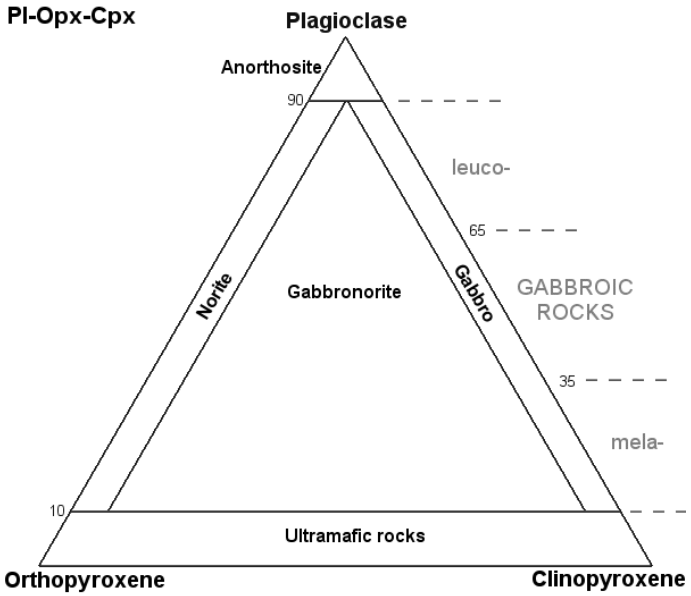

Figure 4.2: Mafic ternary diagram for Pl-Opx-Cpx (Alden, 2013).

If a rock sample shows less than 10% felsic minerals, (i.e. feldspars) it is necessary to use the classification diagrams that identify rocks of ultramafic origin. Figure 4.3 illustrates the rocks containing olivine and pyroxenes, classified as ultramafic.

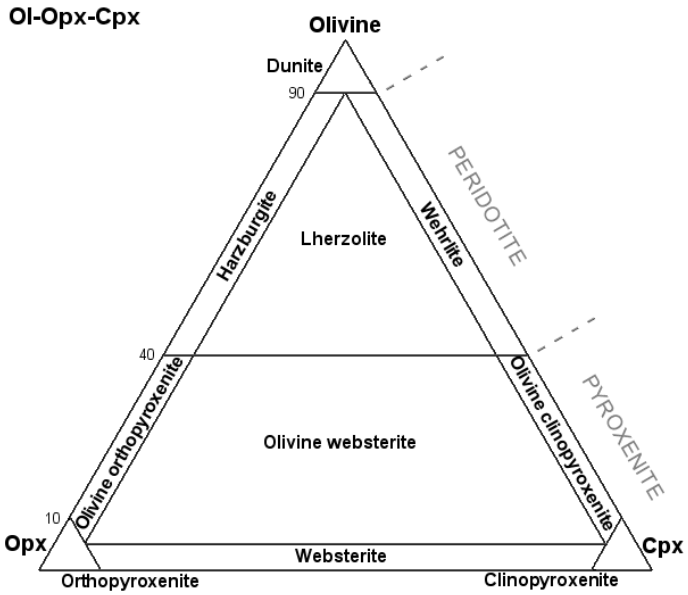

Figure 4.3: Ultramafic ternary diagram for Ol-Px-Hbl (Alden, 2013).

Hornblende may also may form ultramafic rocks with olivine and pyroxenes ± biotite (figure 4.4).

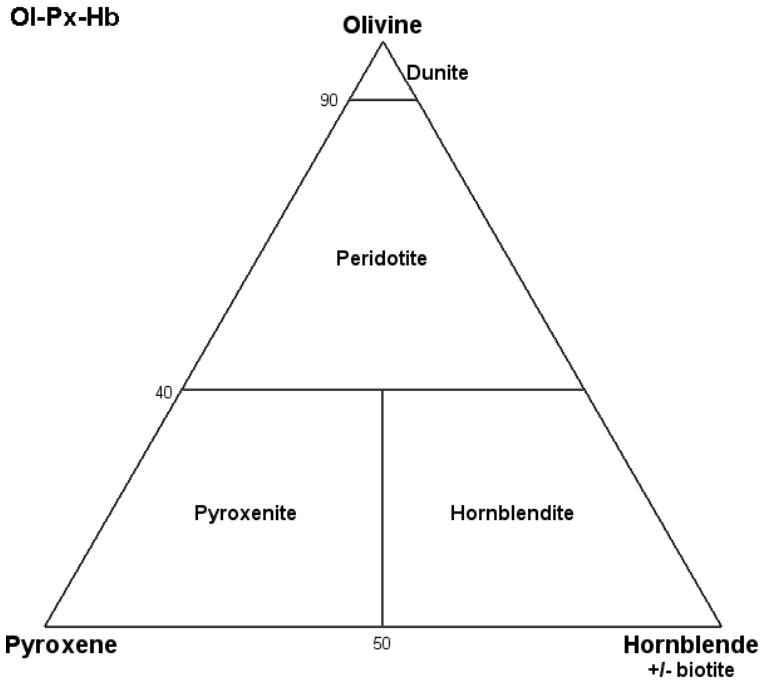

Figure 4.4: Ultramafic ternary diagram for Ol-Px-Hbl (Alden, 2013).

4.2 Textures, Grain size and Accessory Minerals

Textures include grain shape (anhedral, subhedral and euhedral), alteration and how the grains relate to each other. These observations may provide important clues to possible rock forming processes before, under and after final crystallization. Accessory minerals provides important clues, for example to the detailed chemistry of the fluids, alteration and fugacities of volatile constituents (e.g. H_2O, CO_2, O_2, S_2 etc.).

Grain size may give kinetic information on crystallization speed, deformation and sub solidus reequilibration of the mineral assemblage. The extreme endmembers are either very fine-grained rocks or those with large crystals, where pegmatites represents the coarse-grained endmember.

4.3 Developing a PGE deposit

Economical deposits of platinum group elements (PGE) are rare, due to the very low abundance of these elements in the asthenosphere and lithosphere. The process of forming these deposits are divided into three main environments: Mafic and ultramafic igneous rocks, rare hydrothermal deposits and placer deposits. The last are rare and will only be briefly touched upon, in section 4.4.

4.4 Komatiite ore deposits

These melts derive from high degree of partial melting of fertile asthenospheric mantle and are therefore strongly under saturated in sulfur at the point of formation, forming a primitive melt with very high MgO content (18%- 30%) (Arndt & Leshler, 2004) and temperatures calculated to 1650°C ± 20°C for Archean komatiites (Green, 1975). These melts intrude the continental crust as shallow intrusions or flows. Due to the high temperatures, they are prone to high degree of country rock assimilation and contamination. According to Keays (1995) country rock sulfur facilitates sulfur saturation, as explained in 4.6.

Several deposits of this kind is known all over the world, with the type locality Kambalda Ni-Cu-PGE (Western Australia), distinct in hosting immiscible sulfide deposits in lava flow channels. Other Ural type deposits like the Konder Massif (Russia), form a clinopyroxenite-dunite diapir, with PGE deposits mined from alluvial placer deposits. The PGE's here is mainly cooperite (PtS), sperrylite ($PtAs_2$) and minor occurrence of tulameeite, sobolevskite, braggite, keithconnite and isoferroplatinum (Rudashevskiy, Fomenko, & Malitch,

1994). *"The low 187Os/186Os ratio of the PGM in clinopyroxenite-dunite massives confirm the mantle source for the PGE mineralization*" (Malitch, 1998).

4.5 Layered intrusions

PGE deposits that form in layered intrusions are deviants of mafic to ultramafic magmas. Such magmas are thought to be mantle derived, formed by partial melting of asthenospheric and/or lithospheric mantle. When ascending through the lithosphere they may become contaminated, thus increasing the potential in forming a Cu-Ni-PGE deposit. The melt either continue throughout the lithosphere and erupts at the surface or is trapped in magma chambers, forming intrusive bodies.

The term "layered intrusions" comes from the signature created by the sharp lateral differences between gravitational segregated silicates, formed by crystal fractionation and settling of minerals in layers on the chamber floor. Following Bowens reaction series, olivine crystallizes at the highest temperatures, followed by pyroxene (Bowen, 1922). These silicates form by different processes (see section 4.8) inside the magma and start to sink at a rate of 40-1000m yr^{-1}, depending on size and composition (Hall, 1996). The correct set of minor differences in the mantle composition, crust contamination and degree of partial melting, can result in the forming of a mineral deposits of economic interest.

As crystal fractionation proceeds, the chemical composition and density of the magma will change as elements are partitioned in the melt. Olivine contain elements that have high densities and therefore reduces the total density of the melt when removed. When feldspar crystallizes, the melt densities will increase. In a totally closed magma chamber, the crystal fractionation progresses without any addition or withdrawal of chemical components. On the contrary, in an open system the magma chamber experience recharge episodes, where density and chemical composition have a major impact in the formation of a layered intrusion ore deposit. In these events, the chemical differences of the stationary vs intruding magma can cause two scenarios: Fountain vs Plume (Naldrett & Von Gruenewaldt, 1989).

The "Fountain" theory is based on the new injected melt composition to be denser than the melt already present in the magma chamber. Resulting in the newly injected melt to stay close to the chamber floor, restricting mixing of the two phases to this area of the magma chamber (visually expressed in figure 4.5). A theory most likely in a lesser evolved magma chamber, subjected to injection early in the crystallization sequence. Not the environment know to form PGE rich ore deposits.

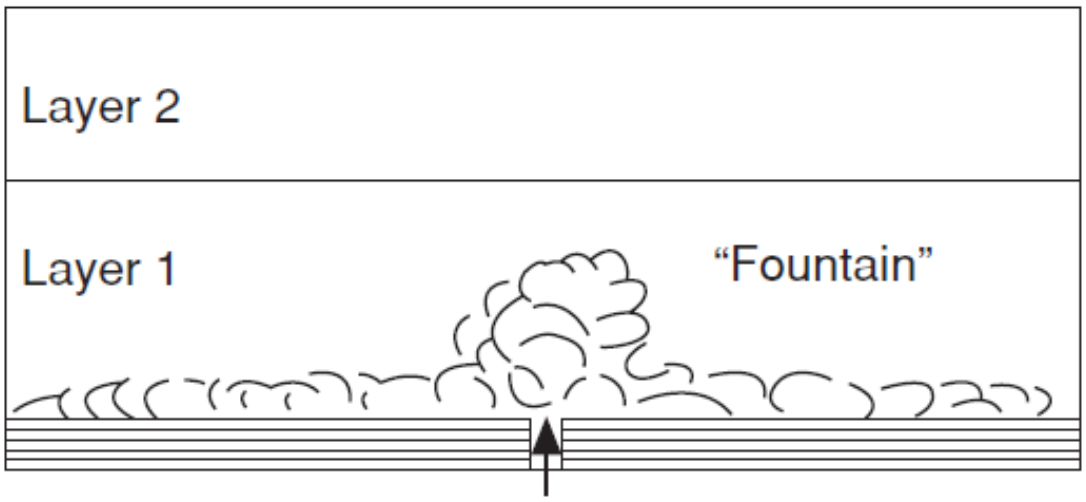

Figure 4.5: Injection (arrow) of a new heavier magma that settles at the bottom of the magma chamber. Never in contact with layer two and therefore does not undergo extensive mixing. (Robb, 2008).

The “Plume” theory explains the scenario of injecting a melt with lower density, creating a plume that rises through the magma chamber. Resulting in turbulence and more thorough mixing of the two liquids, throughout the whole magma chamber. This is an important aspect in the formation of a PGE ore deposit and the preferred theory that forms s PGE rich deposit in the Bushveld Complex, South Africa (Kinnaird, Kruger, Nex, & Cawthorn, 2002), together with other enrichment factors described in sections 4.6 and 4.7.

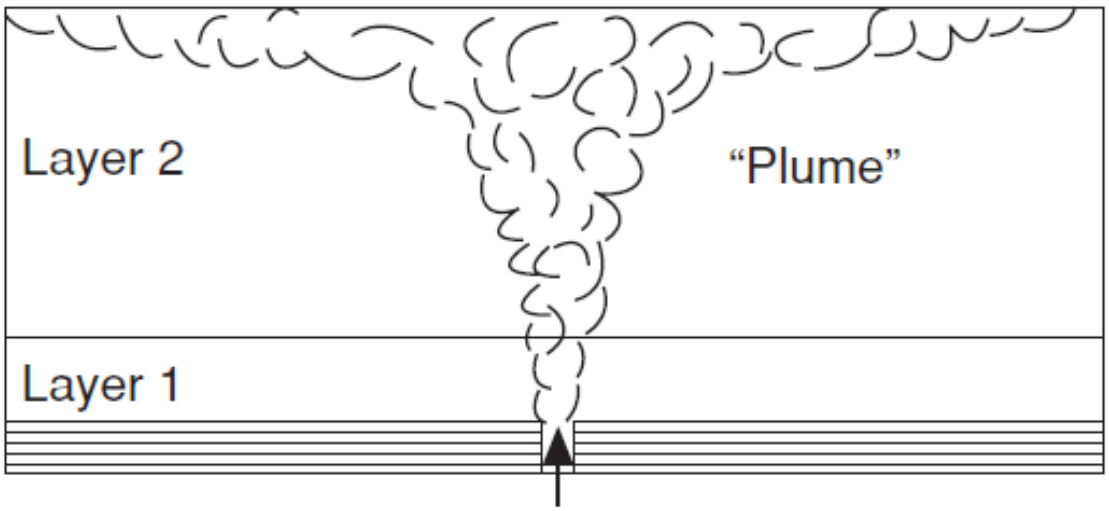

Figure 4.6: Injection (arrow) of a lighter, less dense magma that rises upward to come in contact with the magma chamber roof. Introducing turbulence and mixing of the chamber components. (Robb, 2008).

4.6 Liquid immiscibility

At any point in the evolution of a magma, liquids can start to separate into unmixable phases. Minerals like pyrrhotite, pentlandite and chalcopyrite is evidence of sulfide immiscibility. A chemical reaction that happens when a magma is no longer able to dissolve all of the sulfide and rather form immiscible sulfide droplets scattered throughout the melt. Elements that are more compatible with sulfide melts, will partition in to this phase as the sulfide circulates in the magma chamber. Ni, Fe, Cu and Co are the most common compatible elements with sulfide and will partition in to sulfide liquid when given the opportunity. Rarer elements such as Au and PGE's will also bond to the immiscible sulfide, but at a much slower rate due to the scarcity of these elements in the melt (Robb, 2008). Processes that control sulfur saturation includes oxygen fugacity, cooling, silica enrichment, mixing, external sulfur source and pressure.

Sulfur is dissolved in the magmas by displacing oxygen bonded to iron and is therefore strongly controlled by the oxygen fugacity (fO_2) (MacLean, 1969). The ability for a magma to dissolve sulfur is falling as fO_2 increases.

Cooling of a magma will lead to crystal forming. As crystals fractionate and starts sinking, the volume that is left to dissolve sulfur decreases, lowering the sulfur saturation threshold and therefore promoting sulfur saturation at an earlier stage in the magma evolution.

Contamination of silica rich components, like assimilation from silica rich country rock will act as a factor in sulfur saturation. Such a reaction can push the magma in to the sulfide saturation field in figure 4.7 (Robb, 2008).

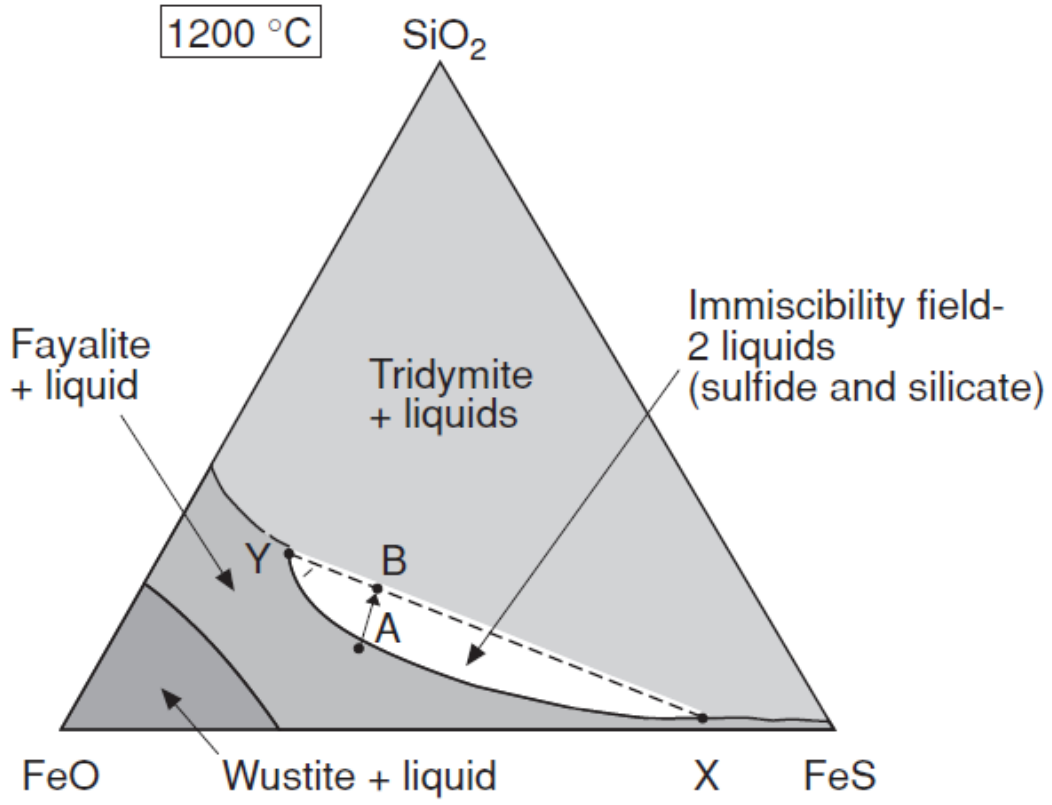

Figure 4.7: A magma contaminated by a silica rich source will throw the crystallization equilibrium from point A to B. Moving away from the solid crystallization window of fayalite and into the immiscibility field between point X and Y. This causes the melt to achieve sulfur immiscibility. (Naldrett & MacDonald, 1980).

Mixing between magmas of different compositions may also promote sulfide saturation, with reference to figure 4.8 from Robb (2008). We are starting with a batch melt of composition A, that is under saturated in sulfur until it reaches the sulfur saturation curve at point B. Here the magma continue to crystallize orthopyroxene by following the equilibrium curve and lowering the weight percent of sulfur as the magma gradually crystallize with decreasing temperature. At 20% total crystallization, the magma undergoes a replenishment episode represented by point C (1180°C) of a magma similar to the composition in A. The mixing of A-C would form on the line connecting A and C. If the final mixing resulted in a composition represented by AC, then the magma would be under saturated and all sulfur would be dissolved in the magma. Another scenario would unfold if the same replenishment occurred instead at point D with 35% total crystallization. Still with a replenishment that is similar in composition to A, the mixing result at AD would be oversaturated in sulfur. Then leading to the excess sulfur to form an immiscible phase in the magma.

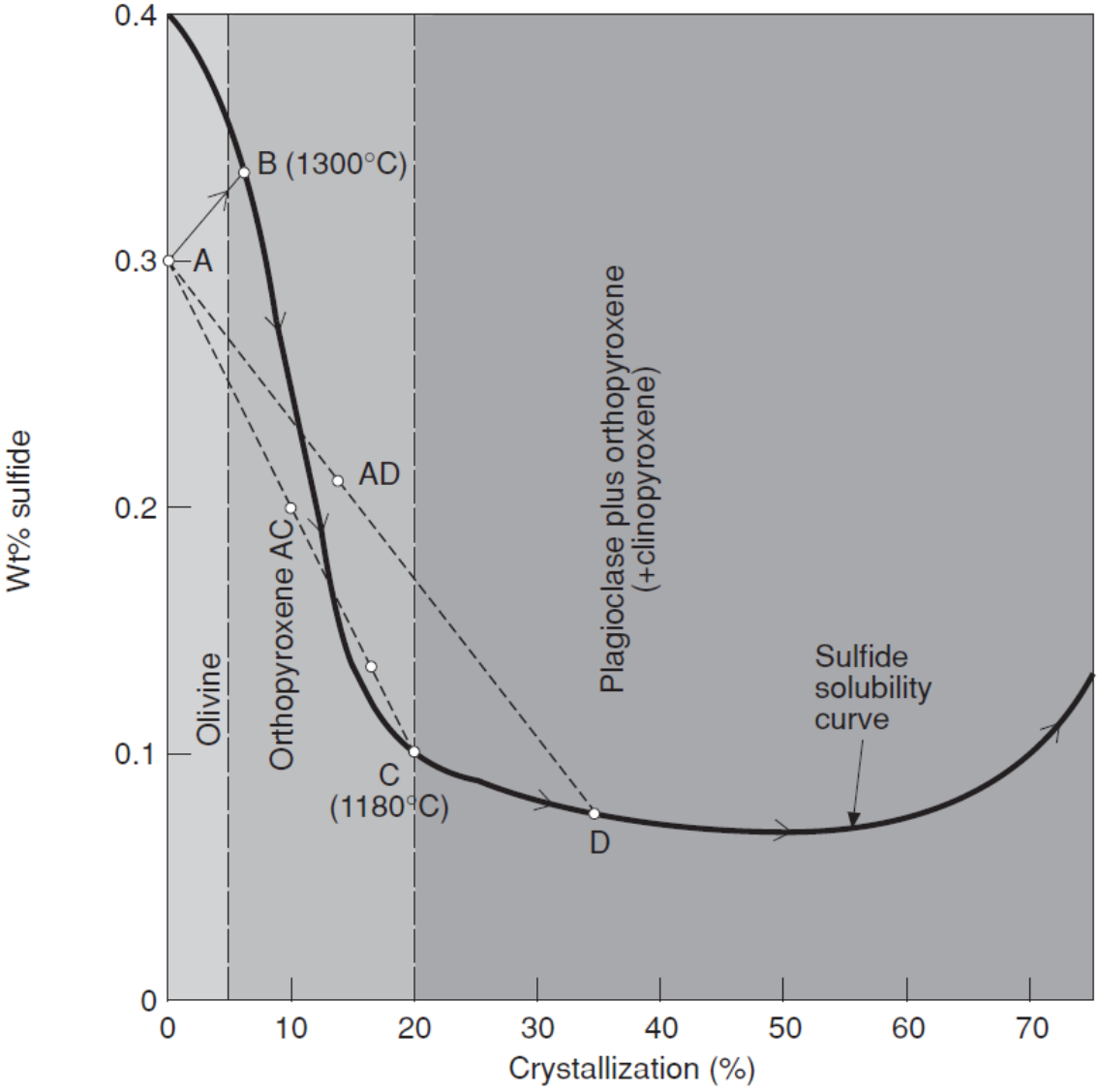

Figure 4.8: Sulfur solubility as a magma progressively crystalize in a magma chamber, such as Bushveld in South Africa (Naldrett & Von Gruenewaldt, 1989).

Sulfur can also be added to a magma by the melting of a sulfur rich country rock resulting in sulfide oversaturation. An explanation often suggested for magma that have been in contact with sedimentary rock such as “chert, bonded Iron formation or shale” (Robb, 2008).

With increasing pressure, mafic magmas shows exponentially decreasing ability to dissolve sulfur (Mavrogenes & O’neill, 1997)

4.7 R-factor

The R-factor simply explains the liquid mass ratio of silicate/sulfide in a magma chamber. A high R-factor means that an amount of sulfide have been in contact with ten times the amount of silicate melt. Because of the scarcity of some elements like Au and PGE's, a large volume of melt must be in contact with the sulfur to bind enough precious metals necessary to form an economic deposit. Campbell and Naldrett (1979) explained the terms of the R-factor as presented in the equation:

$$C_{sul} = C_0 D(R + 1)/(R + D)$$

C_{sul} = trace element concentration
C_0 = Original trace element concentration in the host rock
D = Sulfide / silicate partition coefficient
R = R-factor

Processes that results in a large R-factor, is when the immiscible sulfide interact with a large volume of silicate melt, like letting the sulfide droplet trough a high column or keep it suspended in the melt by turbulence. Both these factors are enhanced by "pluming" (figure 4.6), where replenishment of lighter magma induce turbulence in the magma chamber. In such an environment, magma will be well mixed and exposed to the chamber roof. Resulting in a high R-factor, creating in theory the correct environment to form a PGE deposit

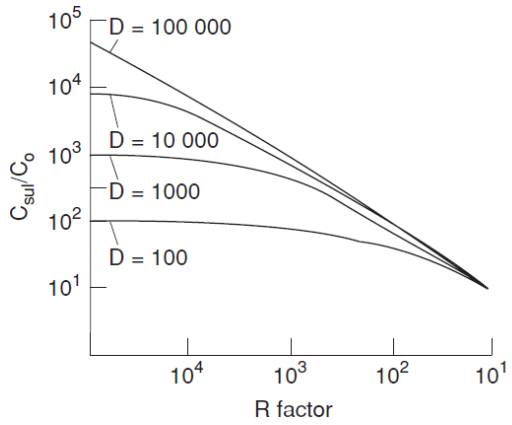

Figure 4.9: The relationship between enrichment (C_{sul}/C_0), partition coefficient (D) and R-Factor (S.-J. Barnes & Francis, 1995).

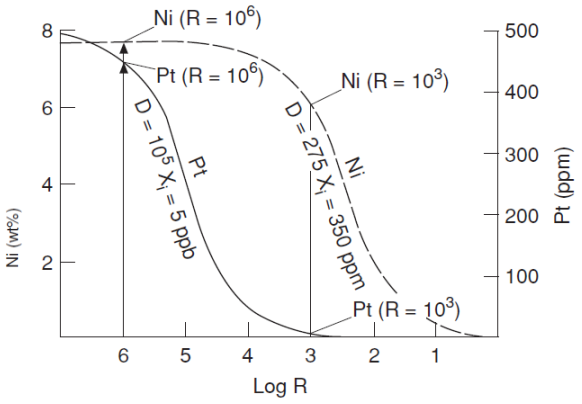

Figure 4.10: Effect of varying R-factor (Naldrett, 1989).

As seen in figure 4.10, Robb (2008) explains that a magma chamber subjected to processes that result in a low R-factor have the potential to form a Ni ore, but would contain very low amounts of Pt. This is because of the relative high initial Ni composition (350 ppm) and that there is not enough time to scavenge for Pt before the sulfide melts deposits on the chamber floor. In the example with high R-factor, a Pt deposit will form with a total of 480 ppm Pt. If the time for the sulfides to scavenge for Pt is substantial enough, a melt with a very low initial composition (5ppm) of Pt is able to produce a deposit of economic value. The Pt is being concentrated into the sulfur that sinks and settles on the magma chamber floor, forming a thin but rich layer of sulfide and Pt.

4.8 The Irvine model

Bowen (1922) explained how minerals would form in a cooling melt, dependent on their specific crystallization temperature. However, given the replenishment episodes subjected by an intruding magma, the temperature and the chemical composition of the magma will be in constant change. Therefore, minerals will crystalize to restore the chemical balance in the melt, a process explained in the Irvine model (Irvine, 1977) by using ternary phase diagrams. His study shows two models, one that is left to crystalize at equilibrium (figure 4.11) and one subjected to contamination (figure 4.12) during crystallization.

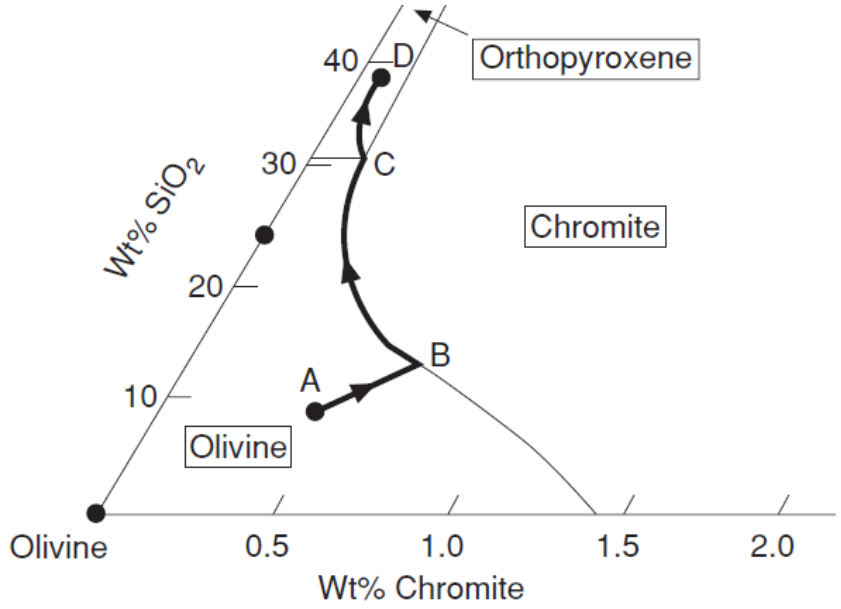

Figure 4.11: Irvine model, showing the general crystallization trajectory for a melt of mafic composition (Irvine, 1977).

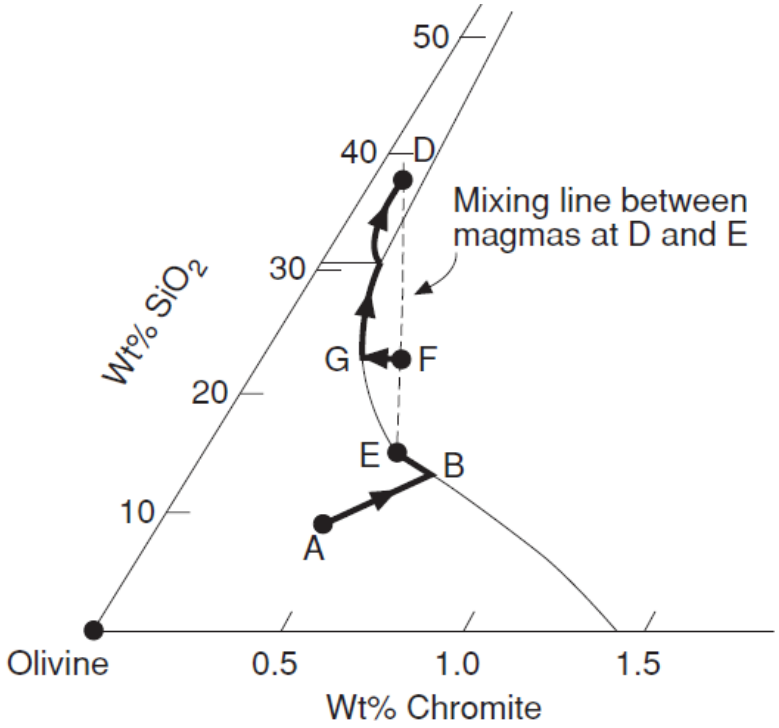

Figure 4.12: Irvine model, showing a magma subjected to contamination (Irvine, 1977).

A batch melt with composition represented by point A (figure 4.11) will only crystallize olivine, forming a cumulate rock until the composition reaches the cotectic line at point B. The melt will then crystallize along the cotectic line forming small amounts of chromite together with olivine. As the melt crystallizes along this cotectic line, the SiO_2 will begin to build up in the melt until point C. Here, SiO_2 will be so high that chromite is no longer stable and orthopyroxene will start to form a bronzite cumulate rock (Robb, 2008). This crystallization path would not form a chromite layer, but chromite as accessory phases in the forming cumulate rock.

Figure 4.12 shows a scenario where the magma is subjected to replenishment at point D, with a composition similar to point E. This throws the chemical composition off the cotectic line and into the stability field of chromite along the D-E line. The new composition after mixing is represented by point F, leading the magma to only crystallize chromite until it again meets the cotectic line at point G. This can explain the sudden forming of a chromite layer in a layered intrusion and if one see the bigger picture, could help explain the rapid changes between layers in a layered intrusion.

4.9 Layered intrusion PGE deposits

Major intrusions with world famous PGE deposits includes the Bushveld complex in South Africa, Norilsk (Russia), Stillwater (Montana, USA) and the Skaergaard intrusion (Greenland). All of these intrusions experienced a chain of events that leads to the forming of strata bound Cu-Ni-PGE horizons. This chapter will look into these well-known locations and the events connected to the ore forming history.

4.9.1 Bushveld Complex

Situated north of Johannesburg in South Africa, is the gigantic, 2060Ma (Walraven, Armstrong, & Kruger, 1990) Bushveld Intrusive Complex that contain the world largest reserve of PGE, producing 80% Pt and 20% Pd of the total PGE mined every year. The layered intrusive part of the bushveld, the Rustenburg Layered Suite covers an area of 65,000 km^2 and has a maximum thickness of 9 km. It developed during the Paleoproterozoic within a very short time interval of 10 Ma (Kinnaird, 2005) as a large volume of magma that exploited cracks in the continental crust and collected in a large magma chamber. Here it was subjected to many episodes of replenishment and crystallized as mafic to ultramafic lithologies, with three PGE reefs located in the "critical zone" (figure 6.6). A zone made up by gabbronorite, norite, anorthosite, pyroxeneite and chromitite that dips 26° W and NW (Merwe, 2007). The PGE ore is found in reefs named UG-2 (Upper Group 2) chromitite, Merensky Reef and the Plat Reef.

The UG2 chromitite has abnormal contents of PGE, with chromite content varying from 60-90% (Mungall, 2005) and a thickness varying from 40-120cm. The chromite layers are situated in a feldspathic pyroxeneite that underneath UG-2 is pegmatitic in texture with an irregular contact. Grades of PGE goes as high as 10 $g.t^{-1}$, but have an average of 5 $g.t^{-1}$ and is mostly concentrated in the lowest part (Lee, 1996). PGM's in UG-2 comprises of laurite, cooperite, braggite, vysotskite and isoferroplatinum (McLaren & De Villiers, 1982), indicating a Pt rich unit.

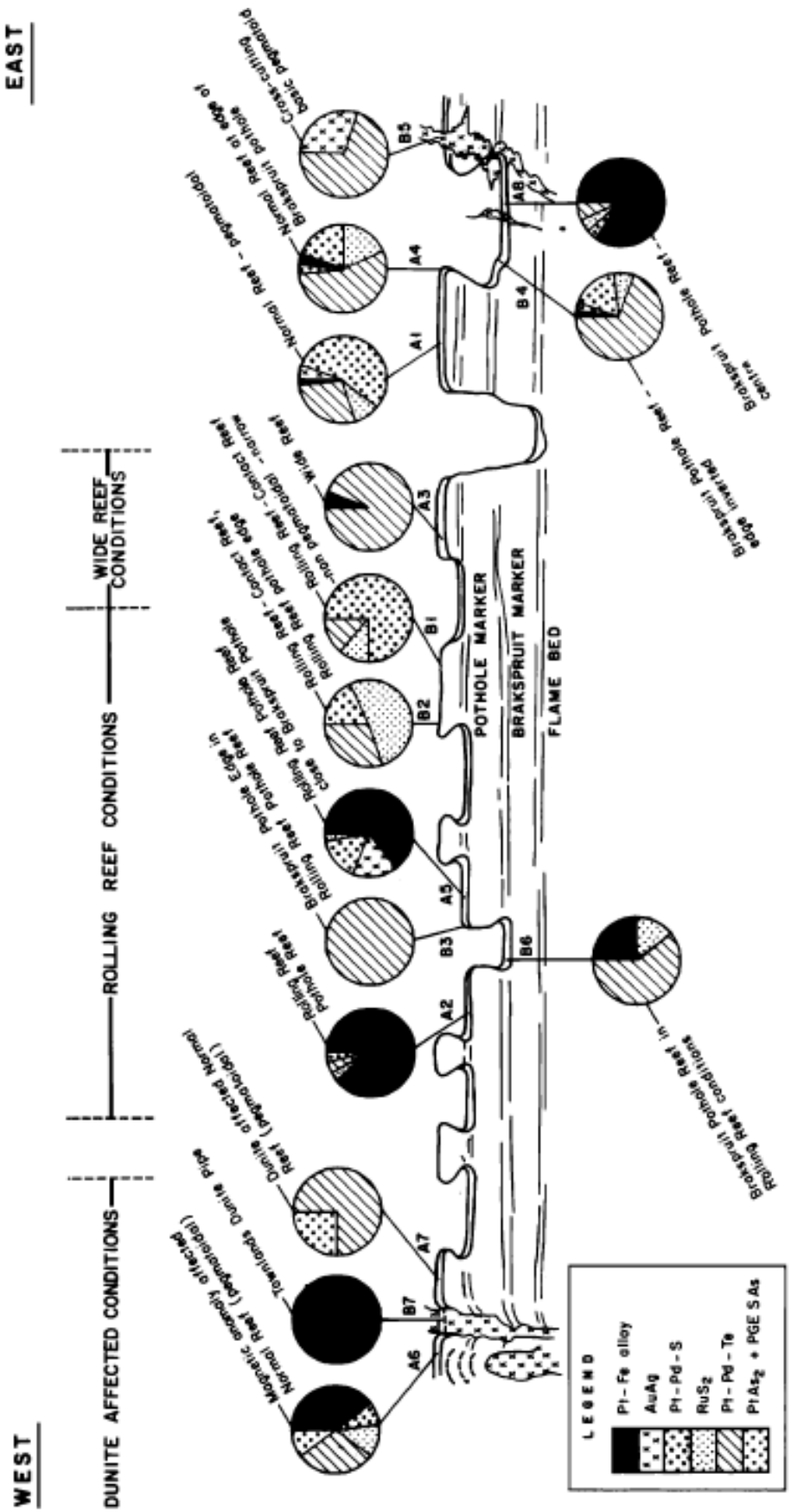

Figure 4.13: Cross section of Merensky Reef that show the different reef structures and the associated PGM's (Kinloch & Peyerl, 1990).

Merensky reef lies at the base of a very thin basal chromitite layer, overlain by pyroxeneite, norite and anorthosite (Vermaak & Hendriks, 1976). While mineralization varies to a larger extent in Merensky reef than UG-2, the high PGE tenors is mainly localized in pyroxenite or pegmatitic feldspathic pyroxenite containing thin slivers of chromitite. The general thickness is 30-35 cm, but the stratigraphic level is very complicated due to layers that suddenly disappear and the formation of oval "potholes" up to 50 meters deep (Kinloch & Peyerl, 1990). The PGE are associated with interstitial sulfides (pyrrhotite, pentlandite and chalcopyrite), a common ore forming relation in the Bushveld complex, but with variable sulfide concentrations. Grades varies from 5,6 – 9,2 $g.t^{-1}$ of Pt+Pd+Rh+Au, with a relative uniform average concentration of Pt/Pd value close to 2 (Cawthorn, Lee, Schouwstra, & Mellowship, 2002). The PGE mineral assemblage in the Merensky reef have huge variations when looking into details from several mines. Kinloch and Peyerl (1990) gives a good overview in their figure 7 (figure 4.13) and shows that the different lithologies accumulate different PGM's. The PGM's that are most common are Pt-Fe alloys, Pt-Pd-Te (monchite, merenskynite and kotulskite) and Pt-Pd-S.

Platreef is a 10 to 400m thick pyroxenitic (orthopyroxene, plagioclase and up to 5% clinopyroxene) layers that is located at the base level of the Bushveld complex (Holwell & McDonald, 2007). The most abundant PGM's in this reef is moncheite ($PtTe_2$), kotulskite (PdTe) and sobolevskite (PdBi), where all of them are associated with base metal sulfides (BMS). The distribution of PGM's show that all grains were located at the rim of sulfides, but only the Pt grains were located as inclusions within the sulfides (Holwell & McDonald, 2007).

4.9.2 Norilsk-Talnakh

Located in the middle of Russia is the Norilsk-Talnakh Cu-Ni-Pd deposits that is estimated to be the largest deposits of its kind in the world. It formed in the Upper Permian – Lower Triassic and interpreted as a feeding system to the Siberian flood basalts (Naldrett, 2013). The formation of the Cu-Ni-PGE rich deposit here, is presented as a large volume of magma with replenishment episodes in several magma chambers, with mixing between magmas of different level of enrichment (Naldrett, 1997). The Tuklonsky suite is the strongest enriched with PGE and "consist of 8-10 flows of poikilophitic tholeiitic basalts that in many places intercalated with Khakanchansky tuffite. The total thickness amounts to 220m, including 1 to 3 flows (60-65 m) of picritic basalt" (Naldrett, 2013). Sulfide immiscibility is explained by two possible mechanisms. One is the mixing between the mafic magma and a felsic component

in a deep-seated magma chamber from which the volcanic pile at the surface originated (Arndt, 2005). Ascending magma then collected more sulfur when assimilating the hosting sedimentary rocks, which were reduced to sulfide by coal contamination. The upward motion, kept immiscible sulfide in suspension and only started to sink when the melt intruded as a horizontal sill, where sulfides formed ore known as massive sulfides. The PGM's that are found in the different ores of the Norilsk layered intrusion is atokite, rustenburgite, isoferroplatinum, tetraferroplatinum, paolovite, stannopalladinite, plumbopalladinite, sobolevskite, kotulskite, moncheite, insizwaite, mayakite, cooperite, braggite, vysotskite, sperrylite and hollingworthite (Distler et al., 1999).

4.9.3 Stillwater

Located in the southern part of Montana in the USA is the 2.7 Ga Stillwater complex (Premo, Helz, Zientek, & Langston, 1990) that intruded middle Archean metasedimentary rocks. Containing partly metamorphosed olivine and pyroxenite rich ultramafic to mafic rocks that hosts several sulfide rich strata bound sections with PGE anomalies (Mungall, 2005). One of these sulfide rich sections is the palladium rich J-M Reef, located near the middle of "olivine-bearing zone I" and is mainly hosted by norite and troctolite. The PGE mineralization is associated with disseminated sulfide mineralization (pyrrhotite, pentlandite and chalcopyrite), but very unevenly distributed as barren patches also occur. The PGM's found and described by Godel and Barnes (2008) in J-M reef are Pt-Fe alloy (isoferroplatinum), Pt+Pd sulfides (Braggite, cooperate and vysotskite), Pd-Pt telluride (telluropalladinite, keithconneite, kotulskite, moncheite and merenskyite) and other minor Pd-rich phases (zvyagintsevite (Pd-Pb) and palladian electrum (Au-Ag-Pd).

4.9.4 Skaergaard Intrusion

Located on the eastern Greenland coast is the 56Ma, 300 Km^3 Skaergaard Intrusion (Wotzlaw, Bindeman, Schaltegger, Brooks, & Naslund, 2012), a layered gabbro that formed in a closed magma chamber. Because of the unique crystal setting, this layered intrusion differs from the other intrusions presented above. The PGE mineralization is restricted to a continuous zone, the Platinova Reef located in the upper third of the intrusion. This mineralized zone is Au and strongly Pd rich (Nielsen, Andersen, & Brooks, 2005) that have a very clear repeated stratigraphic distribution, a signature unlike other layered intrusions. Nielsen et al. (2015) argues that the models which embraces sulfide saturation cannot explain the deposit formed in

Skaergaard and therefore can only be explained by liquid separation and PGE remobilization. As they state *"the sulphide melt droplets do not sink, but are re-dissolved in subsequently formed immiscible Fe-rich mush melt, and it is this Fe-rich melts that concentrates and transports the precious metals to the floor"* (Nielsen et al., 2015). An explanation that is very different from the processes presented by Campbell and Naldrett (1979). The dominating mineralization of precious metals occurs as Cu-Ag-Pd alloys in close relation to sulfides (digenite and bornite) (Andersen, Rasmussen, Nielsen, & Ronsbo, 1998). Other precious metal alloys like electrum, atokite and zvyagintsevite have also been described by Arnason and Bird (1994) and Bird, Brooks, Gannicott, and Turner (1991). Nobel metals as sulfides (vasilite) or tellurides (keithconnite) are very rare and only occurs in accessory phases.

4.10 Alaskan type deposit (formerly called Ural-Alaska type)

Related with the Komatiite melts (section 4.4) is the Ural-Alaskan type deposits that form in subduction zones (Thakurta, Ripley, & Li, 2008). They form as circular or elliptical pipe-like complexes (Johan, 2002) that usually occur in groups along trends of major faults (Himmelberg & Loney, 1995). Sulfide horizons have only been reported from a few Alaskan type deposit as Salt Chuck Complex (Johan, 2002) and Duke Island (Thakurta et al., 2008). The magma genesis in subduction zones gives primitive basalts and peridotites derived from highly oxidized magmas. Under high oxidizing condition (fO_2) the PGE's form as Ferro-alloys in association with chromite (Mungall, 2002). These conditions does not represent the optimal conditions to form a Cu-Ni-PGE deposit (Thakurta et al., 2008). The same author described the minerology of Duke Island, a good representation of the typical Alaskan type intrusion. Dunite is Mg olivine rich, with high degree of alteration in the form of serpentine and magnetite with some disseminated chromite. Wehrlite composed of olivine and clinopyroxene that often show triple junction at grain contact. Olivine clinopyroxenite with 80% clinopyroxene and 20% olivine with some minor hornblende. This is also the lithology that hosts most of the sulfides. Hornblende-magnetite clinopyroxenite is relatively coarse grained with minor interstitial hornblende. The sulfides is located as massive sulfides deposits, where 95% is represented by pyrrhotite, ~5% chalcopyrite and minor occurrence of pentlandite. However, this types of deposits differs from the typical layered intrusions with a concentric zonation arrangement of the lithological units and that orthopyroxene is absent from the whole ultramafic assemblage. Plagioclase is only found in the narrow marginal zones (Thakurta et al., 2008). The general distribution of economical elements gives depleted values of Ni, Os, Ir and Ru and enrichment

in Pt, Pd and Cu (Thakurta, Ripley, & Li, 2014). Further description of the individual PGM's in this complex is not available at this time.

4.11 Platinum group minerals

PGM's are minerals that have one or more PGE incorporated in the crystallographic lattice. These elements are represented by Pt, Pd, Rh, Ir, Ru and Os and belong to Group VII transitional metals in the periodic table of elements, together with Fe, Co and Ni. These elements can be further subdivided into two groups, the light (Ru, Rh and Pd) and the heavy (Ir, Os and Pt). Their low abundance on earth and the strong siderophile nature has resulted in these elements becoming concentrated in the Earth's core. Therefore the major PGE deposits like Bushveld and Norilsk are all derived from a parental melt, that formed by partial melting of the mantle, which contains intermediate concentrations of PGE. They can then become concentrated into economic ore deposits due to sulfur immiscibility and replenishment in a larger magma chamber in the Earth's crust (Daltry & Wilson, 1997).

Daltry and Wilson (1997) published a full review of the PGM's documented throughout the world. They describe ninety-six PGE minerals that have been accepted as a PGM, and mention more than 500 unidentified PG – phases. The most abundant PGM's form with sulfur (Cooperite, Braggite, Vysotskite), arsenic (Sperrylite and Hollingworthite), tellurium (Monchite and Merenskyite) or iron (Tetraferroplatinum and Isoferroplatinum) as the bonding elements.

PGM's forming with S, As and Te all occur in ultrabasic magmatic systems and often within mss (monosulfide solution) as inclusions in pyrrhotite, pentlandite and chalcopyrite. Based on their crystallographic structure, the main PGM's can be divided into 5 mineral groups

- Arsenopyrite group: osarsite and rusarsite
- Nickeline group: niggliite, sobolevskite, stumpflite and sudburyite
- Pyrite group: laurite, maslovite, michenerite and sperrylite
- Melonite group: merenskyite and moncheite
- Cobalite group: hollingworthite, israrite, platarsite and tolovkite

The UG-2 layer in the Bushveld layered intrusion contains an ore deposit that is very rich in PGM and a good example of the ore-forming environment where PGE prefer to form

minerals with sulfur. McLaren and De Villiers (1982) describes the UG-2 ore forming environment at temperatures of 1200°C with log fO2 < -10 and log fS2 at -1 to 0.

The Platreef show a very different PGE mineralization to both Merensky reef and the UG-2 layer. Fifty percent of the PGM's in this reef are tellurides, compared to only 20% in Merensky reef. Sulfide immiscibility is thought to occur in a deep stage prior to the intrusion (Holwell, McDonald, & Butler, 2011). This already PGE enriched magma entered Bushveld, but due to the high density, was restricted to the base of the magma chamber. Later crystal contamination ($\delta^{34}S$ of 2.6 – 9.1) and reaction with Bushveld cumulates (Holwell, Boyce, & McDonald, 2007; Manyeruke, Maier, & Barnes, 2005), increased the metal tenor of the melt. Because of the crustal contamination, Holwell et al. (2011) point to the possible increase in oxygen fugacity from assimilation of felsic country rock as presented by Li and Naldrett (1993).

The J-M reef in the Stillwater complex represents a slightly different association of PGM. The reef is dominated by the braggite-vysotskite PGM series hosted by BMS that formed at temperatures of 1100°C (Barnes & Naldrett, 1985). Elliott, Grandstaff, Ulmer, Buntin, and Gold (1982) concluded that the J-M reef is strongly oxidized due to metamorphic redox re equilibration. The 9.6 wt% iron in Ferroplatinum alloys correlates within one log unit of the fO2 that Elliott et al. (1982) predicted at 1200°C. The missing iron is suggested to have been lost due to later fluid interaction with the Ferroplatinum alloys.

The most abundant PGM's discovered in the RIC are those forming minerals with Te. The most important solid solutions known to form between Pt, Pd and Ni tellurides, occur between melonite and merenskyite (Rucklidge, 1969), Ni-poor merenskyite and moncheite (Cabri & Laflamme, 1976) and between moncheite and melonite (Hudson, 1986). These minerals form in high temperature magmatic systems as inclusions in pyrrhotite and pentlandite, and in lower temperature hydrothermal systems in chalcopyrite (Helmy, Ballhaus, & Berndt-Gerdes, 2005). Helmy, Ballhaus, Berndt, Bockrath, and Wohlgemuth-Ueberwasser (2006) described the interaction between PGE-tellurides and sulfide solution. Above 1000°C, the two phases are completely miscible, but this changes at 900°C, where sulfide and telluride solutions start to separate. At this temperature, monchite forms patchy, elongated grains within sulfide and occur in the center with a palladium rich corona. This suggests that sulfides rich in Te, Sb and Bi, form from a separate phase that fractionates into discrete bismuthotellurides and "*semimetals like Te, Sb, and Bi are such potent complexing agents for Pt and Pd that in their presence, no Pt and little Pd will enter the lattices of high-temperature sulfides."*

According to their research, Pt forms minerals at significantly higher temperatures than Pd. Pt rich minerals start to crystallize at temperatures of 920-900°C, dependent on the Te

content in the experiments (Helmy et al., 2005; Helmy et al., 2006). Pd rich minerals in the same experiments started to crystallize at temperatures of 725°C.

The presence of Ni incorporated in tellurides can serve as a quantitative indicator for the melts richness in PGE. "*If Ni-rich tellurides occur in abundance, both the (Pt + Pd)/semimetal bulk ratio and the absolute Pt and Pd concentrations in the sulfide melt are likely to have been low at the time of telluride crystallization"* (Helmy et al., 2006). PGE rich deposits like Bushveld, have very little Ni incorporated in the crystal lattice of PGM's.

5 Results

5.1 Remapping of the RUC

Previous maps by Emblin (1985), Øen (2013) and Rasch (2013) suggested that the eastern marginal zone was up to 300m wide in certain areas from the “Lake District” (figure 5.7) and to the north. This description contradicted with field observations by Grannes and Nikolaisen. Therefore, a teamed effort was made to revise and create a new map of the RUC that correctly shows the relationship between ultramafic series and the country rock.

At close evaluation, the eastern marginal series south of the largest lake bellow the *finger* locality (marginal zone cumulates that interfingers the gabbro, visible on the map in the eastern corner of the east-west striking 700m ridge (figure 5.7)) was correctly mapped. Scree material form the gabbronorite cliff face covering the contact south in the lake district, prevented detailed observations. Most of the major revisions are located north of the lake. The final map as seen in figure 5.7, was assembled by Grannes, K, R. and is explained in more detail in his thesis (Grannes, 2016) (in prep). The following subsection only describes the field observations that supports the arguments by Grannes and Nikolaisen, leading to the decision of minor changes to earlier maps of the RUC.

The map by Emblin (1985) show the marginal zone to be subdivided based on location and parent lithology. In the new 2016 revision, the marginal zones are all given the same color regardless of local mineral content. Therefore, not to cause any confusion, the following headings only describe observations tied to locations and not subdivisions within the marginal zone.

5.1.1 Eastern Marginal Zone

Between the large lake and the *finger*, the MZ thins with a clearly visible boundary towards the gabbronorite (figure 5.1A). The contact with the ULS is defined as the point where intergranular feldspar (figure 5.1B) is no longer visible under hand lens in the ultramafic cumulates.

On the north side of the 700m ridge and the *finger* (figure 5.7), the marginal zone appearance changes drastically. Defined by increased grain size (figure 5.1C), higher amounts of interstitial plagioclase and large pyroxene oikocrysts (figure 5.1D). The MZ thickens marginally and continues with a sharp contact against gabbro for about 700m to the north.

According to older interpretations, this is where the “upper marginal zone” gives way and the “north eastern marginal zone” starts (figure 5.8). Mapping in 2015, demonstrated that this zone does not exist. The MZ was found to continue with an N-S strike and the contrast between the two lithologies is clearly visible at distance. At the cliff face with the gabbro xenoliths (figure 5.3) the MZ widens and proceeds towards the east. This E-W striking the MZ is difficult to follow eastward, as it appears and disappears over short distances before it again changes direction towards the north visible in a near vertical mountain side. This complexity is associated with the appearance of bronzite pyroxenite with patches of plagioclase (figure 5.1E). When mapping westward, the bronzite can be followed 200 height meters into the ultramafic cumulates, before it disappear underneath the ULS.

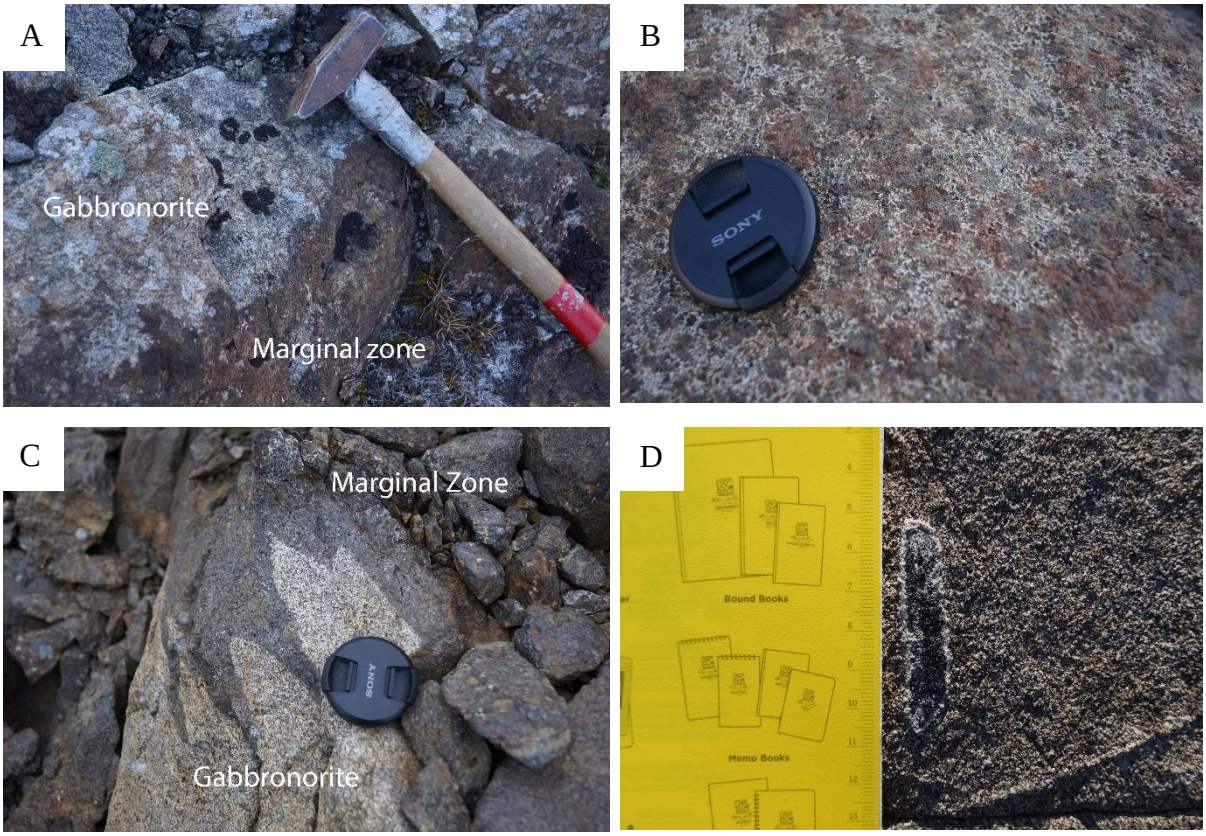

Figure 5.1: A) The MZ in contact with gabbronorite south of the *finger*. B) Intergranular feldspar in the MZ. C) The MZ in contact with gabbronorite north of the *finger*. D) Pyroxene oikocryst. E) Coarse grained bronzite with "patchy" interstitial feldspar.

Figure 5.2: The MZ north of the *finger*. Photo taken towards N-NE.

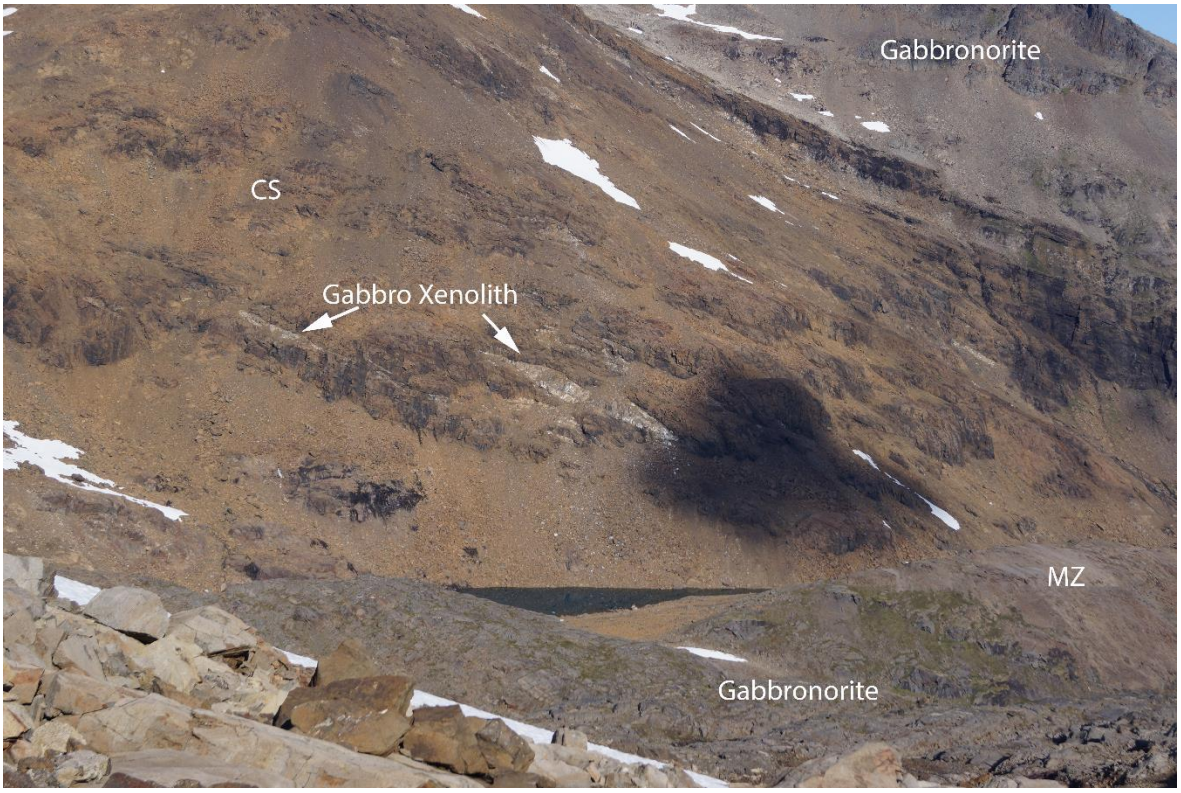

Figure 5.3: The cliff face with gabbro xenoliths. Photo taken towards N-NE.

5.1.2 Western Marginal Zone and Lower Layered Series

The lowest part directly east of Storvannet river, is a 25-30m thick layer containing distinct pyroxene porphyroclasts with a rim of plagioclase in a fine grained matrix (figure 5.4), with occasional pyroxene pegmatites intersecting the layering. Sulfides are visible as discontinues accumulations in the top part of the first layer. The texture observed here is consistent with that observed directly north of the "finger" and agrees with the "lower marginal zone" description by Emblin (1985). As this layer disappear under scree material, close outcrops of gneiss gave a good indication of the contact's approximate path and therefore resulted in a thinner interpretation compared with Emblin, Øen and Rasch.

Further up stratigraphy, the LLS changes abruptly with the appearance of a coarse-grained, 15-25 m layer that is identified with large pyroxene porphyroclasts in plagioclase matrix (figure 5.5A). This layer resemble observations further north in Isdalen, where the ULS and the gneiss is in direct contact (figure 5.5B).

The last stratigraphic section is a copy of the first layer with pyroxene porphyroclasts in a fine-grained matrix. Due to large loose scree fans, the rest of the unit is inaccessible for detailed mapping.

Figure 5.4: Black pyroxene porphyroclasts with a white rim of feldspar, in fine grained matrix

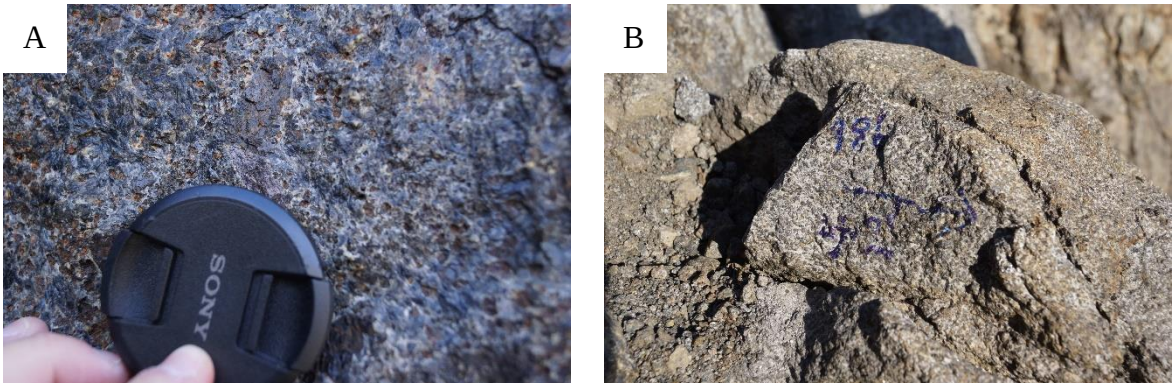

Figure 5.5: A) showing the lower layered texture with black pyroxene porphyries in the LLS, East of Storvannet river. B) Showing the eastern marginal zone between upper layered series and gabbro/gneiss in northern slope of Isdalen.

Along the southern side of Storvannet, only minor revisions were done to the Emblin map. Generally, we observe the MZ to be thinner than previously described. Emblin (1985) presented three major faults at the eastern end of Storvannet that of set the MZ and the gabbro. Revisions by Øen (2013) and Rasch (2013) presented a straight contact along the hillside with one fault, only. Our 2014-15 mapping suggest that faults are absent (figure 5.6). Rather, we observe an uneven marginal zone that is molded by the ragged gabbro sidewall of the magma

chamber. The MZ in figure 5.6 only represents a thin shell that gradually changes to ULS underneath.

Access to Isdalen was challenging, with large boulders, scree material, and steep hillsides. Hence only minor, but important revisions were applied to more accurately show lithological contacts.

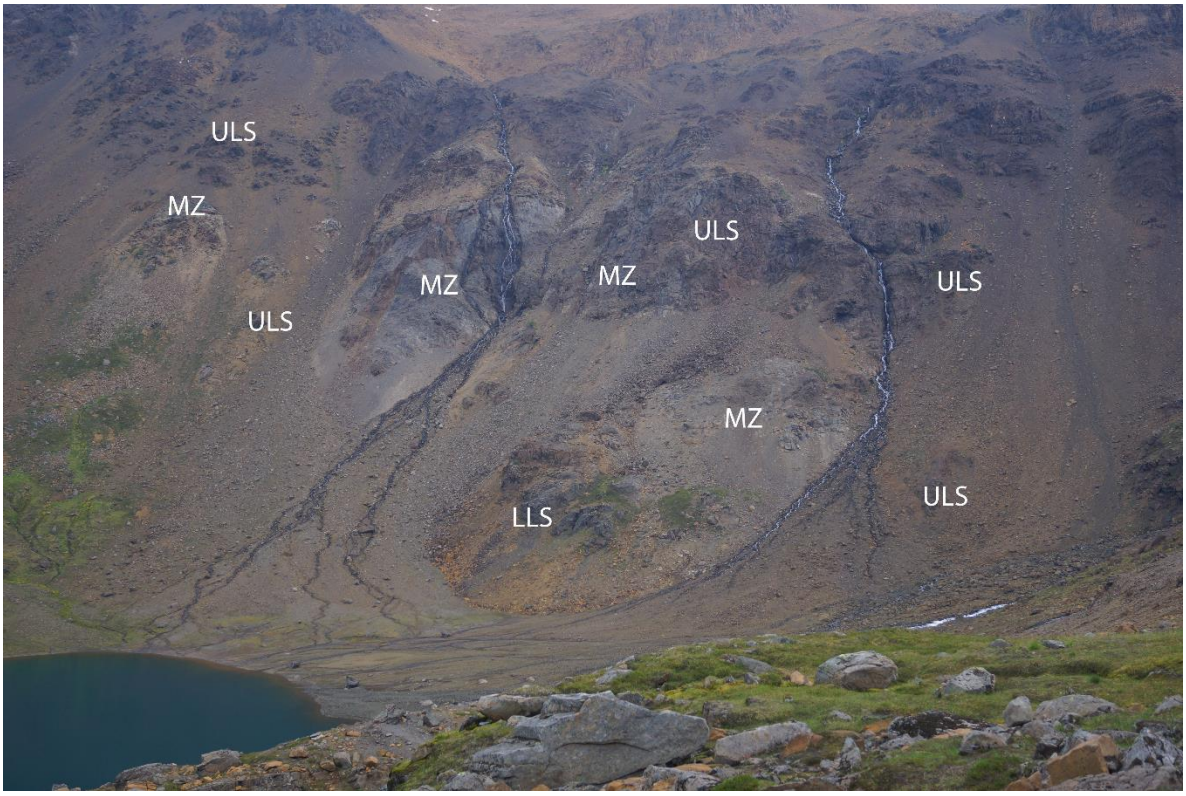

Figure 5.6: Eastern end of Storvannet, showing the irregular contact of the ULS and the MZ against the now eroded gabbro. Photo taken when standing on the gabbro, towards the N-E.

5.1.3 Upper Layered Series

The main target of the 2014 field season was to improve mapping of the lithologies and particularly the irregular contacts between the ULS and the CS. The ULS can be observed as "rafts or island" enclosed by the CS lithologies. In the new map by Grannes (2016) (in prep), the observed islands of ULS are particularly visible northeast in the "Lake District" (figure 5.7).

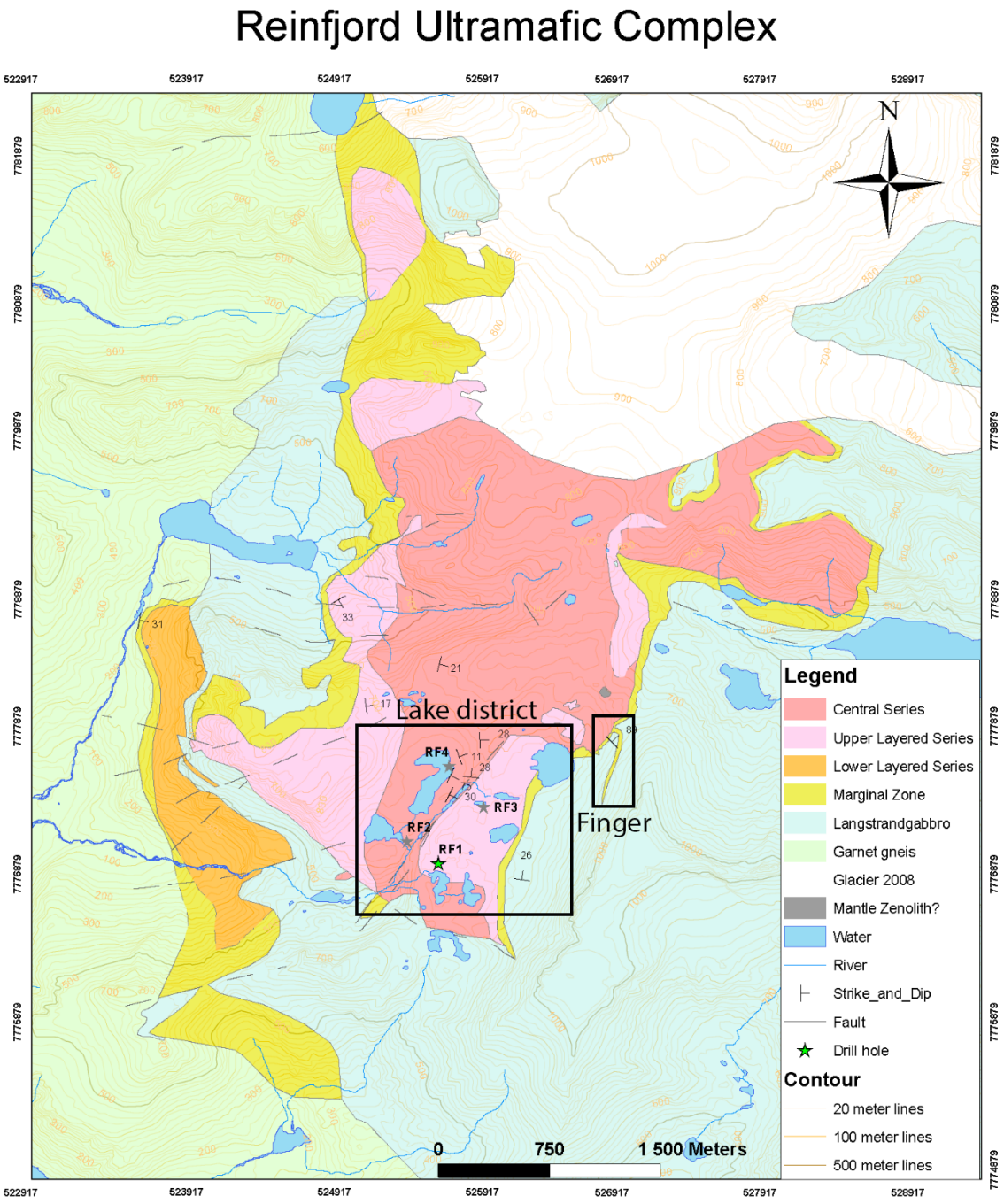

Figure 5.7: Revised map of the RUC. (Grannes, 2016) (In prep).

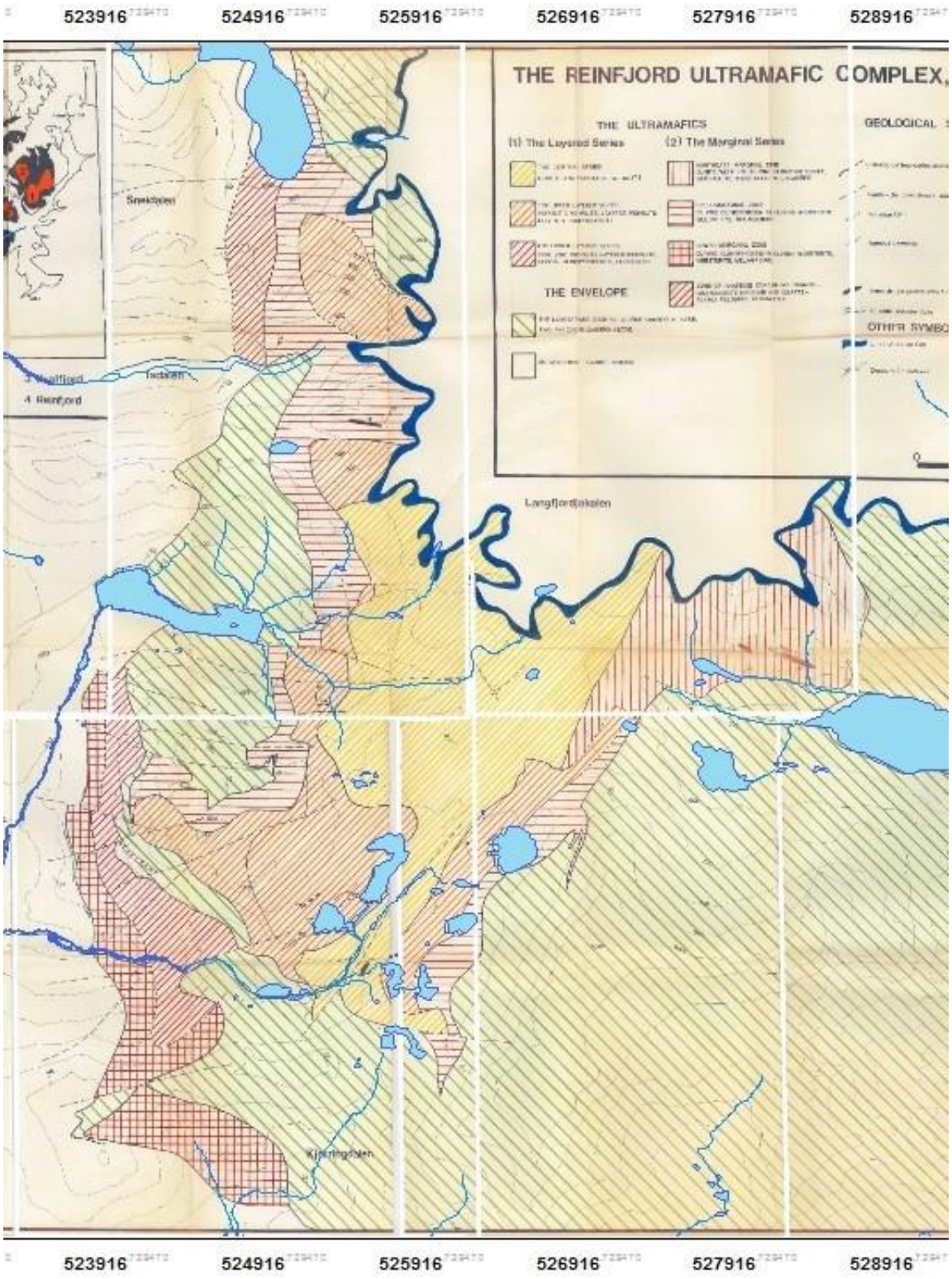

Figure 5.8: The RUC lithology map by Emblin (1985). (Geo reference by Grannes (2016)). N-S spatial reference is visible in figure 5.7

5.2 Minerology and petrology

Assessing and identifying the mineral assemblage required a combination of several of the methods described in chapter 3. Together with EPMA data, the following sections describe all the visual and chemical aspects of each mineral found in the four selected thin sections. All minerals were identified according to criteria outlined in Raith, Raase, and Reinhardt (2012).

5.2.1 Silicates

5.2.1.1 Olivine: $((Mg, Fe)_2SiO_4)$

Olivine is a nesosilicate identified optically in xpl by the third order interference colors, the very high refraction index and the irregular micro fractures. Olivine is colorless in ppl and shows no pleochroism. Serpentinization is common in the RUC, but rare in the thin sections provided for this thesis.

Two generations of olivine are present in thin sections 109.4 and 109.55. One comprises large grains with irregular boundaries (figure 5.9A), showing common alteration to serpentine and magnesite (figure 5.21). Fractures are partially or completely filled by carbonate an undulose extinction patterns in xpl imply these crystals formed during deformation.

The second olivine generation is fine-grained and formed interstitial together with fine-grained orthopyroxene and carbonate. They are anhedral to subhedral, show little deformation and form distinct triple junctions (figure 5.9B).

EPMA data on chemical composition of olivine show that both interstitial and primocryst olivine has the same composition as confirmed by Grant et al. (2016).

Table 5.1: EPMA data of olivine (appendix table F 4).

	SiO_2	MgO	FeO
Wt% Oxide	39.159	41.711	19.586

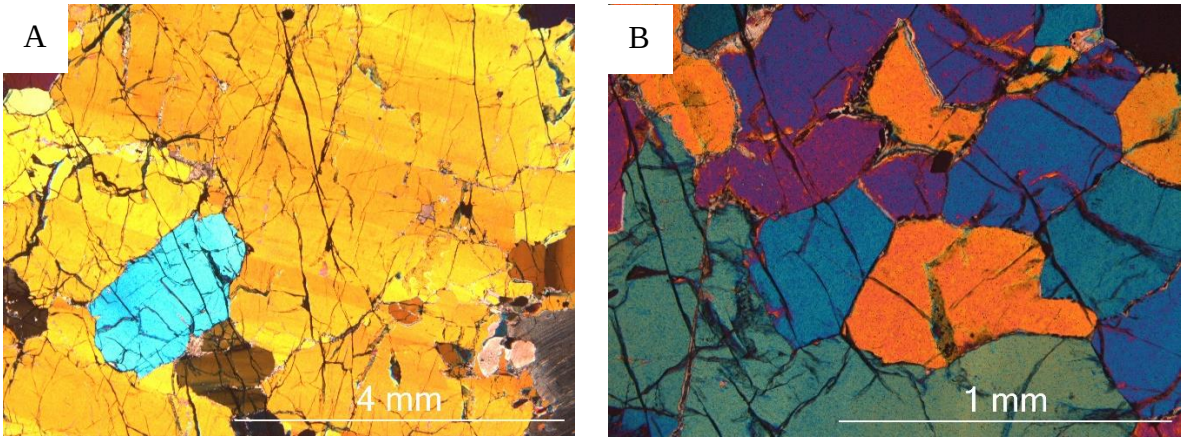

Figure 5.9: A) Large olivine, distinct by the deformation bands (xpl). B) Small olivine, with triple junction (xpl).

5.2.1.2 Clinopyroxene: (Diopside ($CaMgSi_2O_6$))

Clinopyroxene is an inosilicate that is identified by second order interference colors (figure 5.10A), high refraction index, extinction angle and two visible cleavage planes with 87° between them. The mineral is colorless in ppl and may have weak pleochroism of green or brown depending on iron content.

In the pyroxene pegmatite, the mineral occur as inclusions or exsolution lamellae in orthopyroxene (figure 5.10B). The interference colors when not obscured by alteration, is low second order blue-purple. Single grains are sub- to euhedral and show one good cleavage. In the dunite appearances change slightly, showing less alteration and forming grains surrounded by olivine, but also often with orthopyroxene, amphibole and magnesite (appendix figure B 23). Here, clinopyroxene is mainly euhedral and with similar grain size.

Table 5.2: EPMA data of clinopyroxene (appendix figure F 2)

	SiO2	Al2O3	MgO	CaO	FeO
Wt% Oxide	52.653	6.263	15.712	22.35	4.958

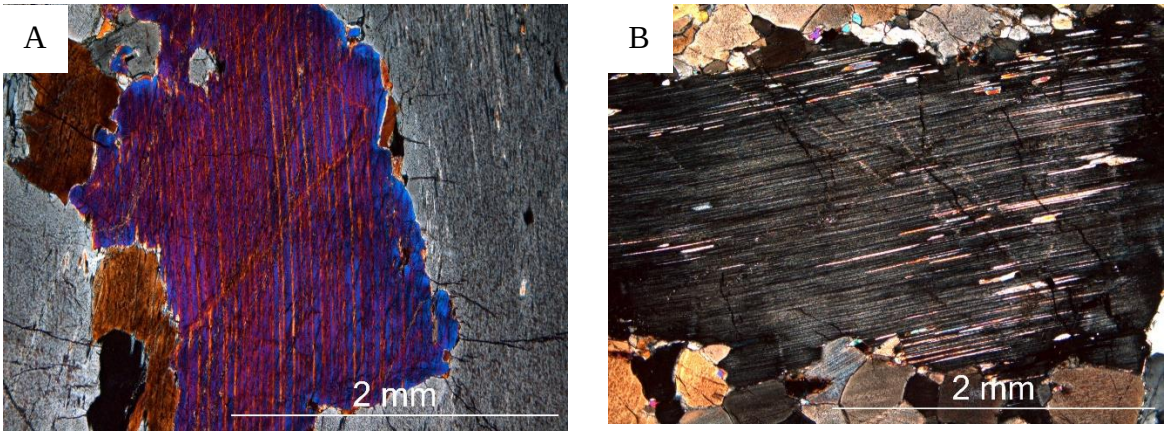

Figure 5.10: A) Interfernence colors of clinopyroxene (xpl). B) Orthopyroxene (almost extinct) with exsolution lamellae of clinopyroxene (xpl).

5.2.1.3 Orthopyroxene: Enstatite ($Mg_2Si_2O_6$)

Hypersthene ($(Mg,Fe^{2+})Si_2O_6$)

Orthopyroxene is identified in ppl by a weak yellow tint (figure 5.11B) and light brown to pink pleochroism. Xpl show extinction parallel to cleavages, first order interference colors and ilmenite exsolutions (figure 5.11A). Is distinguished from clinopyroxene by having parallel extinction.

This silicate is the main phase in pegmatite, where it forms large an- to subhedral crystals that can be 5 cm and bigger. It also forms intergranular rounded euhedral grains at the pegmatite interior and boarder. In the dunite, orthopyroxene form large euhedral crystals, but also appear as smaller grains with strong connection to amphibole, clinopyroxene and magnesite (appendix figure B 23).

All orthopyroxene analysis plot at the boundary between enstatite and hypersthene. Where the content of Al_2O_3 can give an indication for which is primary forming at the same time as ultramafic cumulates. In the pegmatite, the Al_2O_3 is significantly higher (>3.5 wt% Al_2O_3), probably reflecting an increased Al concentration in the pegmatite forming melt. The same is observed for orthopyroxene in the dunite, with close relation to both amphibole and clinopyroxene. These relations always occur inside smaller volumes and veins, with a sharp contact towards surrounding olivine (appendix figure B 23).

Table 5.3: EPMA data of orthopyroxene (appendix table F 6).

	SiO2	Al2O3	MgO	FeO
Wt% Oxide (Enstatite)	57.174	1.392	29.601	13.287
Wt% Oxide (Hypersthene)	55.715	4.057	28.816	13.384

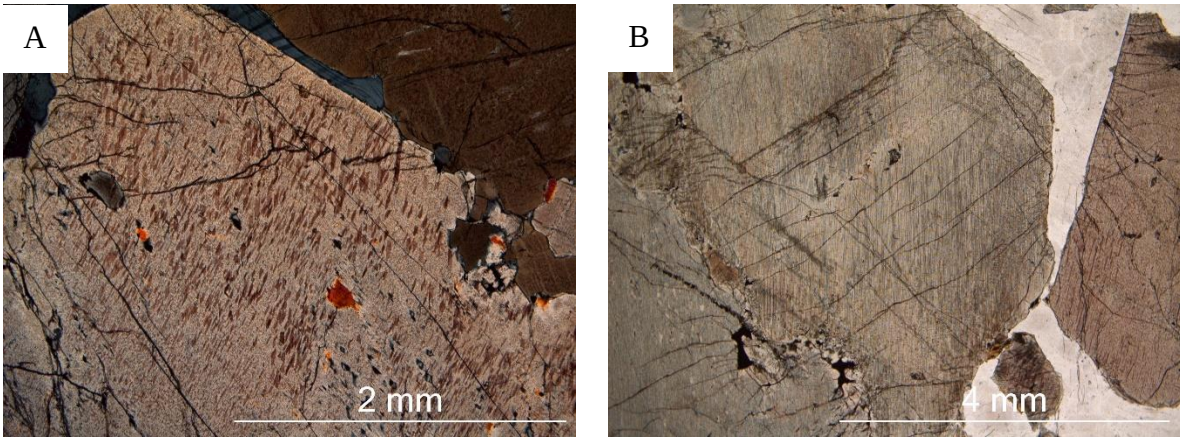

Figure 5.11: A) Orthopyroxene with ilmenite lamellae (xpl). B) Orthopyroxene from the pegmatite (ppl).

5.2.1.4 Biotite: $(K(Mg,Fe)_3AlSi_3O_{10}(F,OH)_2)$

Biotite is a phyllosilicate identified in ppl by its perfect cleavage and strong brown to dark brown pleochroism (figure 5.12A). Xpl shows fourth order interference colors (figure 5.12B) and parallel extinction.

The mineral is present in plagioclase dikes within the pegmatite. Crystallizing as small anhedral to subhedral tabular grains parallel to the dike wall, in contact with orthopyroxene, clinopyroxene, rutile and sulfides. In the dunite, biotite also appears with larger amounts of amphibole and cubanite (appendix figure B 59). Here the mineral was difficult to identify using optical microscope and was only found by its high K content during EDS mapping. EPMA also shows a distinct chemical difference presented in table 5.4

Table 5.4: EPMA data of biotite (appendix table F 3)

	Na2O	SiO2	Al2O3	K2O	MgO	FeO	TiO2
Wt% Oxide (Bt in dunite)	3.283	37.492	17.909	4.546	21.169	5.473	1.588
Wt% Oxide (Bt in pegmatite)	0.366	37.539	15.849	9.461	19.073	6.951	3.821

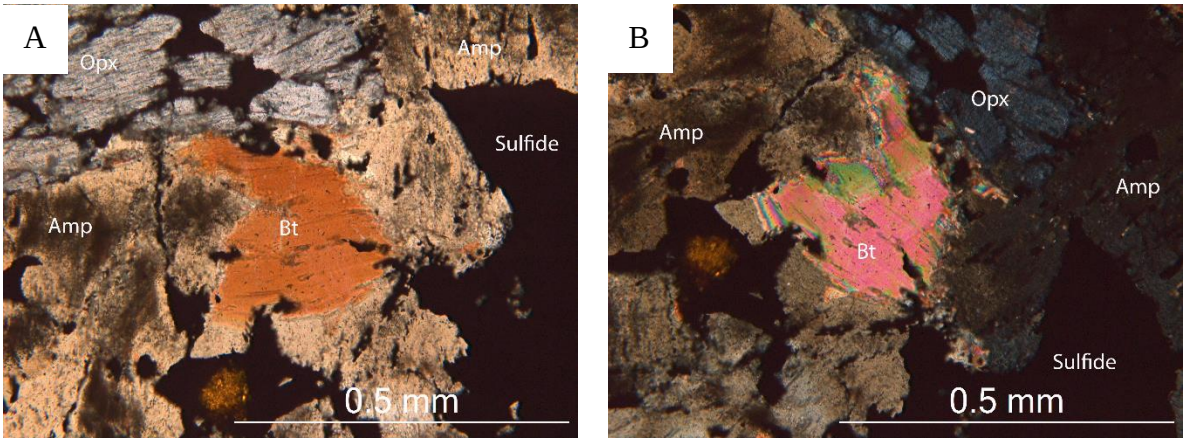

Figure 5.12: A) Biotite embedded within an amphibole (ppl). B) Same mineral rotated 60°, showing the high interference colors of biotite (xpl).

5.2.1.5 Amphibole: Magnesiohastingsite ($NaCa_2(Mg_4,Fe^{2+})Si_6Al_2O_{22}(OH)_2$)

Magnesiohornblende ($Ca_2Mg_4(Al,Fe^{3+})\ Si_7AlO_{22}(OH)_2$))

Amphibole is an inosilicate identified by its strong pleochroism and strongly altered texture. In ppl, the color shows a yellow to light brown. Interference colors go from high first to low second order and one dominant cleavage direction with extinction at a low angle.

Amphibole appears both in the pegmatite and in dunite but shows a very similar relation in appearances in both lithologies. A distinct feature is the strong alteration, which has almost completely altered some of the grains, making the interference colors difficult to identify (figure 5.13A). When the colors are visible, they show a low second order blue-purple and therefore overlap with clinopyroxene (figure 5.13B). As both amphibole and clinopyroxene have inclined extinction, these two minerals are difficult to tell apart and EDS analyses were necessary to distinguish between them.

EPMA shows the presence of mainly one type of amphibole, but a zoned amphibole (appendix figure B 42) within the pegmatite (Pd-cluster) exists as both hastingsite and hornblende. The zoning was not visible optically.

Table 5.5: EPMA data of amphibole (appendix table F 5)

	Na2O	SiO2	Al2O3	MgO	CaO	FeO	TiO2
Wt% Oxide (Magnesiohastingsite)	3.785	42.334	14.227	15.183	10.594	8.326	1.104
Wt% Oxide (Magnesiohornblende)	1.766	49.157	7.882	17.988	12.257	5.881	0.921

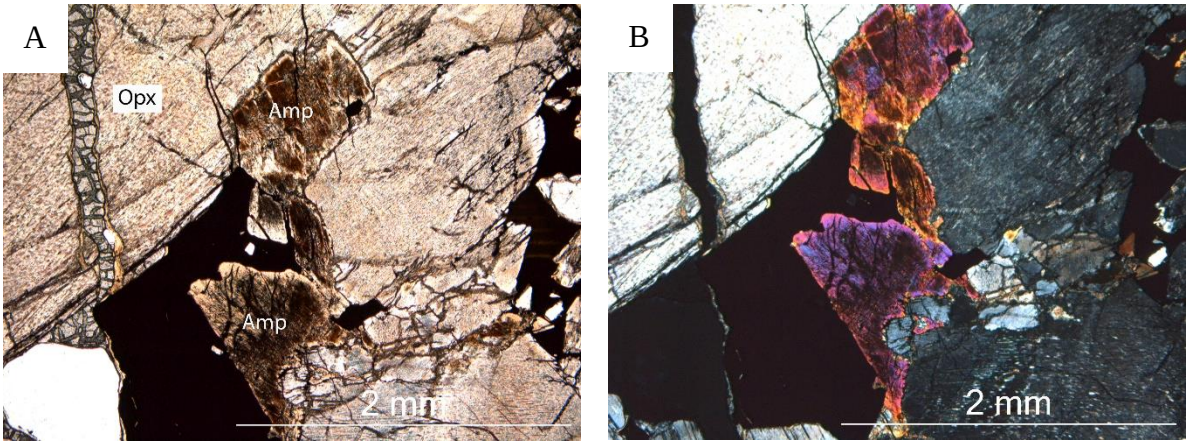

Figure 5.13: A) Typical amphibole with the altered texture as observed in the PGE reef (ppl). B) Most observations does not show any visual changes between ppl and xpl for amphibole, but occasionally with low second order interference colors (pegmatite).

5.2.1.6 Plagioclase: Labradorite ($(Ca,Na)(Si,Al)_4O_8$)

Plagioclase is a tectosilicate identified by its twinning texture (figure 5.14) visible in xpl and its parallel extinction. The twinning is a result of two crystals sharing the same crystal lattice but grow with different configurations. In the case of plagioclase, these twins are polysynthetic because of the parallel alignment. In ppl, the mineral is colorless and often shows evidence of very low amounts of alteration.

Plagioclase forms veins of euhedral crystals in the pyroxene pegmatite. Boundaries are sharp when in contact with the large pyroxene crystals. Grain size varies from larger grains with intergranular fine-grained plagioclase. The associated minerals are biotite, amphibole, rutile and sulfides that contain very low amount of noble metals. In thin section 110.3 such a vein shows a clear zoning with the mineral assemblage changing towards the closing end from plagioclase → amphibole → biotite → rutile → sulfide (figure 5.15).

Table 5.6: EPMA data of plagioclase (appendix table F 1).

	Na2O	SiO2	Al2O3	CaO
Wt% Oxide	5.692	55.868	28.129	10.489

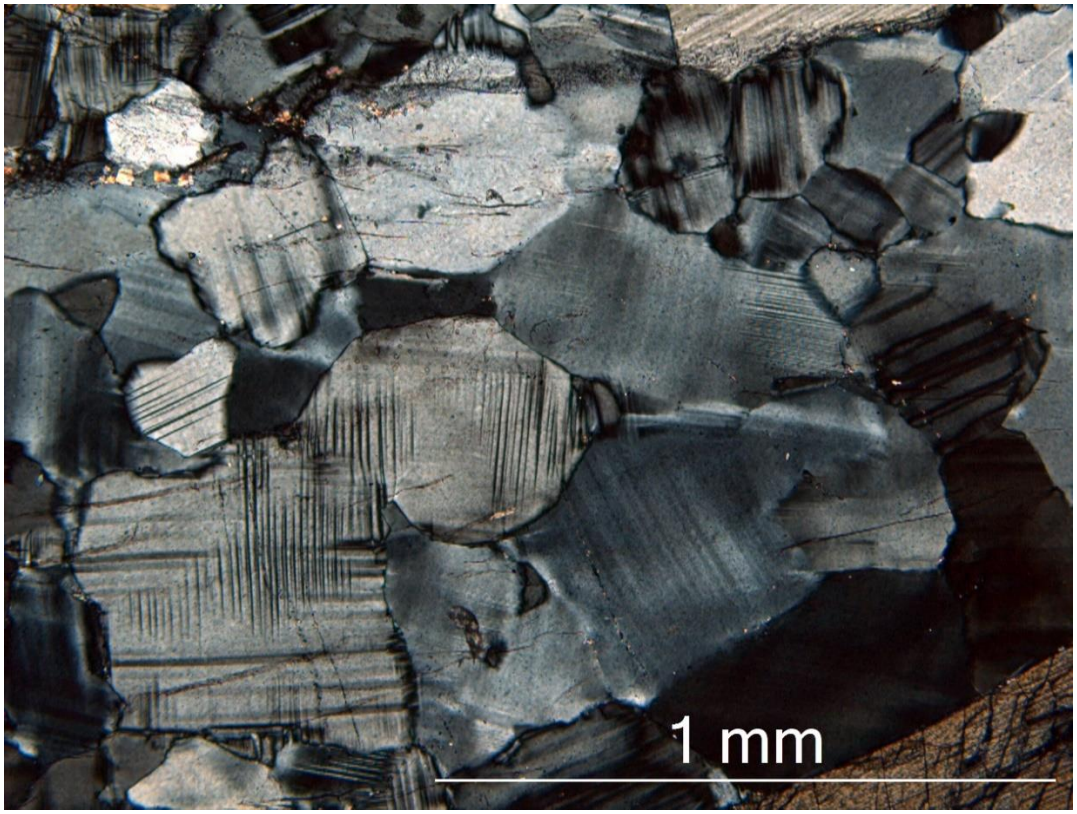

Figure 5.14: Twinning pattern in plagioclase (xpl) observed in thin section 110.3.

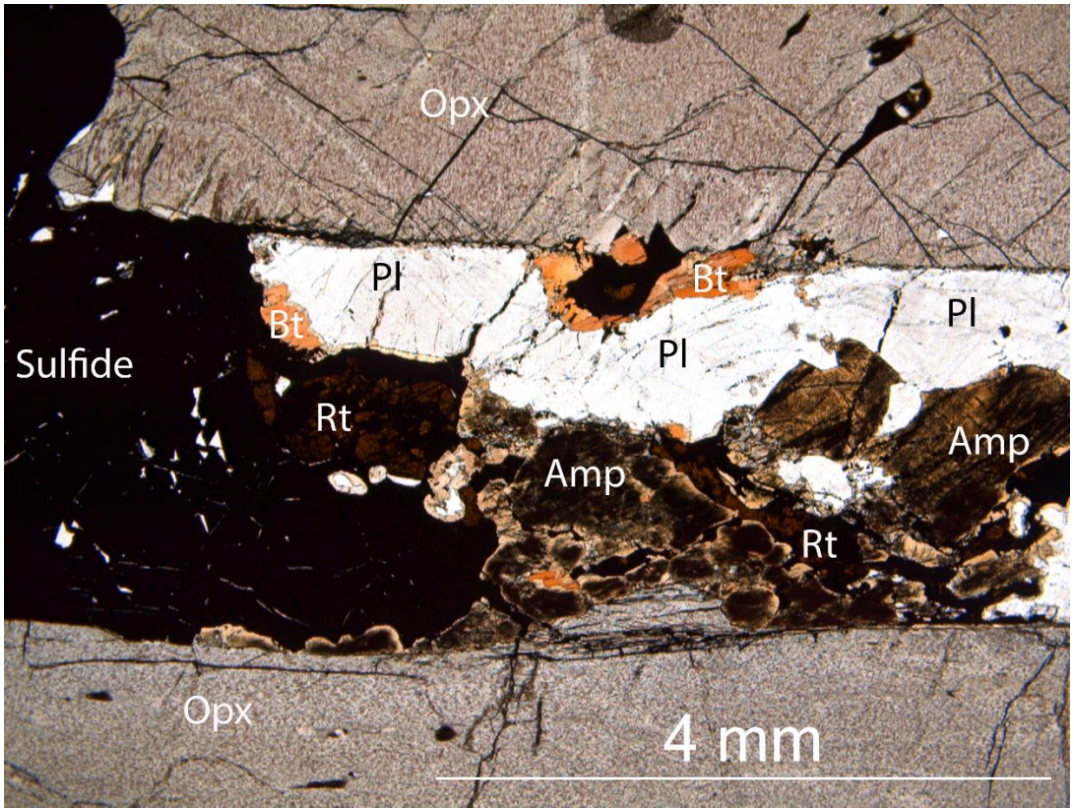

Figure 5.15: The mineral relationship (ppl) at the end of a plagioclase (Pl) vein. Othopyroxene (Opx) host and a crystallization relationship from plagioclase – amphibole (Amp) – biotite (Bt) – rutile (Rt) – sulfide. Observed in thin section 110.3.

5.2.2 Sulfides

Optical identification (reflected light microscopy) of opaque minerals such as sulfides and oxides is done according to individual mineral descriptions in “Atlas of Ore Minerals” by Picot and Johan (1982) and was subsequently verified by EPMA analysis.

5.2.2.1 Chalcopyrite ($CuFeS_2$)

Chalcopyrite is a common copper sulfide that often appear in close relation to pyrrhotite and pentlandite. It is characterized by its pale “brass” yellow reflectance (figure 5.16). Chalcopyrite forms as inclusions within pyrrhotite - pentlandite grains, as isolated chalcopyrite sections or in symplectite structures with pyrite (figure 5.19). When together with pyrrhotite and pentlandite, the hosting silicates are olivine and orthopyroxene. When forming in other relations the hosting minerals are amphibole, cubanite and orthopyroxene. Alteration appears as chalcopyrite → pyrrhotite that is visible as thinning bands from the grain edge when in contact with serpentine. This alteration abruptly stops when reaching a fracture, a feature that is evident both in the pegmatite (figure 6.11) and the dunite (figure 6.12)

Table 5.7: EPMA data of chalcopyrite (appendix table F 11).

	Cu	S	Fe
Wt%	34.736	33.364	27.506

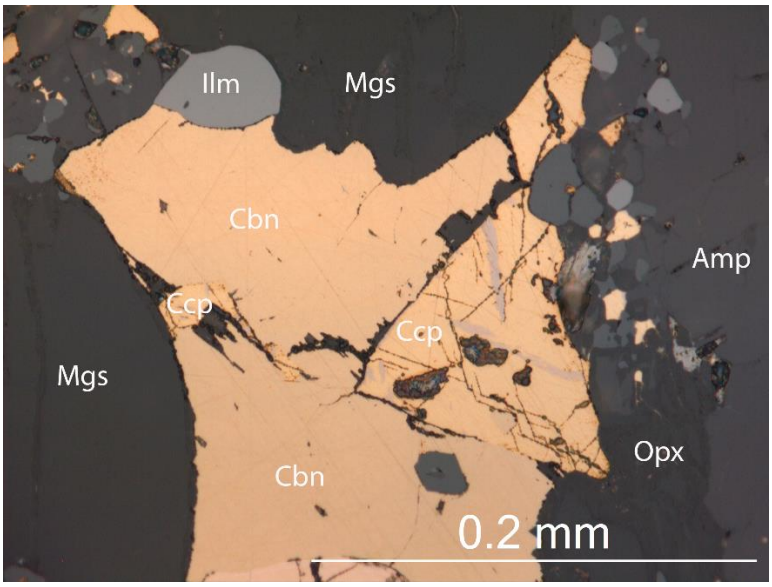

Figure 5.16: Color contrast between cubanite (Cbn) and chalcopyrite (Ccp). Hosted by magnesite (Mgs), amphibole (Amp) and orthopyroxene (Opx). (“gold cluster” in thin section 109.55)

5.2.2.2 Cubanite ($CuFe_2S_3$)

Cubanite is a mineral that is very similar to chalcopyrite and optically the two phases can be difficult to differentiate from one another (figure 5.16). Cubanite does show a pale to creamy-yellow and has only been observed in association of other copper sulfides. The host silicates to coexist with cubanite is amphibole and orthopyroxene with carbonates. It is also present as exsolution lamellae within chalcopyrite (figure 6.12) and in the dunite as the main copper bearing grain in the center of the "gold-cluster".

Table 5.8: EDS data of cubanite.

	Cu	S	Fe
Wt% (EDS)	25.67	22.85	36.81

5.2.2.3 Chalcocite (Cu_2S)

Chalcocite is a copper rich sulfide that can be identified by the grey-blue color (figure 5.17), clearly visible in reflected light. It has only been observed in the "gold cluster", where it always forms smaller satellite grains together with chalcopyrite occasionally in a gold hosting relationship.

Table 5.9: EDS data of chalcocite.

	Cu	S	Fe
Wt% (EDS)	53.31	15.75	10.36

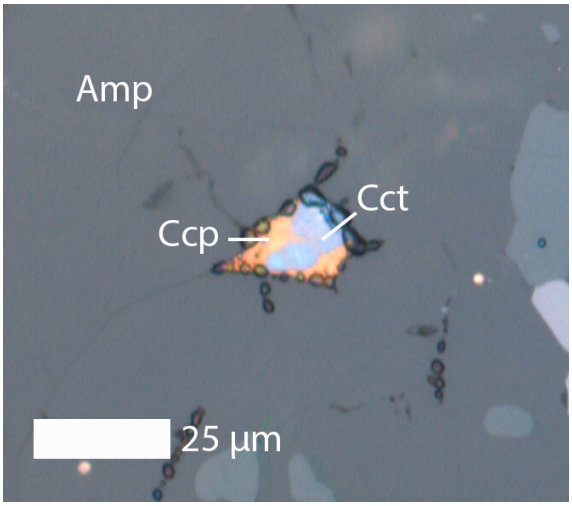

Figure 5.17: Small grain of chalcocite (Cct) with chalcopyrite (Ccp) hosted by amphibole (Amp) in association with the "gold cluster" in thin section 109.55.

5.2.2.4 Pentlandite ($(Fe,Ni)_9S_8$)

Pentlandite is a cubic nickel-iron sulfide and often forming flame lamellae in pyrrhotite (figure 5.18), but also as isolated sections (figure 6.12). It is difficult to distinguish the difference between them based only on their reflectance. Pentlandite is an isotropic mineral having a creamy white color with a reflection brighter than pyrrhotite. This sulfide is often the host mineral of PGM's

Table 5.10: EPMA data of pentlandite (appendix table 15).

	Ni	S	Fe
Wt%	34.147	32.194	31.202

5.2.2.5 Pyrrhotite ($Fe_{1-x}S$)

Pyrrhotite is a monoclinic or hexagonal iron monosulfide that frequently occur as the main sulfide mineral in the dunite. The color in reflected light is creamy pale brown and has a reflectance lower than pentlandite (figure 5.18). Anisotropy has been used as a distinct feature to document the minerals occurrence as an alteration product in chalcopyrite. This mineral forms together with pentlandite, often with "flame" structure as described in the section regarding pentlandite (5.2.2.4).

Table 5.11: EPMA data of pyrrhotite (appendix table F 13).

	S	Fe
Wt%	50.673	43.728

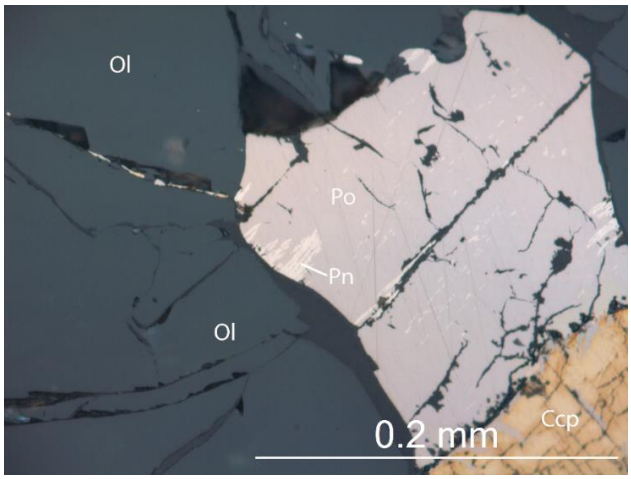

Figure 5.18: Pentlandite (Pn) lamellae in pyrrhotite (Po). Forming larger sulfides with chalcopyrite (Ccp) hosted by olivine. Observed in thin section 109.55.

5.2.2.6 Pyrite (FeS_2)

Pyrite is a cubic iron sulfide that occur together with chalcopyrite, pentlandite and pyrrhotite in all of the four thin sections. It is optically recognizable by its white color and higher reflection compared to its neighboring minerals. It forms as elongated independent crystals hosted by pentlandite that lack the typical cubic shape, but also as a distinct symplectic texture with chalcopyrite (figure 5.19). This texture is visible in close relation to Pd-275 (appendix figure B 38), but it is not associated with any of the other PGM's.

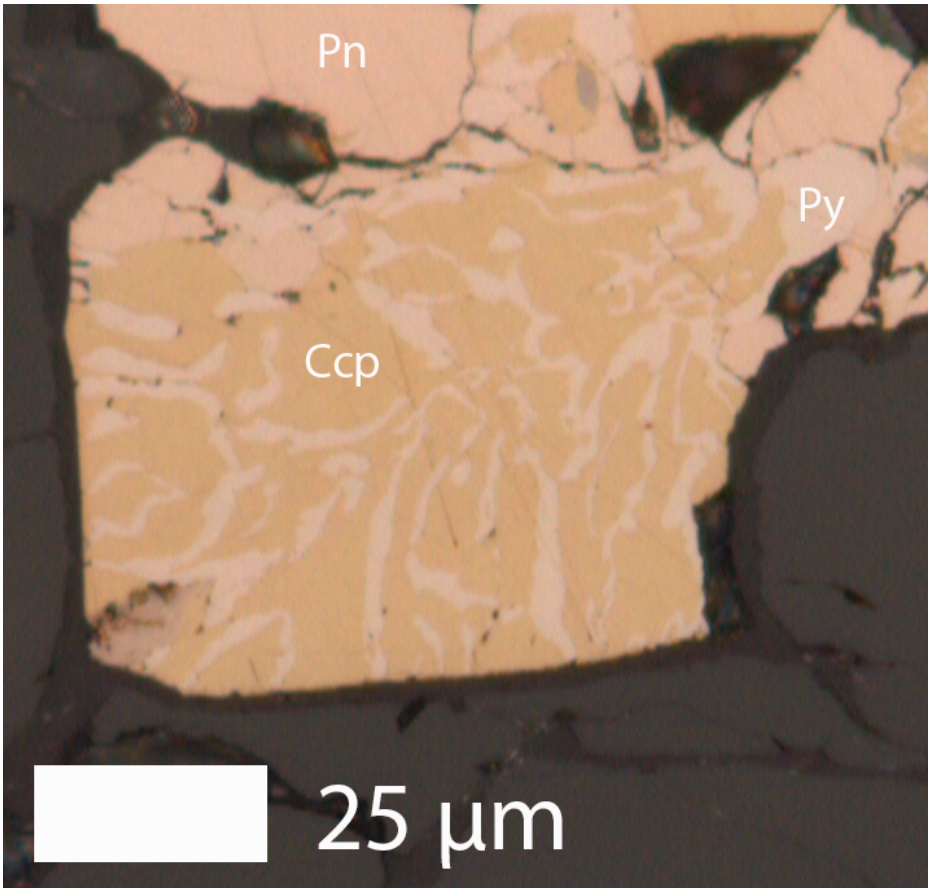

Figure 5.19: Symplectic pyrite (Py) in chalcopyrite (Ccp), hosted by pentlandite (Pn). Close by Pt-107 in thin section 109.55.

5.2.3 Carbonate

5.2.3.1 Dolomite ($CaMg(CO_3)_2$)

Dolomite is forming fine-grained euhedral intergranular clusters or inclusions in orthopyroxene and olivine. White in ppl and a showing the high birefringence so typical for carbonate in xpl, viewed as a rainbow of different colors, especially at the edge of the grain

(figure 5.20). The mineral is mostly observed in the dunite, but also in one small cluster in thin section 110.3.

Table 5.12: EPMA data of dolomite (appendix table F 8)

	MgO	CaO	FeO	CO_2
Wt% oxide	18.241	26.302	2.568	52.701

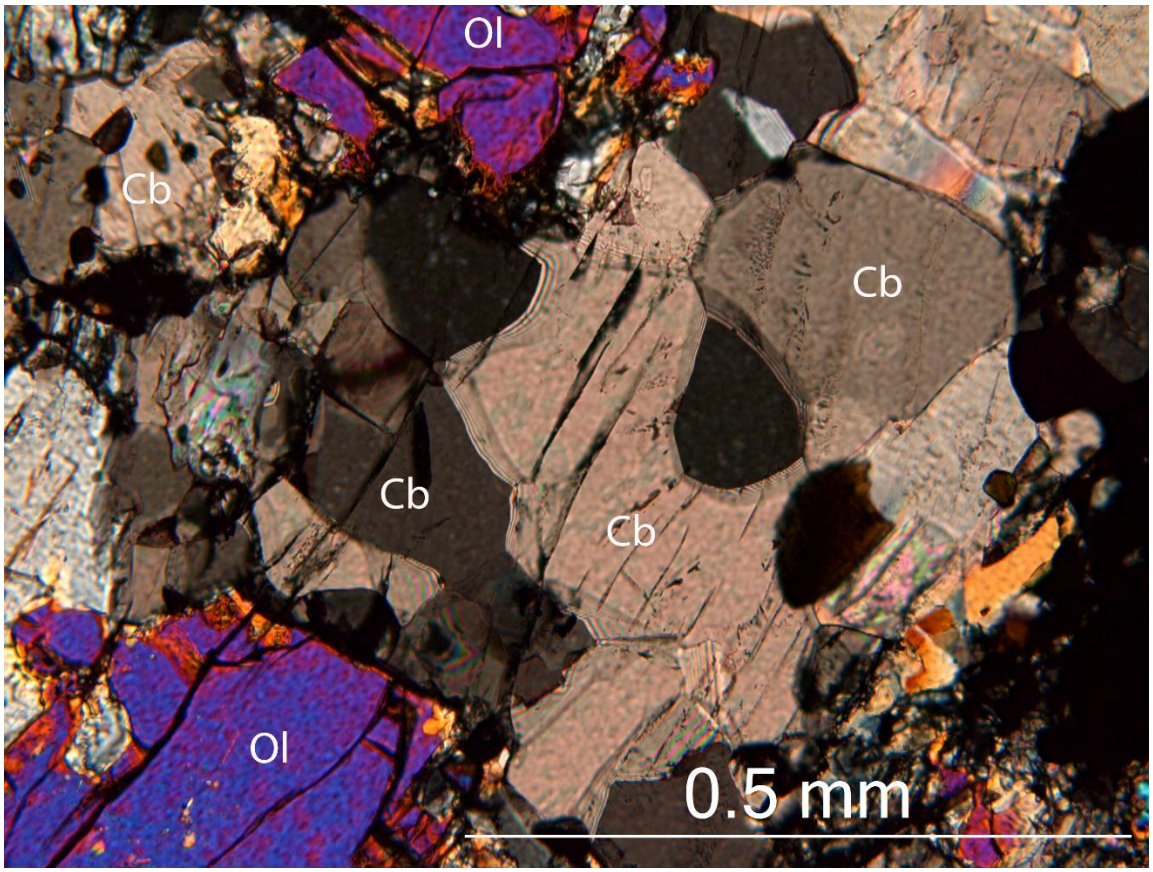

Figure 5.20: Carbonates (Cb) associated with the “gold cluster”, hosted by olivine (Ol).

5.2.3.2 Magnesite ($MgCO_3$)

Magnesite is very similar to dolomite, but with a slighter more greyish hue in xpl. The big difference is that magnesite forms larger single anhedral-subhedral crystals and only occurs at the edge of silicates. Olivine and magnesite have very strong reactions at a couple of places, where olivine is partially consumed by magnesite (figure 5.21). This carbonate is also observed in contact with several sulfides that host noble metals. Especially in the “gold-cluster”, where it forms the outer rim towards olivine.

Table 5.13: EPMA data of magnesite (appendix table F 9).

	MgO	CaO	FeO	CO_2
Wt% oxide	37.41	0.592	8.968	52.37

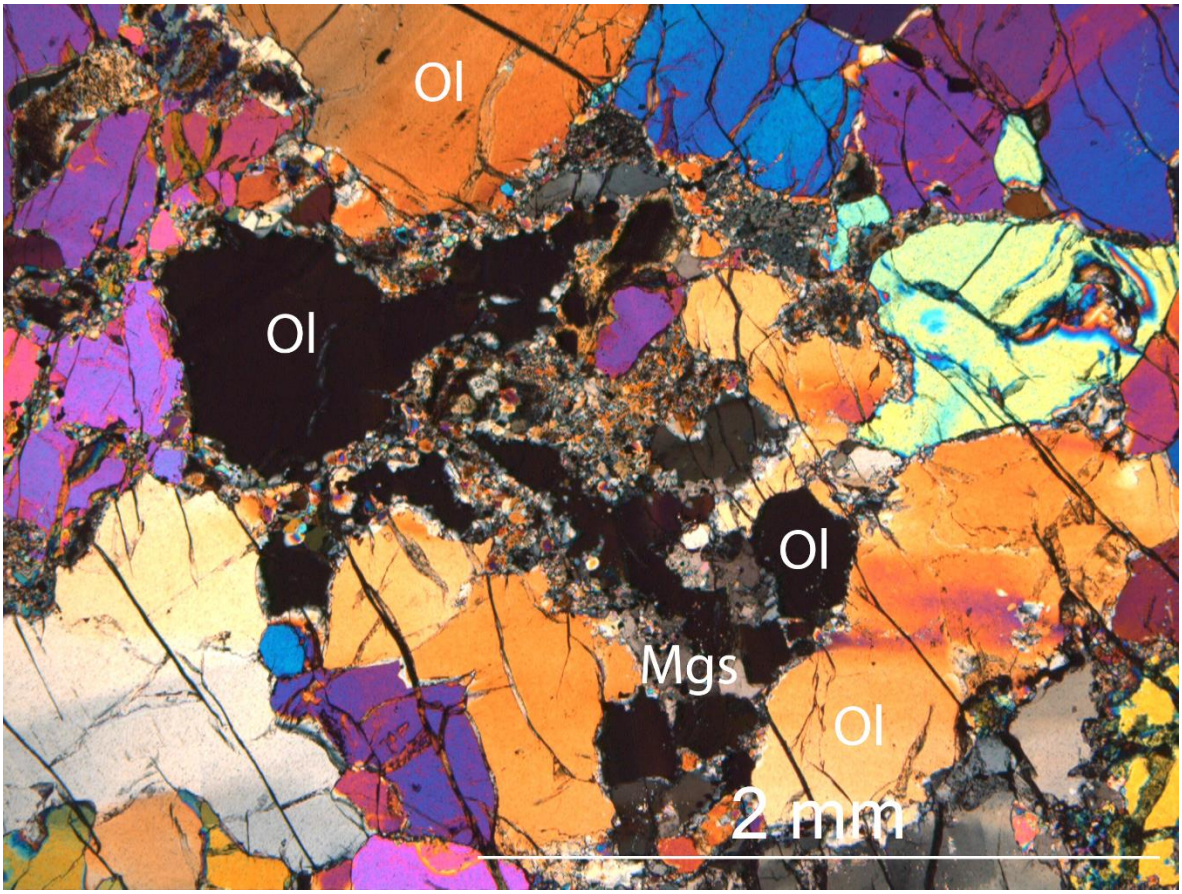

Figure 5.21: Olivine (Ol) (here extinct) that is partly consumed by magnesite (Mgs). This is only observed in the first generation of olivine. Observed in thin section 105.0.

5.2.3.3 Calcite ($CaCO_3$)

Calcite have the same optical features as dolomite and difficult to tell apart from the other carbonates, but EDS shows a strong Ca peak and no peak for magnesium. This mineral has mostly been observed in between amphibole and Cu sulfides, in the two areas of Pt-179 (appendix figure B 19) and "Pd-cluster" (appendix figure B 42). Especially where calcite form in contact with chalcopyrite ("Pd-cluster") at the end of a zoned amphibole. The mineral has also been observed as vein fillings close to sulfides that hosts PGE (Pt-179).

Table 5.14: EPMA data of calcite (appendix table F 10).

	MgO	CaO	FeO	CO_2
Wt% oxide	0.627	48.713	0.68	48.881

5.2.4 Oxides

5.2.4.1 Rutile (TiO_2)

Rutile is identified by its very high refraction indices and for not having any optical changes when the analyzer is applied. The color can vary from red to yellow, but in the observations done for this thesis, only show rutile having a very dark yellow color (figure 5.22A). It only occurs in the pegmatite with direct contact to pentlandite and pyrrhotite (figure 5.22B). Amphibole, biotite and plagioclase is the main hosting silicates, but often almost completely embedded in amphibole.

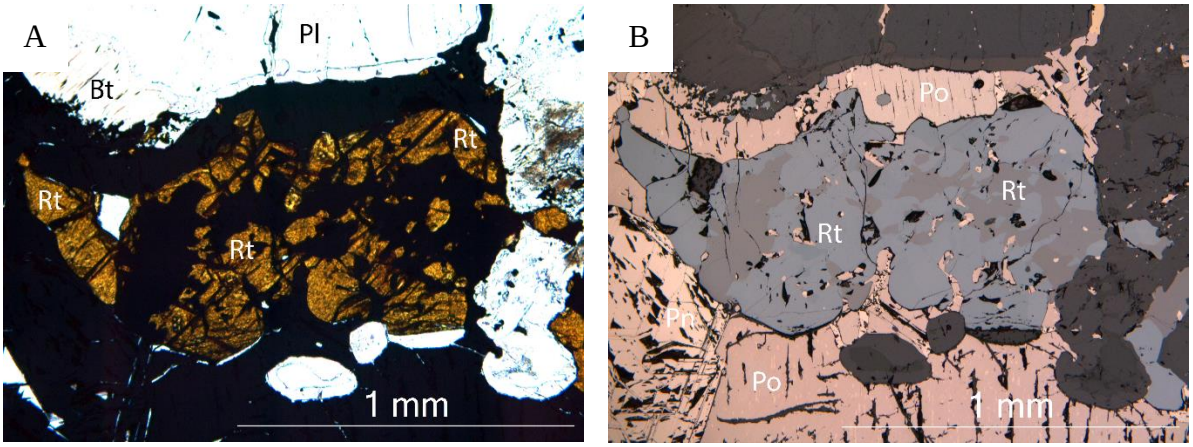

Figure 5.22: A) Photo of rutile (ppl), showing the associated silicates. B) Reflected light photo of A), showing the hosting pentlandite (Pn) and pyrrhotite (Po). Observed in thin section 110.3.

5.2.4.2 Ilmenite ($Fe^{2+}TiO_3$)

Ilmenite is found in three separate phases, occurring in the "gold cluster" (figure 5.16), spinel (figure 5.23) and as exsolution lamellae in orthopyroxene (figure 5.11A). In reflected light, this mineral have a very low reflectance together with anisotropy that are the primary mineral identification indicators. The individual minerals is rounded and forming together with cubanite and often close to sulfides. Ilmenite is also present in the Cr-Al spinel, occurring at the outer rim, surrounded by the Al rich portions.

Table 5.15: EPMA data of ilmenite.

	FeO	TiO_2
Wt% oxide	40.385	51.944

5.2.4.3 Chrome and Aluminum spinel $(A,B)_2X_4$

Spinel is a very common opaque mineral within the dunite, where it form separate minerals that are either Cr or Al dominant, but larger grains show both element occurring with a zoned relation to each other. Cr rich spinel forms at the center and with Al rich spinel as the outer rim (figure 5.23). The transition is very thin, but not sharp, as close EDS/BSD maps shows a gradual enrichment of Al towards the edge (appendix figure B 2). EDS confirms that there is Mg in these mineral phases, but in EPMA analyses for some reasons Mg had not been added to the element selection. The time restrains on the EPMA, did not make it possible to redo these analyses. Based on the EDS results it is most probable that chrome rich phase is picotite ($(Mg,Fe)(Al,Cr)_2O_4$) (rejected by the International Mineralogical Association) and the Al rich phase is an iron spinel of celyonite ($(Mg,Fe)Al_2O_4$) to hercynite group ($(Fe^{2+})Al_2O_4$).

Table 5.16: EPMA data of spinel.

	Al2O3	FeO	Cr2O3	TiO2
Wt% oxide (Al-Spl)	37.243	34.54	24.405	0.868
Wt% oxide (Cr-Spl)	6.71	64.878	18.172	2.957

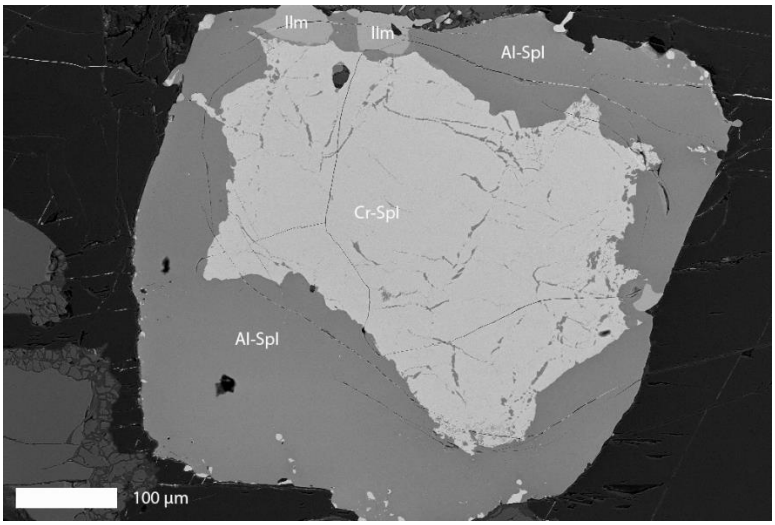

Figure 5.23: BSD photo of a spinel separated in a Chromium (Cr-Spl) and Aluminum (Al-Spl) rich phase. At the spinel edge, there is occasionally ilmenite (Ilm). Observed in thin section 109.55

5.3 PGE host rock

The thin sections originally assigned to this thesis was all sampled from the pegmatite, but during the revision of RF-1 in 2015 it became evident that the largest PGE spike is located in the dunite, which is confirmed by a reevaluation of the chemical results from RF-1. This encouraged resampling of RF-1 and these new thin sections are labeled with the sampling depth in meters below the drilling surface, e.g.: 109.55.

The results for this thesis is highly dependent on choosing thin sections with the highest probability of identifying PGE's. Therefore, four thin sections were chosen, two from the dunite and two from the pegmatite. Evaluation was based on thin sections that contained the highest amount of opaque minerals in either dunite or pegmatite. Other thin sections from the PGE-reef are mapped and presented in appendix A.

In order to correctly determine the rock classification as described in 4.1, each mineral have been labeled (see figures 5.24, 5.26, 5.28, and 5.30) and colored according to the type. This was done by importing the thin section scans into Adobe Photoshop and selecting areas represented by a single mineral phase and then colorizing them (see figures 5.25, 5.27, 5.29 and 5.31). The sum of pixels covered by each color was calculated as a percentage (tables 1-4) and then plotted in ultramafic ternary diagrams (figure 4.3).

(Insertion of blank page to improve readability for the following figures)

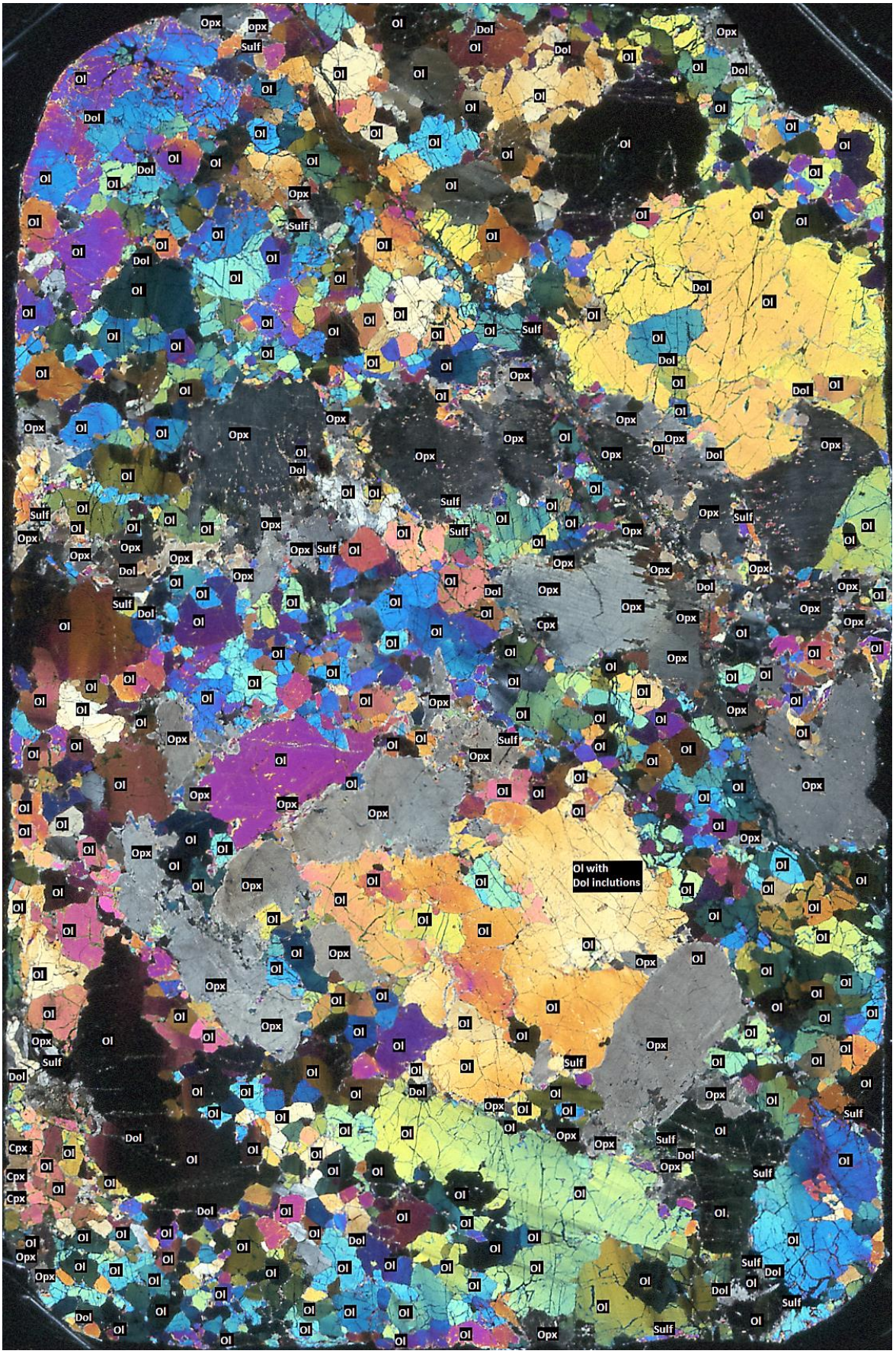

Figure 5.24: Thin section 109.40 with mineral identifications.

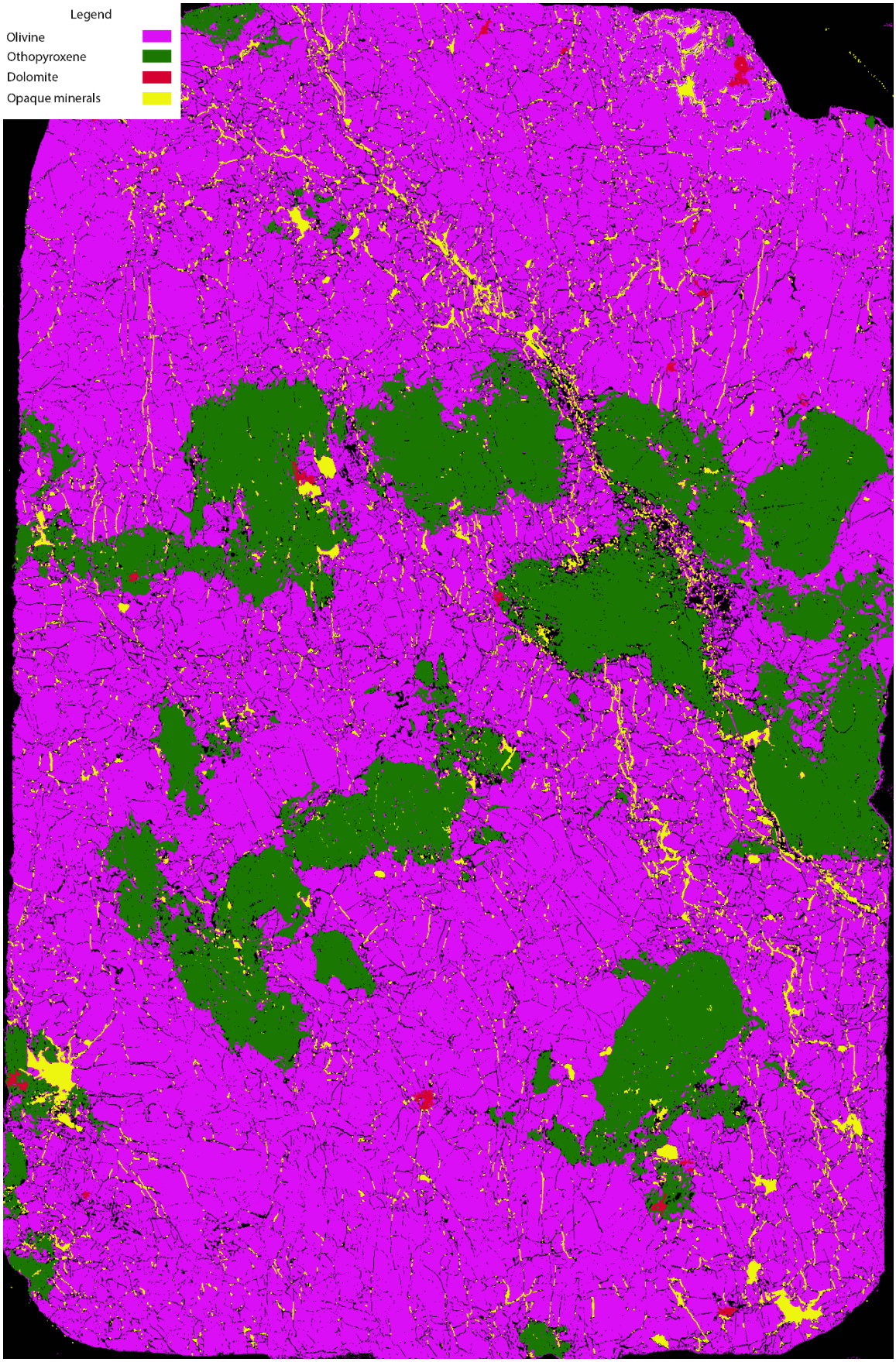

Figure 5.25: Mineral map of thin section 109.40.

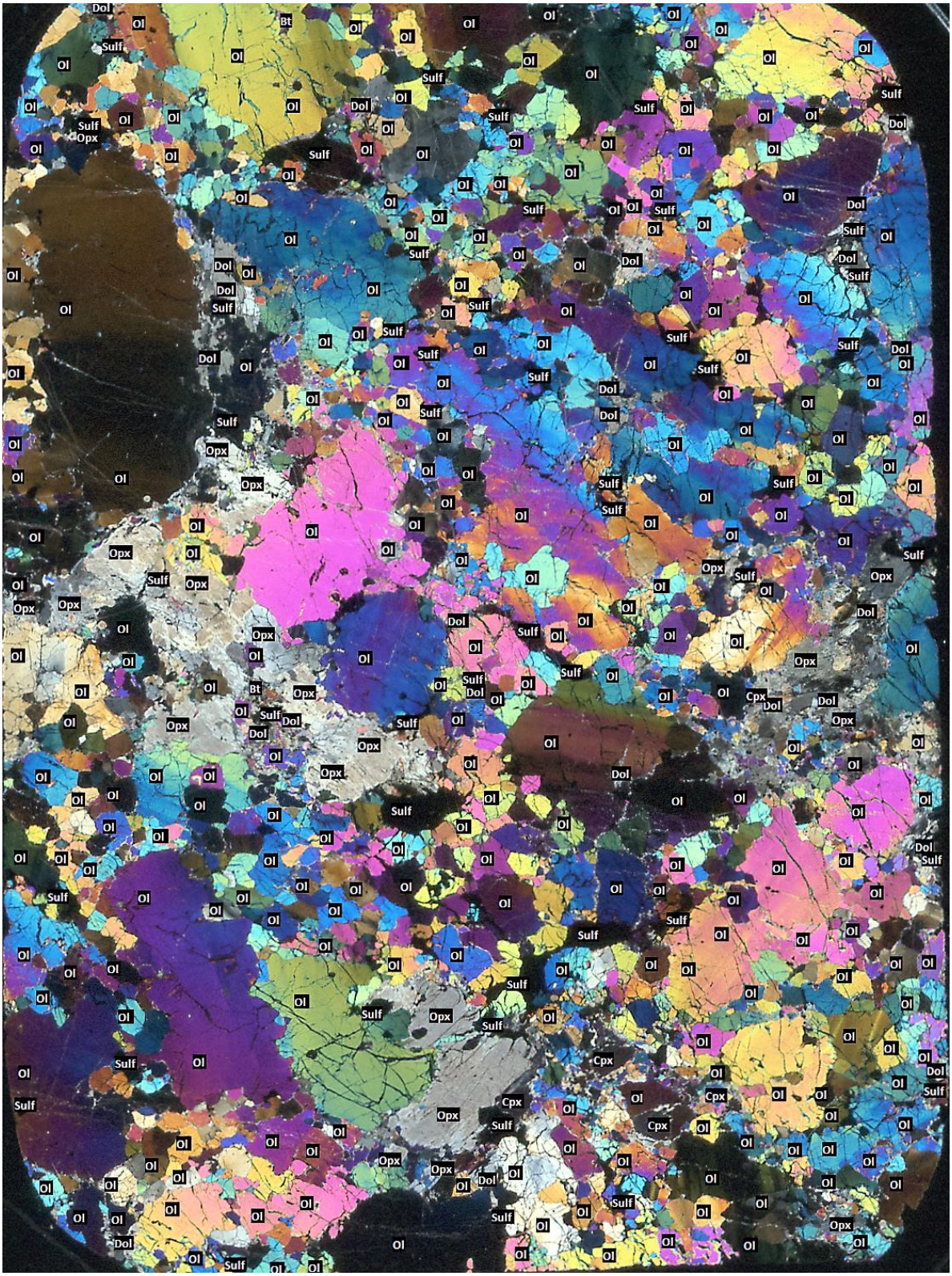

Figure 5.26: Thin section 109.55 with mineral identifications.

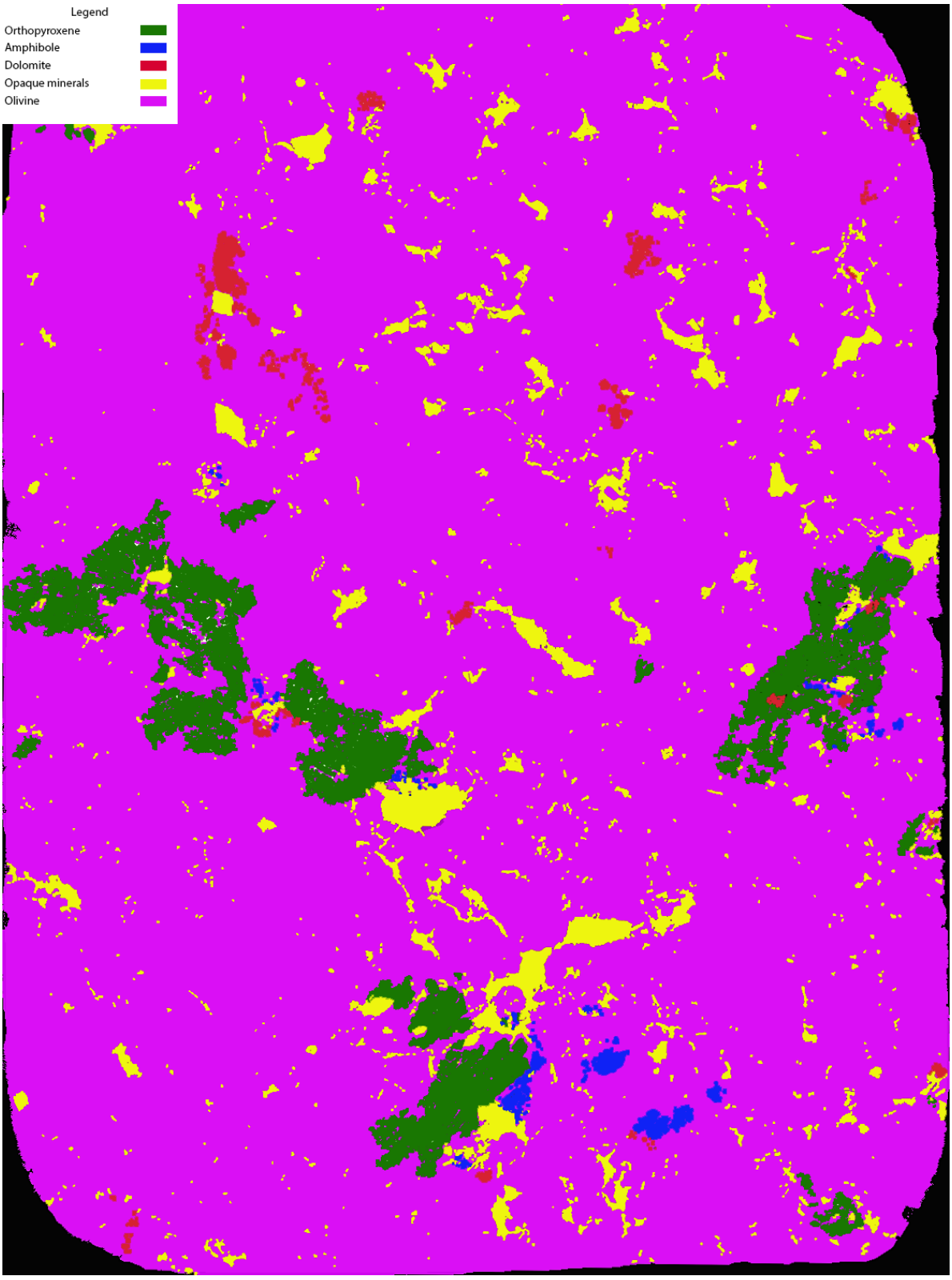

Figure 5.27: Mineral map of thin section 109.55.

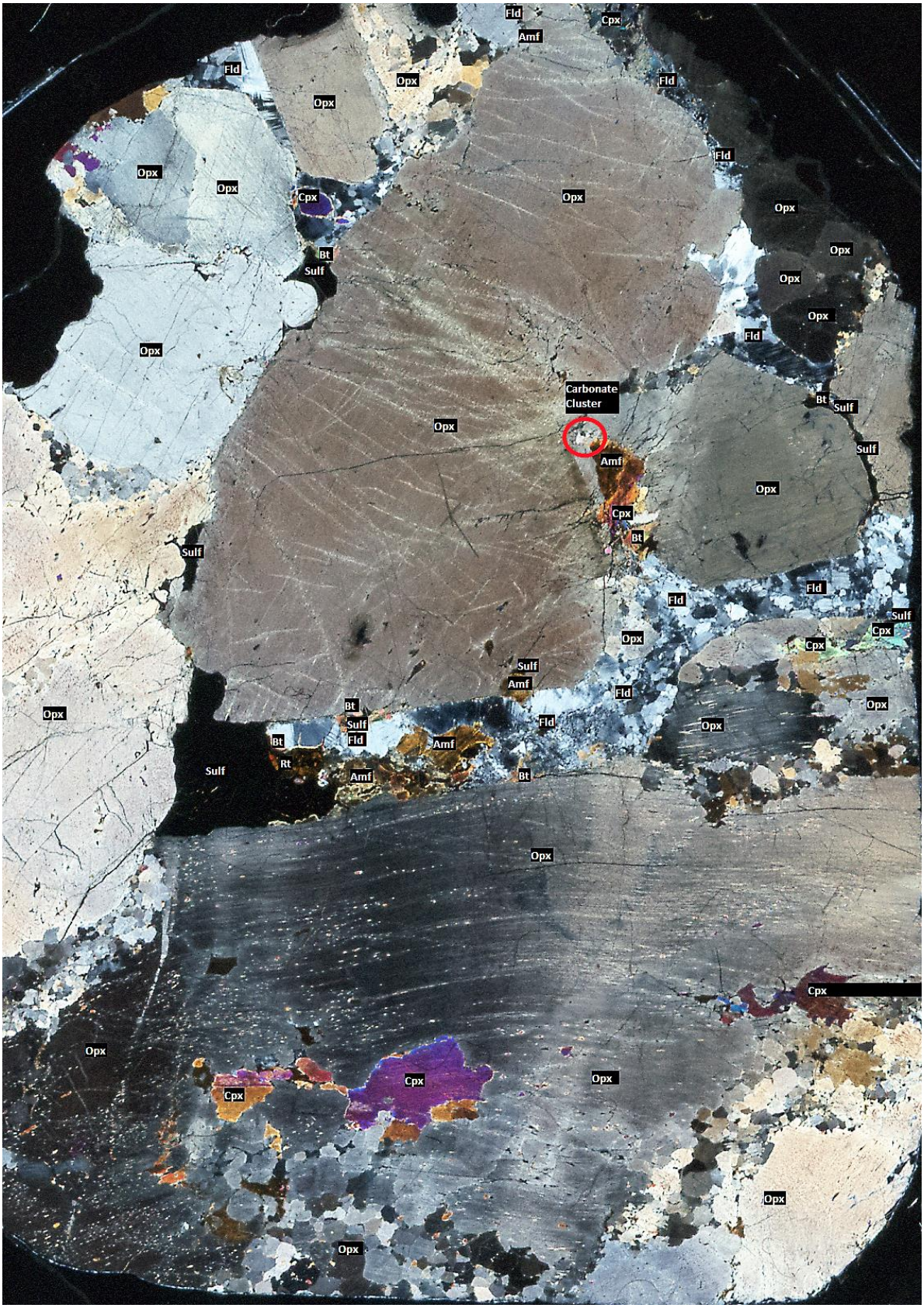

Figure 5.28: Thin section 110.30 with mineral identifications.

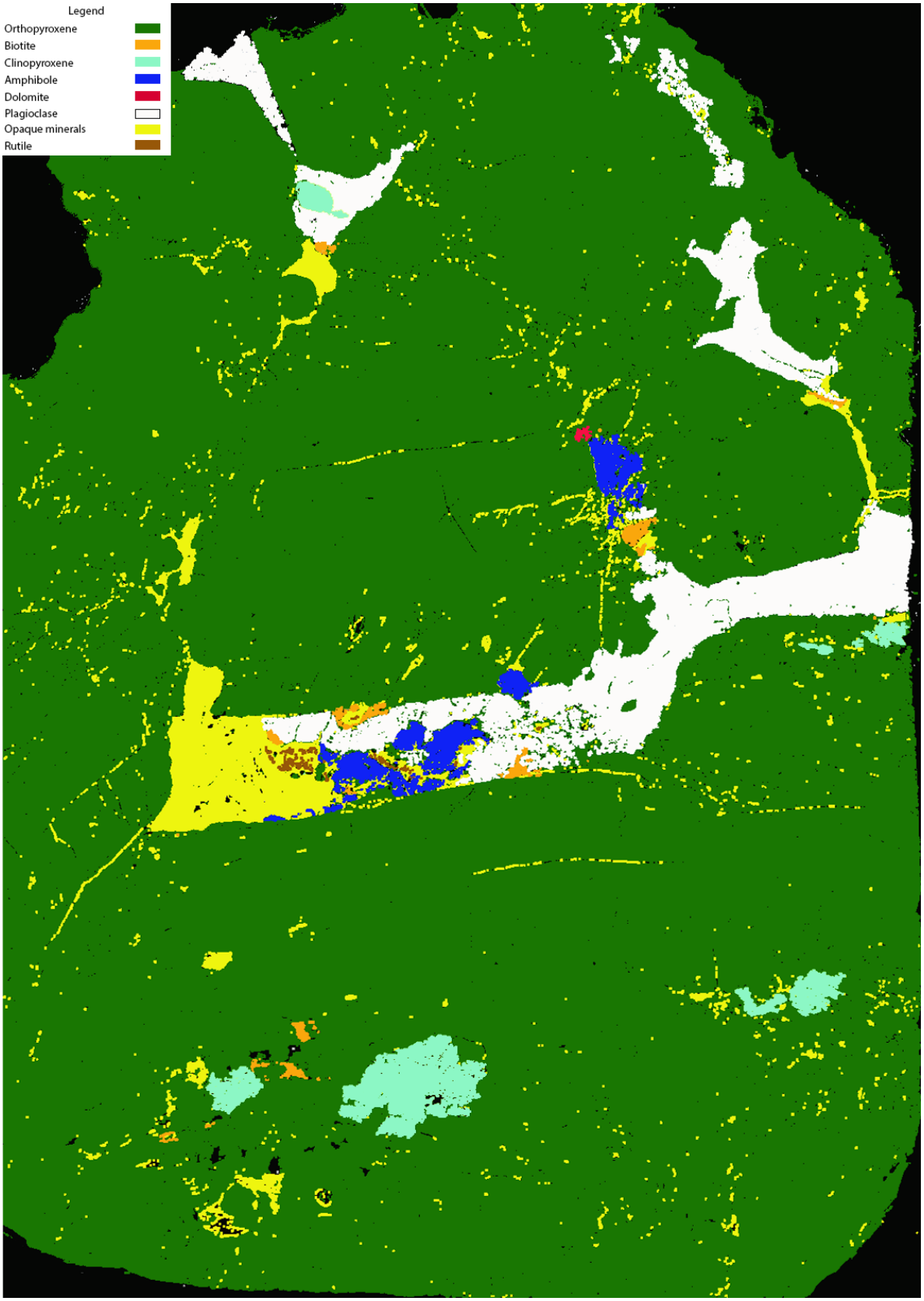

Figure 5.29: Mineral map of thin section 110.30.

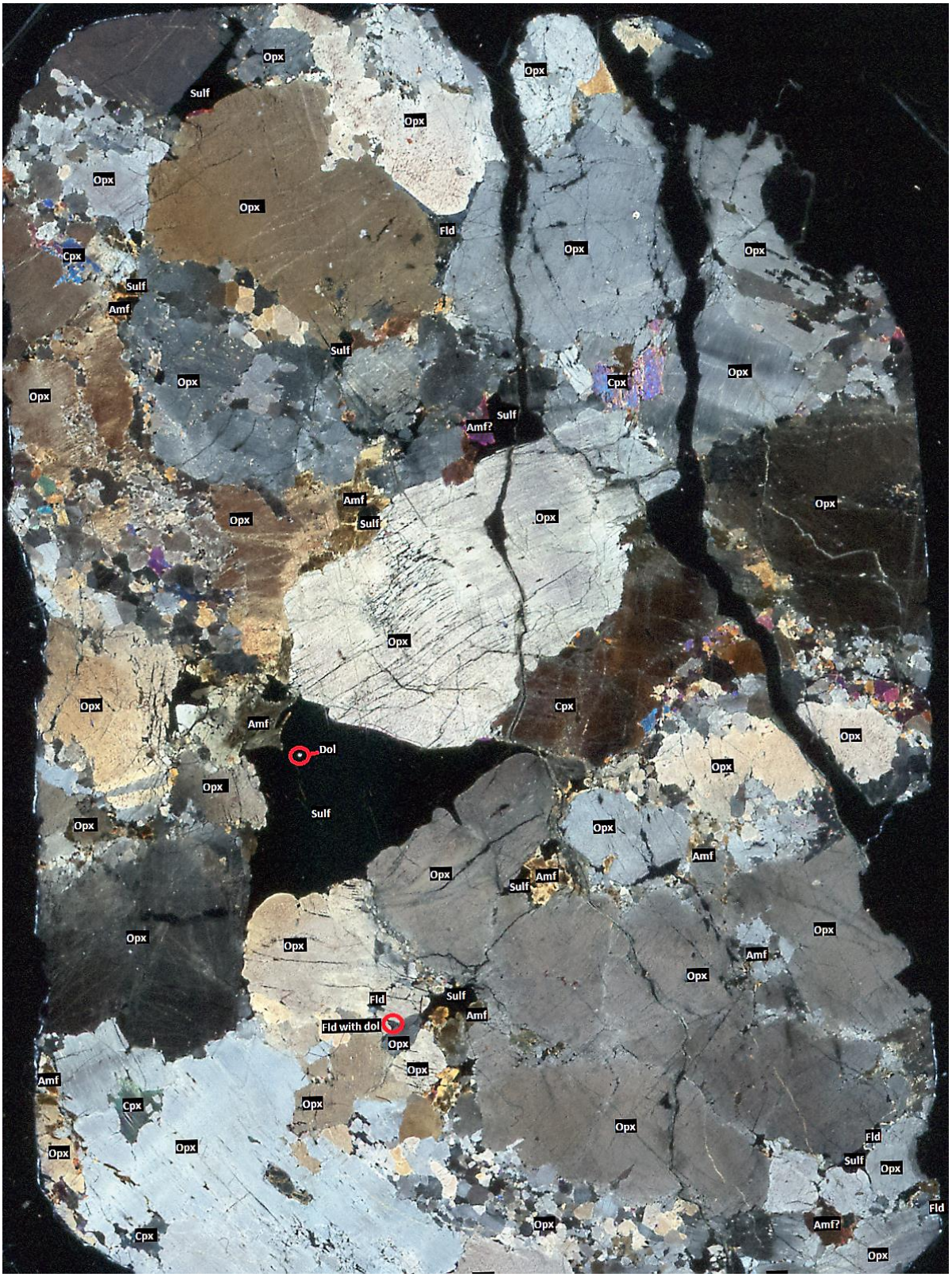

Figure 5.30: Thin section 110.45 with mineral identifications.

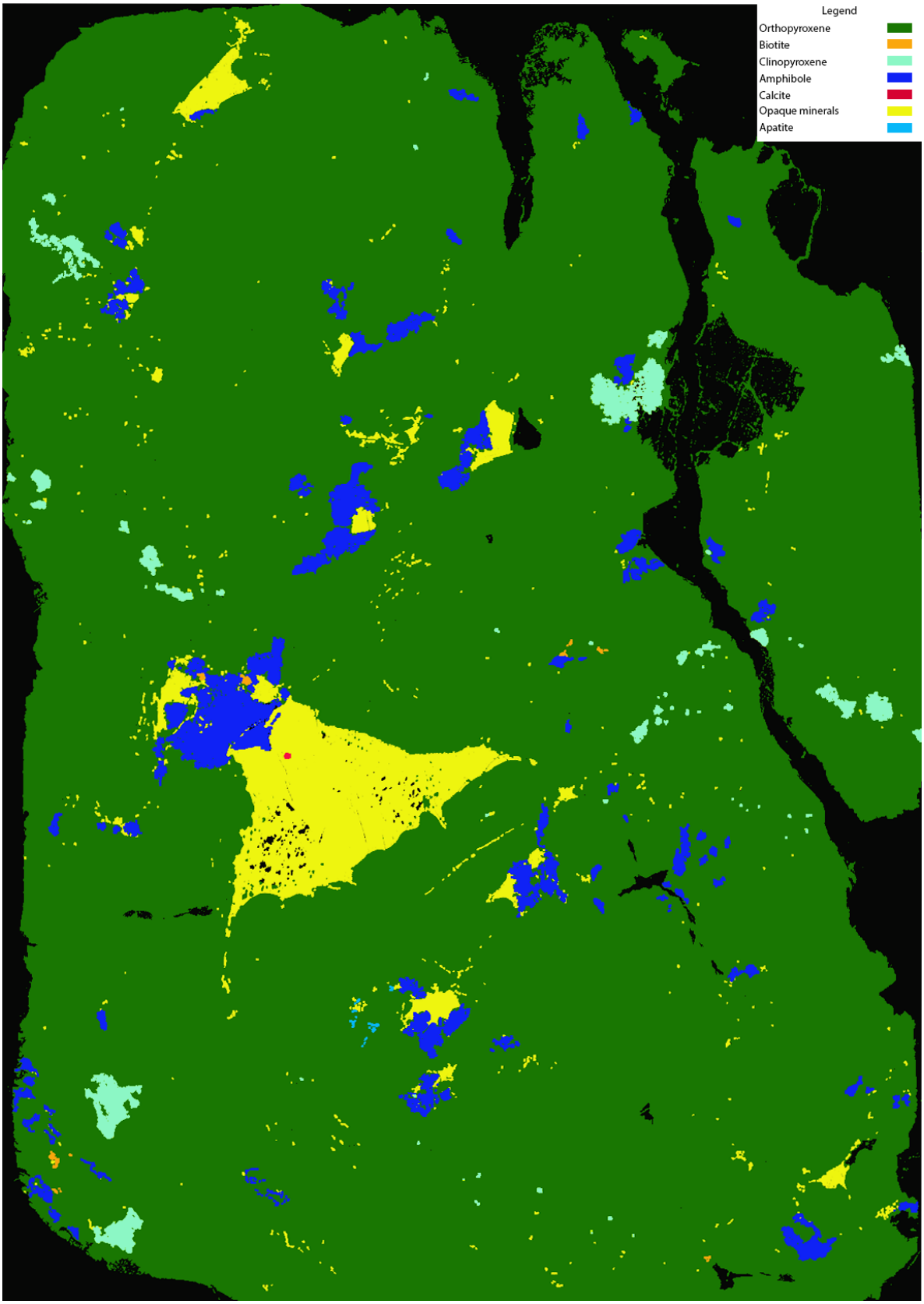

Figure 5.31: Mineral map of thin section 110.45.

Table 5.17: Composition calculation and ternary plot of thin section 109.4.

Thin section 109.40		
Mineral	Pixels	Percentage
Orthopyroxene (Green)	2345634	18.7%
Olivine (Purple)	9683302	77%
Carbonate	21413	0.2%
Opaque minerals (Yellow)	521460	4,1%
	12571809	100%

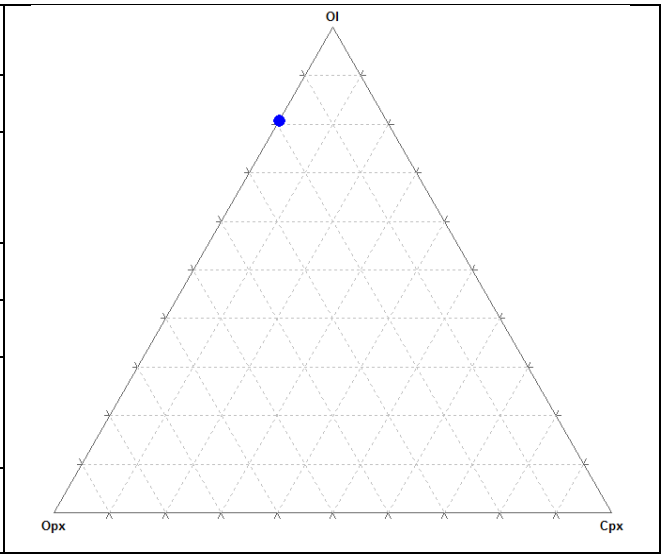

Table 5.18: Composition calculation and ternary plot of thin section 109.55.

Thin section 109.55		
Mineral	Pixels	Percentage
Orthopyroxene (Green)	87522	5.3%
Olivine (Purple)	1471723	88.6%
Amphibole (Blue)	5619	0.3%
Carbonate (Red)	9683	0.6%
Opaque minerals (Yellow)	86763	5.2%
	1661310	100%

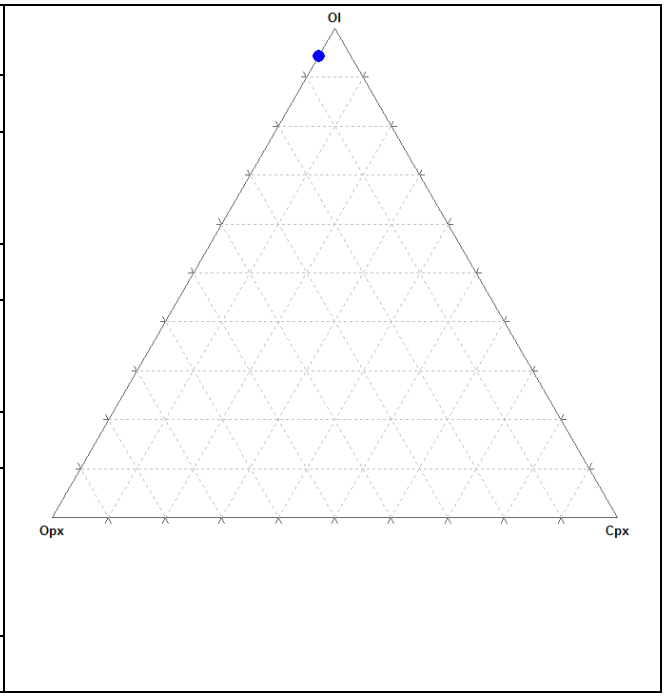

Table 5.19: Composition calculation and ternary plot of thin section 110.3.

Thin section 110.3		
Mineral	Pixels	Percentage
Orthopyroxene (Green)	1486063	88%
Clinopyroxene (Light green)	20798	1.2%
Plagioclase (White)	85101	5%
Biotite (Orange)	4605	0.2%
Amphibole (Blue)	12696	0.7%
Carbonate (Red)	254	0.01%
Rutile (Brown)	1348	0.07%
Opaque minerals (Yellow)	78215	4.82%
	1689071	100%

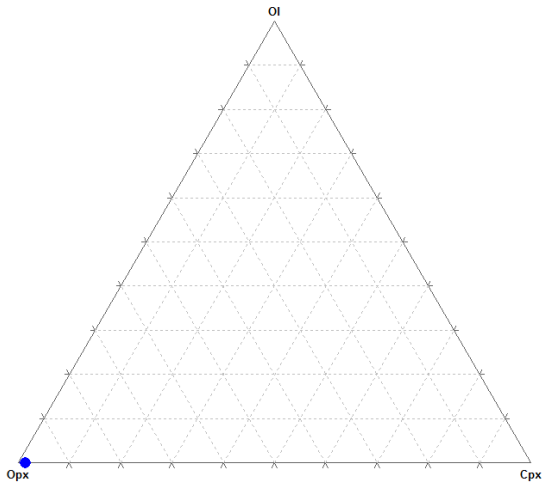

Table 5.20: Composition calculation and ternary plot of thin section 110.45.

Thin section 110.45		
Mineral	Pixels	Percentage
Orthopyroxene (Green)	1488796	91.6%
Clinopyroxene (Light green)	16853	1%
Amphibole (Blue	45917	2.8%
Carbonate (Red)	61	0%
Apatite (Light blue)	272	0.01%
Biotite (Orange)	610	0.04%
Opaque minerals (Yellow)	72558	4.55%
	1625067	100%

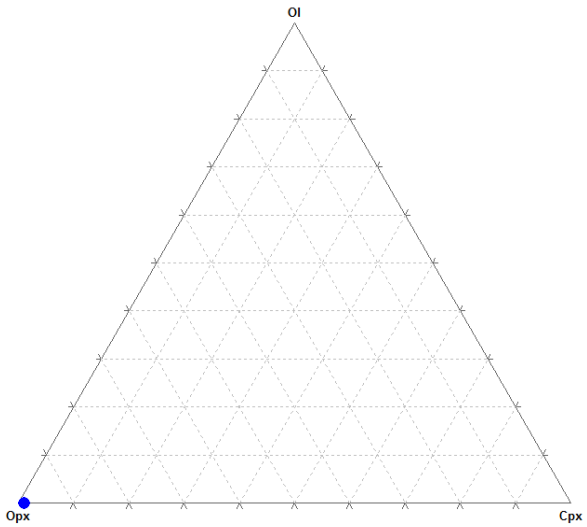

5.4 Platinum group minerals and Gold

Sixty-one minerals containing PGE + gold were identified in the four thin sections. Of these, 29 minerals are large enough to provide quantitative EPMA analysis (appendix table c 1). However, due to the small size of the PGM's, several analyses were contaminated by the host sulfide. To compensate for this, all analyzes were plotted Fe vs S for both the PGM's and the host sulfides. The average Fe, Ni and S content in pentlandite, pyrrhotite and chalcopyrite generated a factor that was eliminated for the PGM's, hence removing the Fe, Ni and S contamination. Based on this recalculation, all minerals were categorized into Pt-dominant, Pt-Pd-dominant, Pd-dominant (figure 5.32) and Au.

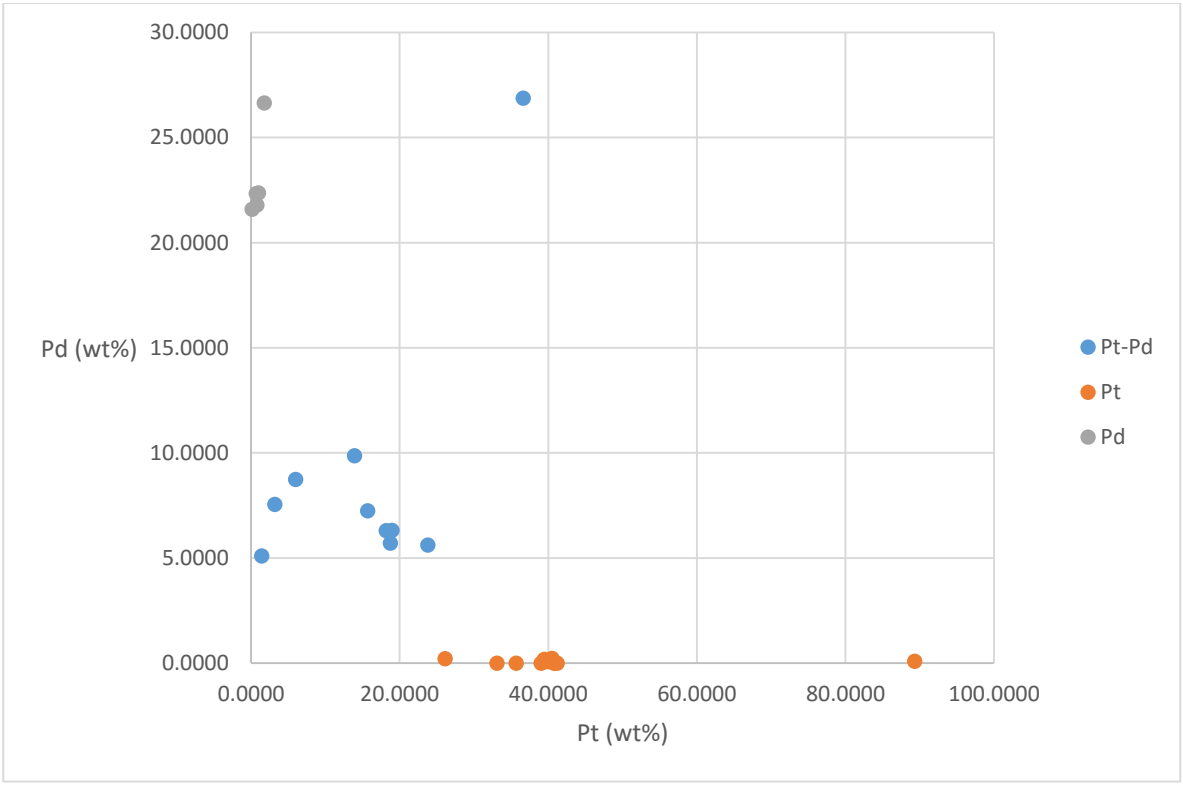

Figure 5.32: EPMA data, visually showing the general Pt-Pd (wt%) categorization of the PGM's.

Figures 5.33-36 show the final maps based on SEM. A full list of mineral details, photos and mineral interpretation charts are available in appendix B.

.

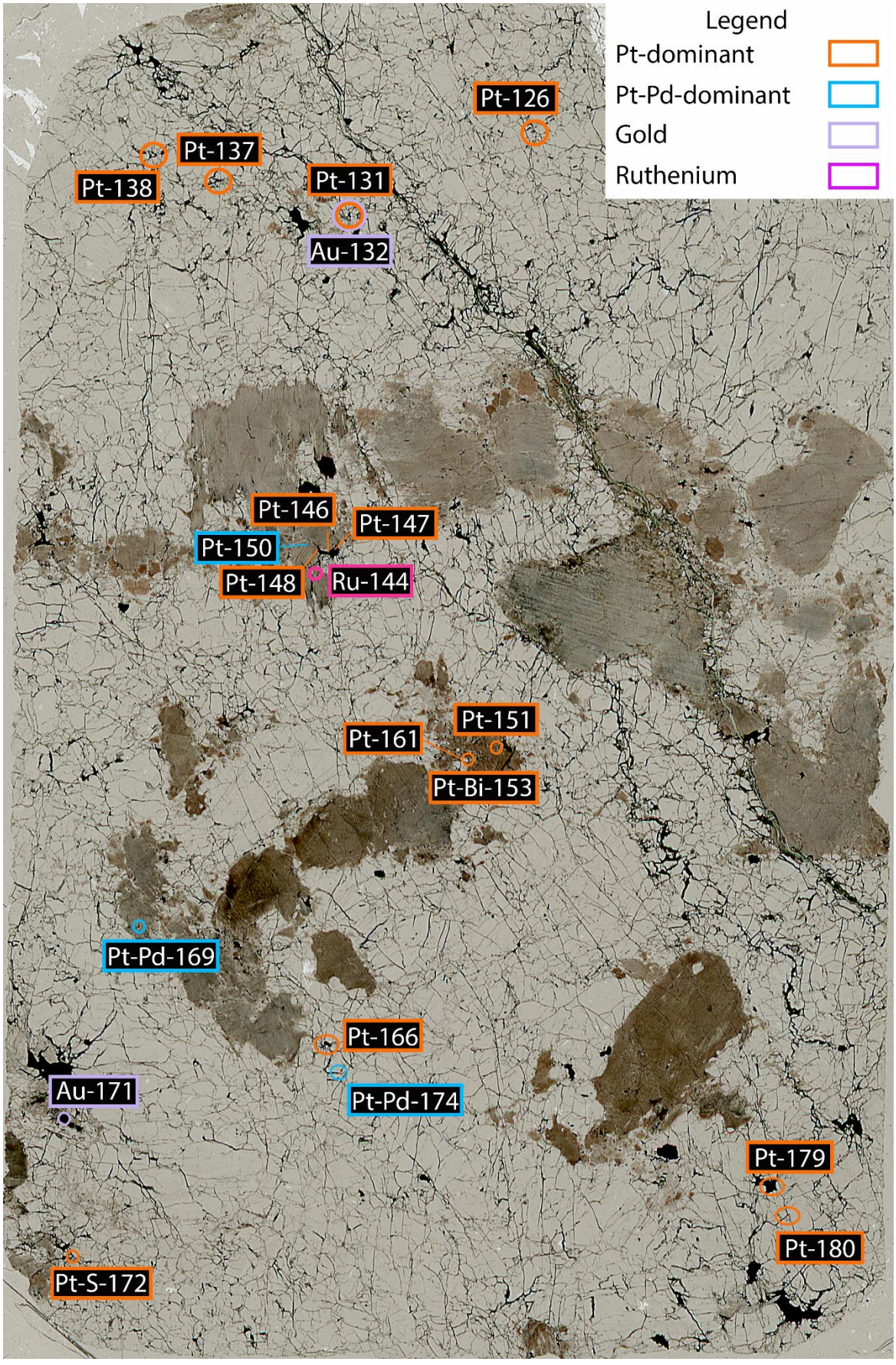

Figure 5.33: PGM location in thin section 109.40.

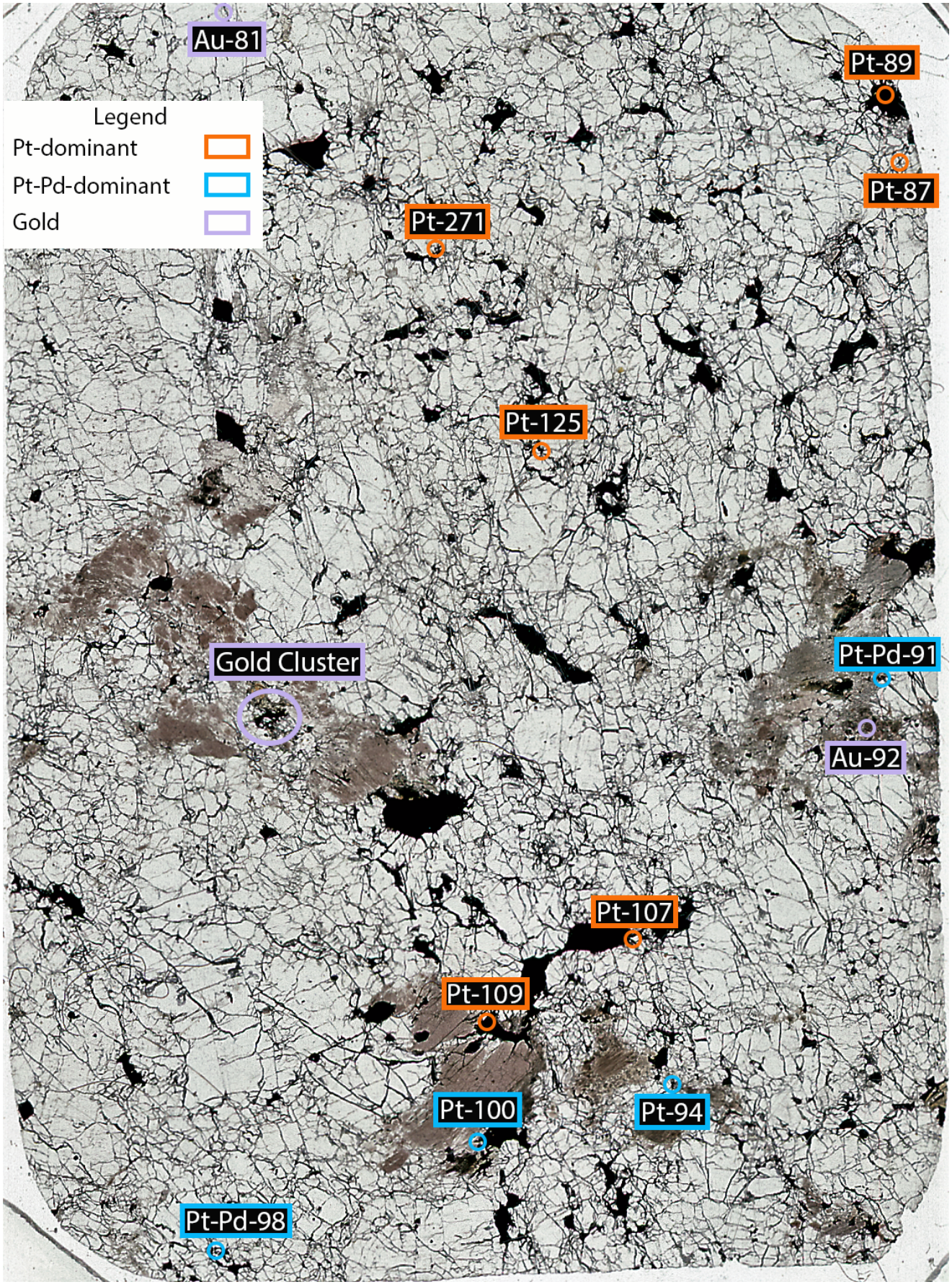

Figure 5.34: PGM location in thin section 109.55.

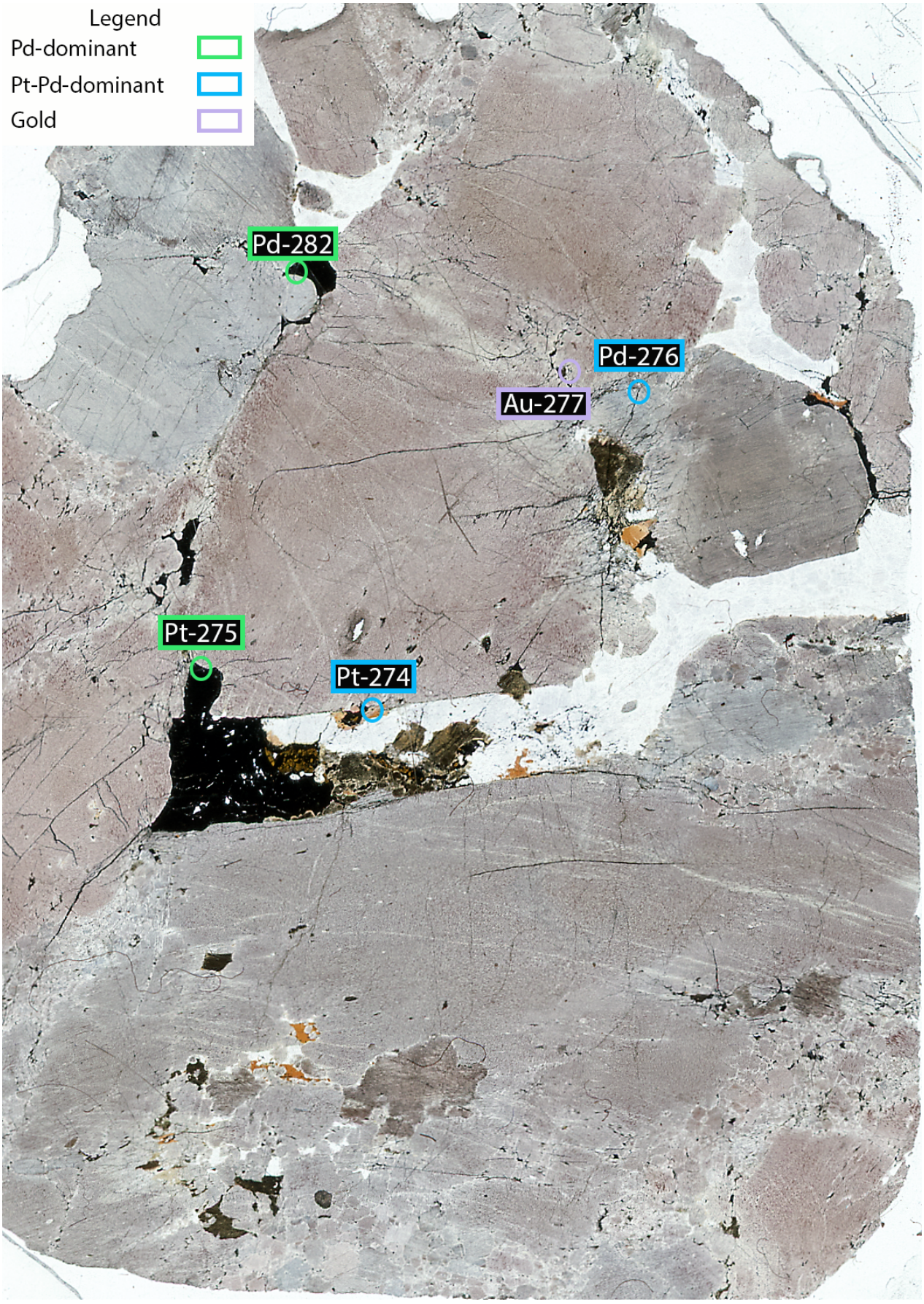

Figure 5.35: PGM location in thin section 110.30.

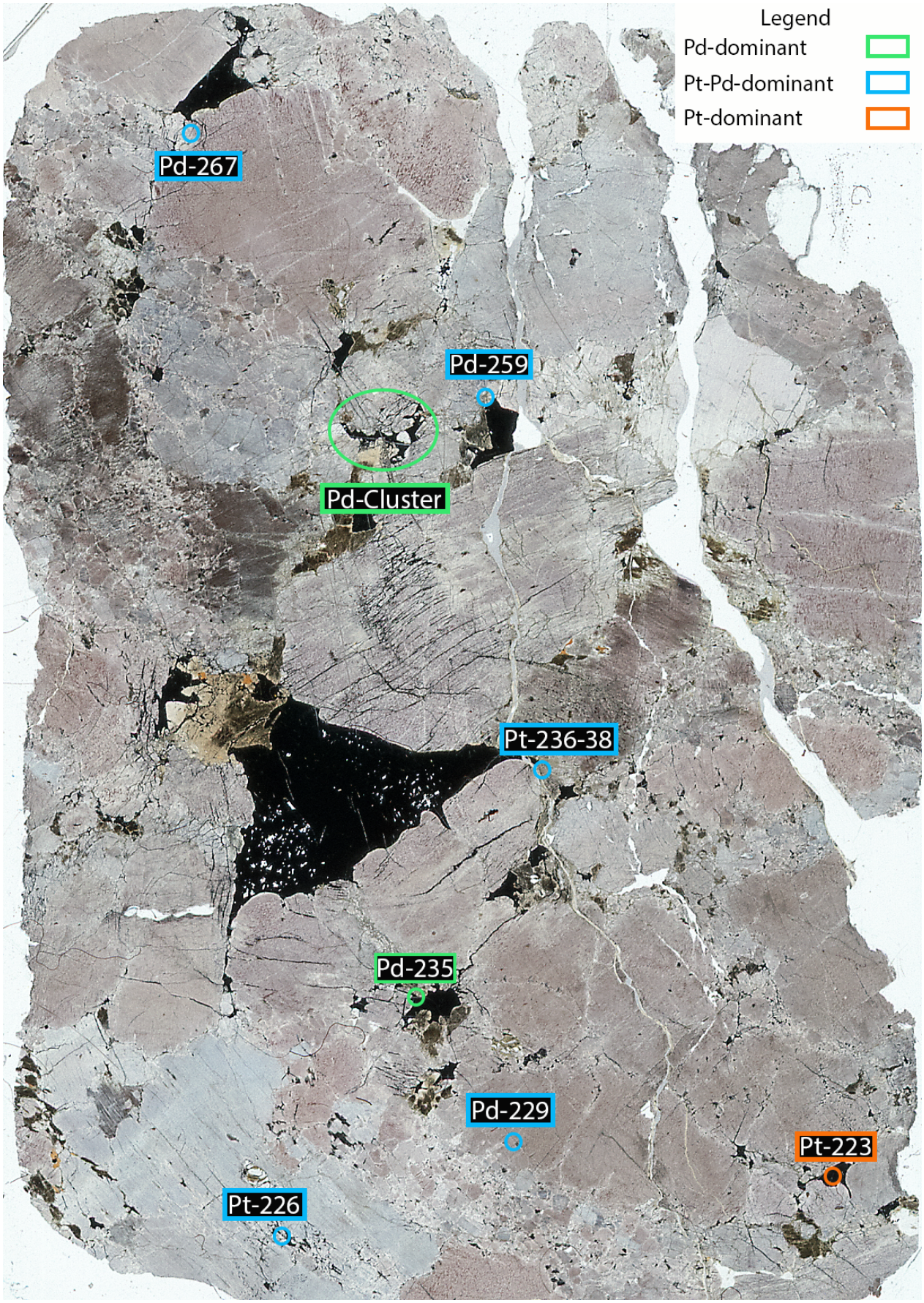

Figure 5.36: PGM location in thin section 110.45.

5.4.1 Pt-dominant

Twenty-one PGM's are Pt-dominant (appendix table B 1) and occasionally contain Bi and Pd at trace level. These minerals appear as alloys with Te to form tellurides, hosted by pyrrhotite and pentlandite. All Pt-dominated minerals, except one are located in thin section 109.40 and 109.55. Pt-Te-(Bi) show a strong correlation with pyrrhotite as the main host sulfide, but often form in pentlandite exsolution lamellae. These tellurides are observed as droplets and needles, located inside and at the edge of the hosting sulfide. In all cases where these tellurides are forming needles, the orientation is the same as the pentlandite lamellae (figure 5.37). Whenever Pd is present, the tellurides are associated with a larger amount of pentlandite, forming totally enclosed or in a separation boarder with other sulfides.

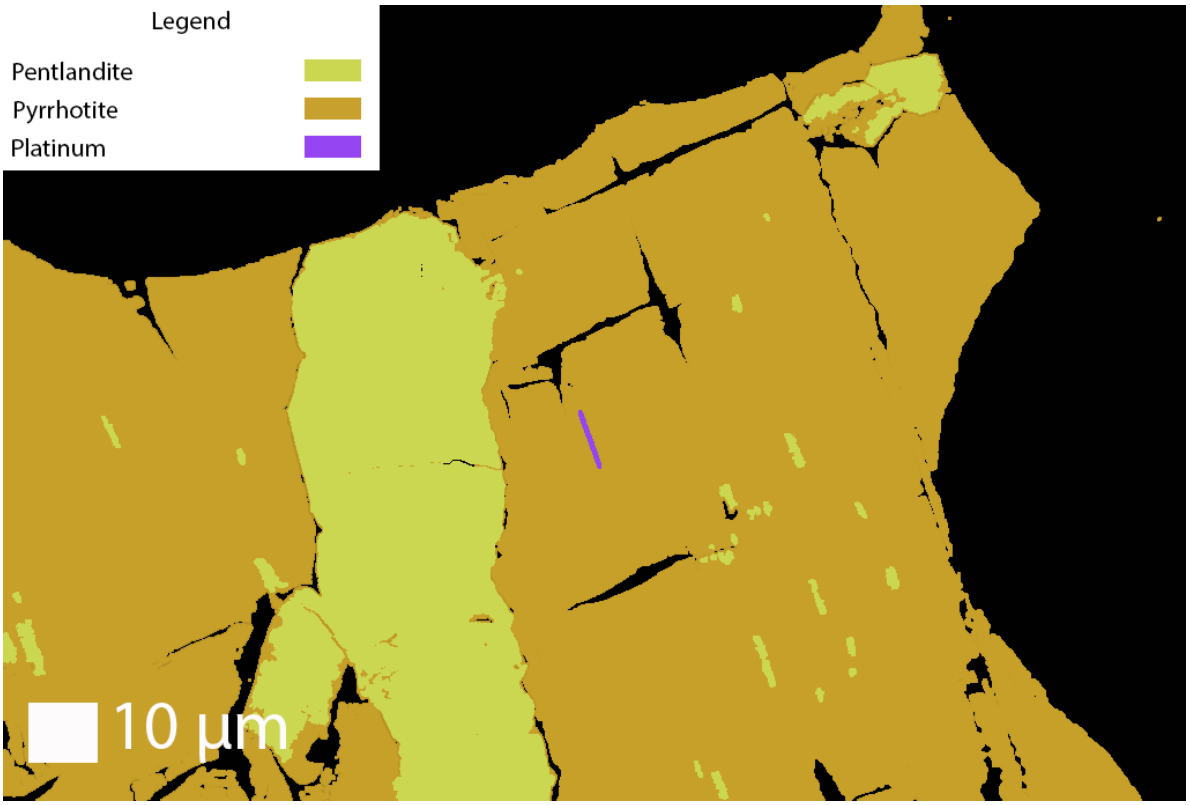

Figure 5.37: Color interpretation chart of Pt-179.

Seven Pt-dominant minerals stands out from the rest, Pt-137, 138, 152 (figure 5.38), 146, 147, 180 and 223.The first three are located in 109.4, forming in contact with chalcopyrite and show elevated contents of Bi together with Pt and Te. The last four are pure Pt, where 146 and 147 together with a few smaller observations are totally enclosed by pentlandite. They form as needles in a single large pyrrhotite grain with a gradual transition from Pt to pentlandite to

pyrrhotite. Pt-180 have the same shape and host relation, but form in a different setting at the end of a sulfide vein. This PGM has an elevated content of Ag that is not observed in the other Pt-dominant minerals. Pt-223 is the only pure Pt mineral, located in 110.45 (pegmatite) and is situated in a fracture within ilmenite.

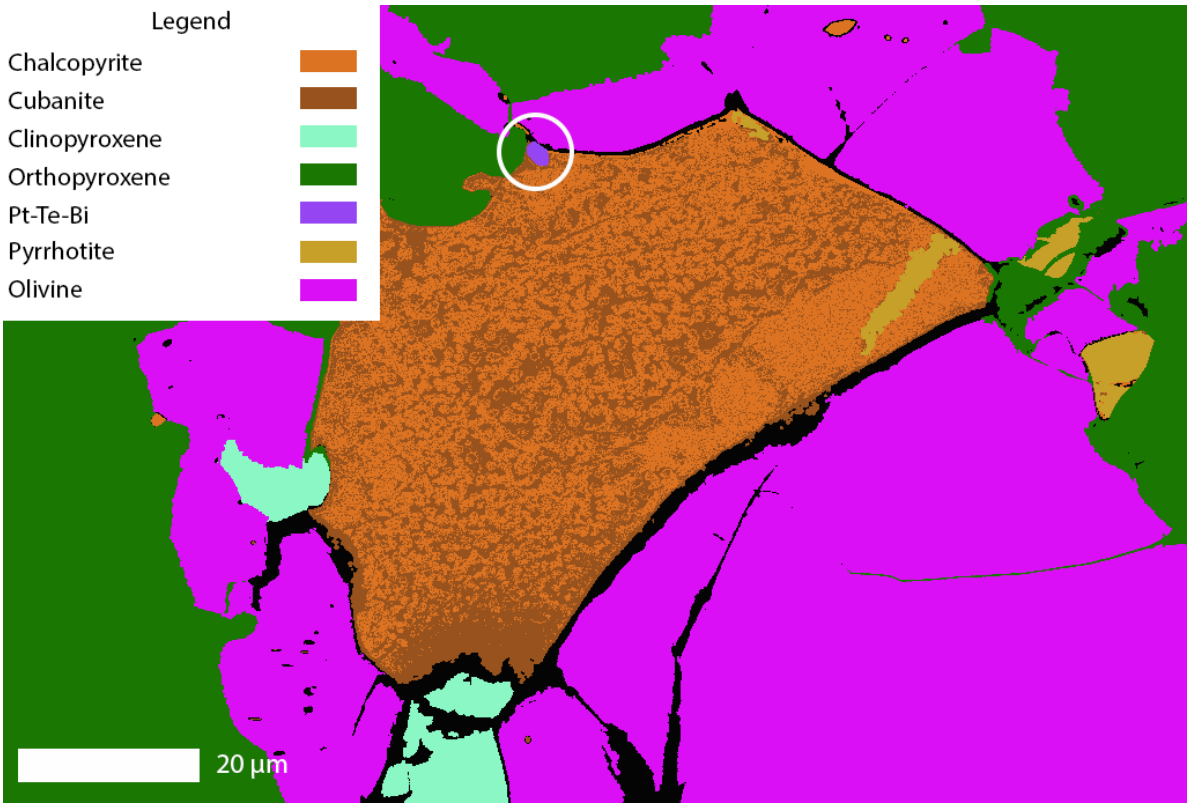

Figure 5.38: Color interpretation chart of Pt-152.

Generally, these Pt-dominated tellurides show little correlations with other elements. Se (figure 5.39) and Rh (figure 5.40) are the only elements that gave any results.

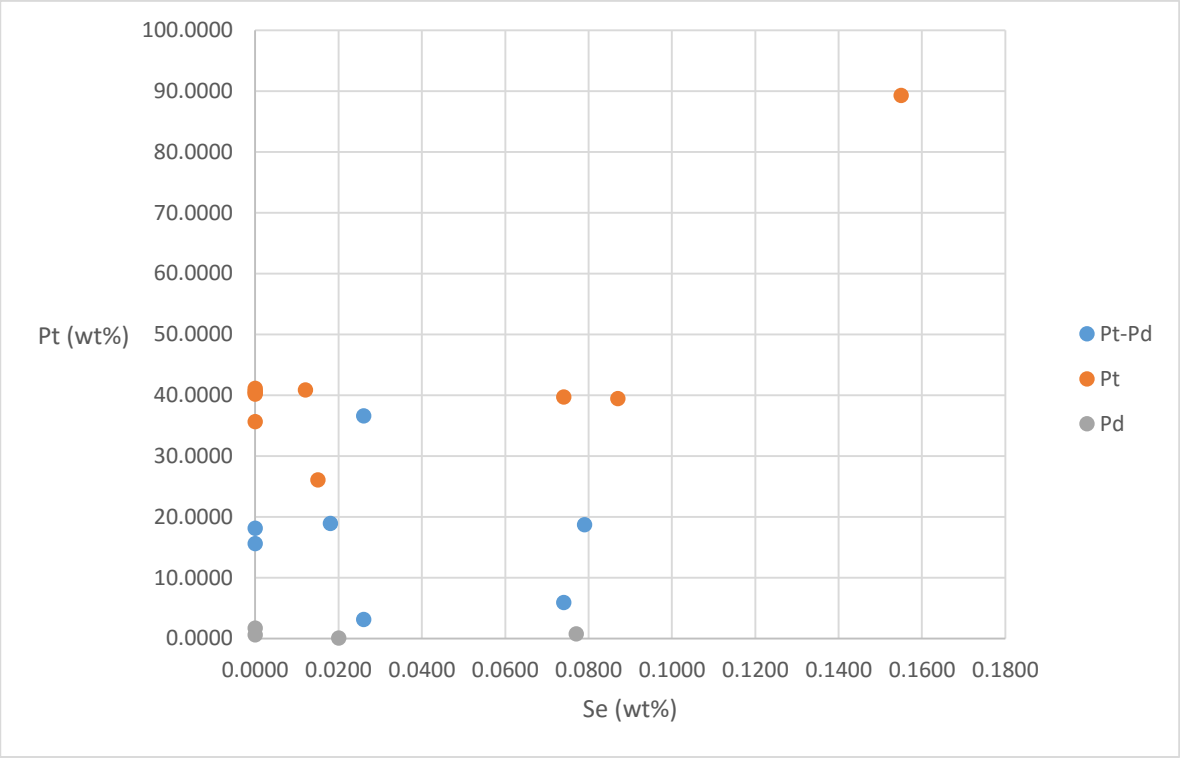

Figure 5.39: Plot of Pt vs Se (wt%).

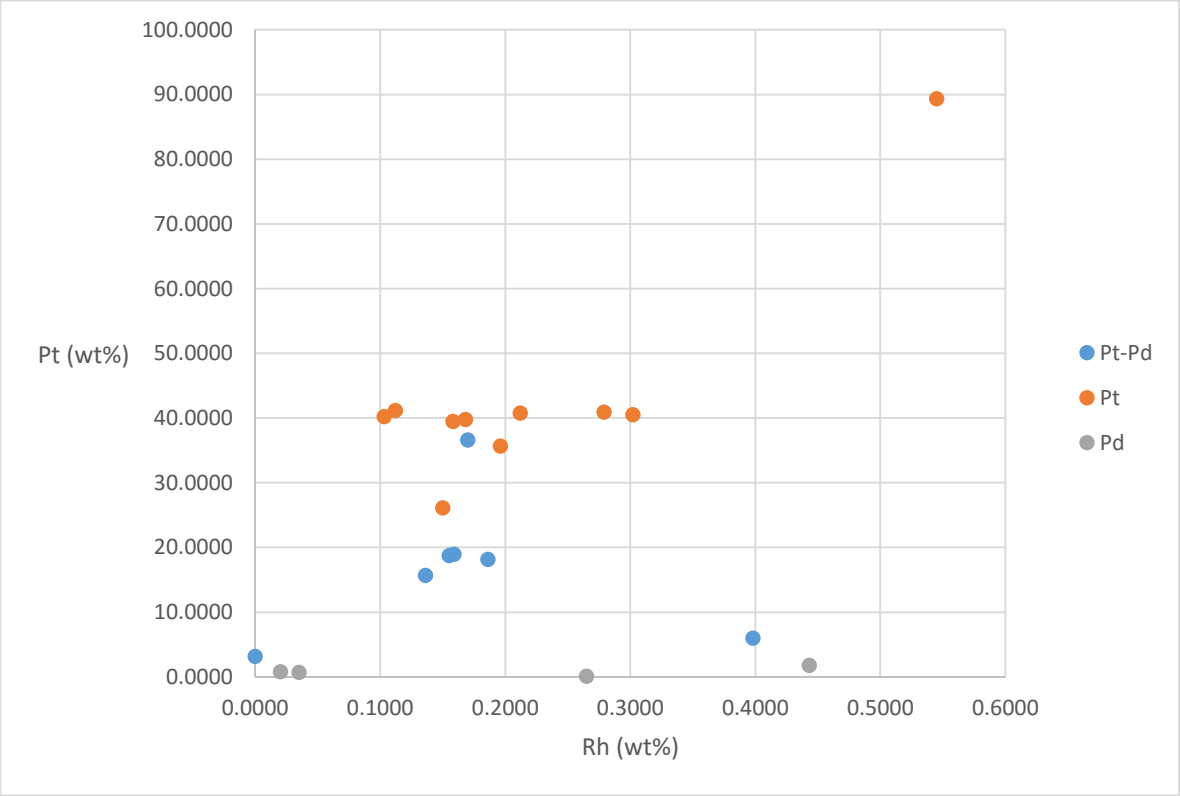

Figure 5.40: Plot of Pt vs Rh (wt%).

Pt hosting sulfides are in most observations bordered by a rim of serpentine. This rim is either completely or partly enclosing the sulfide. Where serpentine is absent, olivine and lesser amounts of orthopyroxene is the main hosting silicates, together with minor amount of carbonate, amphibole, ilmenite and clinopyroxene. The grain size varies, but coarse-grained olivine is commonly present. Other silicates and carbonates are fine-grained.

5.4.2 Pt-Pd dominant

Seventeen Pt-Pd dominant minerals show a continuum between the end members of Pt and Pd (appendix table B 2), but EPMA analyses show that the heterogeneous distribution of these two elements in the PGM's. EDS mapping confirms this relation where Pt and Pd enrich different sections of the same mineral. The majority of the Pt-Pd dominant minerals are observed in the pegmatite, within sulfide veins that shoot out from larger grains of pentlandite, pyrrhotite and chalcopyrite. However, in these observations, chalcopyrite is the main sulfide phase and is most commonly in direct contact with the tellurides (figure 5.41).

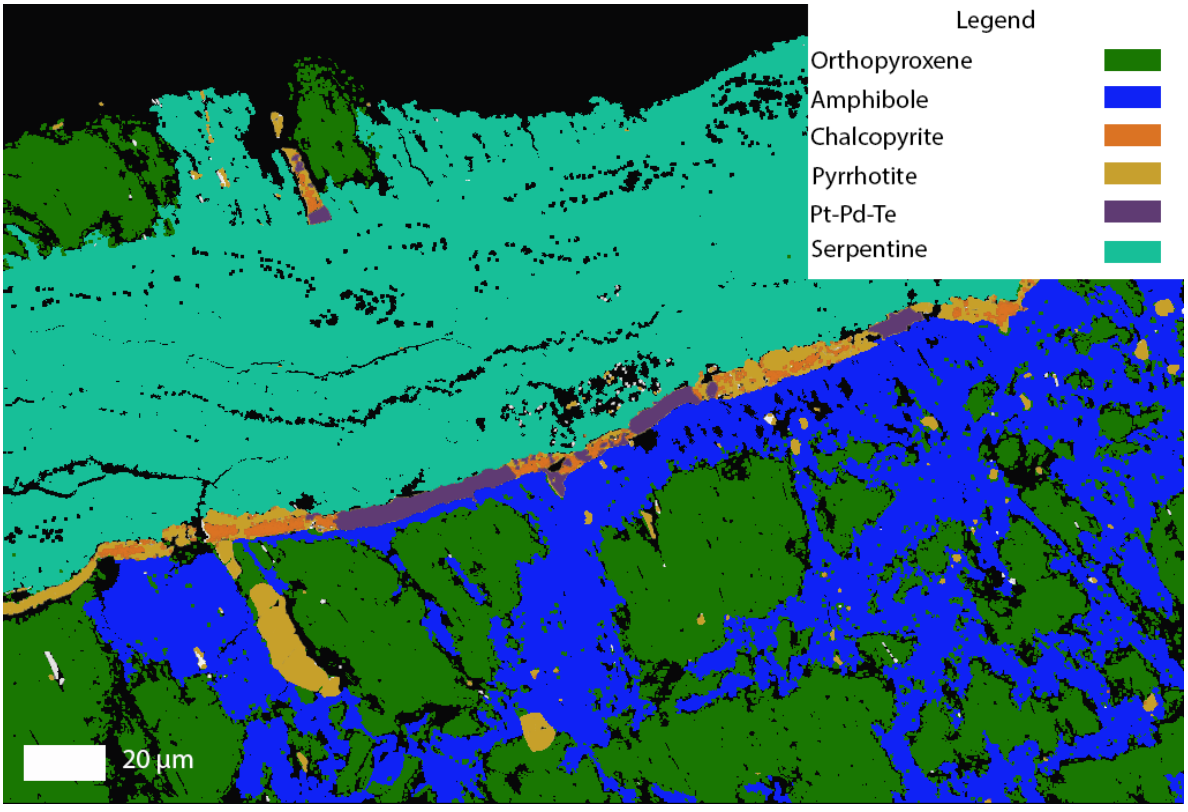

Figure 5.41: Color interpretation chart of Pt-Pd-236 to 250.

Four grains differ from the rest by being situated within large sulfide grains. Pd-226 and 274 form droplets, totally enclosed by chalcopyrite at the edge of a pyrrhotite grain. Pd-282 is the only observed grain of Pt-Pd-dominated telluride forming a needle shaped mineral. However, this grain is not oriented parallel to pentlandite lamellae, but at an angle of approximately 60° to the lamellae. Pt-169 is the only non-telluride within this subdivision. It is rounded and situated at the edge of a sulfide grain in contact with pentlandite. EPMA show Pt, Pd and Bi at near equal proportions.

Elements correlations for this mineral group does, as expected fall in between the two endmembers. They show correlation with both Rh and Se (as seen in figure 5.39 and 5.40), but also with a strong correlation between Pd and Ag (as seen in figure 5.45).

Two correlation is unique to these PGM's. The elevated Ni content (figure 5.42) and the increasing Te content with decreasing Pt (figure 5.43).

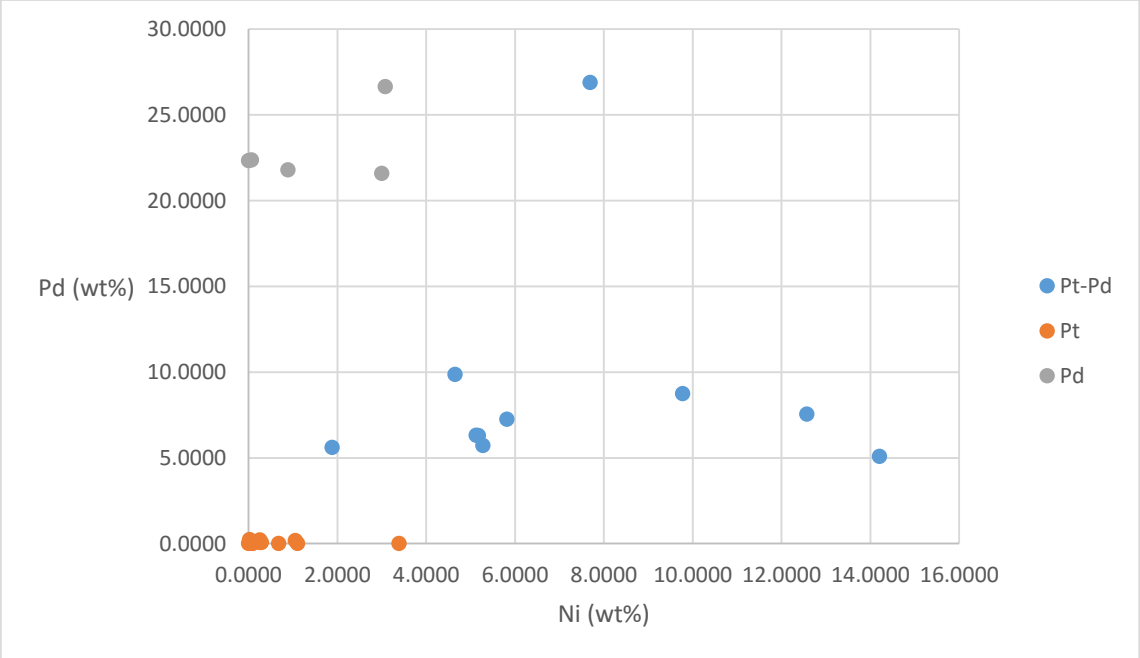

Figure 5.42: Plot of Pd vs Ni (wt%).

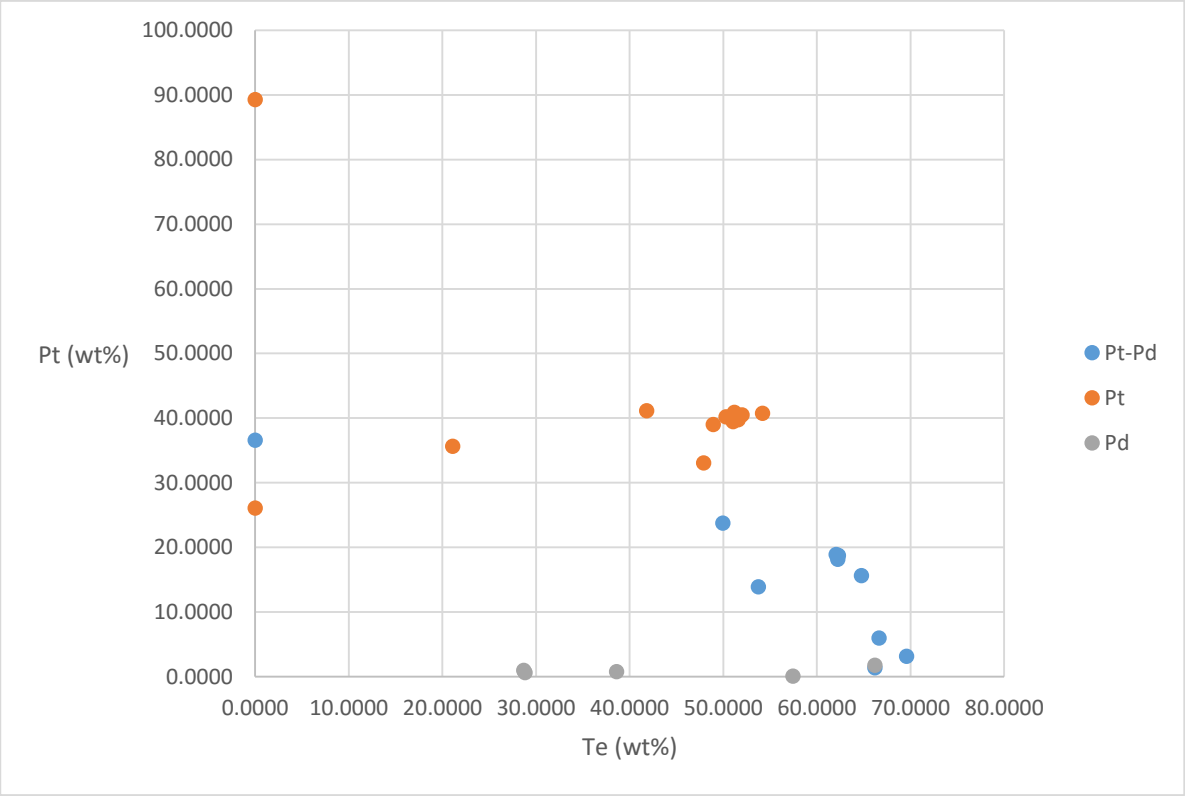

Figure 5.43: Plot of Pt vs Te (wt%).

Orthopyroxene is the main host silicate, together with minor amphibole, clinopyroxene and in one case (Pt-274) biotite. Serpentine is concentrated in veins that appear to be of secondary origin and does not form around the PGE hosting sulfide as is often observed elsewhere. This relation is obvious in the case of Pt-236, where serpentine intersect the PGE vein.

5.4.3 Pd-dominant

Eighteen minerals are Pd-dominant (appendix table B 3), most of which occur in and around a single chalcopyrite grain in 110.45 named “Pd-cluster”. Here, Pd form minerals with Te, Bi and Ag. These occur in an environment where Pb and Ag form minerals with Se and Te, both in and around the major grain of chalcopyrite that hosts the PGM’s.

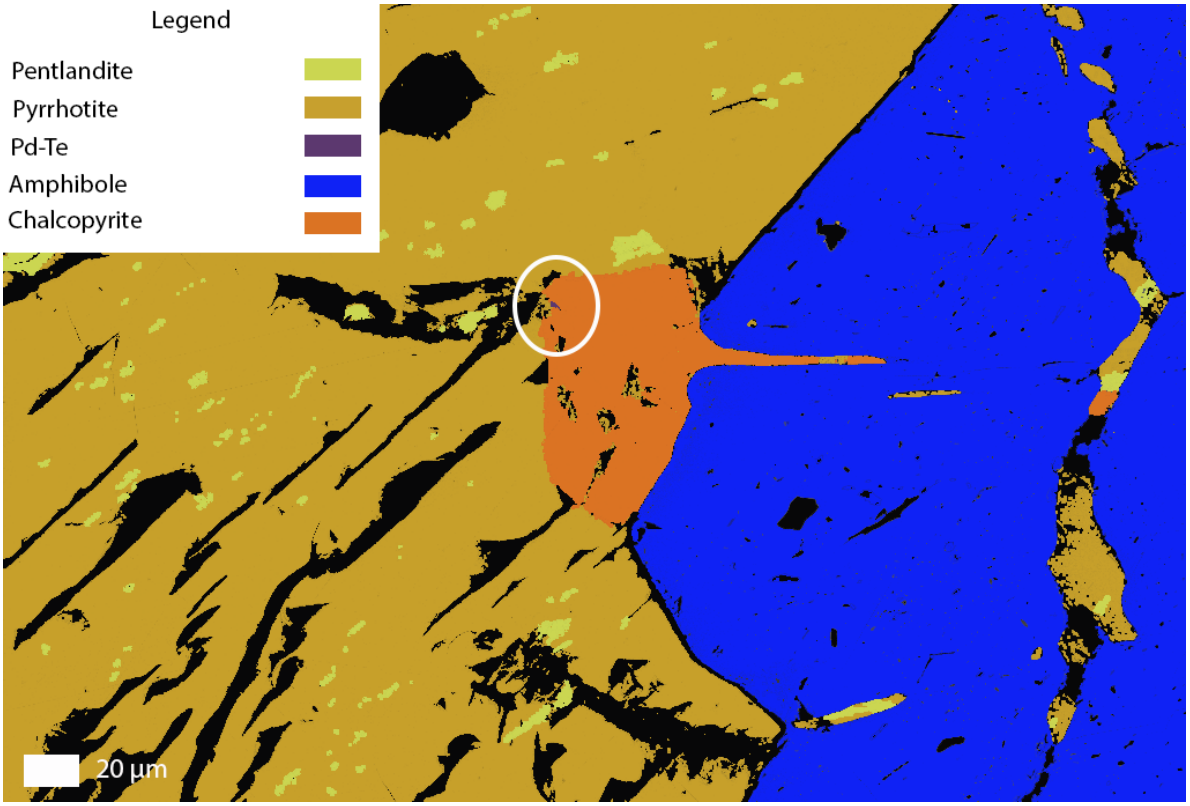

Figure 5.44: Color interpretation chart of Pd-235.

Two other minerals with high Pd contents have been documented; these are not associated with the "Pd-cluster" and contain significantly higher amounts of Te. Pd 235 (figure 5.44) is a needle shaped Pd-telluride, located in 110.45 and is situated in a chalcopyrite section of a larger grain of mainly pyrrhotite and pentlandite. Pd-275 is a round grain of Pd-telluride, located in 110.3 and enclosed by pentlandite.

The only correlation that Pd shows against any other element is Ag, as seen in figure 5.45.

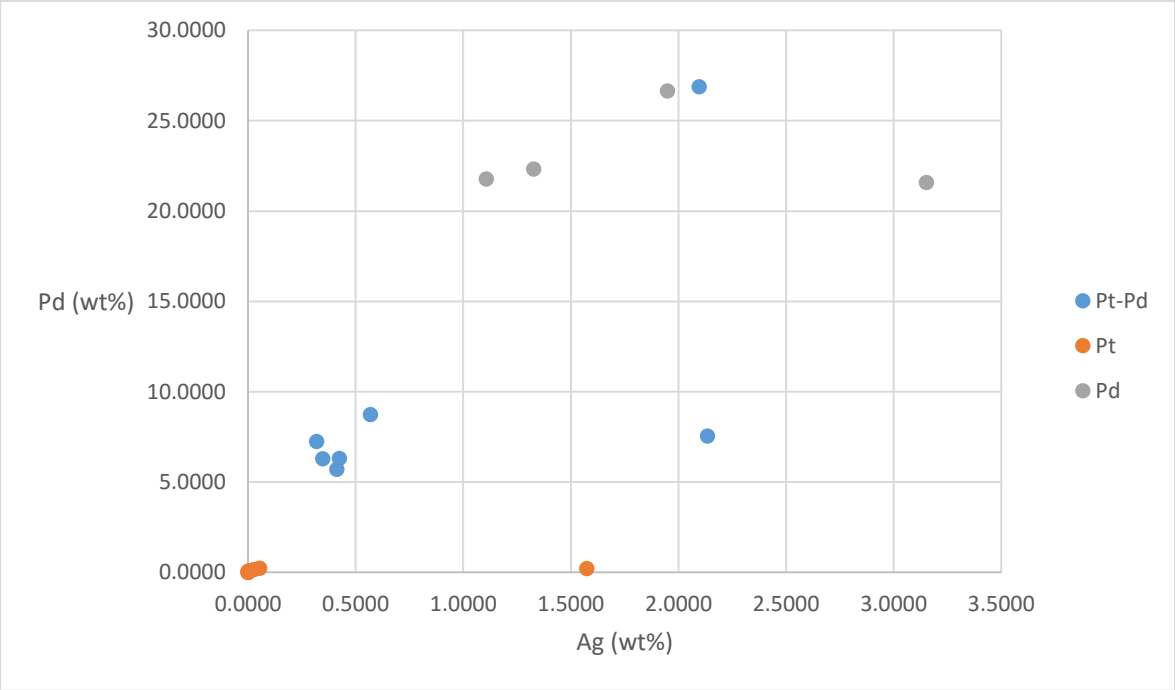

Figure 5.45: Plot of Pd vs Ag (wt%).

Around the "Pd-cluster", a thin rim of serpentine is present, which shows many similarities to the observations of the Pt-dominant minerals in 109.55 and 109.4. For all locations, orthopyroxene and amphibole are the main host-silicates and these are accompanied by carbonates.

5.4.4 Au

Twenty-two gold containing minerals were observed (appendix table B 4). Three were pure gold, whereas the rest are Ag bearing. Au-132 occurs in 109.4 and is enclosed by chalcopyrite, but is located in the same sulfide grain that hosts Pt-131. The rest are located in veins or environments, different from the main lithology. The most significant feature is the named "gold-cluster", located in 109.55. Here, Au-Ag alloys are hosted by chalcopyrite that form satellite grains together with Pb-Te, Pb-Ag, pure Pb and Bi around a larger grain of cubanite, chalcopyrite and pentlandite. The main cubanite grain also comprises rare assemblages of Pd-Sn and Cd-Zn. These are only observed at this location.

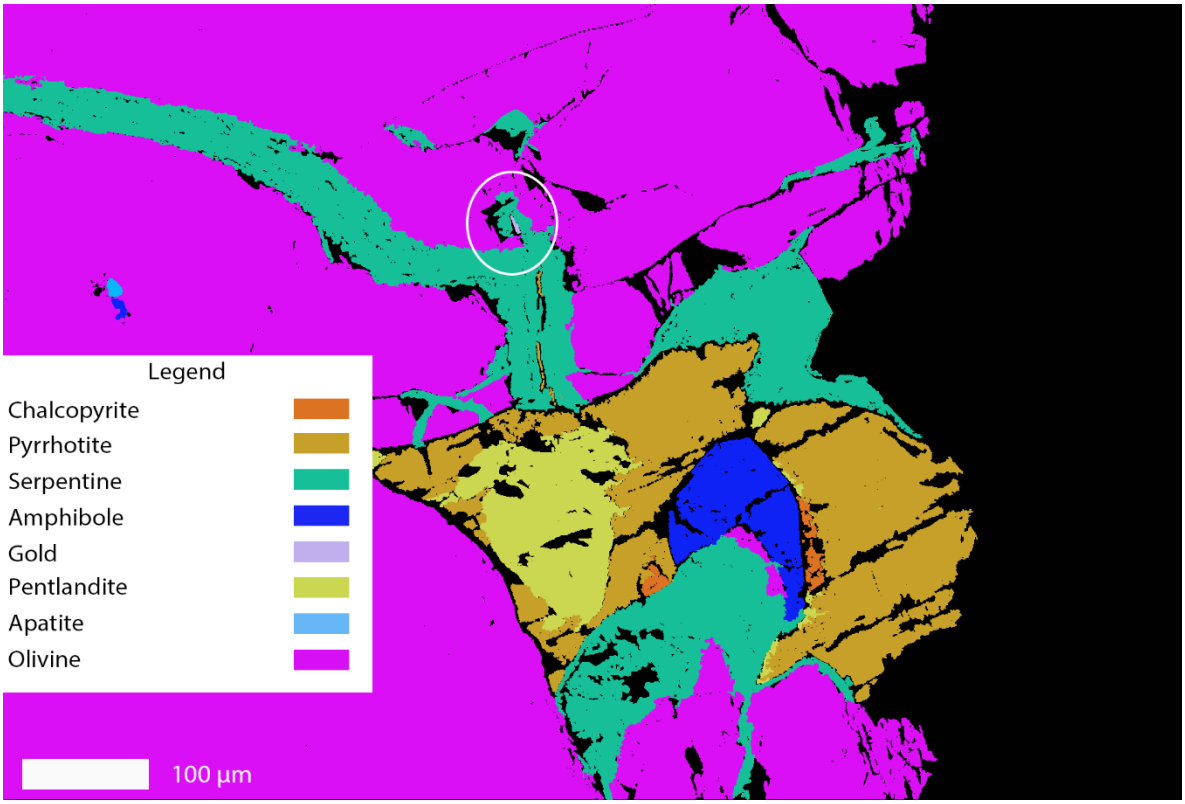

Figure 5.46: Color interpretation chart of Au-81.

The “gold cluster” is directly associated with elevated amounts of carbonate, amphibole, biotite and orthopyroxene. Some serpentine occur as fracture filling material in both silicates and carbonates. The area is also associated with fine-grained ilmenite and Cr-spinel that are abundant compared to other areas.

Two other observations of Au are documented as Au-81 and Au-92. Au-81 is a large Au grain located in a fracture in olivine and partially connected to a seam of serpentine. The grain is in direct contact with serpentine and a very small amount of carbonate. Characteristics of this serpentine vein is the zonal pattern of serpentine and pyrrhotite core, ending with a chalcopyrite core (figure 6.9). Au-92 form together with pentlandite, pyrrhotite and chalcopyrite that intersect orthopyroxene.

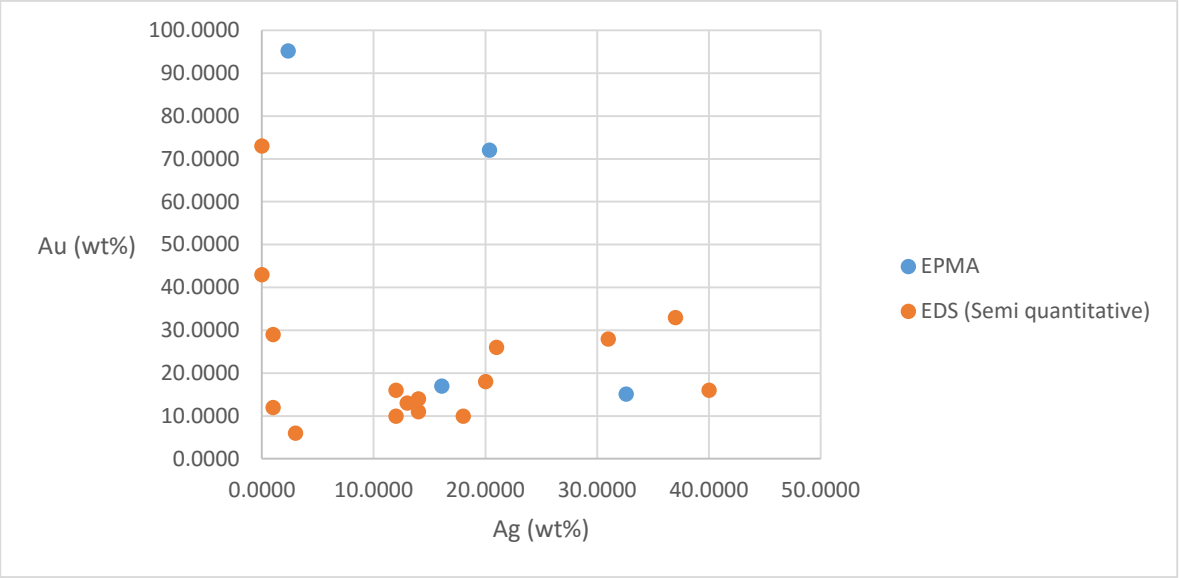

Figure 5.47: Plot of Au vs Ag (wt%).

5.4.5 Other PGM's

One mineral found in 109.4 contains Ru, Ir and Os, and is named Ru-144 (appendix table B 4). It is located in a sulfide at the transition between chalcopyrite and pyrrhotite, but mainly with pyrrhotite as the host sulfide. Silicates consist of orthopyroxene and clinopyroxene, together with some oxides as ilmenite and Cr-spinel.

As this is a single event, it will not be discussed any further.

5.5 Empirical formulas

By using the wt% of the PGE's provided by the EPMA data, empirical formulas were calculated. The full calculation is presented in Appendix E with the final results in table 5.21. The formulas approach is based on accepted stoichiometry for known tellurides found in the web library "webmineral" (Barthelmy, 1997-2014). Pt, Pd, Ni and Ag are normalized to one by a factor, which is then added to the molar percent of Te and Bi. The variable amounts of Ag and Ni, enforced a difficult calculation process. This required an evaluation whether or not to include these elements. The first process was to eliminate elements that only appear as contamination within the PGM's crystallographic matrix. All elements other than Pt and Pd, with less than 2.0 wt%, were excluded from the empirical formula. In formulas that include Ni, the presence of this element came with no increase in either S or Fe. This together with the indication if the Pd count is higher than Pt in Pt-Pd dominated PGM's, Ni content doubles. This

suggests that Ni is not derived from contamination by nearby pentlandite, but is incorporated in the crystal matrix as a substituting element.

Table 5.21: Calculated empirical formulas for analyzed PGM's.

Calculated formula	Point name
(Ni, Pd, Pt) $(Te, Bi)_2$	Pd-274
(Pt, Ni, Pd) Te_2	Pt-236
(Pt, Ni, Pd) Te_2	Pt-237
(Ni, Pd, Pt) $(Te, Bi)_{1,7}$	Pt-238
(Pt, Ni, Pd) Te_2	Pt-239
(Ni, Pd, Pt) $(Te, Bi)_{2,1}$	Pt-240
$Pd_4Pt_3Ni_2$	Pt-169
(Ni, Pd) $(Te, Bi)_{1,8}$	Pd-282
(Pd, Pt, Ni) $(Te, Bi)_{1,9}$	Pd-259
(Pt, Pd) $(Te, Bi)_{2,4}$	Pd-226
(Pd, Pt, Ni, Ag) $(Te, Bi)_{1,6}$	Pd-41
Pt	Pt-223
Pt $(Te, Bi)_{2,1}$	Pt-109-1
Pt $(Te, Bi)_{2,1}$	Pt-109-2
Pt $(Te, Bi)_{2,1}$	Pt-109-3
Pt $(Te, Bi)_2$	Pt-125
Pt	Pt-180
Pt $(Te, Bi)_2$	Pt-166-1
Pt $(Te, Bi)_2$	Pt-166-2
PtTeBi	Pt-152

Pt (Te, Bi)$_2$	Pt-107
Pt (Te, Bi)$_{2,5}$	Pt-138
(Pt, Ni) Te	Pt-87
PdTeBi	Pd-204-1
PdTeBi	Pd-204-2
Pd (Te, Bi)$_2$	Pd-209
(Pd, Ni) Te$_{1,7}$	Pd-275
(Pd, Ni, Ag) Te$_{1,6}$	Pd-235

Ternary diagrams provide a good way of presenting element data. Values are normalized to 100% and plotted to compare the composition of several minerals, while empirical formulas can give a good indication of which mineral the PGM's can be.

The accepted PGM's element wt% from "webmineral" (Barthelmy, 1997-2014) are plotted in ternary diagram (figure 5.49) and compared against the EPMA data that are plotted separately (figure 5.48).

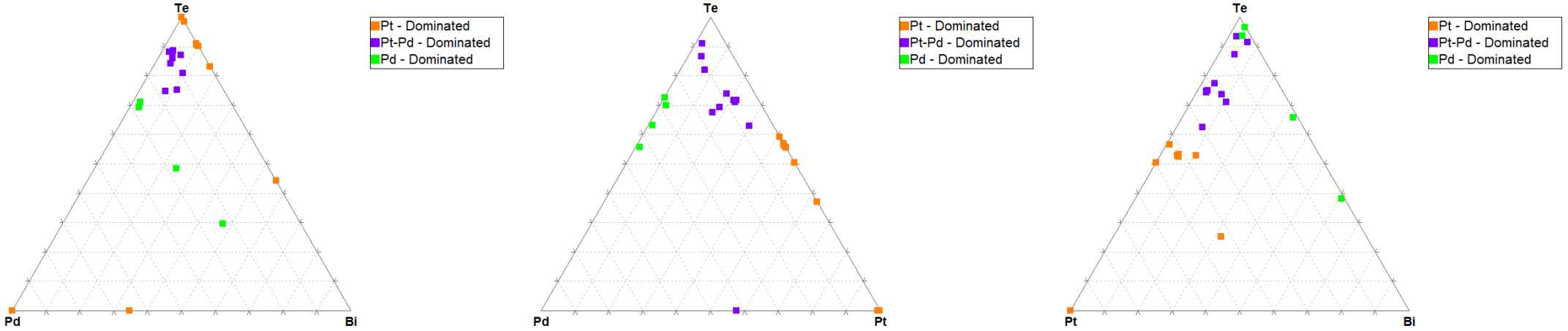

Figure 5.48: EPMA data plotted for Pd-Te-Bi, Pd-Pt-Te and Pt-Te-Bi. All points are represented by elemental wt%.

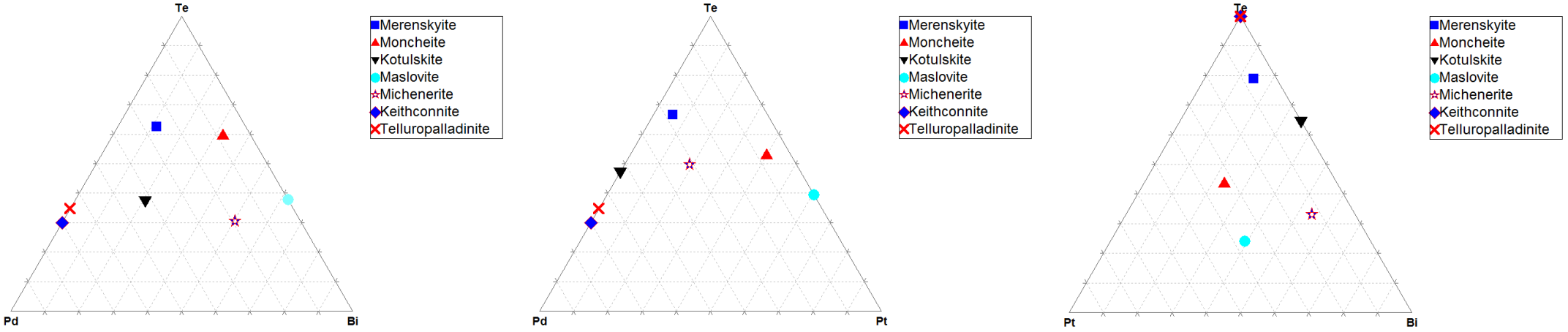

Figure 5.49: Known PGM's plotted for Pd-Te-Bi, Pd-Pt-Te and Pt-Te-Bi. All points are represented by elemental wt%.

6 Discussion

6.1 PGE minerals

In order to understand the PGE ore in the RUC, it is necessary to identify the ore forming PGM's. The empirical formulas calculated in section 5.5 have been compared through webmineral internet database (Barthelmy, 1997-2014), and resulted in the following tables 6.1 – 6.4.

Table 6.1: Pt – Minerals, based on EPMA analysis and empirical formula calculation.

Pt - Minerals		
$Pt(Te, Bi)_2$	-	Moncheite
PtBiTe	-	Maslovite (Pt-152)
Pt	-	Native platinum
(Pt, Ni) Te	-	Unknown (Pt-87)

Moncheite and Maslovite have been widely documented in PGE deposits as described in section 4.11. These minerals are associated with magmatic processes and form as inclusions in monosulfide solution.

Pt can in rare cases occur as native metal, known from nuggets in alluvial deposits (Mungall, 2005). However, due to the size of Pt-146 (0.8 x 0.1 µm) it is difficult to obtain quantitative chemical analysis with the instruments available for this thesis. EDS mapping does not show any traces of other elements incorporated in the crystallographic lattice, and therefore have led to the interpretation of in situ native Pt.

The unknown Pt-telluride is only represented once in this study and the size (2.5 x 2.5 µm) can suggest the Ni content is deriving as contamination from the hosting pentlandite. Another explanation can be the description by Hudson (1986) as an reaction product between moncheite and melonite ($NiTe_2$). In this case the content of Te is too low in order to fit the mineral formula of moncheite – melonite. Similar mineral composition have been discussed by McLaren and De Villiers (1982) and Genkin and Korolev (1961), but for now this composition have not been accepted as a distinct PGM.

From the ternary plots in figure 5.48 it is clear that Pt and Te are displayed an interchanging relationship, while Pd and Bi are stable. Correlation for Pt have only been found

with Se (figure 5.39) and Rh (figure 5.40), but in both figures the content of Pt is stable. In figure 5.43 it is evident for Pt-Pd-dominated minerals that a decrease in Pt results in an increase in Te. This can suggest that Te is substituting for Pt, but the same artifact is absent for the Pt-dominated minerals. The chemical explanation for this interaction cannot be resolved based on the available results provided by this thesis.

Table 6.2: Pt-Pd – Minerals, based on EPMA analysis and empirical formula calculation.

Pd - Minerals		
PdTeBi	-	Kotulskite
Pd (Te, $Bi)_2$	-	Merenskyite
(Pd, Ni) $Te_{1,7}$	-	Merenskyite
(Pd, Ni, Ag) $Te_{1,6}$	-	Merenskyite

Both kotulskite and merenskyite is known to be associated in similar ore forming environments. Experiments by Helmy et al. (2005) describes these tellurides to be the first mineral assemblage that crystalize from the Pd-rich portions. In the PGE reef, Pd is strongly enriched in chalcopyrite within the pegmatitic orthopyroxenite. This element is more chalcophile than Pt (Vogel & Keays, 1997) and will therefore preferably partition into a copper enriched magma or liquid (Lightfoot & Keays, 2005). The clear separation between Pt and Pd in the PGE reef, can suggest that Pd might have been re mobilized during lower temperature hydrous liquid and partitioned into chalcopyrite (Gervilla & Kojonen, 2002; Helmy, Stumpfl, & Kamel, 1995; Rowell & Edgar, 1986). Chalcopyrite is a frequently occurring sulfide mineral, both as inclusions in larger sulfides compounds and isolated. One grain of Pd enriched isolated chalcopyrite (Pd-cluster) display a possible remobilized signature. Coexisting mineral compositions Pb-Ag, Pb-Te, Pb-Se and Ag-Te, is unlike any other PGE mineral association elsewhere in the dunite or the pegmatite. Watkinson and Melling (1992) describe a similar PGE occurrence for the Salt Chuck intrusion, Alaska. Here, high content of Cu and precious metals are interpreted to form by remobilization in a Ca bearing fluid after solidification of the magma.

Table 6.3: Pd – Minerals, based on EPMA analysis and empirical formula calculation.

Pt - Pd - Minerals		
$(Ni, Pd, Pt)(Te, Bi)_2$	-	Merenskyite
$(Pt, Ni, Pd)Te_2$	-	Moncheite
$Pd_4Pt_{3(}Ni_{2)}$	-	Unknown (Pt-169)
$(Ni, Pd)(Te, Bi)_{1,8}$	-	Melonite (Pd-282)

Merenskyite and moncheite with this chemical assembly are enriched in Ni, which according to Helmy et al. (2006), is a result when crystallizing from a PGE under saturated melt. Ni then substitute for the PGE's due to an interaction between melonite and merenskyite-moncheite (see section 4.11). Another simpler explanation is possible contamination due to a 3D effect. The scarcity of these minerals makes it highly unlikely they would completely fill the vein sections they are situated in, but collect as smaller telluride "pools". Therefore, coexisting pentlandite and pyrrhotite located behind the PGM can be a source for contamination. In that case, an increase in both Fe and S should accompany Ni. As this is not evident in these observations, it would make contamination highly unlikely.

The PGM review by (Daltry & Wilson, 1997) does not mention any accepted PGM with close to equal amount of Pt and Pd as seen in the unknown PGM. The Ni is unlikely incorporated into the crystal lattice, since the EPMA data had to be recalculated due to high Ni and S content. The only comparable mineral mentioned in literature was discovered during PGE nugget analysis by Legendre (1992). He discovered a mineral with the composition $(Pd\text{-}Pt)_2S$, which is yet to be accepted as a PGM. The significant S content in Pt-169 increase the possibility of being a sulfur PGM with moderate pentlandite contamination.

No PGM's documented in the review by Daltry and Wilson (1997) is remotely comparable to the properties of Pd-282. The mineral shape and host strikes some similarities with other PGM's in the RUC. However, the low content of PGE and high Ni (appendix table d 1), can indicate this being melonite. Rucklidge (1969) describes this interaction and it is therefore probable that Pt-282 represent a crystallization reaction between merenskyite ($PdTe_2$) and melonite ($NiTe_2$).

Except for the PGE experiment by Helmy et al. (2006), there is no well-documented natural PGE poor deposits. Making it difficult to compare any of the PGE poor minerals.

Enrichment of Au is mainly restricted to one area in thin section 109.55. A few grains of Au-Ag does occur throughout the thin sections, but could not alone cause a significant

anomaly. Therefore clusters such as the "gold cluster" is most likely causing the Au anomaly in the RUC. From EPMA analyses, the mineral composition is varying, but show a high content either of Au or as an Au-Ag alloy.

Table 6.4: Gold alloys, based on EPMA analysis.

Gold alloy		
Au-Ag	-	Electrum (>20wt% Ag)
Au-Ag	-	Native Gold

Electrum and native gold is e frequently occurring and often found in layered intrusions with ore deposits such as Stillwater, Bushveld and Norilsk (Holwell, 2006; Holwell & McDonald, 2007; McLaren & De Villiers, 1982; Sluzhenikin, 2011; Volborth, Tarkian, Stumpfl, & Housley, 1986). Au chalcophile signature is well established and frequently observed, as the majority of Au is located in chalcopyrite.

In the "gold cluster", chalcopyrite hosting Au forms as satellite grains to a larger cubanite grain, hosted by carbonates, amphibole, biotite and orthopyroxene.

6.2 Sulfur isotopes

Sulfur isotope data from Platreef (section 4.11) suggest the ore forming melts were contaminated by crystal sulfur, evident by the reefs high content ($\delta^{34}S$ of 2.6 – 9.1) of heavy sulfides. The thesis by Øen (2013) focus on sulfur isotopes from the different lithologies in the RUC and the two reefs in RF-1. $\delta^{34}S$ (all data presented as ‰).

Isotope data from the CS is -2.71 to 0.45 with an average of -1.46. From the PGE anomaly, results showed $\delta^{34}S$ of -1.93 to 2.65 with an average of 0.39. Even if the RUC have been subjected to crustal contamination, it cannot compare to Platreef. Øen, derived at the same conclusion, while still showing an ultramafic signature it is likely that the CS was contaminated by Langstrand gabbronorite.

Located 20 meters above the PGE anomaly there is a copper anomaly (Iljina, 2013) that have also been analyzed for sulfide isotopes by Øen (2013). Results showed variations from ÷5.74 to ÷1.00 with an average of ÷3.82. A clear mantle derived signature and lighter than the PGE reef. This can indicate a possible later replenishment episode, enriched in copper and not

directly linked to the PGE reef. This suggestion is supported by Grant et al. (2016), where the olivine shows a sudden change from Fo_{79} to Fo_{85}, at 560-562 meters above sea levels in RF-1 (equal to 90 m below the drilling surface).

When comparing the visual descriptions of the Cu-Ni horizon in Øen (2013), with the PGE reef descriptions provided by this thesis, there is no significant change in the appearance of the sulfides. This could strengthen the possibility that both reefs are formed by magmatic processes.

6.3 Evolution

Grant et al. (2016), describes the RUC as an open magmatic system that evolved through several episodes of magma recharge. UG-2 and Merensky reef in Bushveld is perhaps the best representations of reefs forming in such an environment. Both are products of a high R-factor with episodes of magma recharge that were thoroughly mixing with already existing melts within the Bushveld intrusion (see section 4.9.1).

P-T estimates by Grant et al. (2016) suggest the parental melts entered the magma chamber with temperatures between 1120-980°C at 7-9 kbar. These estimates supports previously published data from the SIP with temperature of 1450°C at 6-10 kbar (Bennett et al., 1986; Griffin et al., 2013), which leads to an interpretation where *"the Reinfjord Ultramafic complex provides a link between deep crustal intrusions and the evolution of some continental flood basalts"* (Grant et al., 2016). Crystallization temperatures for Merensky reef of 1100°C (Boudreau, 2008), Platreef of 900°C (Armitage, 2011) and J-M reef of 1000°C (Helz, 1995) does all compare quite well with the RUC. However, the pressure gradients are significantly different, Bushveld max 5 kbar (Armitage, 2011) and Stillwater max 3 kbar (Helz, 1995).

The parental magma composition with Fe/Mn ratios of 76-88 falls within those values expected to derive from a mantle source (Grant et al., 2016). A picritic-komatiite magma (Bennett et al., 1986; Emblin, 1985) and a dry dunitic magma (Griffin et al., 2013) have also been suggested. For Bushveld, the parental melt are primary of a mantle source (Hatton, 1995). Due to the large assimilation of country rock and magma mixing throughout time, the average silica content increased (53%) and consolidated as more evolved magmas. In which the reefs are now preserved and mined.

Based on results from this thesis and related articles, there are three main hypothesizes that possibly could explain how the RUC became enriched in PGE's.

1. Gradual in situ enrichment in the magma chamber that eventually accumulates as a PGE horizon.
2. A later melt recharge with immiscible sulfide, enriched in PGE prior to entering the RUC.
3. Later, re mobilization of the PGE enriched sulfides.

Both of the ideas above embrace the same general principal. Figure 6.1show a simple N – S profile of the magma chamber. As melts passes through, some partitions are diverted by the roof and start mixing with existing magmas, above the partly crystallized mush/slush on the chamber floor. As activity slows down, the suspended sulfides starts to sink and accumulate in metal rich horizons. A signature expected to form in such a situation is a sedimentary pattern of which the larges/heaviest grains fall quicker and form the lowest part of the horizon. During the PGE mapping sequence, exactly this was observed as average PGM grain size in 109.55 (20.7 μm^2) is larger than in 109.40 (7.9μm^2). Indicating that the PGE reef, most likely is a stratigraphic PGE horizon settling on the magma chamber floor.

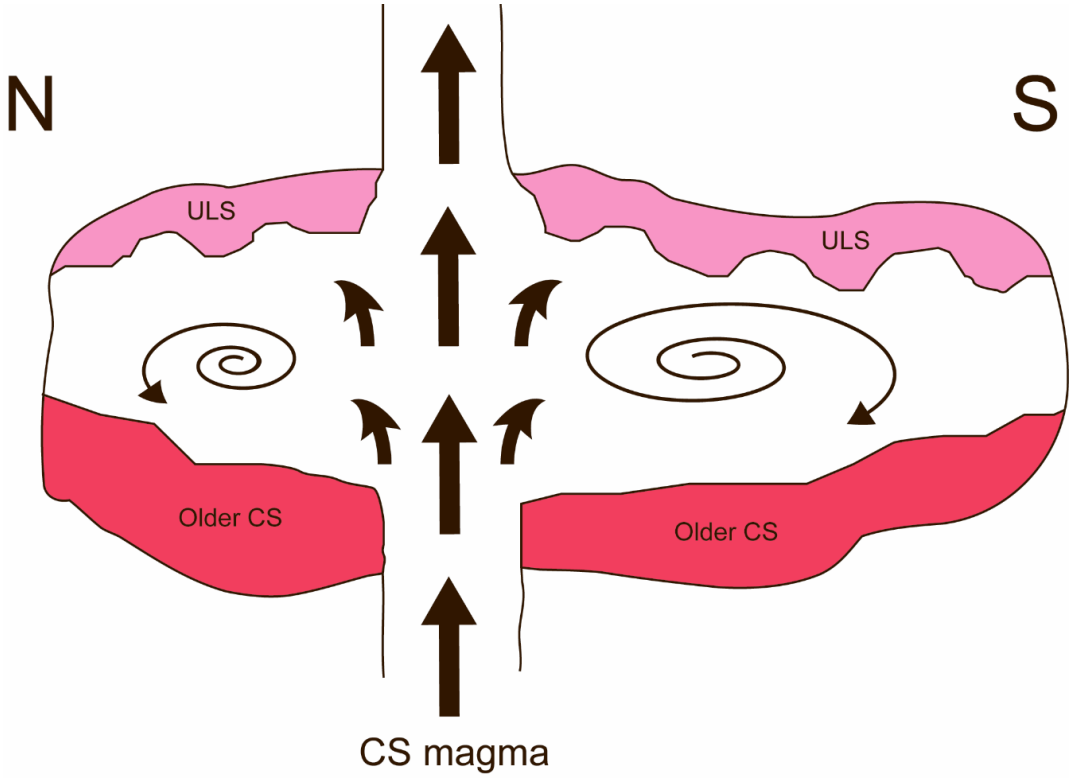

Figure 6.1: Episodes of magma recharge that undergo mixing and crystal fractionation that gradually enriches sulfides in PGE.

The major difference in the first two hypothesis, is that 1) presents a gradual enrichment inside the magma chamber over time by multiple episodes of magma recharge, while 2) discuss

one or a few injections of magma with immiscible sulfide, enriched in PGE's at the end of the RUC's active period.

A plot of MgO in RF-1 (figure 6.2) show the changes in MgO from a depth of 250 meters below the drilling surface. Underneath the PGE reef, there are two main MgO spikes, followed by a gentle decrease without rapid MgO variations. This suggests a stable and more continuous recharge, where the magma chamber could have gradually become enriched in PGE. This idea is represented in figure 6.1, where high and steady volumes of melts are passing through the system over a longer period.

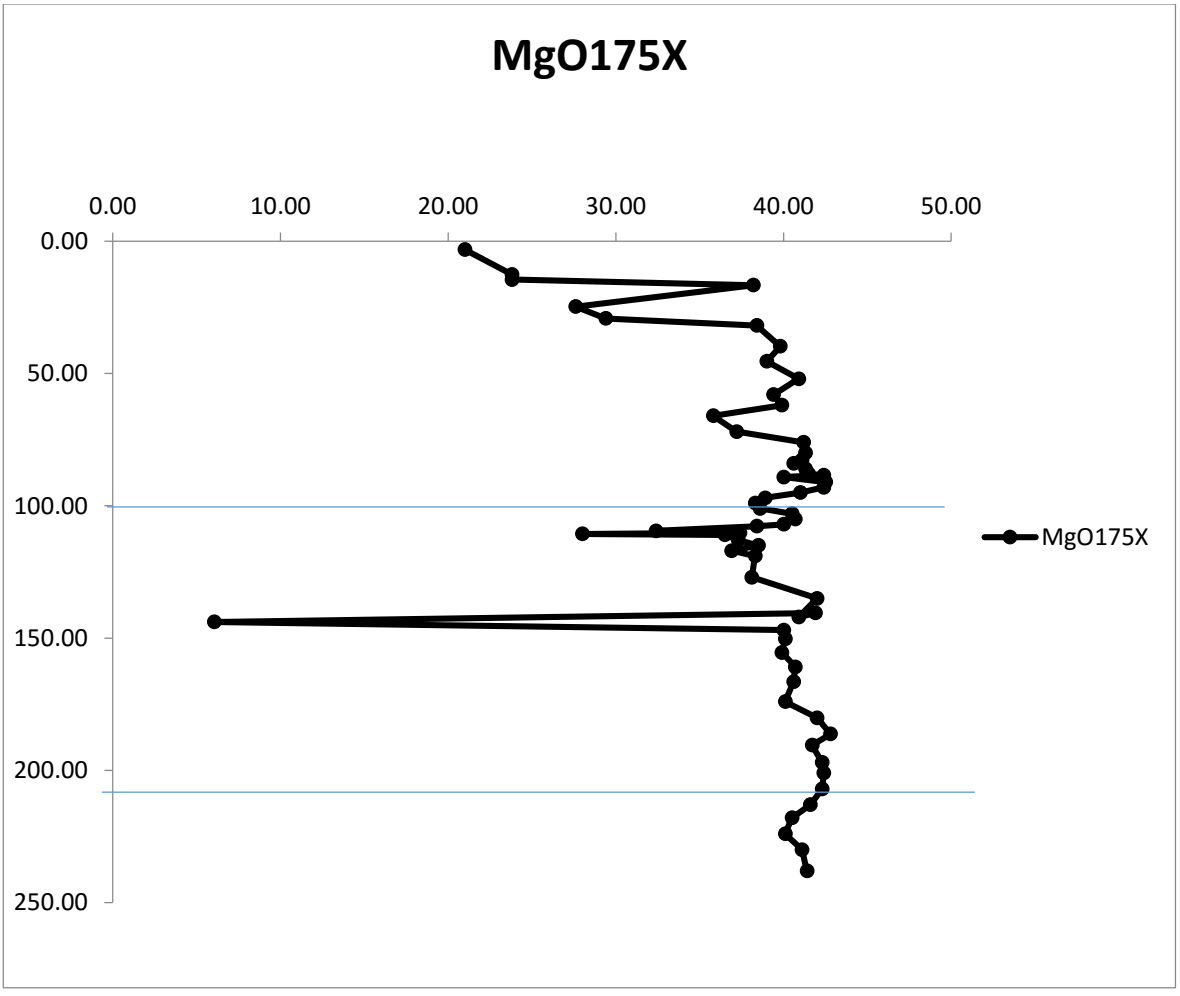

Figure 6.2: MgO plotted against depth from drill hole RF-1.

Hypothesis 1) is a sulfur under saturate magma that reaches sulfur saturation after mixing within the RUC. The lack of Ni that is incorporated in the dunite hosted PGM's, indicate parental melts enriched in PGE's (Helmy et al., 2006). When reaching sulfur saturation, droplets of sulfide will scavenge the melt for PGE and enrich the immiscible sulfide phase. This

is the same magmatic process thought to form the Merensky reef and the UG-2 in Bushveld. However, there is a slight problem associated with this model. The position of the PGE reef in the RUC differs significantly from the Merensky reef and the UG-2, as they appear in the lower third portions of the Bushveld intrusion (figure 6.6). From recent drill holes (RF-4 from 2015), it is found that the dunite continues to a depth greater than 300m beneath the surface. Together with the interpretation of a roof section in the northeast 200-250m above, would suggest the reef position in the middle, to the upper third of the intrusion. The Skaergaard intrusion is another PGE ore forming deposit, where the reefs position in in the similar stratigraphic section as the PGE reef in the RUC. As Skaergaard is a closed system, there is no need for further comparisons.

Right above the PGE-reef at 107m, as described by Grant et al. (2016) there is a significant MgO spike, with a short stable period, followed by a sharp decrease. Figure 6.3 show a thought situation for the Cu-Ni reef, with lower volume of melt injected over a shorter period. After this intrusion the Cu-Ni enriched sulfides quickly sinks and collect in a horizontal layer. Hand samples clearly show a section strongly enriched in sulfides (figure 6.4), but carbonate veins figure 6.7A enriched in Cu could also add to the anomaly. Since no additional data have been collected from this zone, there will not be any further discussion regarding this anomaly

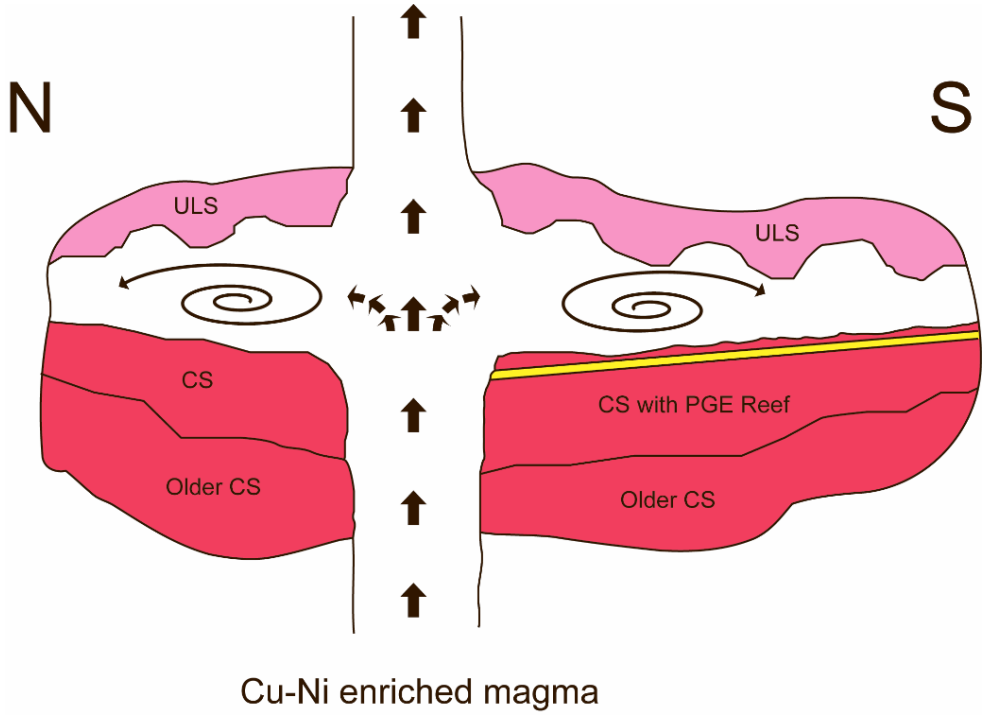

Figure 6.3: A later injection of a Cu-Ni enriched magma that form a reef 20m above the already existing PGE-reef.

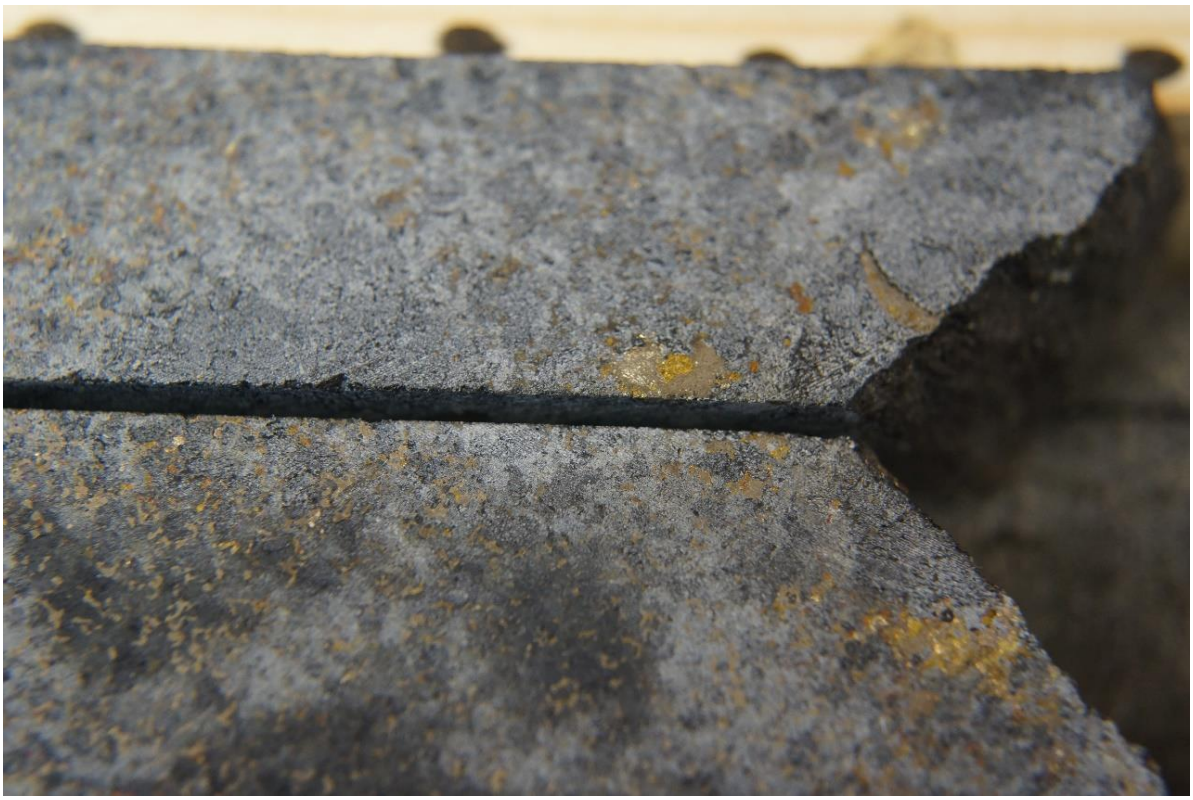

Figure 6.4: Split drill core from RF-1, showing the sulfide enrichment in the Cu-Ni reef.

Hypothesis 2), introduces a later melt at sulfur saturation where immiscible sulfides are already enriched in PGE (figure 6.5). A similar situation is suggested to form the Platreef in Bushveld and it is the strong enrichment of tellurides in the Platreef that gave rise to the comparison. Such a melt would be very dense and in Platreef, it could never thoroughly mix with the overlaying cumulates. It flowed near the magma chamber floor (figure 6.6), forming a layer 10-400m thick with massive sulfides both in the country rock gneisses and the magma chamber. A direct comparison between the ore forming processes in Platreef with the PGE reef in the RUC would not be adequate. Because of the shallow emplacement and large assimilation of country rock.

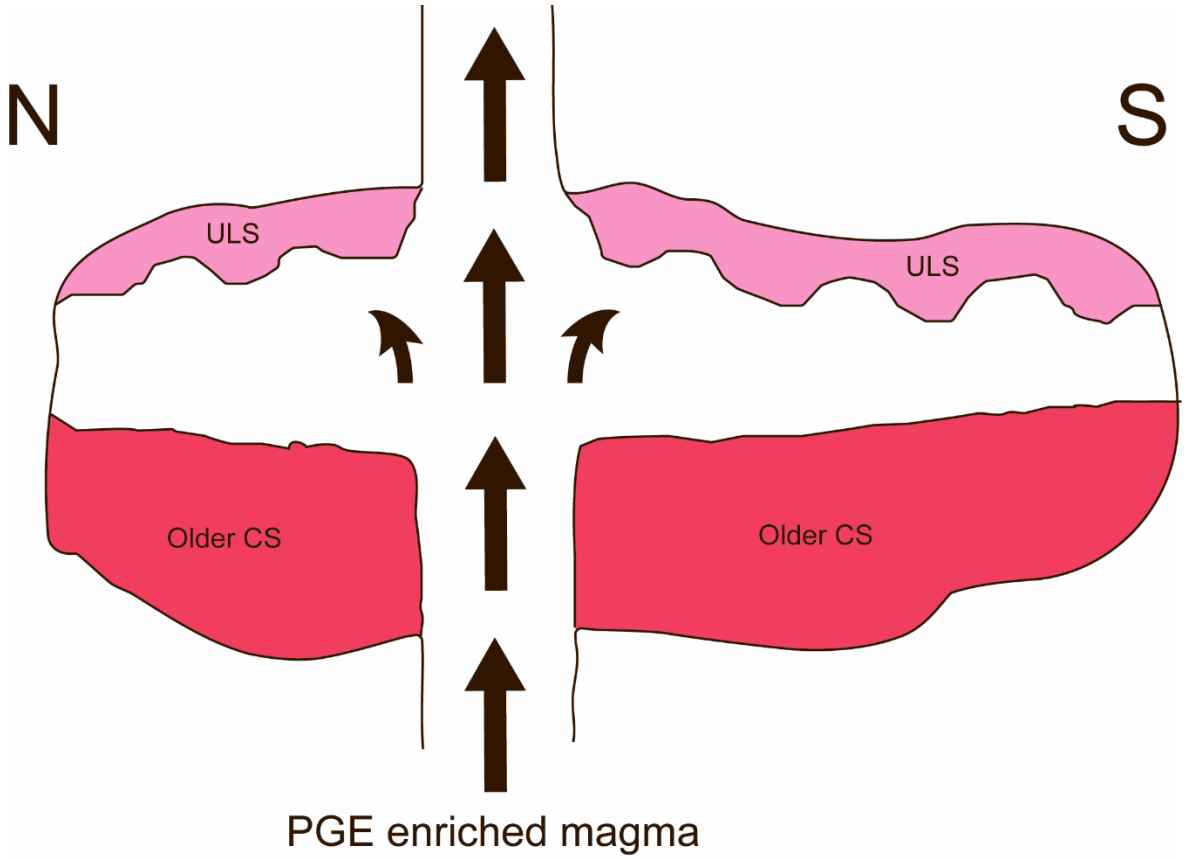

Figure 6.5: Injection of a PGE enriched magma later in the magma chamber evolution.

As mentioned at the start of section 6.3, “the RUC represents a link between deep crustal intrusions and flood basalts”, and this is where the Platreef and Norilsk share an important magmatic process. Both parental magmas are thought to have reached sulfur saturation and PGE enrichment in deeper chamber, then being transported to the final emplacement (Naldrett, 2013). As melts progressively ascend trough the crust it will exploit weakness zones, forming sills and smaller chambers that experience recharge as new batches of magma are moving

through the system. Geophysical studies (Brooks, 1969; Pastore, 2015) interprets a positive Bouguer anomaly to represent a deeper magma chamber positioned west of Sørøya. It is possible that PGE enriched melts dispatched from this deeper magma chamber are represented in the RUC and the rest of the SIP. Such a magma could be injected into the RUC as it ascends to a higher position in the crust. The MgO spike at 140-135m (figure 6.2) could indicate a magma recharge and possibly the entry for such a magma. Turbulence in the magma chamber could keep the sulfides suspended, until they start accumulating at 113m.

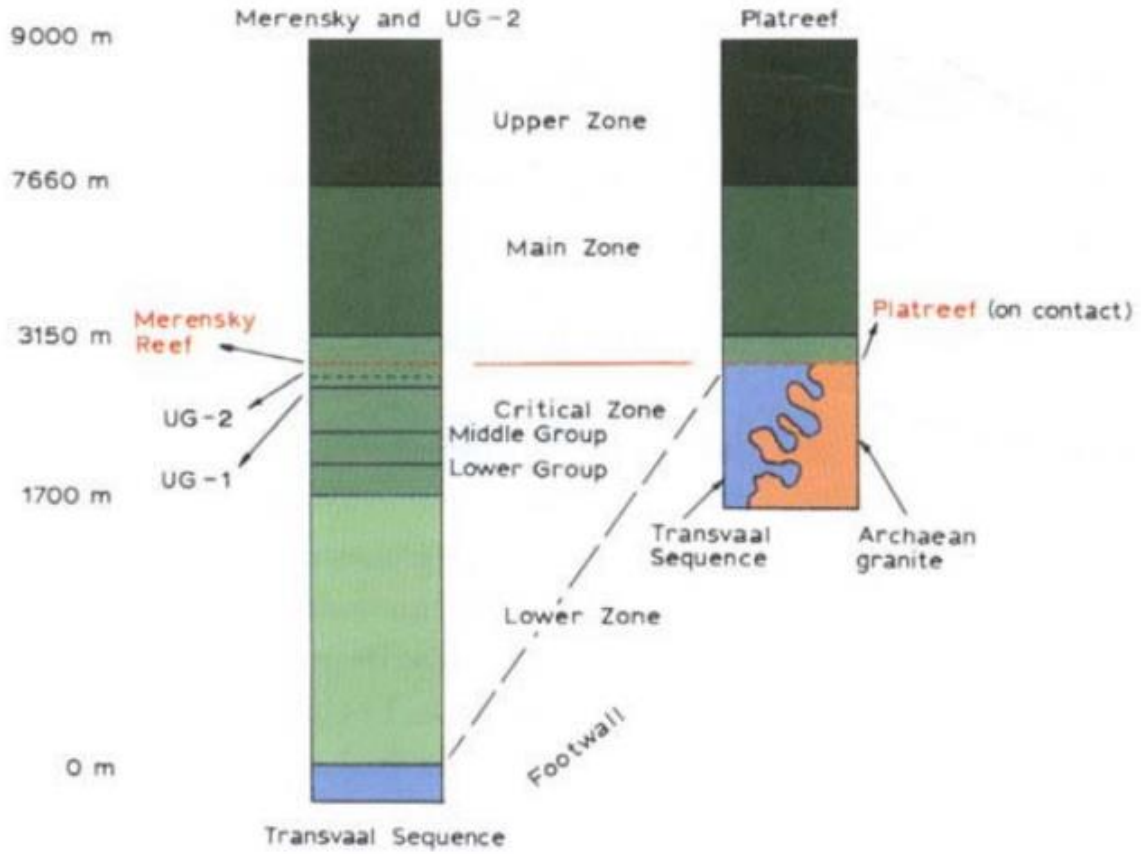

Figure 6.6: Stratigraphic columns representing the Bushveld intrusion and the position of the PGE enriched reefs: UG-2, Merensky reef and Platreef (Schouwstra & Kinloch, 2000).

A third hypothesis presents the possibility that the PGE reef formed by re mobilized PGE's. Very often in close relation to the PGE hosting sulfides, there is observed hydrous silicates and carbonates. The Pt deposits of the Waterberg, South Africa, is known to derive from hydrothermal activity where PGE's are found isolated in silicates or incorporated in chalcopyrite (McDonald, Vaughan, & Tredoux, 1995).

If the PGE's where removed and transported with a secondary CO_2 rich fluid/melt, then the PGE should show its chalcophile nature. In the dunite, moncheite show a strong connection

to the crystal orientation of pyrrhotite, crystallizing needle shaped minerals parallel to pentlandite lamellae. Moncheite is documented to form such mineral shapes in mono sulfide solution at high temperatures (Helmy et al., 2005; Meijer, 1955). These clear host mineral differences and the crystallization signature of moncheite, strongly suggest the PGM's hosted by dunite formed due to magmatic processes. However, the pegmatite and "gold cluster" show a situation where noble metals are forming with copper sulfides, indicating these PGE's are probably remobilized.

The pegmatitic pyroxeneite is the other lithology proven to host PGE's. Earlier description in section 5.2.1.3 show that while visually similar, the orthopyroxene in the pegmatite and the dunite have a significant difference in Al_2O_3 (appendix table F 6). When forming in the dunite, surrounding the sulfides and with carbonates, orthopyroxene share the signature of low Al_2O_3 content (< 1.5 wt%). However, in the pegmatite this silicate have a significantly higher Al_2O_3 (> 3.5 wt%). Appendix figure a 2 show the contact between the dunite and pegmatite as a quenched zone of fine-grained orthopyroxene. This suggest a later deriving, hotter pegmatite melt, who came in to contact with a cooler dunite. The pegmatite also lacks the interstitial carbonates that are so frequently observed in the dunite.

Documentation in this thesis suggest the PGE reef is mostly composed of moncheite (PtTe2). When referring back to table 1.1 the largest single anomaly belongs to Pd. The occupation of Pd in the dunite and the pegmatite is very low. However, a strong local Pd enrichment like the "Pd-cluster" (appendix figure B 42 and figure B 43) could possibly explanation the elevated Pd anomaly. Section 6.1 discuss the Pd signature and associated minerals.

The "Pd-cluster" is situated in orthopyroxene and amphibole, where the amphibole show a chemical zonation towards the sulfide (appendix figure B 42). Elsewhere in the pegmatite, this is not the case for any of the amphiboles in contact with other sulfides containing PGE. The abrupt element transition suggest a chemical change in the liquid as the amphibole crystalized. Resulting in an amphibole, lower in Al and enriched in Mg and Si (see section 5.2.1.5). Orthopyroxene, also in contact with the "Pd-cluster", show no zonation and grained chalcopyrite that are situated in fractures close to the main chalcopyrite grain. Suggesting that orthopyroxene was solid when introduced to a Cu, Mg and Si rich hydrothermal fluid. Most likely, this hydrothermal activity exploited the more permeable and fractured pegmatite, forming very local enrichments of Pd.

The appearance of Au is also a significant anomaly together with the PGE. Observations confirm the strongest enrichment of gold to occur with carbonate (dolomite and magnesite) and

hydrous minerals (amphibole and biotite). Grant et al. (2016) suggest the appearance of the carbonatitic portions may represents a later infiltration of a CO_2 rich fluid that lead to metasomatism of the dunite, evident by the negative trace elements anomalies. Further, Grant et al. (2016) describes distinct carbonatitic processes, the presence of *"veins with the assemblage; feldspar + amphibole + carbonate ± phlogopite ± apatite ± sulphide"* (figure 6.7A) and pervasive *"clots of carbonate (dolomite or magnesite) ± orthopyroxene ± amphibole"* (figure 6.7B).

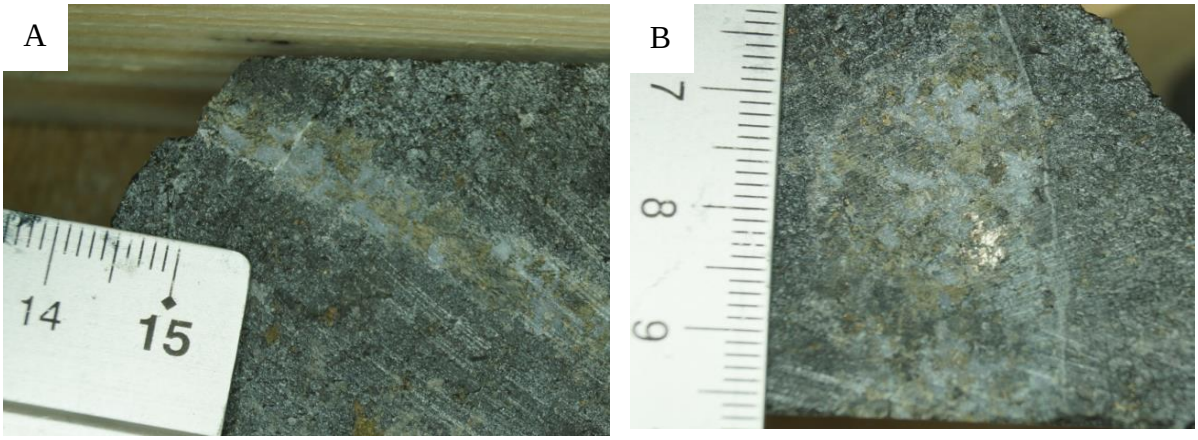

Figure 6.7: A) Vein located in RF-1 at 88.80 m. B) Carbonate cloth from the PGE reef at 109.45 m.

An attempt to calculate the carbonate melt composition is represented by the end results in table 6.5 . A full overview of each calculation stage and uncertainties is presented in appendix E,

Table 6.5: End results from the carbonate forming melt calculation.

Oxide Compound	wt% tot
Na_2O	1.24154
Cr_2O_3	1.62136
SiO_2	28.44189
Al_2O_3	5.66184
K_2O	0.35792
MnO	0.05898
MgO	18.54032
CaO	3.54484
FeO	19.04815
TiO_2	8.22021
H_2O	0.76546
CO_2	12.49750

The melt composition in table 6.5, does share a similar chemical composition as the average kimberlite (Ringwood, Kesson, Hibberson, & Ware, 1992), which could suggest the liquid to be deriving from the mantle. Harmer and Gittins (1997) discuss the forming of a magnesian carbonatite to result from a mantle derived silicate melt, dividing into two immiscible liquids. Chemical analysis of these carbonatites are much higher in CaO then the carbonatite in the RUC.

However, the description of the magnesian carbonatite above could propose an alternative explanation to Grant et al. (2016) carbonatite injection. During fractional crystallization, the separation is promoted by the melts inability to dissolve CO_2. This volatile phase is then exploiting weaknesses in the consolidating ultramafic cumulate. Especially evident in the PGE reef, as hydrous silicates and carbonates which crystallizes as cloths and in the open space between sulfides and olivine.

The mobility of Au in CO_2 rich, supercritical fluids are well known to form orogenic gold deposits (Chi, Dubé, Williamson, & Williams-Jones, 2006). Since carbonate is evident as veins in the Cu-Ni reef, it could indicate that Au here is transported further up the system. The strong contrast between the two visual carbonate textures (figure 6.7) could back up Grant et al. (2016) argument that the formation of the Cu-Ni reef, had relatively little interaction with the underlying cumulates. The Cu-Ni rich cumulates could be less consolidated during the carbonatite intrusion or at the volatile separation phase, resulting in improved mobility for the liquid to eventually form veins.

Serpentine is often observed to form the closest rim around the PGE hosting sulfides (figure 6.8). EDS mapping and EPMA identifies the serpentine to be antigorite (appendix table f 7), forming as thin layers with pyrrhotite ending with a core of chalcopyrite (figure 6.9). As seen in figure 6.10 (pegmatite) and figure 6.11 (dunite), copper is removed whenever chalcopyrite is in contact with serpentine. This feature is only evident in chalcopyrite and does not appear in other copper sulfides

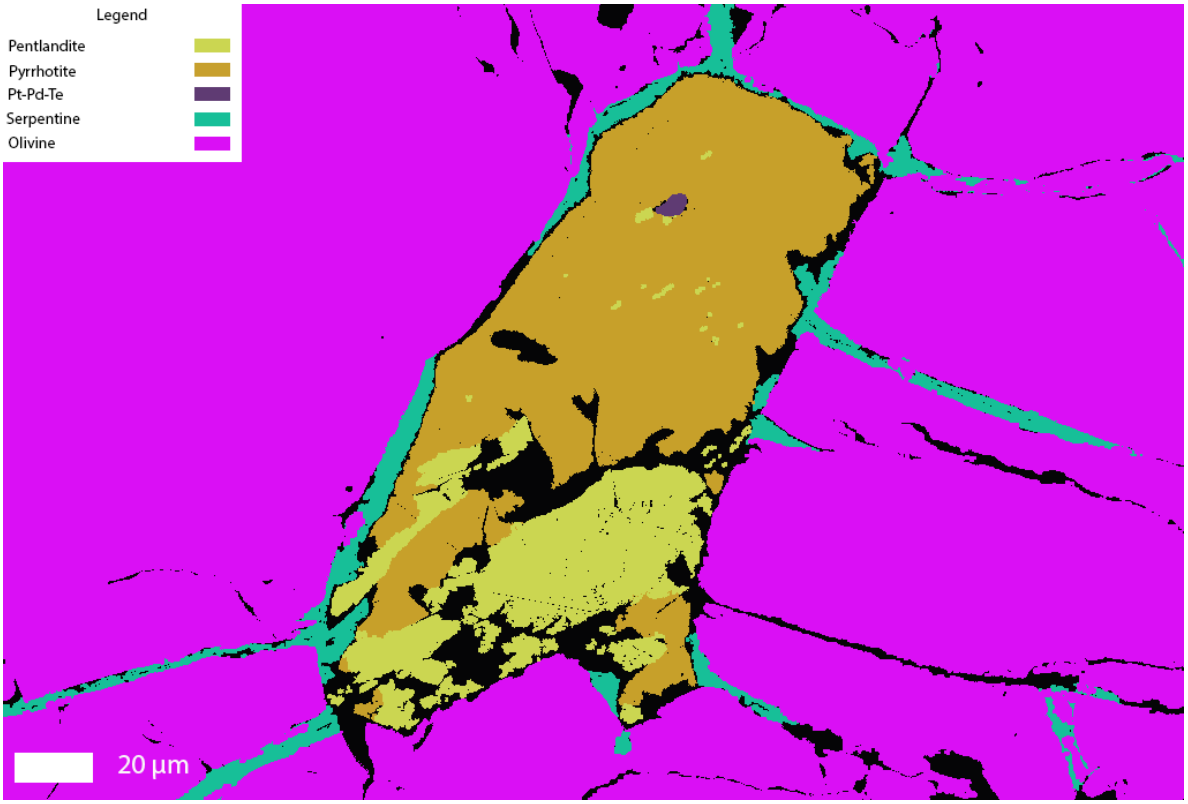

Figure 6.8: Color chart of Pt-166, showing a PGE hosting sulfide with the frequently observed rim of serpentine.

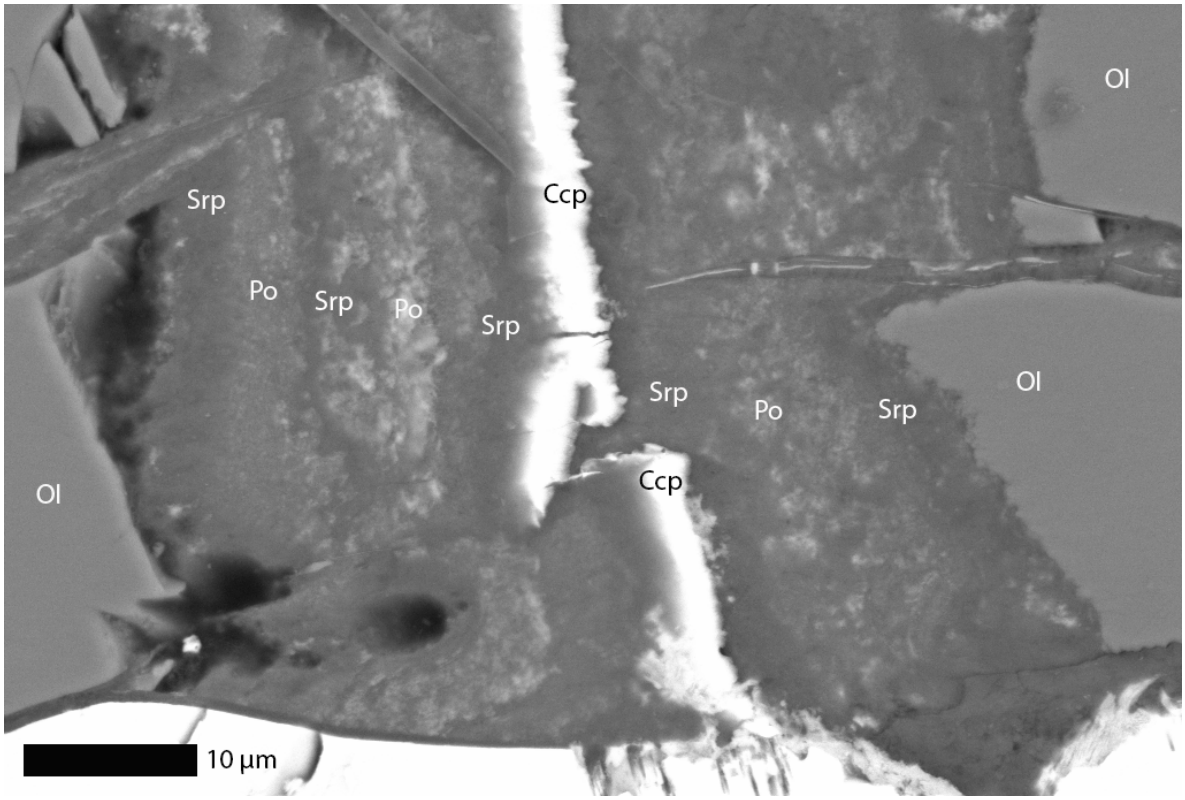

Figure 6.9: Serpentine vein close to Au-81. Showing the layered sequence between serpentine (Srp) and pyrrhotite (Po) that ends with a core of chalcopyrite (Ccp).

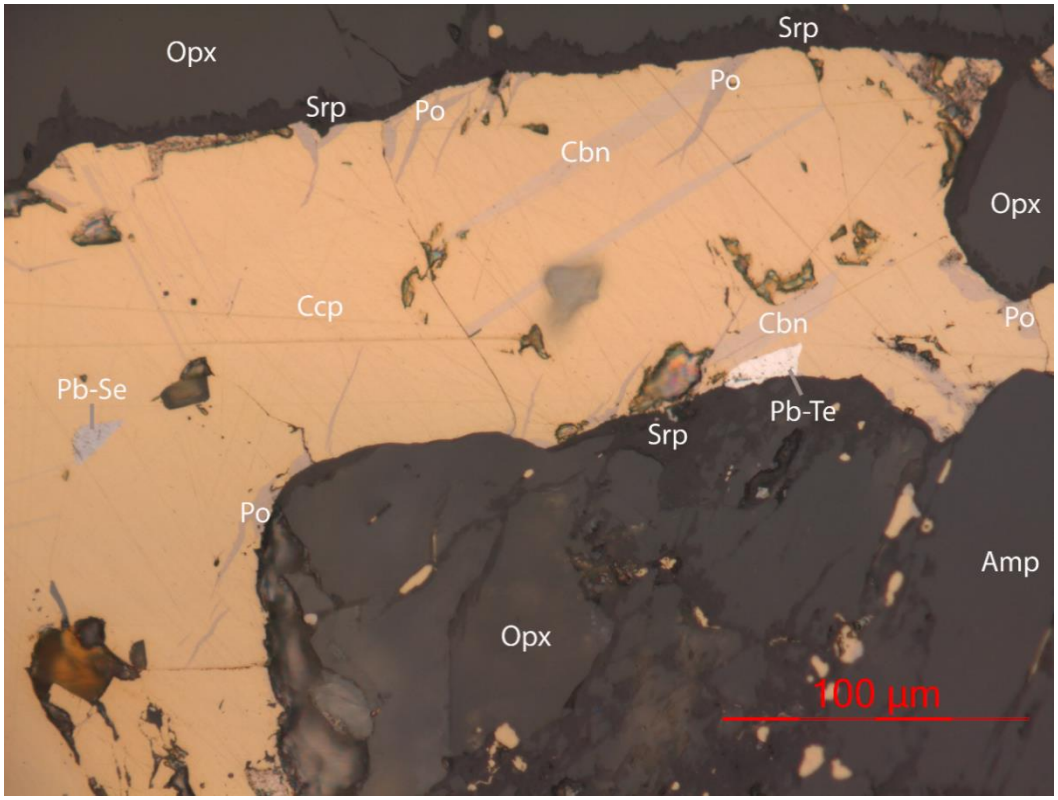

Figure 6.10: Chalcopyrite (Ccp) with cubanite (Cbn) lamellae and later metasomatism to pyrrhotite (Po). Pb-Te and Pb-Se are frequently occurring in this grain of Ccp, with strong enrichment of Pd. From the "Pd-cluster" (thin section 110.45).

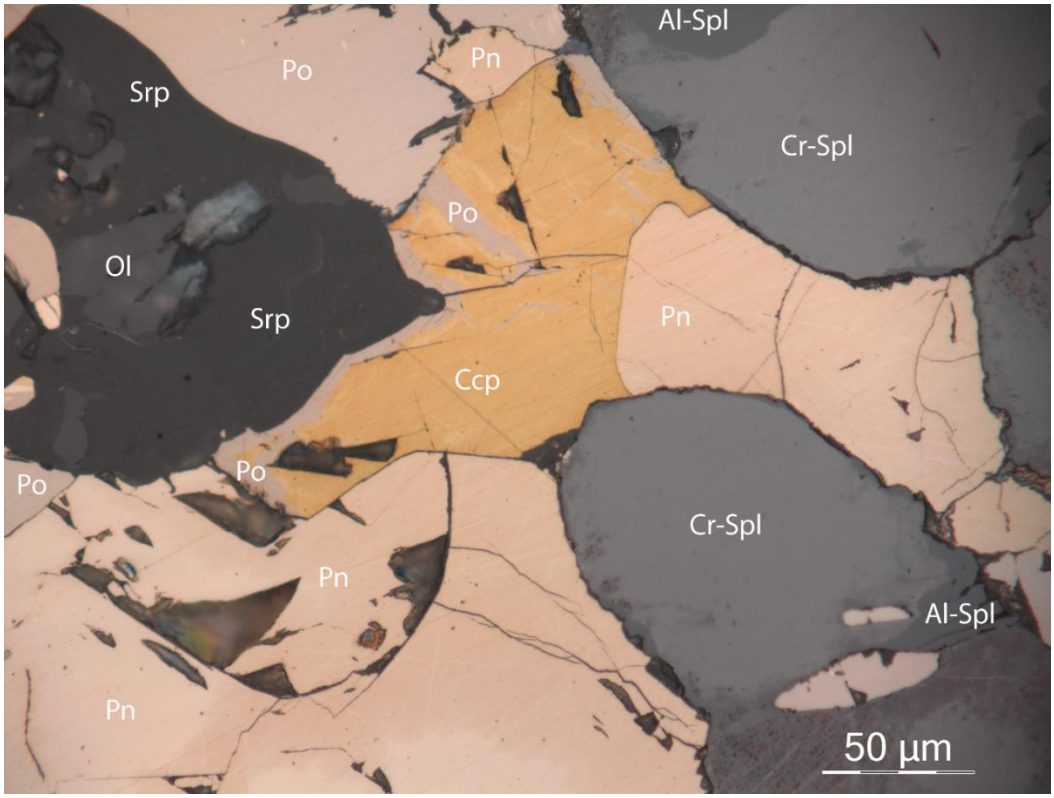

Figure 6.11: Chalcopyrite (Ccp) metasomatism to Pyrrhotite (Po), where Ccp is in contact with Serpentine (Srp). From thin section 109.40.

6.1 The PGE reef

The previous section established two hypotheses that are most likely to represent the process in which a PGE enriched melt was introduced to the RUC.

Figure 6.12: The two main magma enrichment hypothesis, established during discussion of the magma evolution.

In this discussion segment, I will go more into the details of PGM signature and compare the PGE reef in the RUC with the two reefs that do show comparable enrichments.

The most abundant ore forming PGM's are cooperite and ferroplatinum, where both represent very different environments. Cooperite (PtS) which is strongly enriched in UG-2 and Merensky reef is formed in melts with a low fO2, while ferroplatinum in melts that have a high fO2. The PGE reef in the RUC on the other hand differs, where tellurium is in strong overweight and the empirical formulas suggest that a majority of the PGM's can be identified as the Pt-dominated moncheite (5.4.1) and the Pd-dominated merenskyite (5.4.3). Therefore the ore forming magma in the RUC, most likely belongs in between these two endmembers.

The closest analog to the PGM signature in the RUC, are those represented by the Platreef intruding into the wall rock gneisses and at the edge of potholes in the Merensky reef. Holwell (2006) describes the PGM's in Platreef to only form tellurides with some Bi. Ninety-seven % is moncheite with the reminder as merenskyite, a distribution that correlates quite well with that found to exist in the RUC (84% moncheite). Especially remarkable is the needle formed moncheite in pyrrhotite, oriented with the exsolution lamellae of pentlandite as shown in Holwell (2006) figure 7.3e, f. All other PGM's are located at the rim of base metal sulfides (BMS) and only Pt phases are included within the BMS. Kinloch and Peyerl (1990) describes a slightly different scenario in the Merensky reef. Here ultramafic potholes generate localized environments that promotes the forming of different PGM's (see figure 4.13), where PGE

tellurides are associated with pothole edges. The traditional interpretation is that potholes are generated as resorption pits by the influx of hot primitive magma at the Merensky reef level or scars of late magmatic fumarole activity. While other studies suggest *"Potholes are sites of nondeposition, where the missing rock units did not crystallize. They formed where locally high concentrations of dissolved C-H-O-S volatiles lowered the liquidus temperature of the magma and suppressed the crystallization of cumulus plagioclase"* (Ballhaus, 1988)

The RUC is hosted by a garnet gneiss, but sulfur isotopes suggest a mantle source for the sulfides and not crustal contamination like the Platreef (section 6.2). However, the crystallization signature of moncheite is remarkably similar to the observations from the gneiss section in the Platreef. In the RUC, moncheite is most often located inside of BMS, but also as droplets at the edge. This also contradicts with the PGM's descriptions in the Platreef by Holwell (2006)

If crystal contamination does promote the formation of tellurides, then there must be some unknown buffer, other than light sulfur isotopes provided by the gneiss. A study of possible connection between crustal contamination and crystallization of PGE tellurides have not been provided. Probably due to the sub economic concentrations associated with these PGM's.

Kinloch and Peyerl (1990) description of a localized PGM signature in the Merensky reef could provide an alternative model to Platreef. The interpreted gravimetric anomaly in the RUC show a 600m X 600m open bowl shaped conductor (figure 6.13) at 60 to 110m dipping gently towards the NE (Schanche et al., 2012). This structure can represent a pothole, if not for the unusual extension.

With localized enrichment of different PGM's, it is possible for the intersected telluride anomaly in the RUC represent such a pothole. The large open bowl anomaly could have formed by processes that promote the formation of potholes, have been intensified by the RUC small size. Merensky reef is a massive extending lateral horizon, where the impact of a moving magma have to be different close to the entry point vs further away. In Merensky reef, potholes are smaller oval-ellipse shaped structures often no more than 10m wide and few meters deep, but are documented up to 100m wide and 40m deep with gabbroic pegmatites in the center (figure 6.14). A typical distribution is Pt-Pd-tellurides at the pothole edges and Pt-Fe alloys at the pothole center. The gabbroic pegmatites are iron and graphite rich, dominated by Pt-Fe alloys (Ballhaus, 1988; Kinloch & Peyerl, 1990).

This complete hypothesis one, as there is no other documented area in Merensky reef that promotes the formation of strong telluride enrichment.

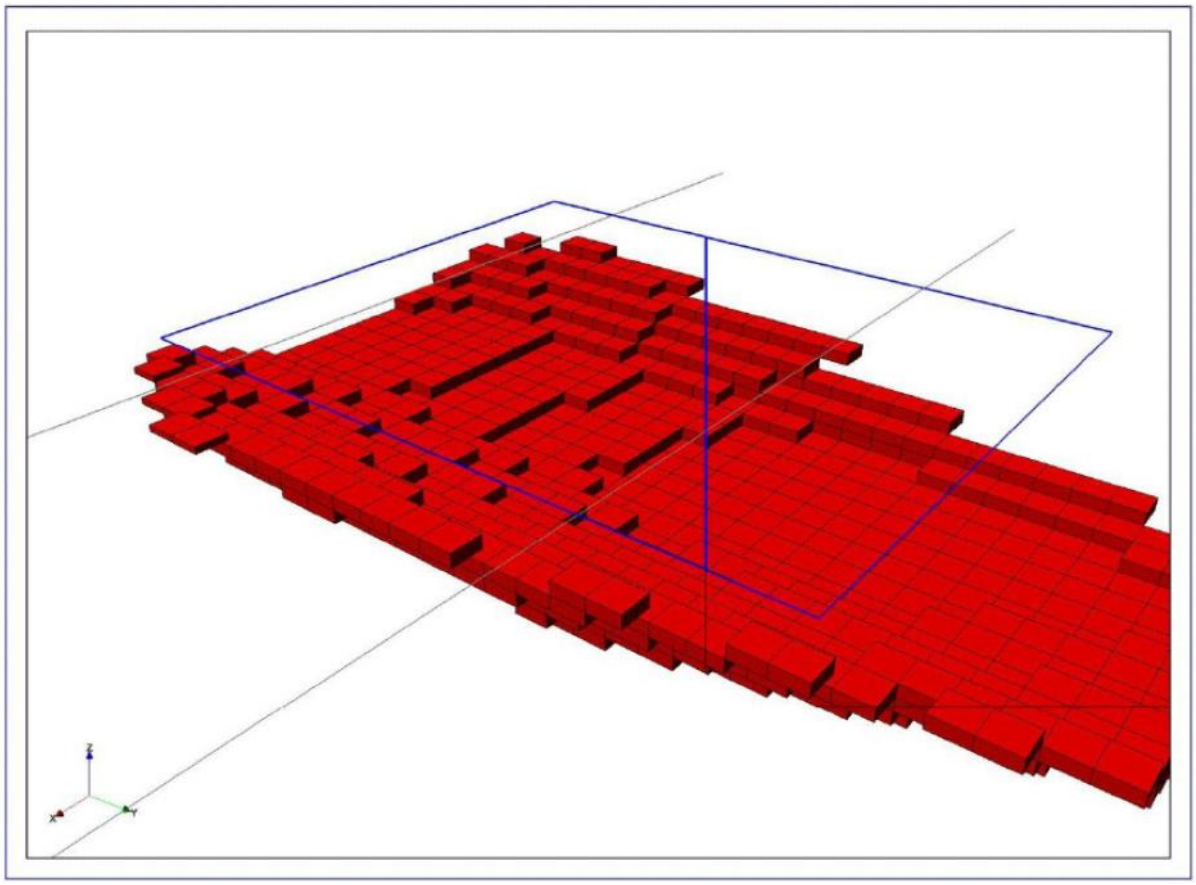

Figure 6.13: 3D model of the Reinfjord conductor, dipping towards NE. Modelled by Geovista AB (Thunehed, 2012). The anomaly extends further NE. Each cell with an estimated resistivity of 5 ohm.

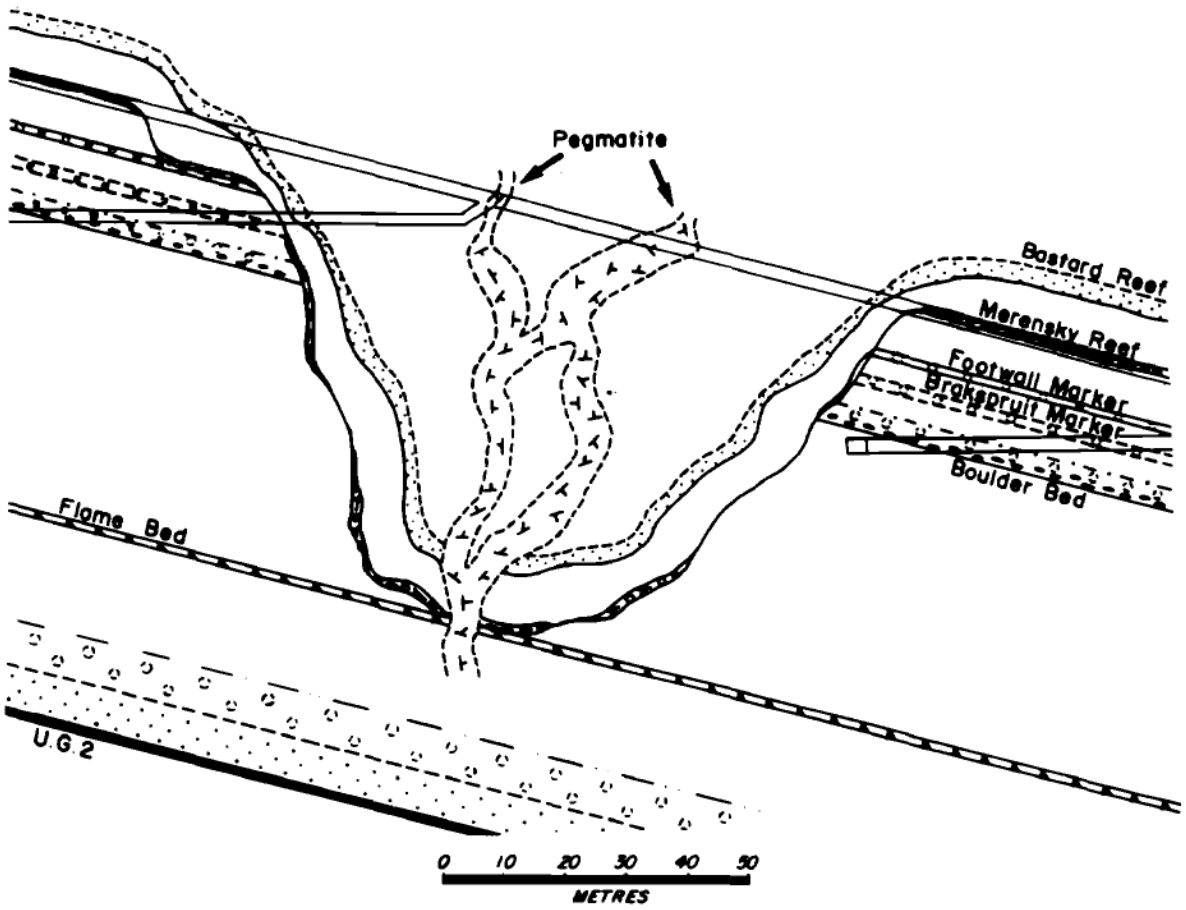

Figure 6.14: Cross section of a Breakspuit-type pothole in Bushveld (Kinloch & Peyerl, 1990).

I would however present three new hypotheses (2.1, 2.2 and 2.3) that is unique to the RUC, where figure 6.13 represents a flow channel or limited space at deposition for the PGE reef. This continues hypothesis two, where a denser melt enriched in PGE intrudes at a late stage. The suspended sulfides starts to accumulate on the chamber floor, that now consist of olivine cumulate slush. At some point, the denser PGE rich accumulation starts to flow towards NE (with the CS layer dip), carving out a channel/funnel in the underlying layers.

Hypothesis 2.1, consider the local setting of this channel to represent a "V" shaped intersection between the 25-30° dip of the CS layering (figure 5.7) and the near vertical gabbro contact (Emblin, 1985) The denser and evenly distributed PGE layer, slowly starts to slide parallel to the dip and accumulates up against the gabbro contact. Here the magma builds in volume and speed to carve out a channel.

Hypothesis 2.2, interprets the anomaly to represent a depression in the underlying cumulates, incapable of holding the new heavier PGE layer. Resulting in increased collection of heavier material that eventually slides towards the NE.

Hypothesis 2.3, suggest the possibility of very limited space when the magma chamber was recharged by the PGE and the Cu-Ni enriched magmas. This resulted in a highly localized metal enrichment, molded by the available space that these melts where emplaced. The PGE anomaly found in RF-4 however, does put a large question mark behind this hypothesis.

The following figure summarize the hypothesis

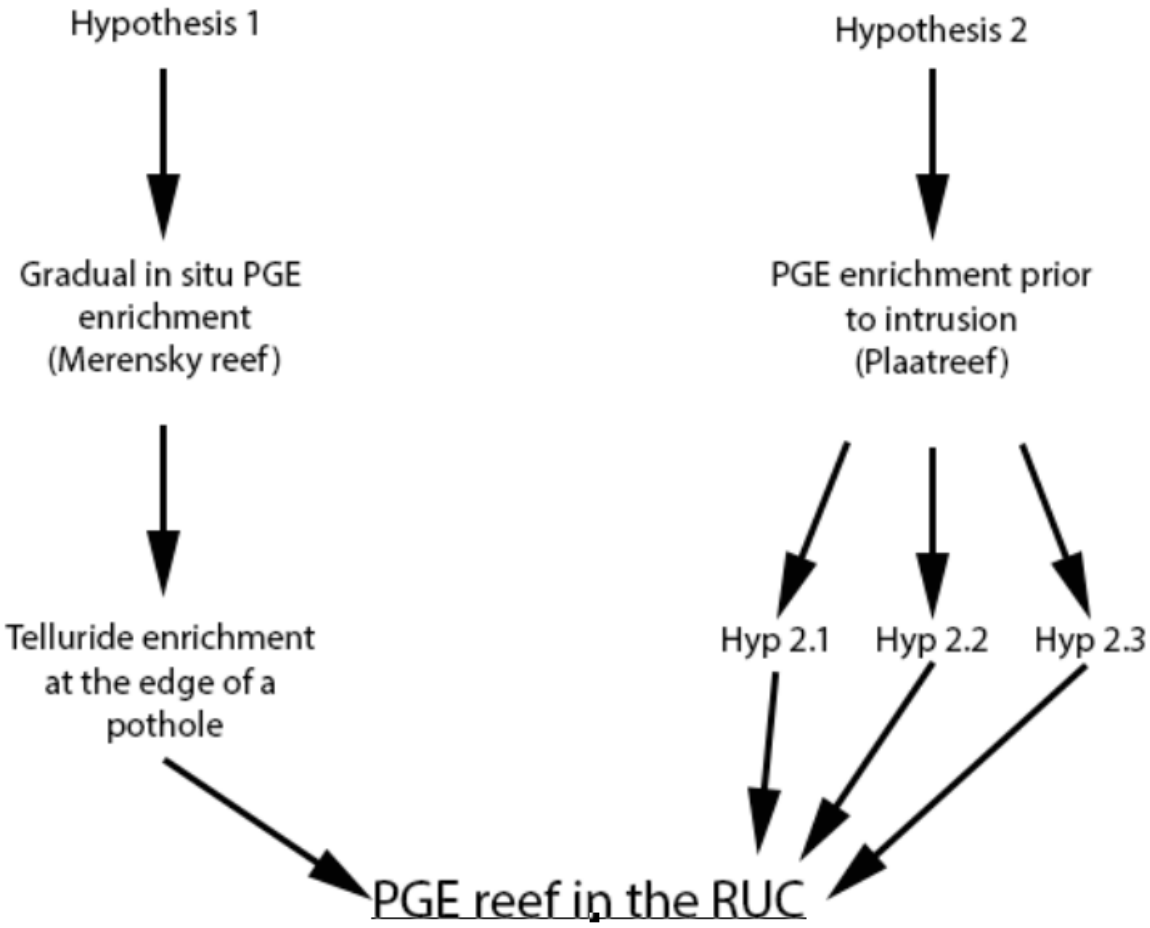

Figure 6.15: Flow chart that summarized the main hypotheses of the most likely ore forming processes that formed the PGE reef in the RUC.

7 Conclusion

This thesis provide a detailed SEM/EPMA study of the different ore forming PGM's, host sulfides and lithology to establish the ore forming processes. Comparisons with major PGE ore forming intrusion, conclude that the PGE reef in the RUC have little in common with Stillwater, Norilsk, Skaergaard or Alaskan type deposits. The mineralized sections that slightly resembles PGE reef are the strong enrichment of tellurides in the Platreef and at pothole edges in Merensky reef, Bushveld.

The enrichment formed when PGE is trapped in immiscible sulfide and form minerals with tellurium within the BMS. These minerals formed as moncheite, merenskyite and a PGE poor melonite, that are all found to form at different stages during the CS evolution. The results and discussion, argues for the following chain of events in RUC that led to the formation of an ore deposits.

1. The CS derived when magma from a mantle source at 1120°C, entered a smaller magma chamber as it ascend through the crust. This magma was either:

A) Already saturated in sulfide and enriched in PGE prior to the intrusion

Or

B) Reached sulfide saturation and PGE enrichment in the RUC.

To form a reef at the upper third of the magma chamber, it is necessary with high magmatic activity to keep the sulfides in suspension. Melts at both stage A and B above can form deposits under such conditions. However, melt A can form a deposit even when injected later and settle after a short amount of time.

2. The Cu-Ni reef 20m above the PGE-reef formed from a later magmatic recharge, evident by the sharp increase in MgO at 90m. The reef position close to the recharge marker indicate a recharge episode followed by lower activity.

3. A carbonatitic intrusion or the formation of a secondary volatile phase that coexisted with the ultramafic cumulates in the magma chamber. This phase form interstitial cloths or veins rich in hydrous silicates, Mg-carbonates and Cu sulfides that host Au. In the PGE reef this phase form cloths, probably trapped by an unknown impermeable barrier.

4. An intruding pyroxene pegmatite that show a thin quenching aureole, as it intruded the cooler dunite. This lithology host PGE poor PGM's and are not primary to the PGE anomaly.

5. Re mobilized Pd-tellurides in chalcopyrite (Pd-cluster) are forming a hydrothermal fluid that migrated in the pegmatite. Probably since the pegmatite was more permeable at the

time. These local Pd enrichments are probably the cause for the high Pd anomaly at 110.20 m in RF-1.

6. Serpentine metasomatism is remobilizing Cu when altering chalcopyrite to pyrrhotite. These serpentine-forming fluids could have transported copper and may have formed a deposit elsewhere.

EPMA data of the PGM's suggest that the parental melt was enriched in PGE, and therefore capable of forming a deposit. The high magmatic activity could indicate that PGE enriched melts could have escaped and that the PGE reef in the RUC is representing a smaller portion left behind. It could also indicate a larger PGE accumulation is yet to be discovered. As seen in the major ore deposits, PGE tellurides have never been the prime source for PGE, as most Pt and Pd is produced from sperrylite, cooperite, braggite and Fe-alloys. PGE tellurides have so far only been reported to form as accessory minerals in smaller concentrations. If the intersected PGE anomaly in the RUC represents an accessory deposit, then there is the possibility that the RUC can contain an economic metal accumulation.

8 Recommendations

During research for this thesis it became apparent, that while PGE deposits are scarce, the in depth research on the conditions that form these minerals are even more so. The ore forming temperature at the major deposits and the RUC are similar, but the pressure is very different. Further understanding of the PGE's behavior at higher pressures could change this thesis interpretation of the anomaly in RF-1, to represent an accessory accumulation of PGE's. The same applies for research on the effect that variable fO2 and fS2 have on the formation of different PGM's.

In the report by Iljina (2013) it is evident that an anomaly of Os showing 144 ppb at 107.75 – 109.45m and 56.5 ppb at 109.45 – 110.20m. The thin section mapping provided only one mineral containing Ru-Os. However, the x-ray peak of Os overlapped with Cu on the EPMA and therefore provided inconclusive results. Analysis of oxides showed the presence of Os and there is therefore the possibility that this element is incorporated in the crystallographic lattice of spinel. Since this Os anomaly is significant, it would be recommended to gain more understanding of how Os is situated in the PGE reef.

When analyzing the spinel phases on the EPMA, MgO was not included. As shown by EDS, this element is incorporated in the spinel and new analysis should have been done to properly calculate the empirical formula for these oxides. The time on EPMA was very limited and new analyses could not be completed in time for the completion of this thesis.

To prove or disprove the lateral extension of the tellurides it is vital with more observations. RF-4 have a PGE anomaly at the stratigraphic level where the PGE reef would be expected to occur. A study of the PGM's causing this anomaly in other areas of the RUC, would contribute to a better understanding of the formation regarding PGE deposits in deep-seated magmatic systems.

BIBLIOGRAPHY

Alden, A. (2013). Retrieved from http://geology.about.com/od/more_igrocks/ss/ultramafic-rock-diagrams.htm

Andersen, J. C., Rasmussen, H., Nielsen, T. F., & Ronsbo, J. G. (1998). The Triple Group and the Platinova gold and palladium reefs in the Skaergaard Intrusion; stratigraphic and petrographic relations. *Economic geology, 93*(4), 488-509.

Andréasson, P. G., Svenningsen, O. M., & Albrecht, L. (1998). Dawn of Phanerozoic orogeny in the North Atlantic tract; evidence from the Seve-Kalak Superterrane, Scandinavian Caledonides. *GFF, 120*(2), 159-172.

Armitage, P. E. B. (2011). *Development of the Platreef in the northern limb of the Bushveld Complex at Sandsloot, Mokopane District, South Africa.* University of Greenwich.

Arnason, J., & Bird, D. (1994). Gold and platinum group minerals in Tertiary mafic intrusions of East Greenland. *EOS, 75*(44), 71.

Arndt, N., & Leshler, C. M. (2004). Komatiite. *Encyclopedia of Geology*, 260-268.

Arndt, N. T. (2005). The conduits of magmatic ore deposits. *Exploration for platinum-group element deposits. Min Assoc Can., Short Course Series, 35*, 181-201.

Astimex. Astimex Standards Ltd. Retrieved from http://astimex.com/com/catalog/min.html

Ballhaus, C. G. (1988). Potholes of the Merensky Reef at Brakspruit Shaft, Rustenburg platinum mines; primary disturbances in the magmatic stratigraphy. *Economic geology, 83*(6), 1140-1158.

Barnes, S. J., & Francis, D. (1995). The distribution of platinum-group elements, nickel, copper, and gold in the Muskox layered intrusion, Northwest Territories, Canada. *Economic geology, 90*(1), 135-154.

Barnes, S. J., & Naldrett, A. J. (1985). Geochemistry of the JM (Howland) Reef of the Stillwater Complex, Minneapolis Adit area; I, Sulfide chemistry and sulfide-olivine equilibrium. *Economic geology, 80*(3), 627-645.

Barth, T. F. W. (1927). Die pegmatitgange der kaledonischen Intrusiv-Gesteine im Seilandgebiet. Skr. utg. av Det Norske Vidensk. *Akad., Oslo. IM-N. Kl*(8).

Barth, T. F. W. (1952). Layered Gabbro Series at Seiland *Norges Geologiske Undersøkelse Årbok, 184*, 191-200.

Barthelmy, D. (1997-2014). Web Mineral. Retrieved from http://webmineral.com/

Bennett, M., Emblin, S., Robins, B., & Yeo, W. (1986). High-temperature ultramafic complexes in the North-Norwegian Caledonides: I, regional setting and field relationships. *Norges geologiske undersøkelse Bull, 405*, 1-40.

Bennett, M., Emblin, S. R., Robins, B., & Yeo, W. J. A. (1985). Synorogenetic intrusive complexes in the Finmarkian Sørøy nappe, Seiland igneous province, N. Norway. *Bulletin*(404-407), 1.

Bennett, M. C. (1971). Reinfjord Ultramafic Complex. *Norges geologiske undersøkelse - The Caledonian Geology of Northern Norway, 269*, 165-171.

Bennett, M. C. (1974). The emplacement of a high temperature peridotite in the Seiland Province of the Norwegian Caledonides. *Journal of the Geological Society, 130*(3), 205-226. doi:10.1144/gsjgs.130.3.0205

Bird, D. K., Brooks, C. K., Gannicott, R. A., & Turner, P. A. (1991). A gold-bearing horizon in the Skaergaard Intrusion. *Economic geology, 86*(5), 1083-1092.

Boudreau, A. E. (2008). Modeling the Merensky Reef, Bushveld Complex, Republic of South Africa. *Contributions to Mineralogy and Petrology, 156*(4), 431-437.

Bowen, N. (1922). The reaction principle in petrogenesis. *The Journal of Geology, 30*(3), 177-198.

Brooks, M. (1969). A gravity survey of coastal areas of West Finnmark, northern Norway. *Quarterly Journal of the Geological Society, 125*(1-4), 171-191.

Cabri, L., & Laflamme, J. G. (1976). The mineralogy of the platinum-group elements from some copper-nickel deposits of the Sudbury area, Ontario. *Economic geology, 71*(7), 1159-1195.

Campbell, I., & Naldrett, A. (1979). The influence of silicate: sulfide ratios on the geochemistry of magmatic sulfides. *Economic geology, 74*(6), 1503-1506.

Cawthorn, R. G., Lee, C. A., Schouwstra, R. P., & Mellowship, P. (2002). Relationship between PGE and PGM in the Bushveld Complex. *The Canadian Mineralogist, 40*(2), 311-328.

Cescas, M. P., Tyner, E. H., & Gray, L. J. (1968). The electron microprobe X-ray analyzer and its use in soil investigations. *Adv. Agron, 20*, 153-198.

Chi, G., Dubé, B., Williamson, K., & Williams-Jones, A. E. (2006). Formation of the Campbell-Red Lake gold deposit by H2O-poor, CO2-dominated fluids. *Mineralium Deposita, 40*(6-7), 726-741.

Daltry, V., & Wilson, A. (1997). Review of platinum-group mineralogy: compositions and elemental associations of the PG-minerals and unidentified PGE-phases. *Mineralogy and Petrology, 60*(3-4), 185-229.

Daly, J., Aitcheson, S., Cliff, R., Gayer, R., & Rice, A. (1991). Geochronological evidence from discordant plutons for a late Proterozoic orogen in the Caledonides of Finnmark, northern Norway. *Journal of the Geological Society, 148*(1), 29-40.

Distler, V., Sluzhenikin, S., Cabri, L., Krivolutskaya, N., Turovtsev, D., Golovanova, T., . . . Oleshkevich, O. (1999). Platinum ores of the Noril'sk layered intrusions: magmatic and fluid concentration of noble metals. *Geology of ore deposits c/c of geologiia rudnykh mestorozhdenii, 41*, 214-237.

Elliott, W., Grandstaff, D., Ulmer, G., Buntin, T., & Gold, D. (1982). An intrinsic oxygen fugacity study of platinum-carbon associations in layered intrusions. *Economic geology, 77*(6), 1493-1510.

Elvevold, S., Reginiussen, H., Krogh, E., & Bjørklund, F. (1994). Reworking of deep-seated gabbros and associated contact metamorphosed paragneisses in the southeastern part of the Seiland Igneous Province, northern Norway. *Journal of Metamorphic Geology, 12*(4), 539-556.

Emblin, S. R. (1985). *The Reinfjord ultramafic complex, Seiland Province: Emplacement history and magma chamber model.* Bristol- Bergen University.

Genkin, A., & Korolev, N. (1961). On methods of determining small grains of minerals in ores. *Geol Rudn Mestorozhd, 5*, 64-79.

Gervilla, F., & Kojonen, K. (2002). The platinum-group minerals in the upper section of the Keivitsansarvi Ni–Cu–PGE deposit, northern Finland. *The Canadian Mineralogist, 40*(2), 377-394.

Godel, B., & Barnes, S.-J. (2008). Image analysis and composition of platinum-group minerals in the JM Reef, Stillwater Complex. *Economic geology, 103*(3), 637-651.

Grannes, K. R. B. (2016). *Cryptic variations of whole rock samples, olivene and clinopyroxene in the RF4 drill-core. Formation of elemental Cu-deposits.* (McS), NTNU.

Grant, T. B., Larsen, R. B., Anker-Rasch, L., Grannes, K. R., Iljina, M., McEnroe, S., . . . Øen, E. (2016). Anatomy of a deep crustal volcanic conduit system; The Reinfjord Ultramafic Complex, Seiland Igneous Province, Northern Norway. *Lithos, 252*, 200-215.

Green, D. (1975). Genesis of Archean peridotitic magmas and constraints on Archean geothermal gradients and tectonics. *Geology, 3*(1), 15-18.

Griffin, W., Sturt, B., O'Neill, C., Kirkland, C., & O'Reilly, S. Y. (2013). Intrusion and contamination of high-temperature dunitic magma: the Nordre Bumandsfjord pluton, Seiland, Arctic Norway. *Contributions to Mineralogy and Petrology, 165*(5), 903-930.

Hafner, B. (2006). Energy Dispersive Spectroscopy on the SEM: a primer. *Characterization Facility, University of Minnesota*, 1-26.

Hall, A. (1996). Igneous Petrology. Harlow: Longman Group.

Hansen, T. S. (1971). *En undersøkelse av nikkel-kopper mineraliseringer i Reinfjord-Jøkkelfjord området, Troms.* (MSc).

Harmer, R. E., & Gittins, J. (1997). The origin of dolomitic carbonatites: field and experimental constraints. *Journal of African Earth Sciences, 25*(1), 5-28.

Hatton, C. (1995). The Bushveld Complex, a product of interaction among magmas derived from a mantle plume. *Communications Geological Survey Namibia, 10*, 93-98.

Helmy, H., Ballhaus, C., & Berndt-Gerdes, J. (2005). The formation of Pt, Pd and Ni tellurides during cooling of Fe-Ni-Cu sulphide: results of experiments and implications for natural systems. *Geochem Miner Petrol, 43*, 87-92.

Helmy, H., Ballhaus, C., Berndt, J., Bockrath, D., & Wohlgemuth-Ueberwasser, C. (2006). Formation of Pt, Pd and Ni tellurides: experiments in sulfide–telluride systems. *Contributions to Mineralogy and Petrology, 153*(5), 577-591. doi:10.1007/s00410-006-0163-7

Helmy, H. M., Stumpfl, E. F., & Kamel, O. A. (1995). Platinum-group minerals from the metamorphosed Abu Swayel Cu-Ni-PGE deposit, South Eastern Desert, Egypt. *Economic Geology and the Bulletin of the Society of Economic Geologists, 90*(8), 2350-2360.

Helz, R. T. (1995). The Stillwater Complex, Montana: a subvolcanic magma chamber? *AMERICAN MINERALOGIST, 80*(11-12), 1343-1346.

Himmelberg, G. R., & Loney, R. A. (1995). *Characteristics and petrogenesis of Alaskan-type ultramafic-mafic intrusions, southeastern Alaska*: US Government Printing Office.

Holwell, D. (2006). *Roles of magmatism, contamination and hydrothermal processes in the development of Platreef mineralization, Bushveld Complex, South Africa.* Cardiff University.

Holwell, D., Boyce, A., & McDonald, I. (2007). Sulfur isotope variations within the Platreef Ni-Cu-PGE deposit: genetic implications for the origin of sulfide mineralization. *Economic geology, 102*(6), 1091-1110.

Holwell, D., & McDonald, I. (2007). Distribution of platinum-group elements in the Platreef at Overysel, northern Bushveld Complex: a combined PGM and LA-ICP-MS study. *Contributions to Mineralogy and Petrology, 154*(2), 171-190.

Holwell, D., McDonald, I., & Butler, I. (2011). Precious metal enrichment in the Platreef, Bushveld Complex, South Africa: evidence from homogenized magmatic sulfide melt inclusions. *Contributions to Mineralogy and Petrology, 161*(6), 1011-1026.

Hooper, P. (1971). The mafic and ultramafic intrusions of SW Finnmark and North Troms. *Norges Geol. Unders, 269*, 147.

Hudson, D. (1986). Platinum-group minerals from the Kambalda nickel deposits, Western Australia. *Economic geology, 81*(5), 1218-1225.

Iljina, M. (2013). *Reinfjord drilling and mapping campaigns in 2012 – geochemical observations, discussion on ore genesis and exploration implications*. Retrieved from

Irvine, T. N. (1977). Origin of chromitite layers in the Muskox Intrusion and other stratiform intrusions: a new interpretation. *Geology, 5*, 273-277.

Johan, Z. (2002). Alaskan-type complexes and their platinum-group element mineralization. *Geology, geochemistry, mineralogy and mineral beneficiation of platinum-group elements, 54*, 669-719.

Keays, R. R. (1995). The role of komatiitic and picritic magmatism and S-saturation in the formation of ore deposits. *Lithos, 34*(1), 1-18.

Kinloch, E., & Peyerl, W. (1990). Platinum-group minerals in various rock types of the Merensky Reef; genetic implications. *Economic geology, 85*(3), 537-555.
Kinnaird, J., Kruger, F., Nex, P., & Cawthorn, R. (2002). Chromitite formation—a key to understanding processes of platinum enrichment. *Applied Earth Science, 111*(1), 23-35.
Kinnaird, J. A. (2005). The Bushveld large igneous province. *Review Paper, The University of the Witwatersrand, Johannesburg, South Africa, 39pp*.
Kirkland, C. L., Daly, J. S., & Whitehouse, M. J. (2007). Provenance and terrane evolution of the Kalak Nappe Complex, Norwegian Caledonides: implications for Neoproterozoic paleogeography and tectonics. *The Journal of Geology, 115*(1), 21-41.
Krinsley, D. H., Pye, K., Boggs Jr, S., & Tovey, N. K. (2005). *Backscattered scanning electron microscopy and image analysis of sediments and sedimentary rocks*: Cambridge University Press.
Lawes, G. (1987). Scanning electron microscopy and X-ray microanalysis.
Lee, C. (1996). A review of mineralization in the Bushveld Complex and some other layered intrusions. *Developments in Petrology, 15*, 103-145.
Legendre, T. (1992). Pt-Fe nuggets from alluvial deposits in eastern Madagascar.
Li, C., & Naldrett, A. (1993). Sulfide capacity of magma; a quantitative model and its application to the formation of sulfide ores at Sudbury, Ontario. *Economic geology, 88*(5), 1253-1260.
Lightfoot, P. C., & Keays, R. R. (2005). Siderophile and chalcophile metal variations in flood basalts from the Siberian Trap, Noril'sk Region: implications for the origin of the Ni-Cu-PGE sulfide ores. *Economic geology, 100*(3), 439-462.
MacLean, W. H. (1969). Liquidus phase relations in the FeS-FeO-Fe 3 O 4-SiO 2 system, and their application in geology. *Economic geology, 64*(8), 865-884.
Malitch, K. (1998). Peculiarities of platinum-group elements distribution in ultramafites of clinopyroxenite-dunite massives as an indicator of their origin. *International Platinum. Theophrastus Publications, St. Petersburg Athens*, 129-140.
Manyeruke, T. D., Maier, W. D., & Barnes, S.-J. (2005). Major and trace element geochemistry of the Platreef on the farm Townlands, northern Bushveld Complex. *South African Journal of Geology, 108*(3), 381-396.
Mavrogenes, J. A., & O'neill, H. S. C. (1997). The relative effects of pressure, temperature and oxygen fugacity on the solubility of sulfide in mafic magmas.
McDonald, I., Vaughan, D., & Tredoux, M. (1995). Platinum mineralization in quartz veins near Naboomspruit, central Transvaal. *S. Afr. J. Geol, 98*, 168-175.
McLaren, C. H., & De Villiers, J. P. (1982). The platinum-group chemistry and mineralogy of the UG-2 chromitite layer of the Bushveld Complex. *Economic geology, 77*(6), 1348-1366.
Meijer, W. (1955). Synthesis, Structures, and Properties of Platinum Metal Tellurides. *American mineralogist, 40*(7-8), 646-657.
Merwe, M. V. (2007). The occurrence of the critical zone along the exposed southeastern sector of the eastern Bushveld Complex. *South African Journal of Geology, 110*, 617-630.
Mungall, J. (2002). *A model for co-precipitation of platinum-group minerals with chromite from silicate melts.* Paper presented at the 9th International Platinum Symposium, Abstract with Program, Billings, Montana.
Mungall, J. E. (2005). *Exploration for platinum-group element deposits* (Vol. 35): Mineralogical association of Canada.
Naldrett, A. (1989). Stratiform PGE deposits in layered intrusions. *Rev Econ Geol, 4*, 135-166.
Naldrett, A. (1997). Key factors in the genesis of Noril'sk, Sudbury, Jinchuan, Voisey's Bay and other world-class Ni-Cu-PGE deposits: Implications for exploration. *Australian Journal of Earth Sciences, 44*(3), 283-315.

Naldrett, A. (2013). *Magmatic sulfide deposits: geology, geochemistry and exploration*: Springer Science & Business Media.

Naldrett, A., & MacDonald, A. (1980). Tectonic settings of Ni-Cu sulphide ores: their importance in genesis and exploration. *The Continental Crust and Its Mineral Deposits: Geological Association of Canada, Special Paper, 20*, 631-637.

Naldrett, A., & Von Gruenewaldt, G. (1989). Association of platinum-group elements with chromitite in layered intrusions and ophiolite complexes. *Economic geology, 84*(1), 180-187.

Nielsen, T., Andersen, J., & Brooks, C. (2005). The platinova reef of the Skaergaard intrusion. *Exploration for platinum-group element deposits. Mineral association can, short course, 35*, 431-455.

Nielsen, T. F., Andersen, J. Ø., Holness, M. B., Keiding, J. K., Rudashevsky, N., Rudashevsky, V., Veksler, I. V. (2015). The Skaergaard PGE and gold deposit: the result of in situ fractionation, sulphide saturation, and magma chamber-scale precious metal redistribution by immiscible Fe-rich melt. *Journal of Petrology, 56*(8), 1643-1676.

Oosterom, M. G. (1963). The ultramafites and layered gabbro sequences. *Leidse Geologische Mededelingen, 28*(1), 177-296.

Pastore, Z. (2015). *Geophysical interpretation of mantle magmatism in the Seiland province and adjacent Barents Sea: Implications for tectonic emplacement of the Kalak Nappe Complex.* Paper presented at the 2015 AGU Fall Meeting.

Pettersen, K. (1875). Short sketch of the geology of the North of Norway. *Geological Magazine, 2*, 385-391.

Picot, P., & Johan, Z. (1982). *Atlas of ore minerals*: BRGM.

Premo, W., Helz, R., Zientek, M., & Langston, R. (1990). U-Pb and Sm-Nd ages for the Stillwater Complex and its associated sills and dikes, Beartooth Mountains, Montana: Identification of a parent magma? *Geology, 18*(11), 1065-1068.

Raith, M. M., Raase, P., & Reinhardt, J. (2012). *Guide to thin section microscopy*.

Rasch, L. A. (2013). *Magmatiske malmdannende prosesser i Reinfjord, Seiland magmatiske provins.*

Reginiussen, H. (1996). *OIB-like magmatism in the Seiland Igneous Province, northern Norway: geochemical constraints from a rift-related mafic dyke swarm on western Sørøy*. Ph. D. University of Tromsø.

Ringwood, A., Kesson, S., Hibberson, W., & Ware, N. (1992). Origin of kimberlites and related magmas. *Earth and Planetary Science Letters, 113*(4), 521-538.

Robb, L. (2008). Introduction to Ore Forming Processes (pp. 19-74).

Roberts, R. J. (2007). *The Seiland Igneous Province, Northern Norway: Age, Provenance, and Tectonic Significance.* (PhD), University of the Witwatersrand, Johannesburg.

Roberts, R. J., Corfu, F., Torsvik, T. H., Ashwal, L. D., & Ramsay, D. M. (2006). Short-lived mafic magmatism at 560–570 Ma in the northern Norwegian Caledonides: U–Pb zircon ages from the Seiland Igneous Province. *Geological Magazine, 143*(06), 887. doi:10.1017/s0016756806002512

Roberts, R. J., Corfu, F., Torsvik, T. H., Hetherington, C. J., & Ashwal, L. D. (2010). Age of alkaline rocks in the Seiland Igneous Province, Northern Norway. *Journal of the Geological Society, 167*(1), 71-81. doi:10.1144/0016-76492009-014

Robins, B., & Gardner, P. (1975). The magmatic evolution of the Seiland Province, and Caledonian plate boundaries in northern Norway. *Earth and Planetary Science Letters, 26*(2), 167-178.

Rowell, W. F., & Edgar, A. D. (1986). Platinum-group element mineralization in a hydrothermal Cu-Ni sulfide occurrence, Rathbun Lake, northeastern Ontario. *Economic geology, 81*(5), 1272-1277.

Rucklidge, J. (1969). Electron microprobe investigation of platinum metal minerals from Ontario. . *Can Mineral 9*, 617–628.
Rudashevskiy, N., Fomenko, A., & KN, M. (1994). Primary PGE mineralization of dunites and clinopyroxenites of the konder intrusion. *IIV intern. Platinum Symp*, 102.
Schanche, M., Iljina, M., & Larsen, R. (2012). New nickel, copper and platinum-group element discoveries in northern Norway.
Schouwstra, R., & Kinloch, E. (2000). A short geological review of the Bushveld Complex.
Sluzhenikin, S. (2011). Platinum-copper-nickel and platinum ores of Norilsk Region and their ore mineralization. *Russian Journal of General Chemistry, 81*(6), 1288-1301.
Streckeisen, A. (1974). Classification and Momenclature of Plutonic Rocks.
Sørensen, B. E. (2013). A revised Michel-Lévy interference colour chart based on first-principles calculations. *European Journal of Mineralogy, 25*(1), 5-10.
Tegner, C., Robins, B., Reginiussen, H., & Grundvig, S. (1990). Assimilation of Crustal Xenoliths in a Basaltic Magma Chamber: Sr and Nd Isotopic Constraints from the Hasvik Layered Intrusion, Norway. *Journal of Petrology, 40*(3), 363-380.
Thakurta, J., Ripley, E. M., & Li, C. (2008). Geochemical constraints on the origin of sulfide mineralization in the Duke Island Complex, southeastern Alaska. *Geochemistry, Geophysics, Geosystems, 9*(7).
Thakurta, J., Ripley, E. M., & Li, C. (2014). Platinum Group Element Geochemistry of Sulfide-Rich Horizons in the Ural-Alaskan–Type Ultramafic Complex of Duke Island, Southeastern Alaska. *Economic geology, 109*(3), 643-659.
Theisen, R. (2013). *Quantitative electron microprobe analysis*: Springer Science & Business Media.
Thunehed, H. (2012). *TEM-survey of Reinfjord - survey and interpretation report*. Retrieved from Luleå, Sweeden:
Tindle, A. Retrieved from: http://www.open.ac.uk/earthresearch/tindle/AGTWebPages/AGTSoft.html
Vermaak, C., & Hendriks, L. (1976). A review of the mineralogy of the Merensky Reef, with specific reference to new data on the precious metal mineralogy. *Economic geology, 71*(7), 1244-1269.
Vogel, D., & Keays, R. (1997). The application of platinum group geochemisty in constraining the source of basalt magmas: results from the Newer Volcanic Province, Victoria, Australia. *Chem Geol, 136*, 181-204.
Volborth, A., Tarkian, M., Stumpfl, E. F., & Housley, R. M. (1986). A survey of the Pd-Pt mineralization along the 35-km strike of the JM Reef, Stillwater complex, Montana. *Can Mineral, 24*, 329-346.
Walraven, F., Armstrong, R., & Kruger, F. (1990). A chronostratigraphic framework for the north-central Kaapvaal craton, the Bushveld Complex and the Vredefort structure. *Tectonophysics, 171*(1), 23-48.
Watkinson, D. H., & Melling, D. R. (1992). Hydrothermal origin of platinum-group mineralization in low-temperature copper sulfide-rich assemblages, Salt Chuck intrusion, Alaska. *Economic geology, 87*(1), 175-184.
Wotzlaw, J. F., Bindeman, I. N., Schaltegger, U., Brooks, C. K., & Naslund, H. R. (2012). High-resolution insights into episodes of crystallization, hydrothermal alteration and remelting in the Skaergaard intrusive complex. *Earth and Planetary Science Letters, 355*, 199-212.
Øen, E. N. (2013). *Dannelse av sulfidforekomster i Reinfjord og Lokkarfjord, Seiland magmatiske provins.* (Master thesis), Norwegian University of Science and Tehcnology.

Appendix A

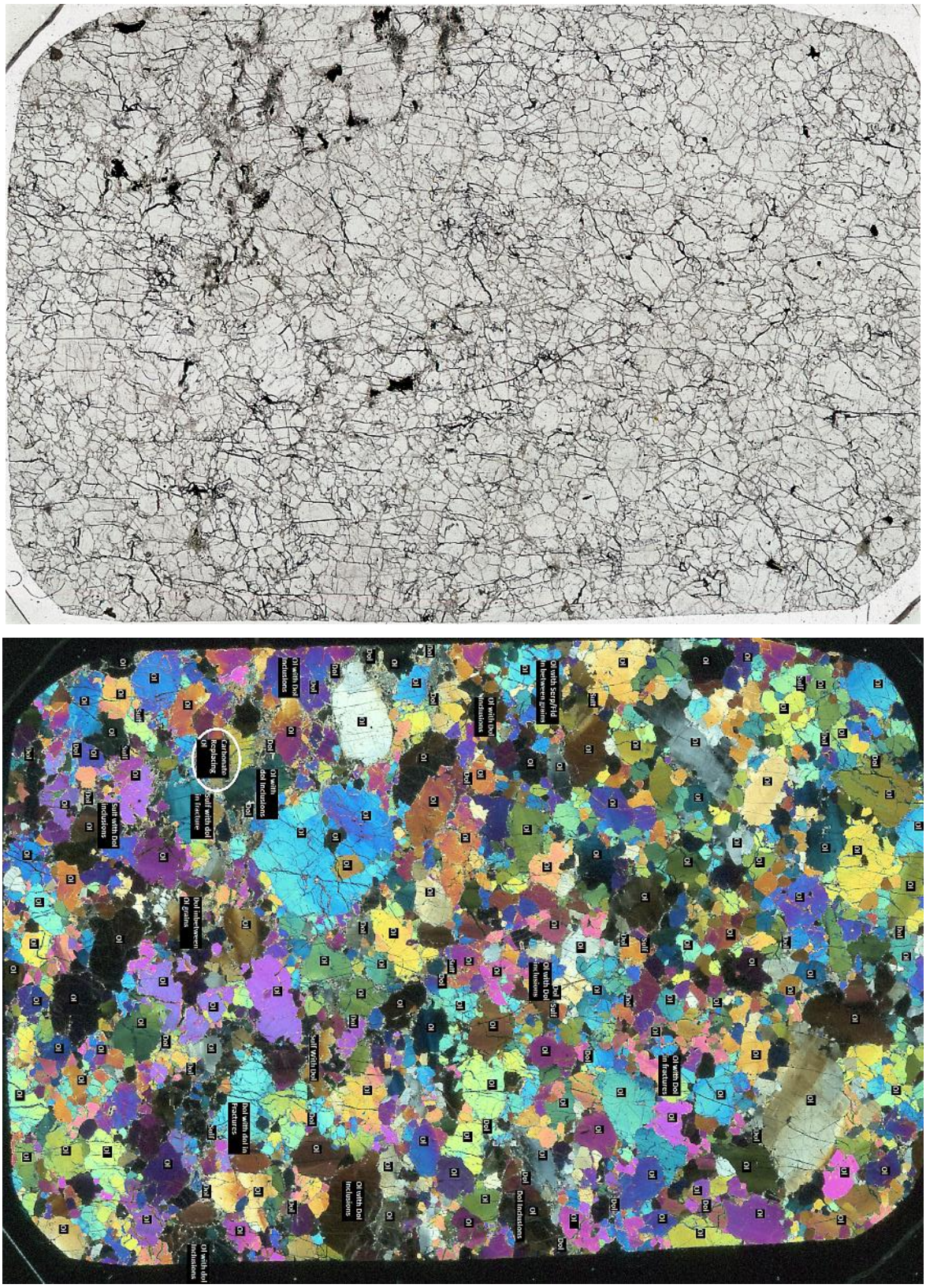

Figure A 1: Scan of thin section 105.0 with silicate labels. Upper scan in Ppl and lower scan in Xpl

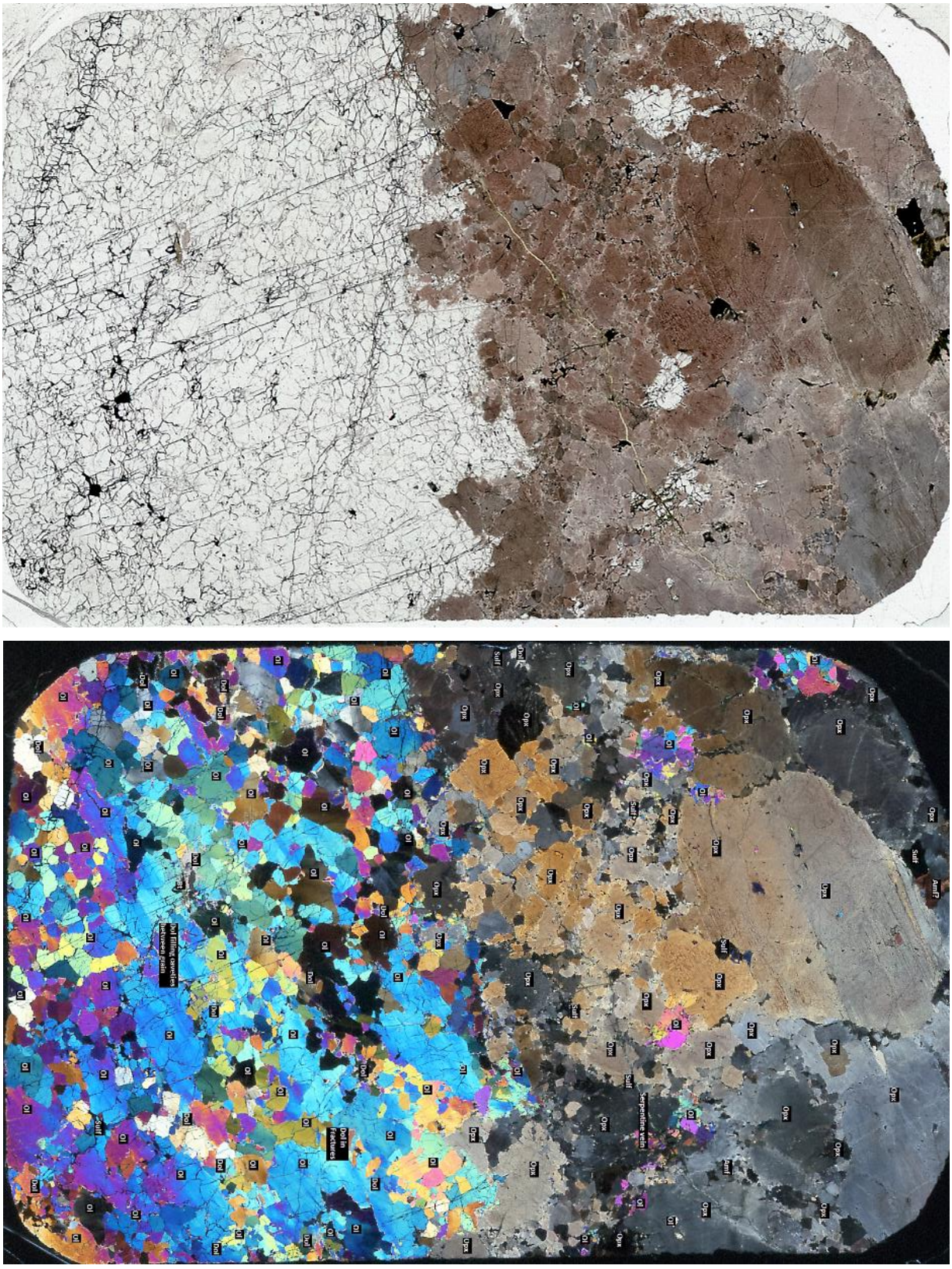

Figure A 2: Scan of thin section 108.95, with silicate labels. Upper scan in Ppl and lower scan in Xpl

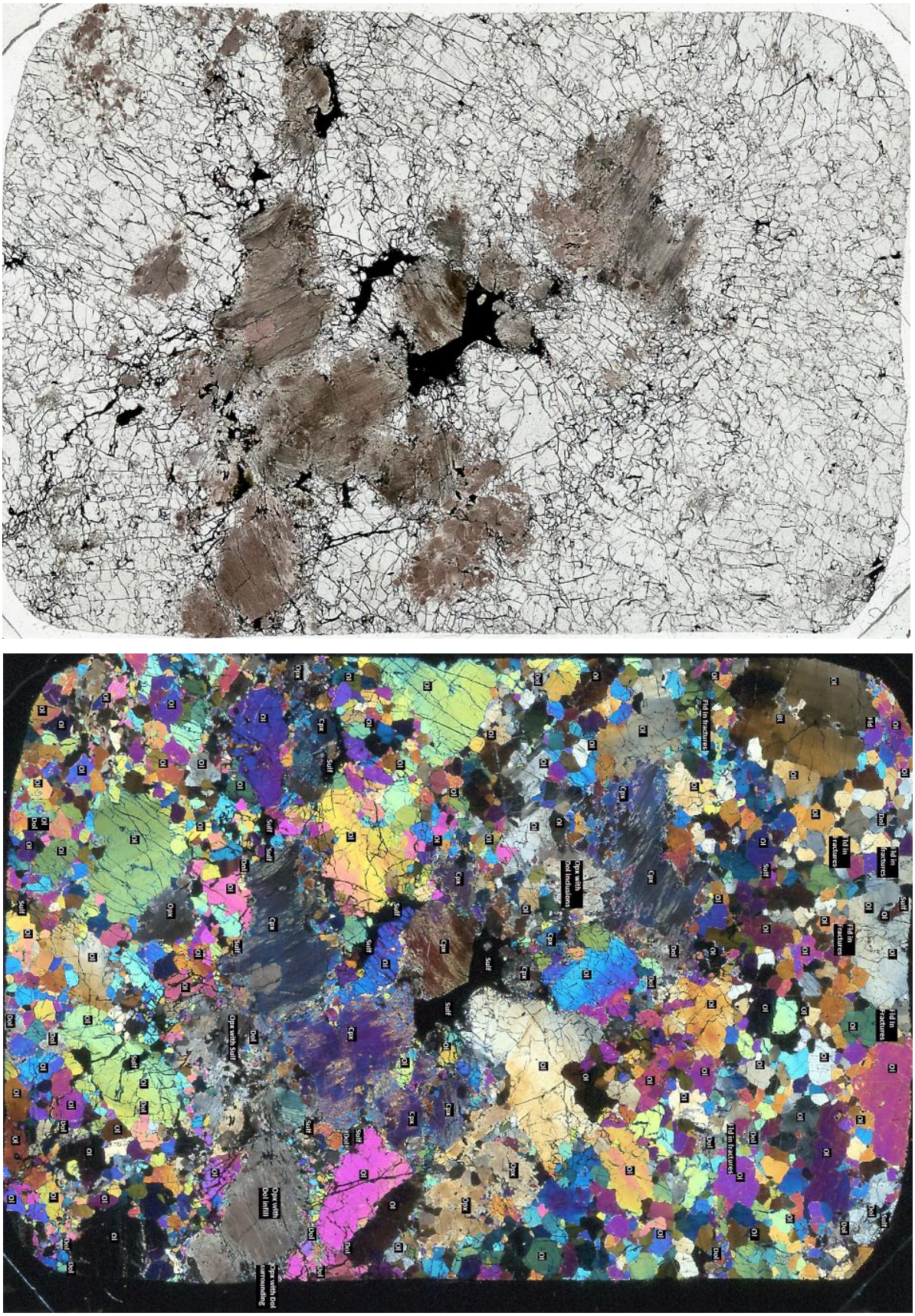

Figure A 3: Scan of thin section 110.2 with silicate labels. Upper scan in Ppl and lower scan in Xpl.

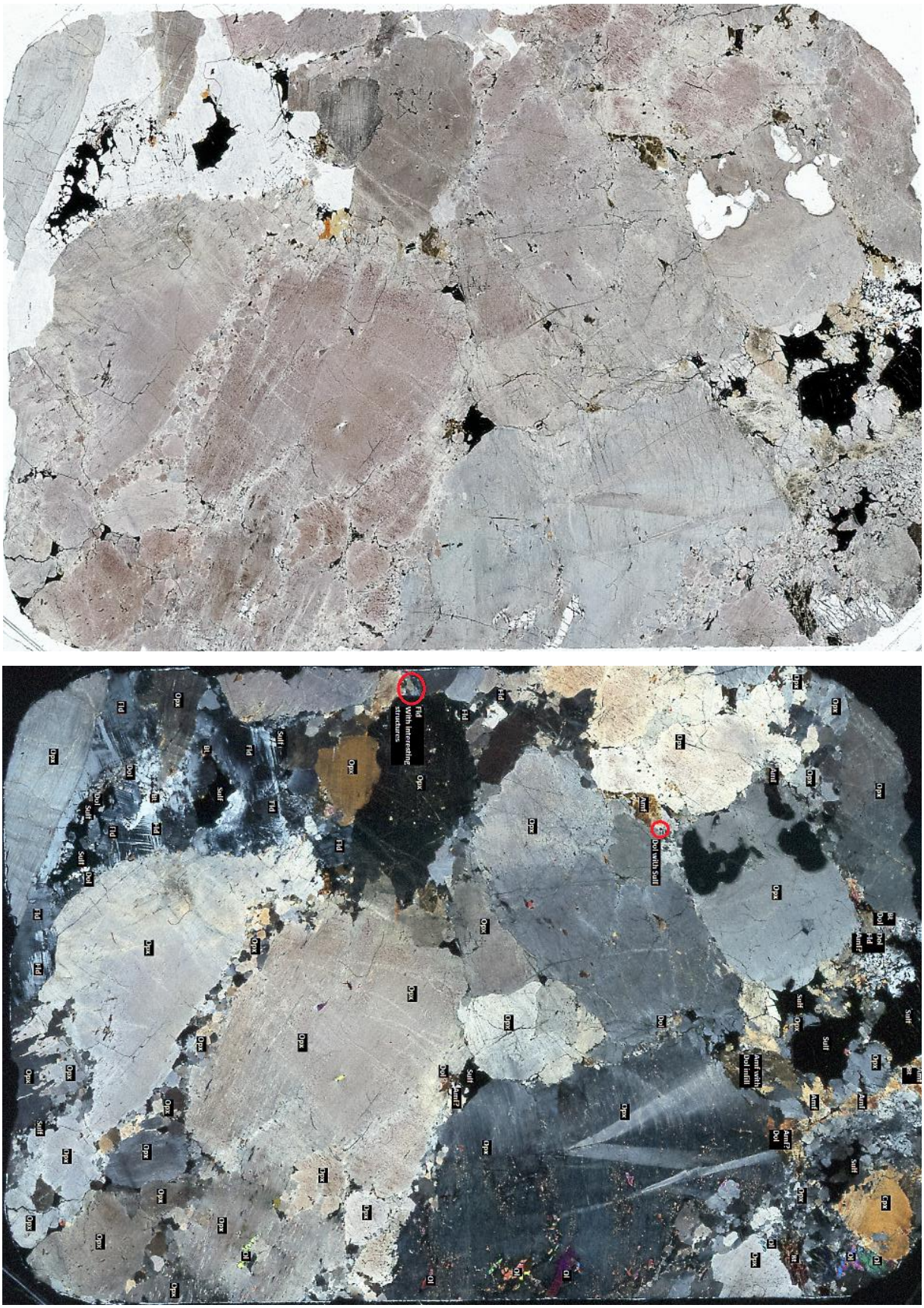

Figure A 4: Scan of thin section 110.4 with silicate labels. Upper scan in Ppl and lower scan in Xpl.

Appendix B

Table B 1	**Pt-Dominated minerals**	Detailed discriptions of all the Platinum dominated minerals, with following photos and color charts.	Appendix page 6-7
Table B 2	**Pt-Pd Dominated minerals**	Detailed discriptions of all the Platinum-Palladium dominated minerals, with following photos and color charts.	Appendix page 20-21
Table B 3	**Pd-Dominated minerals**	Detailed discriptions of all the Palladium dominated minerals, with following photos and color charts.	Appendix page 30-31
Table B 4	**Minerals containing Gold and Ruthenium**	Detailed discriptions of all the occurrence of minerals containing Gold and the one Ruthenium mineral with following photos and color charts.	Appendix page 44-45

Table B 1

Pt-Dominated								
Point	**Thin Section**	**L x W (µm)**	**Location (situated)**	**Host**	**Main Silicate**	**Notes**	**Link**	**EPMA**
87	109.55	2,5x2,5	In sulfide (edge)	Pn	Ol	Rounded Pt-Telluride located in a pentlandite section of a po-pn sulfide.	Figure B 1	Yes
89	109.55	1x1	In sulfide (edge)	Po	Ol	Too small to analyse on EPMA, but could be PtS mineral due to the high Sulphur content. Located in a large Po grain with the Cr bubbles.	Figure B 2	No
107	109.55	5x2,5	In sulfide (edge)	Pn	Ol	Sattelite grain outside the main sulfide that host Pt-109.	Figure B 3	Yes
109	109.55	150x5	In sulfide (inside)	Po	Ol-Opx	Po with Pn lamellas. Pt needle follow Pn direction	Figure B 4	Yes
125	109.55	15x10	In sulfide (inside)	Pn-Po	Ol	Larger grain located in the boarderzone between Pn-Po.	Figure B 5	Yes
271	109.55	6x6	In sulfide (inside)	Pn	Ol	Sits at the edge in contact with a pure MgO phase	Figure B 6	No
126	109.4	1x0,5	In sulfide (inside)	Pn	Ol	Dolomite in close approximation, but not in direct contact with sulfide	Figure B 7	No
131	109.4	1x1	In sulfide (inside)	Po	Opx-Ol	In contact with most Opx and some Ol	Figure B 8	No
137	109.4	3x0,5	In sulfide (inside)	Pn-Ccp	Ol-Amp-Opx-Cpx	Sulfide in contact with all four silicates, with Srp around the grain. PGM located in the boarderzone between Pn and Ccp.	Figure B 9	No
138	109.4	2,5x2,5	In sulfide (edge)	Ccp	Ol-Mgs	situated in a half island of Ccp, in direct contact with Ol and Mgs	Figure B 10	Yes

146	109.4	1,5x1	In sulfide (inside)	Pn	Opx-Cpx-Ol	Native Pt in lammellas of Pn in large Po	Figure B 11	No
147	109.4	3x0,5	In sulfide (edge)	Po	Opx-Cpx-Ol	Native Pt, but no sign of Pn at the rim.	Figure B 12	No
148	109.4	0,5x0,5	In sulfide (inside)	Pn	Opx-Cpx-Ol	Same grain as the Native Pt, bot situated in a pentlandite section as a rounded Pt-Telluride	Figure B 13	No
151	109.4	1x1	In sulfide (inside)	Pn	Opx-Cpx	Host sulfide oriented in a vein in Opx and can suggest emplacement post Opx crystallization.	Figure B 14	No
152	109.4	4x2,5	In sulfide (edge)	Ccp	Ol-Opx-Cpx	In direct contact with Opx, and Ol. Located in chalcopyrite that is altered to Po in certain places.	Figure B 15	Yes
161	109.4	2x1	Silicate (isolated)	Opx	Opx-Ol-Amp	Isolated grain of PGM. Can be an artifact of 3D location in a sulfide that is polished away.	Figure B 16	No
166	109.4	10x5	in sulfide (inside)	Po	Ol	Inside a Po grain with Pn lamellas attached. Ol, with Srp totally surrounding the sulfide.	Figure B 17	Yes
172	109.4	0,4x0,4	in sulfide (inside)	Pn	Opx-Ol	Coarse grained Ol and fine Opx	Figure B 18	No
179	109.4	8x2	in sulfide (inside)	Po	Opx-	Form a needle, oriented with Pn lamellae, but not in any Pn contact. Large amount of carbonate surrounding the host sulfide	Figure B 19	No
180	109.4	5x2	in sulfide (edge)	Pn	Ol-Srp	in a Po-Pn vein in contact with Ol and Srp	Figure B 20	Yes
223	110.45	3x3	Oxide (vein)	Spl	Opx	Forms as a round grain in a crack filled with Opx, cutting through an Ilm.	Figure B 22	Yes

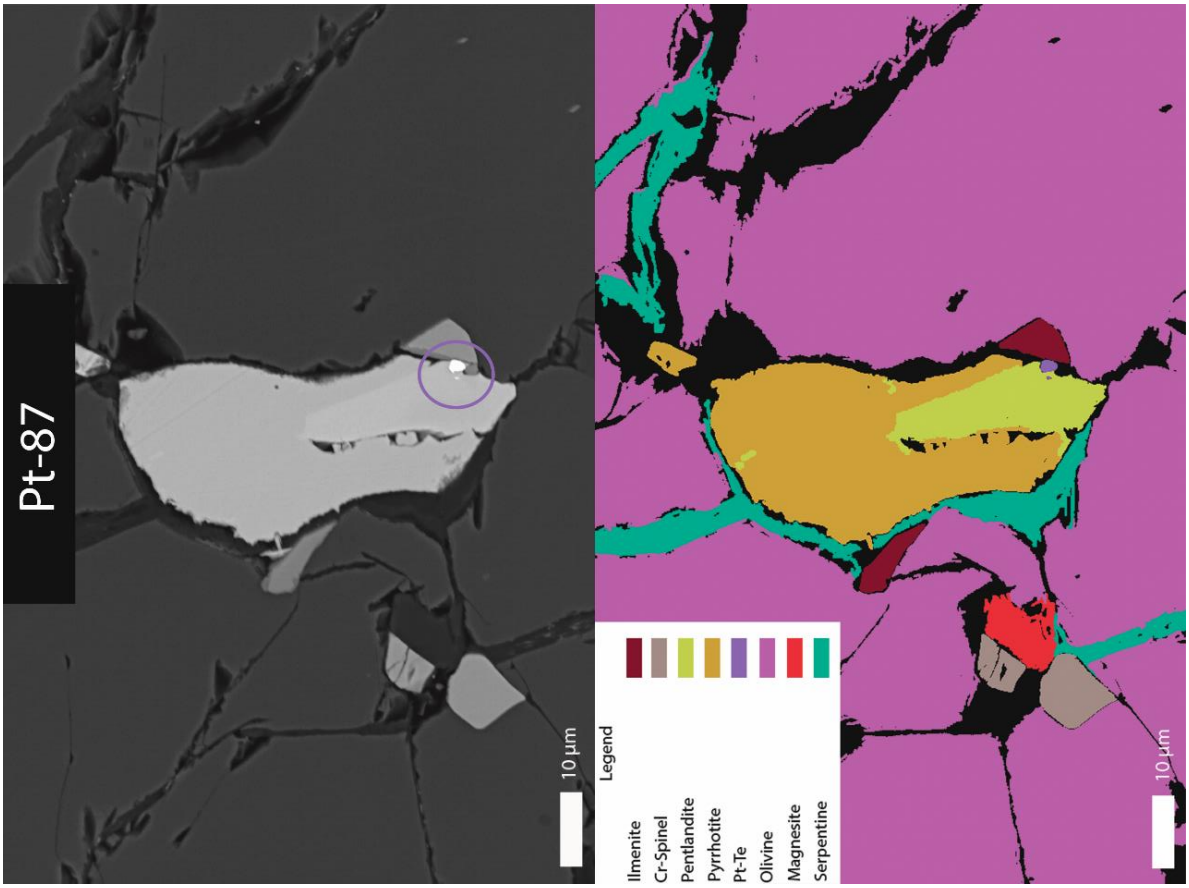

Figure B 1

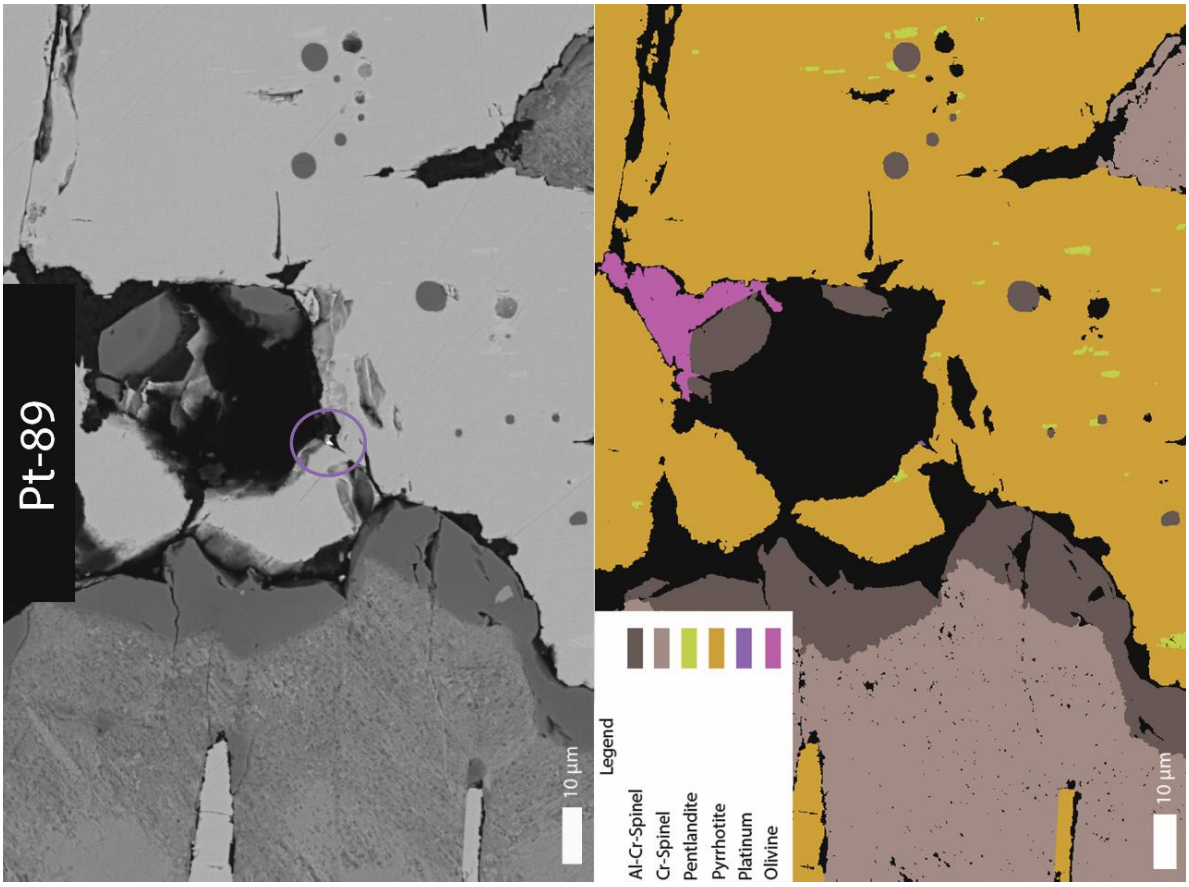

Figure B 2

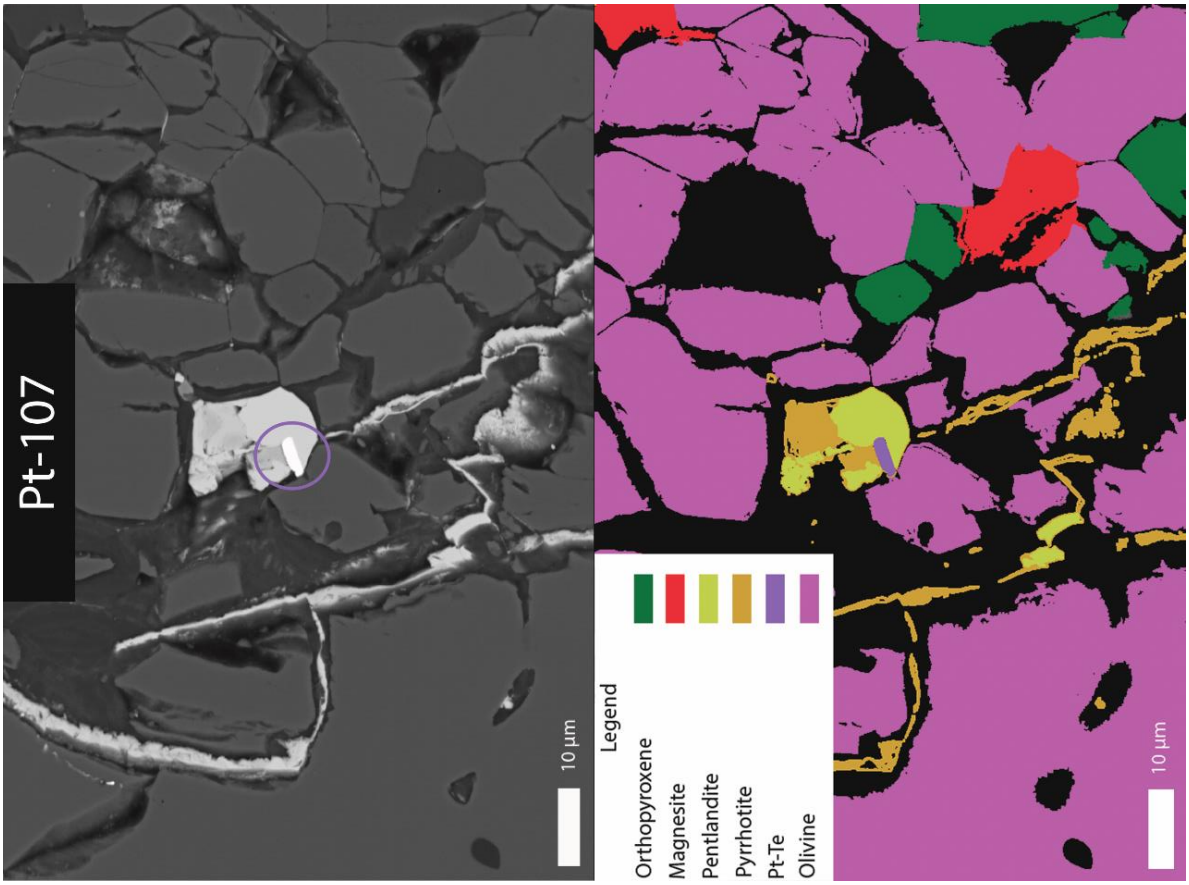

Figure B 3

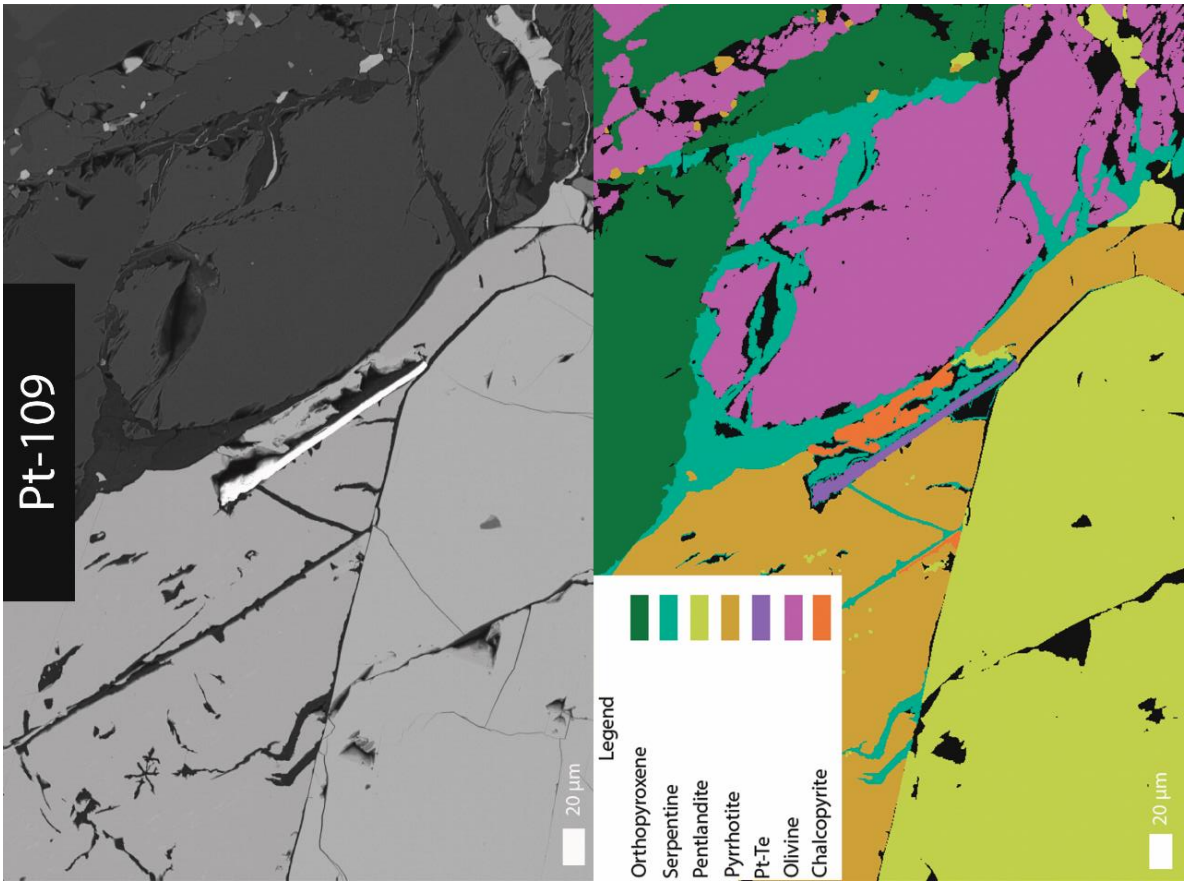

Figure B 4

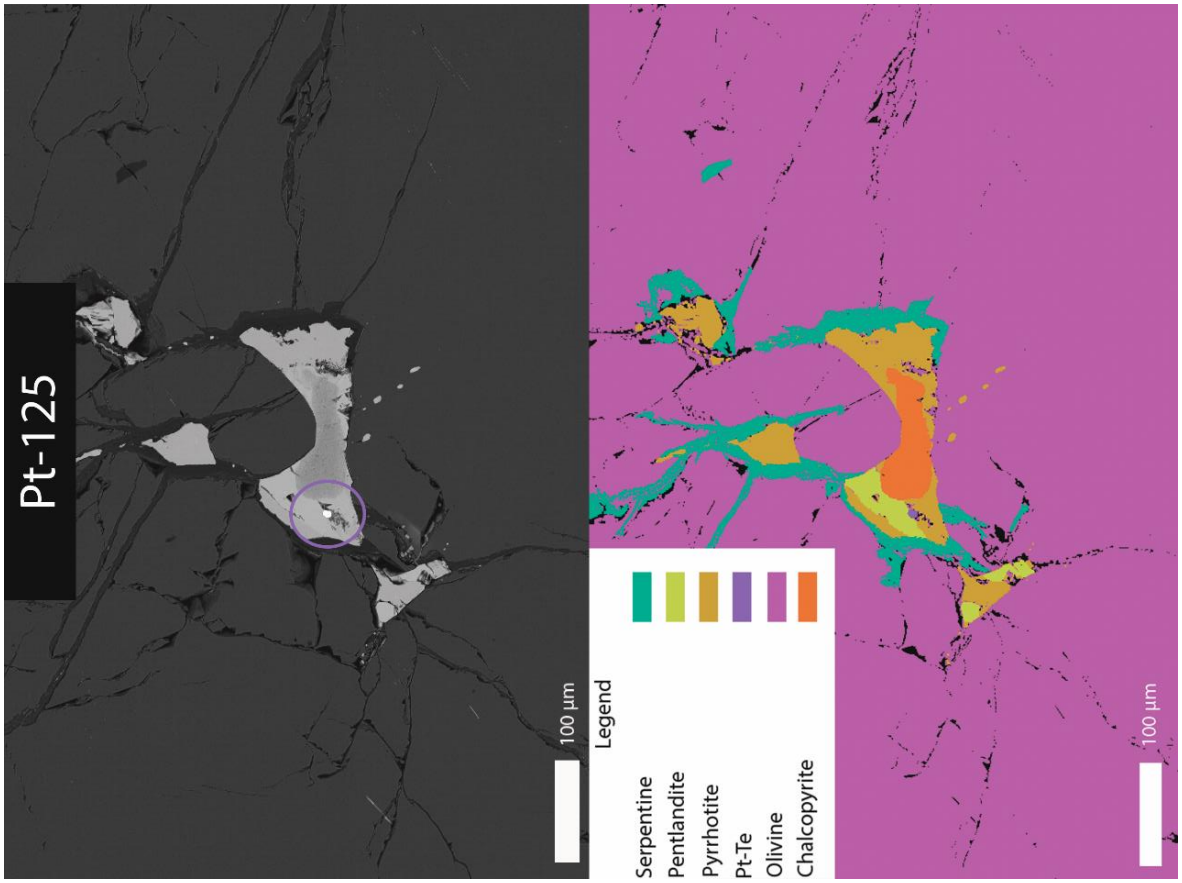

Figure B 5

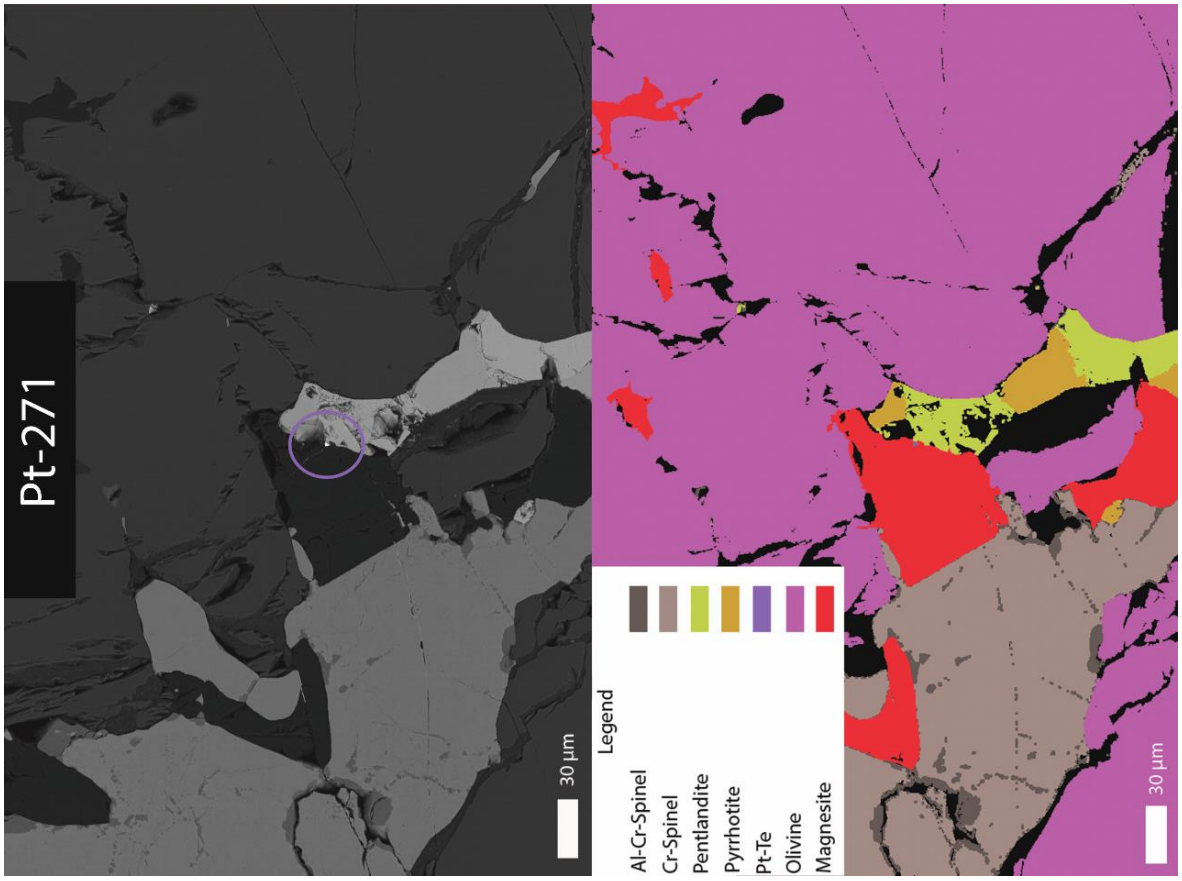

Figure B 6

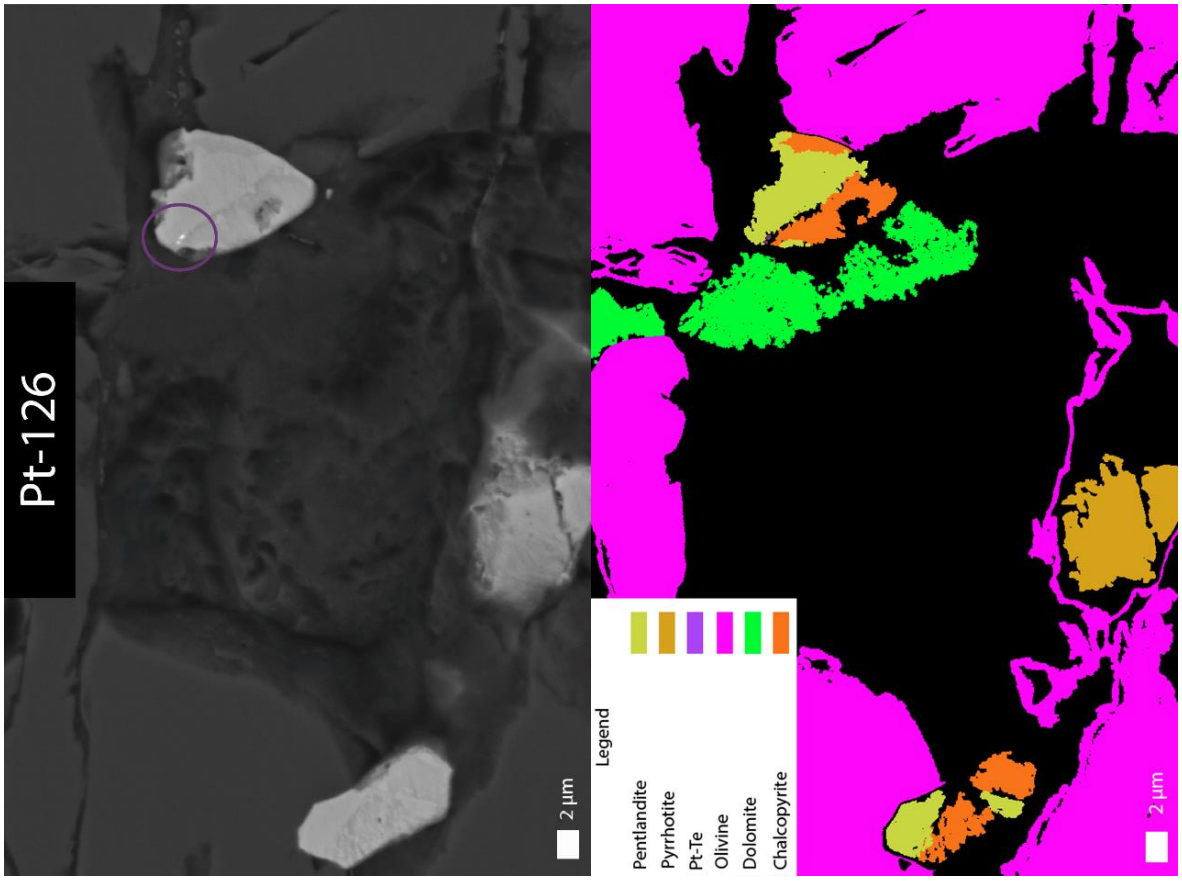

Figure B 7

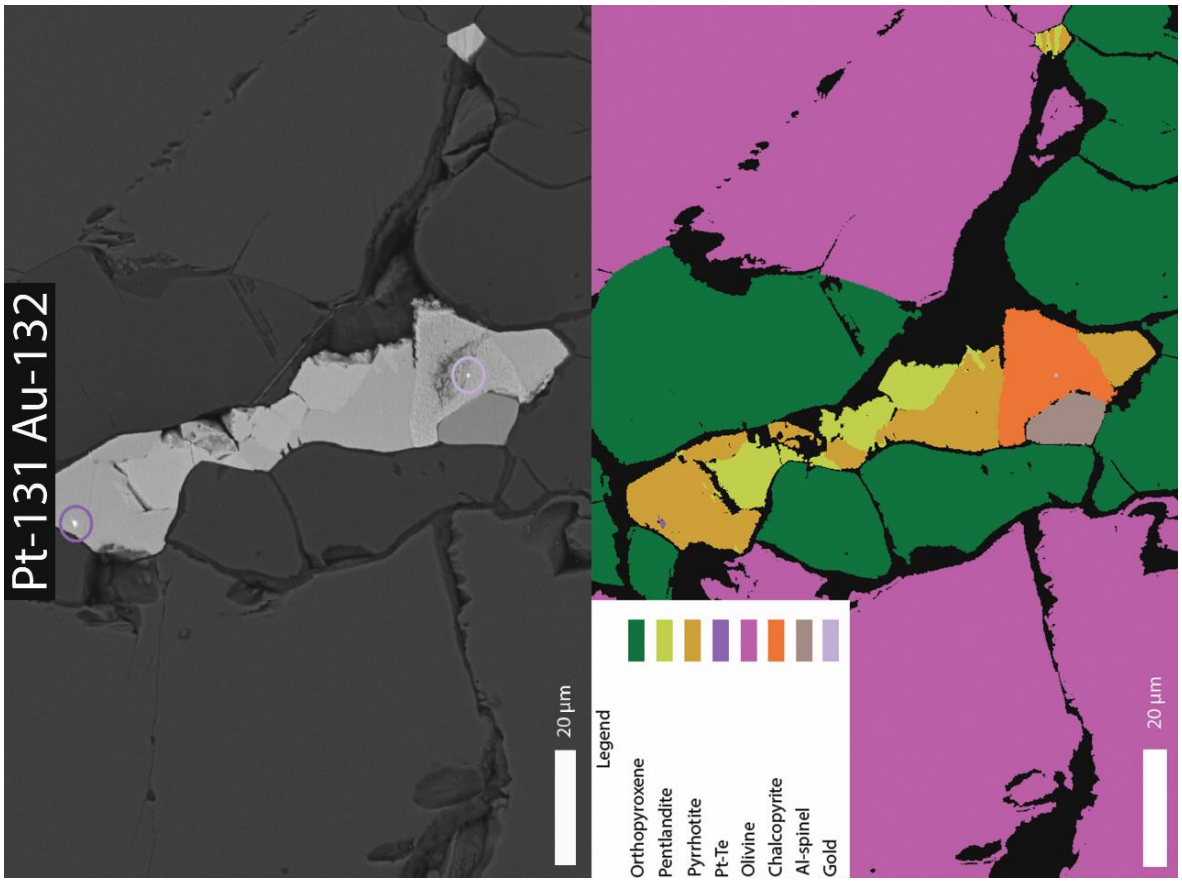

Figure B 8

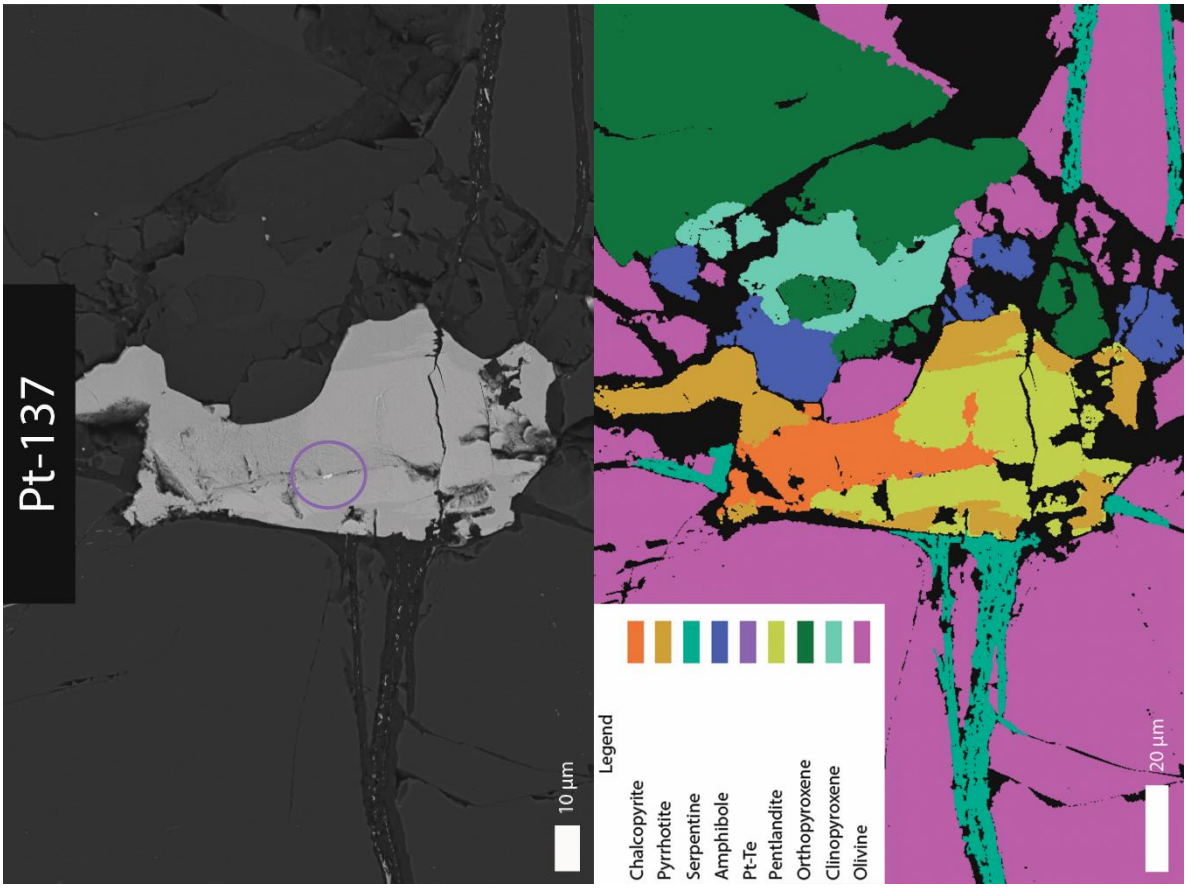

Figure B 9

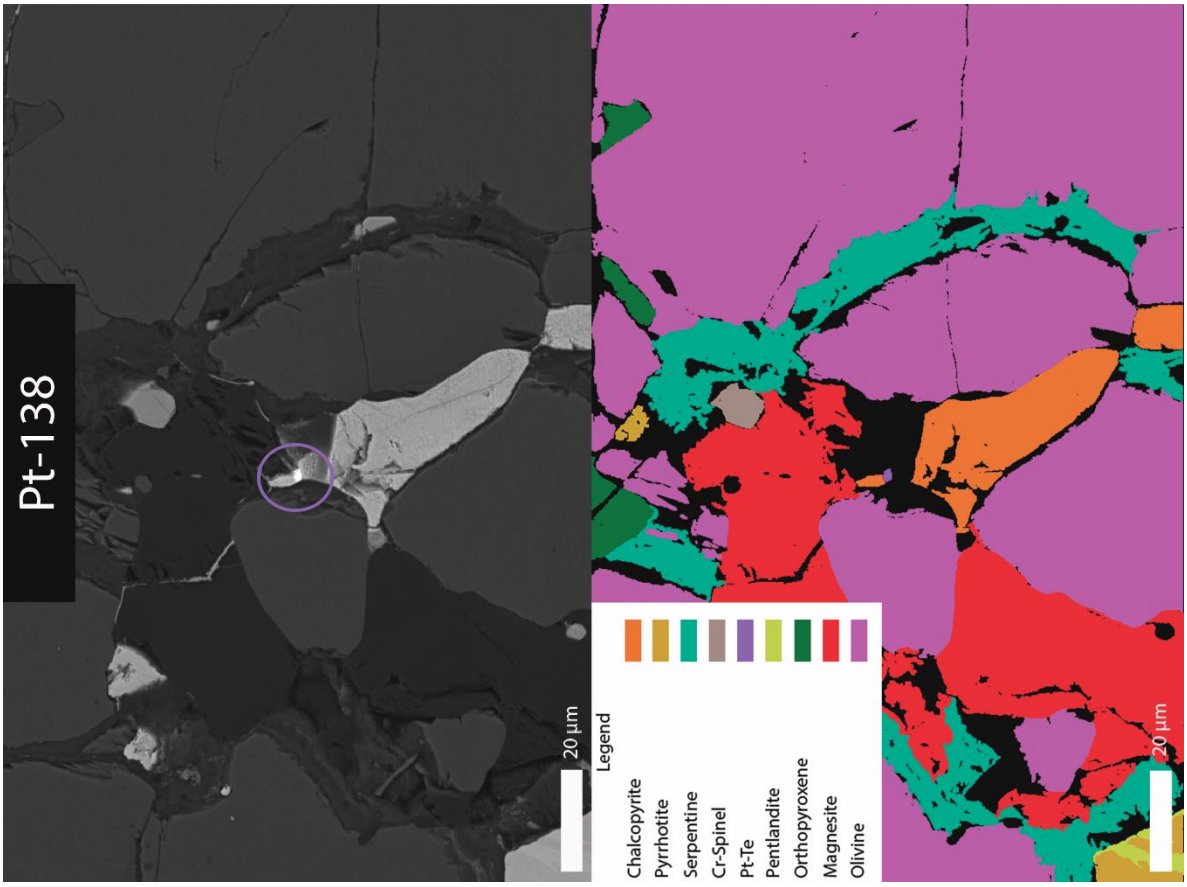

Figure B 10

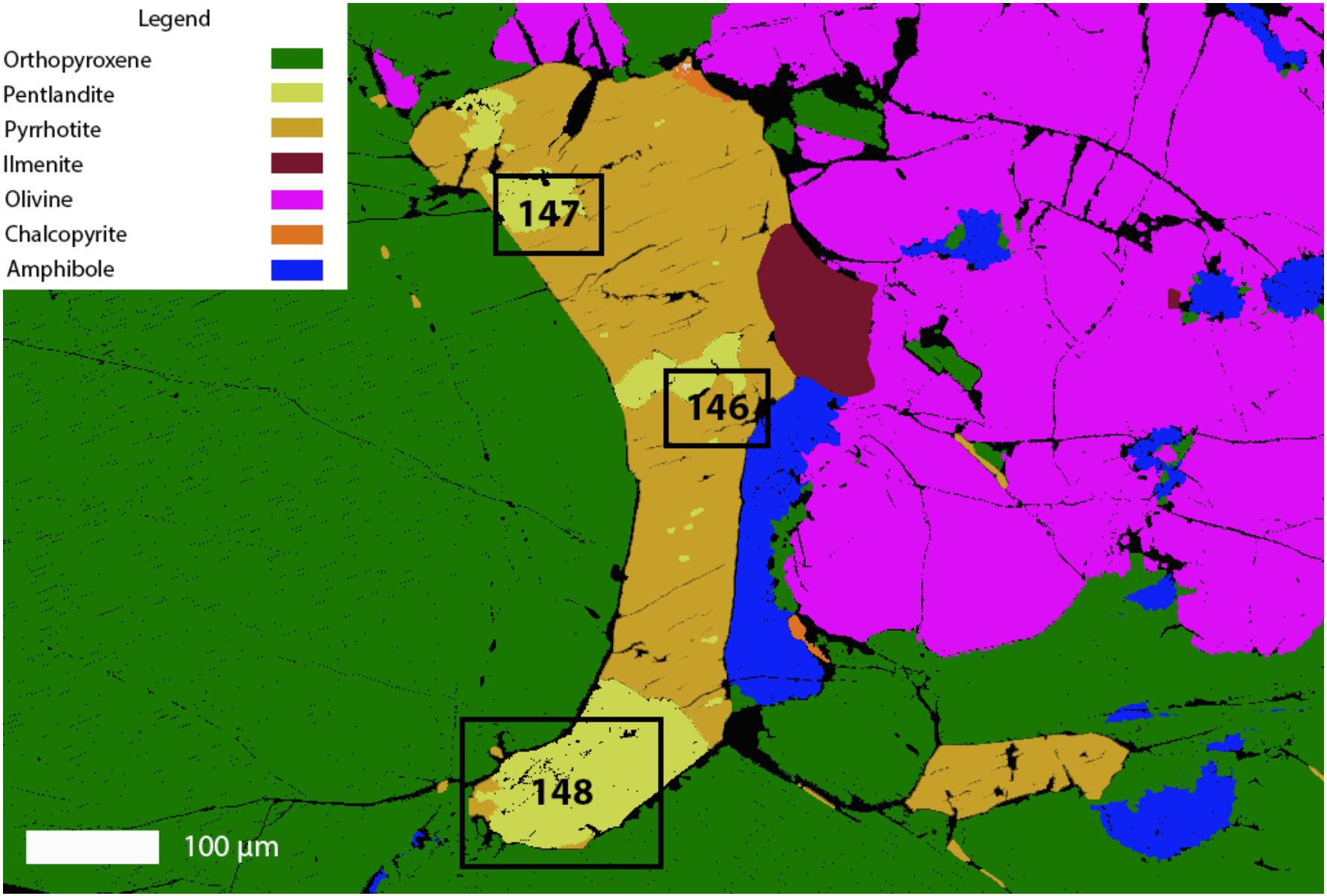
Legend
Orthopyroxene
Pentlandite
Pyrrhotite
Ilmenite
Olivine
Chalcopyrite
Amphibole
147
146
148
100 µm

Figure B 11

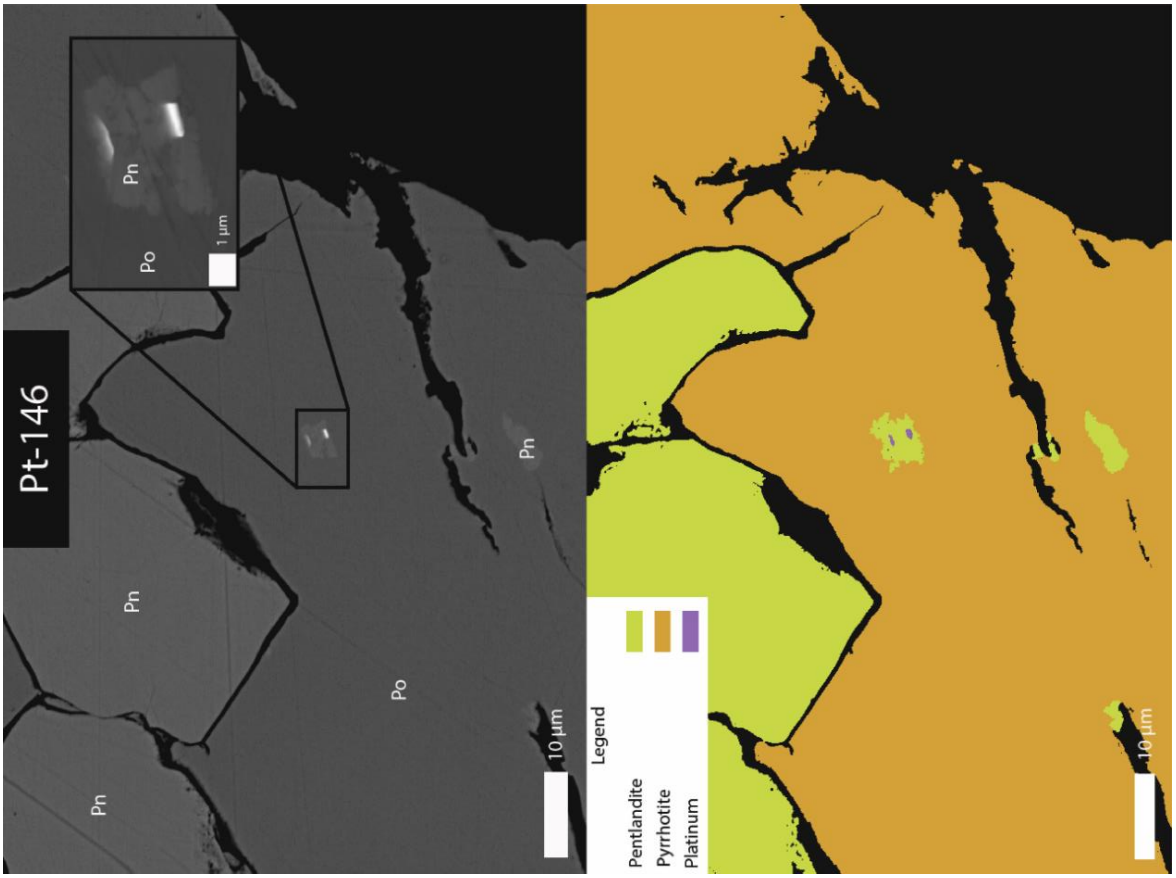

Figure B 12

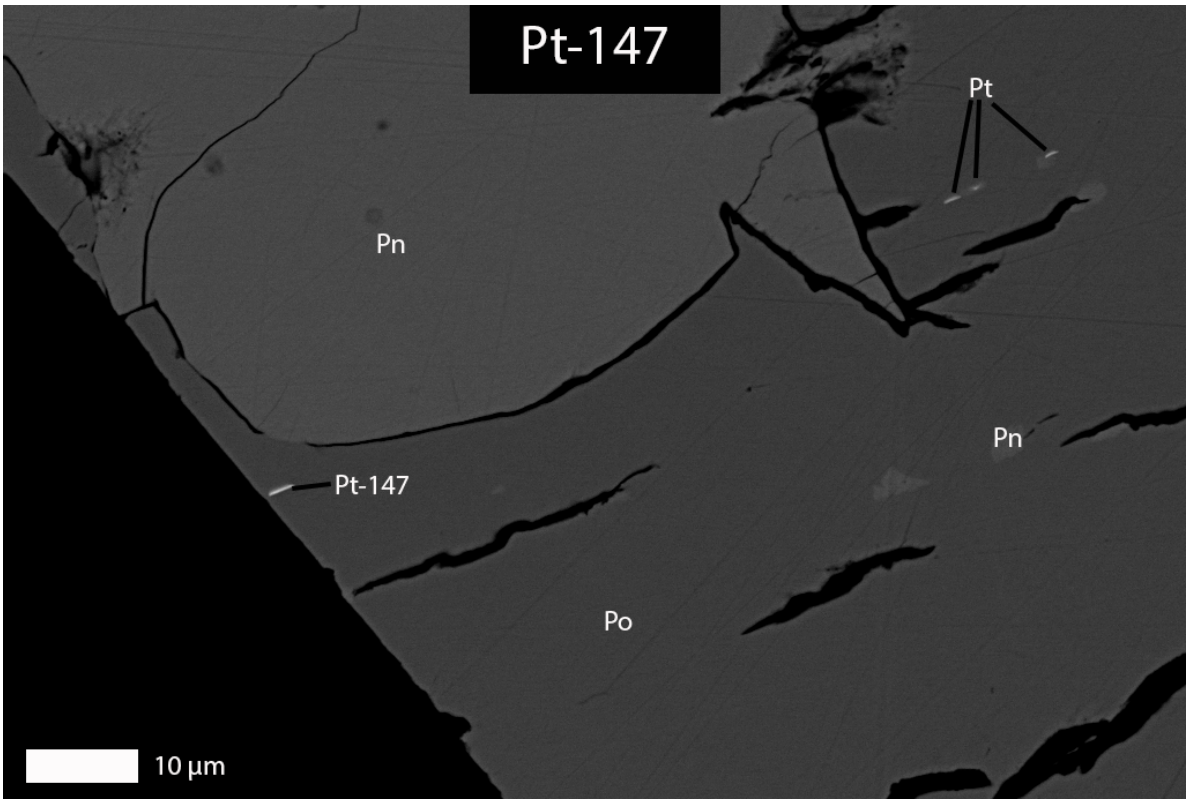

Figure B 13

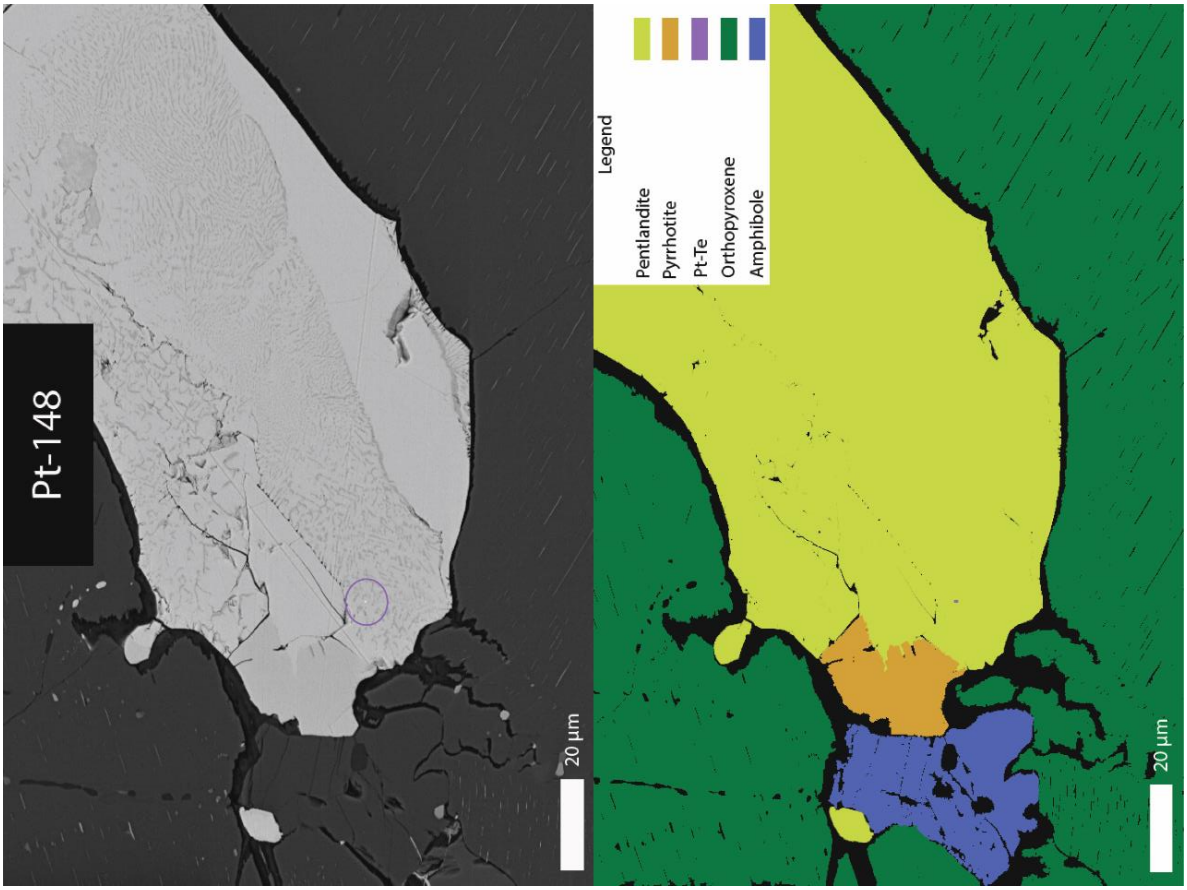

Figure B 14

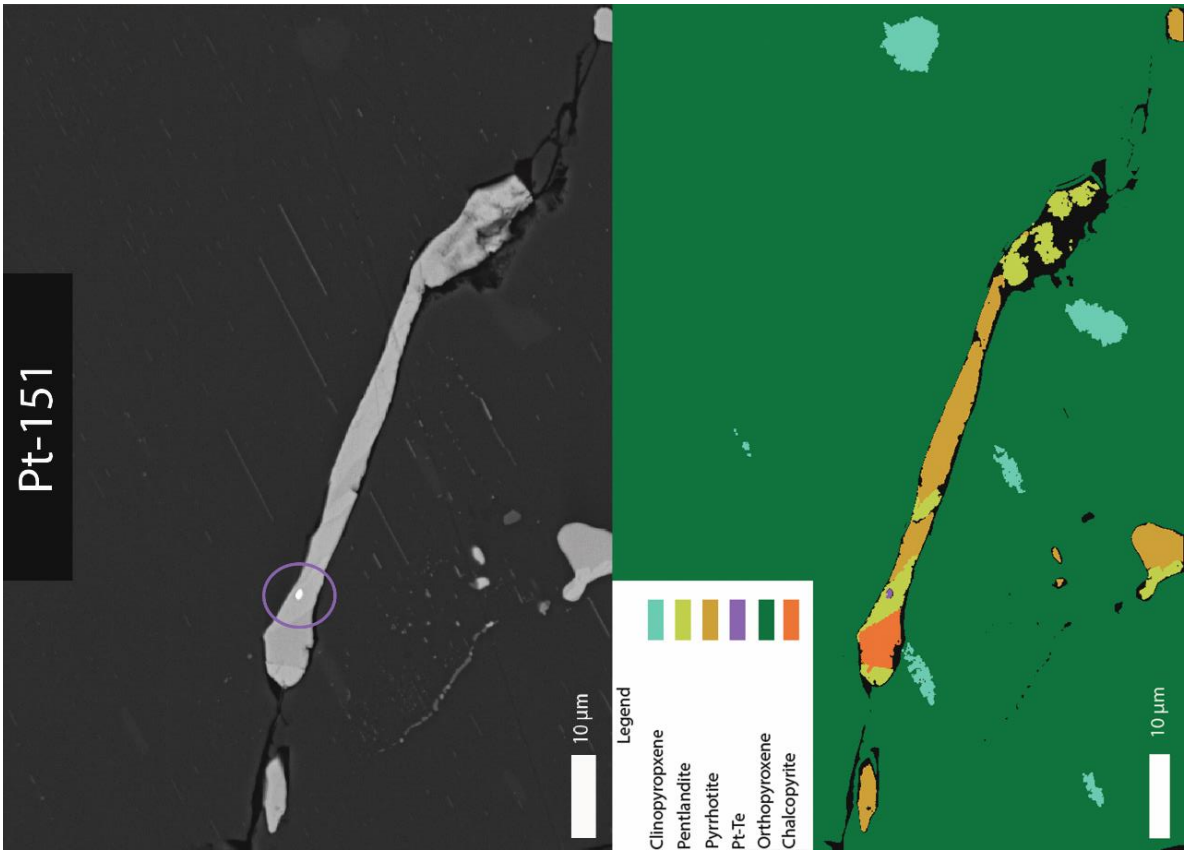

Figure B 15

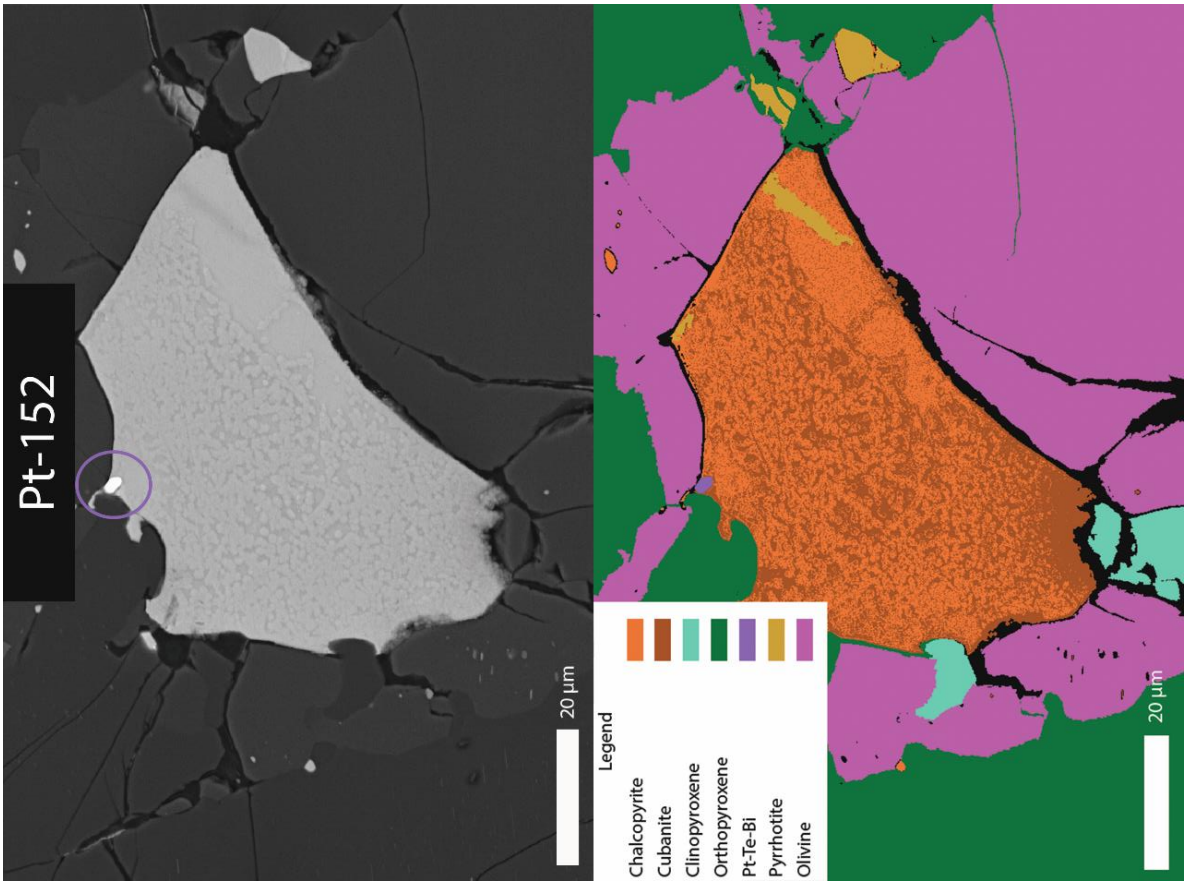

Figure B 16

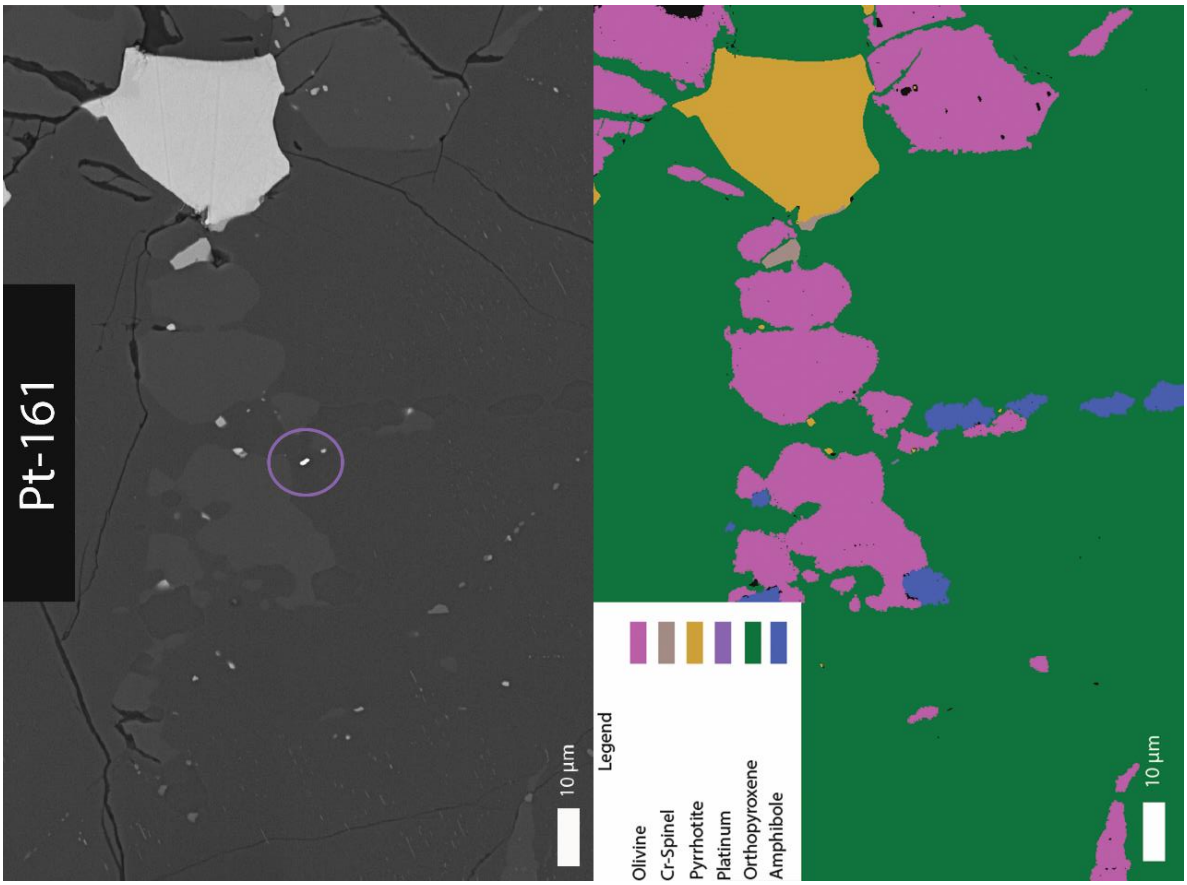

Figure B 17

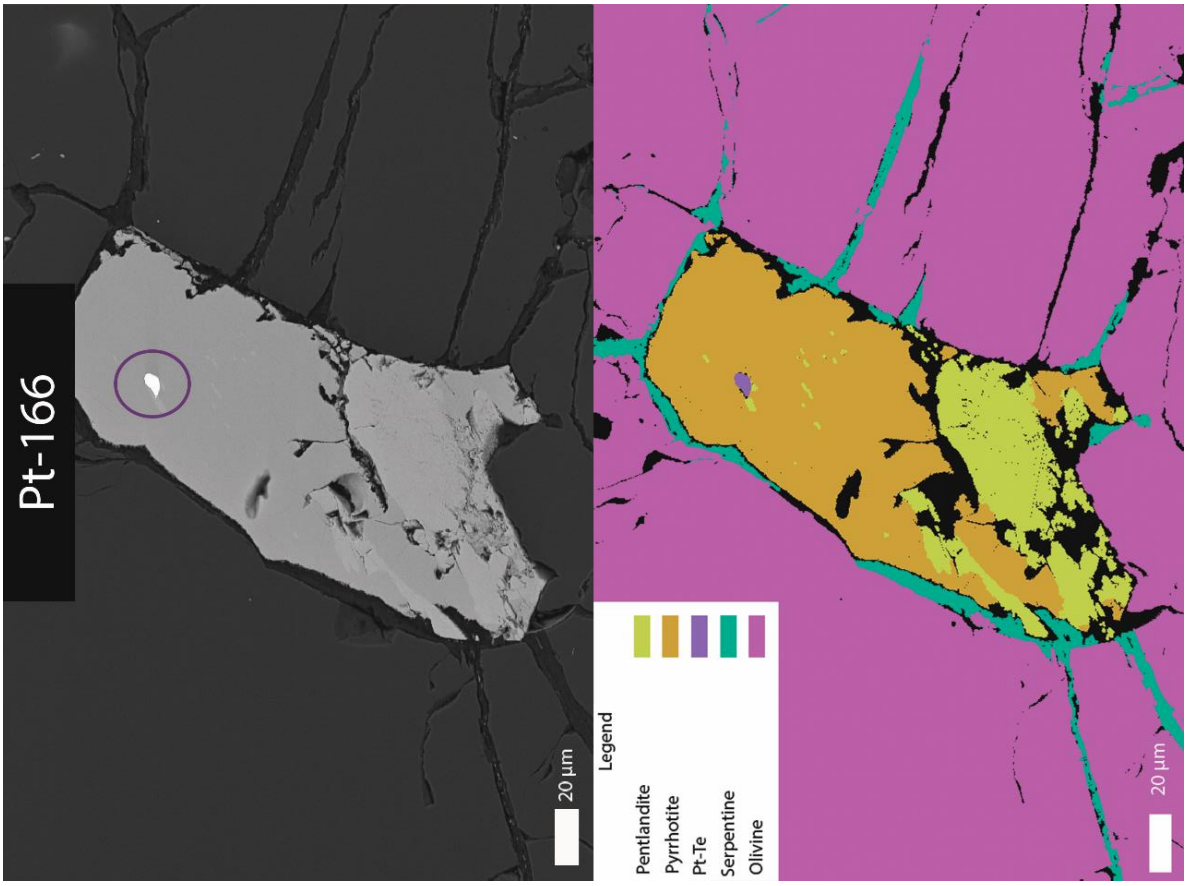

Figure B 18

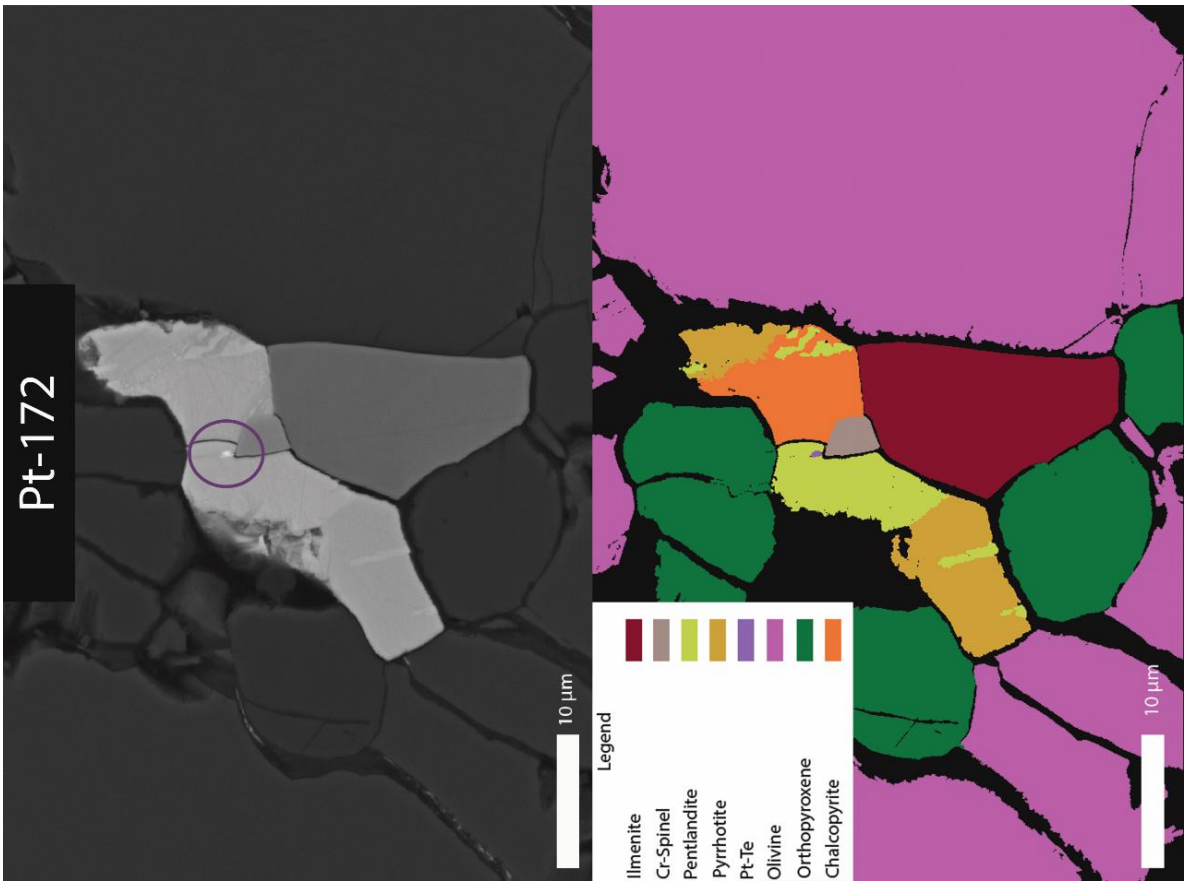

Figure B 19

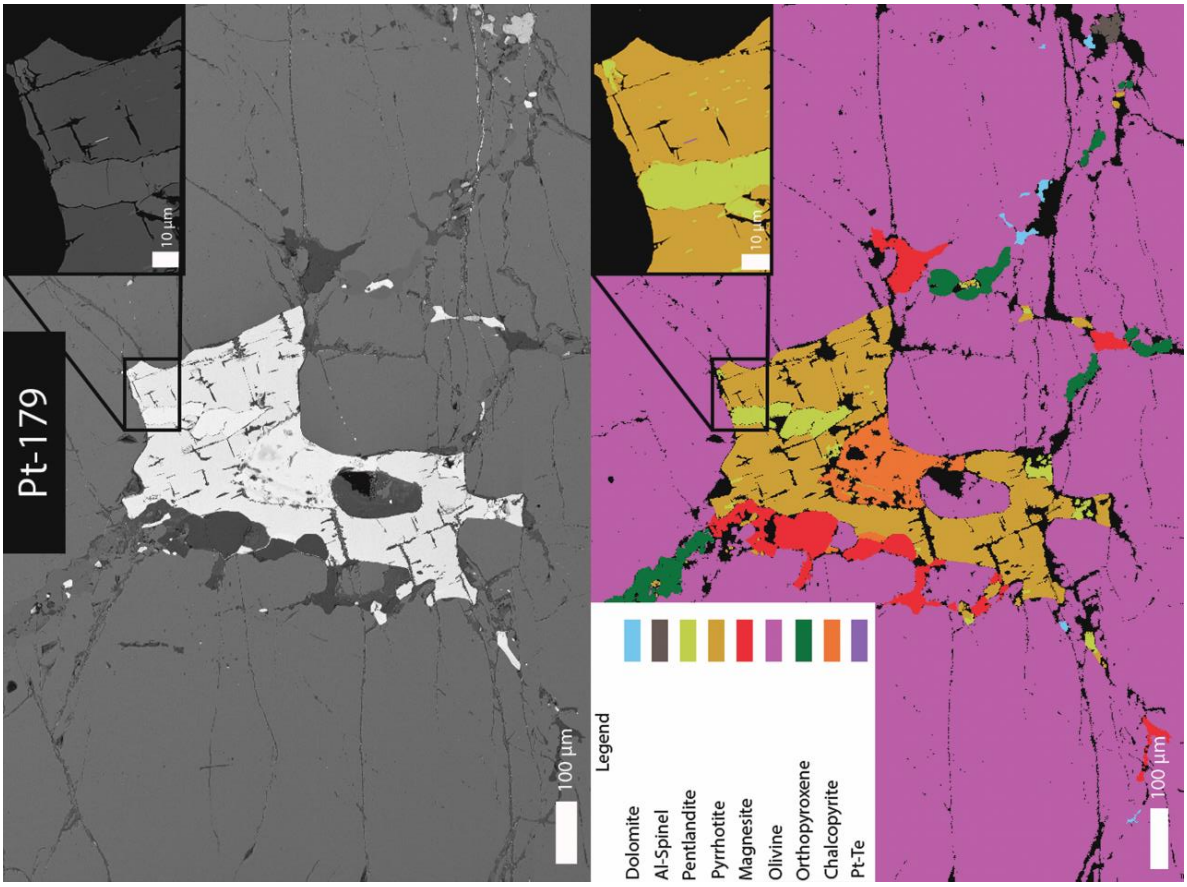

Figure B 19

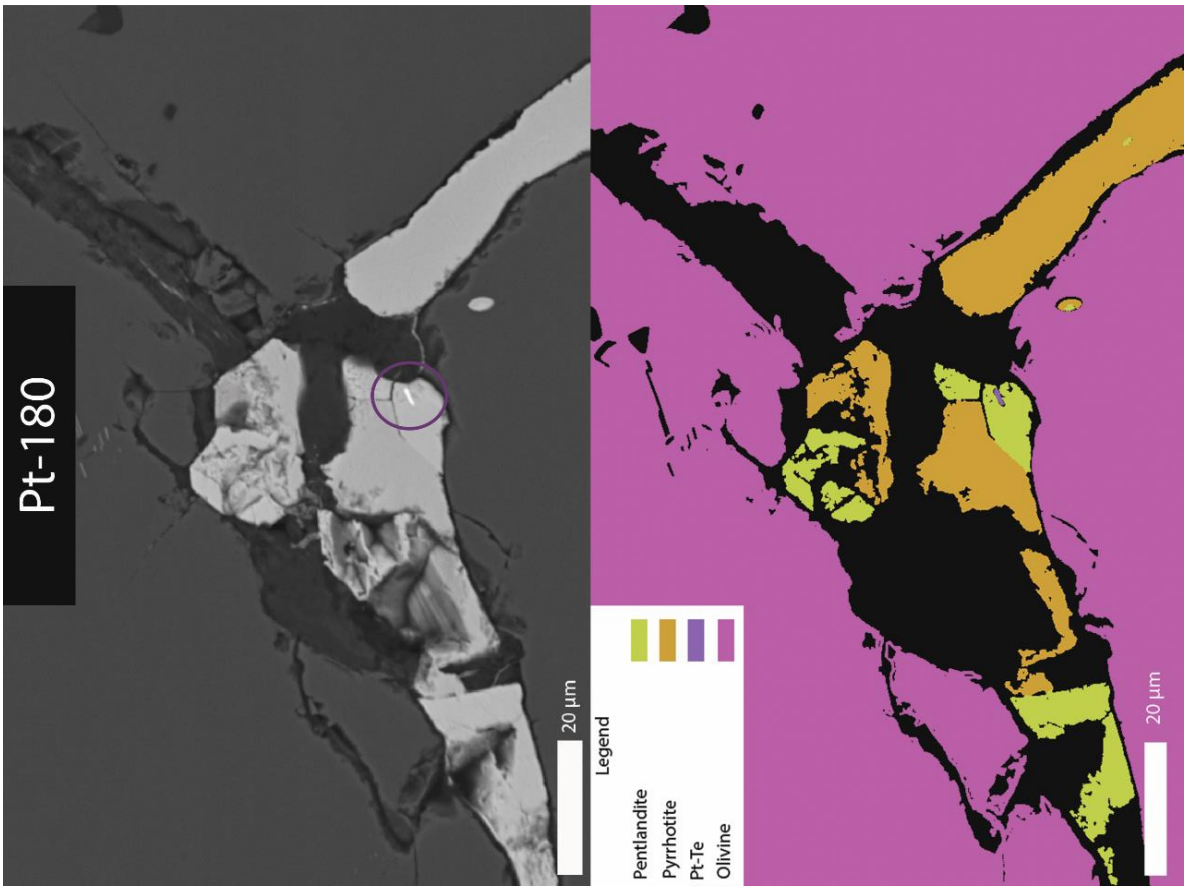

Figure B 21

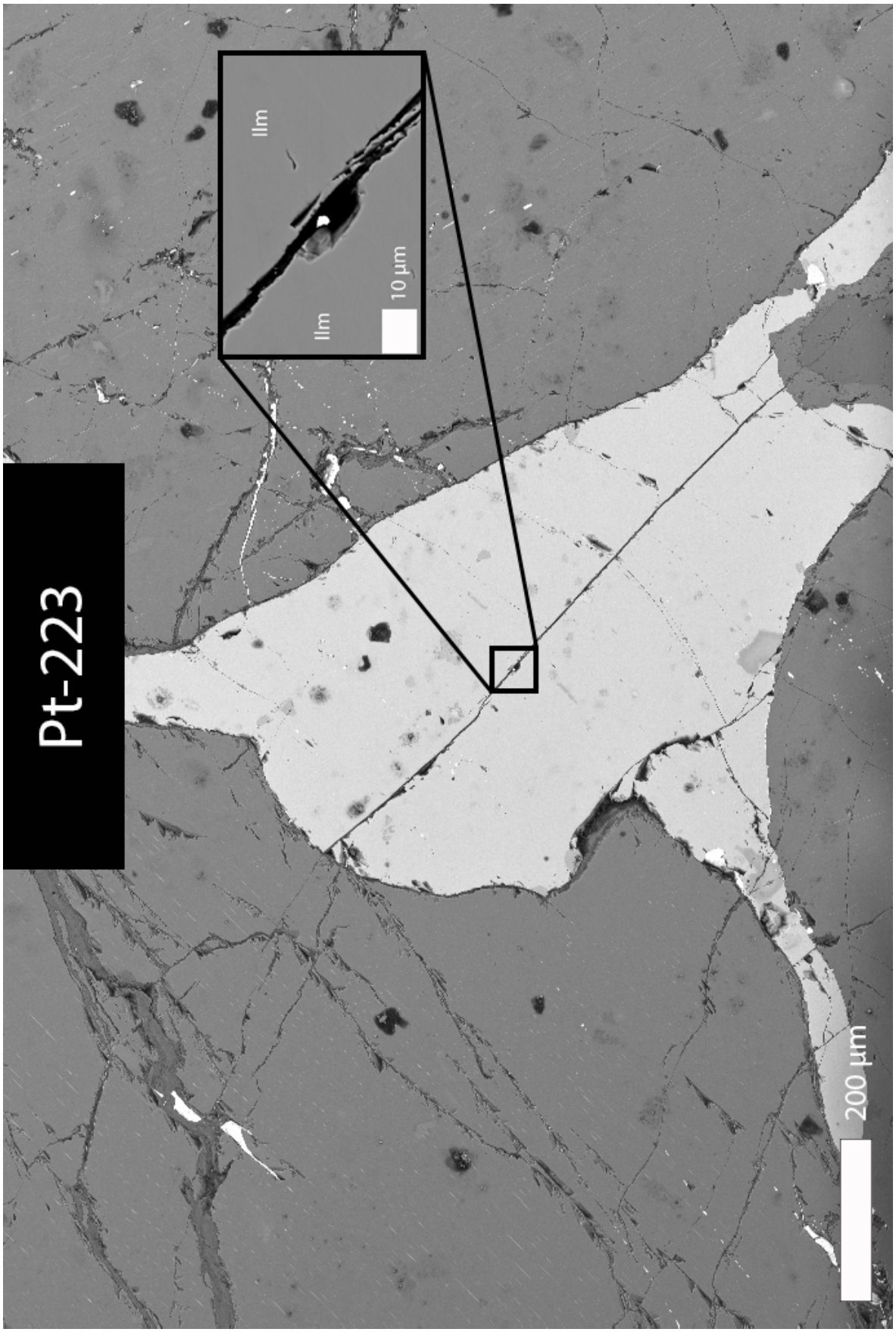

Figure B 22

Table B 2

Pt-Pd-Dominated								
Point	**Thin Section**	**L x W (µm)**	**Location (situated)**	**Host**	**Main Silicate**	**Notes**	**Link**	**EPMA**
91	109.55	5x1	In sulfide (inside)	Pn	Amp Cpx-Ol	Thin needle totally enclosed by Pn. Located in a separation zone between Ol and carbonatitic melt.	Figure B 23	No
94	109.55	5x1	In sulfide (edge)	Pn	Ol-Amp	in a Pn lamellae but also in contact with Po	Figure B 24	No
98	109.55	3x1,5	In sulfide (edge)	Pn	Ol	Totally surrounded by serpentine that also contain sulfide, with hosting Ol	Figure B 25	No
100	109.55	2x1	In sulfide (edge)	Pn	Ol-Spl	Incorporated at the edge of a Ti-Cr spinel, hosted by Ol	Figure B 26	No
150	109.4	0,5x0,5	In sulfide (inside)	Pn	Opx	In a widening of a crack in a large Opx grain	Figure B 27	No
169	109.4	8x3	In sulfide (edge)	Pn	Opx-Cpx	Pd-Pt alloy	Figure B 28	Yes
174	109.4	1x1	Silicate (isolated)	Ol	Ol	Isolated grain in Ol, which shows directional connection as the last phase in a transport sequence because of the sulfide alignment.	Figure B 29	No
226	110.45	4x2	In sulfide (edge)	Ccp	Opx-Amp	Forming in a smaller grain of Ccp close to larger grains of Pn and Po	Figure B 30	Yes
229	110.45	6x3	In vein (middle)	Ccp-Po	Cpx	In a vein that cuts through a larger grain of Opx with smaller inclusions of Cpx, but the PGE is crystallized with boarders to Cpx	Figure B 31	No

236	110.45		In vein (middle)	Ccp-Po	Opx-Srp	Settled in a vein with Opx-Cpx on one side and Srp on the other. Ni incorporated in the PGE	Figure B 32	Yes
243	110.45	15x5	In vein (middle)	Ccp-Po	Opx-Srp	Settled in a vein with Opx-Cpx on one side and Srp on the other. Ni incorporated in the PGE	Figure B 32	Yes
249	110.45	6x2	In vein (middle)	Ccp-Po	Opx-Srp	Settled in a vein with Opx-Cpx on one side and Srp on the other. Ni incorporated in the PGE	Figure B 32	Yes
250	110.45	1x1	In vein (middle)	Ccp-Po	Opx-Srp	Settled in a vein with Opx-Cpx on one side and Srp on the other. Ni incorporated in the PGE	Figure B 32	Yes
259	110.45	15x5	In vein (middle)	Po	Opx	In a vein shooting out from a larger sulfide grain.	Figure B 33	Yes
267	110.45	10x2	In vein (middle)	Ccp	Opx	In a vein shooting out from a larger sulfide grain.	Figure B 34	No
274	110.3	5x5	In sulfide (edge)	Ccp	Cpx-Opx-Bt	At the edge in a contact zone between Pl and Opx. Located at the sulfide edge enclosed by Ccp.	Figure B 35	Yes
276	110.3	8x2	In vein (middle)	Ccp	Opx	In the last portion of a long vein running out form a larger sulfide.	Figure B 36	No

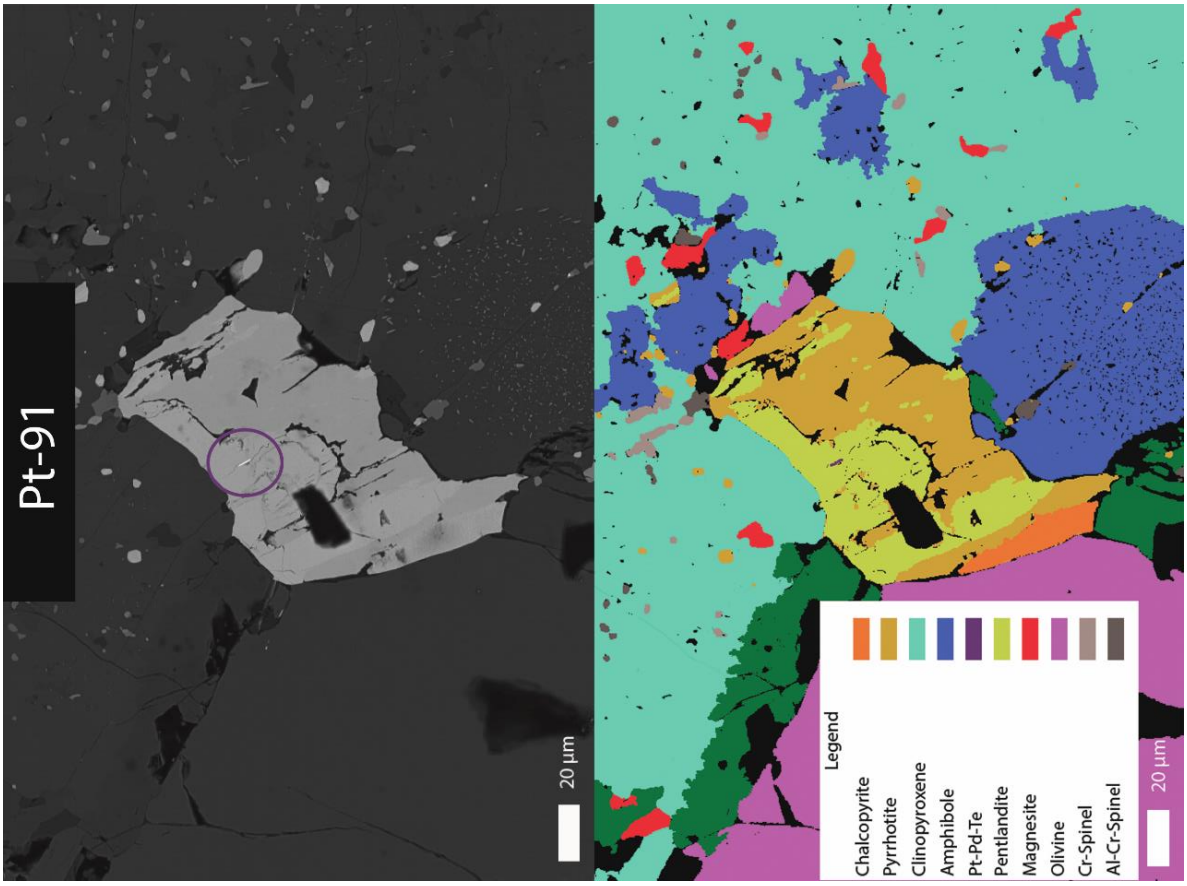

Figure B 23

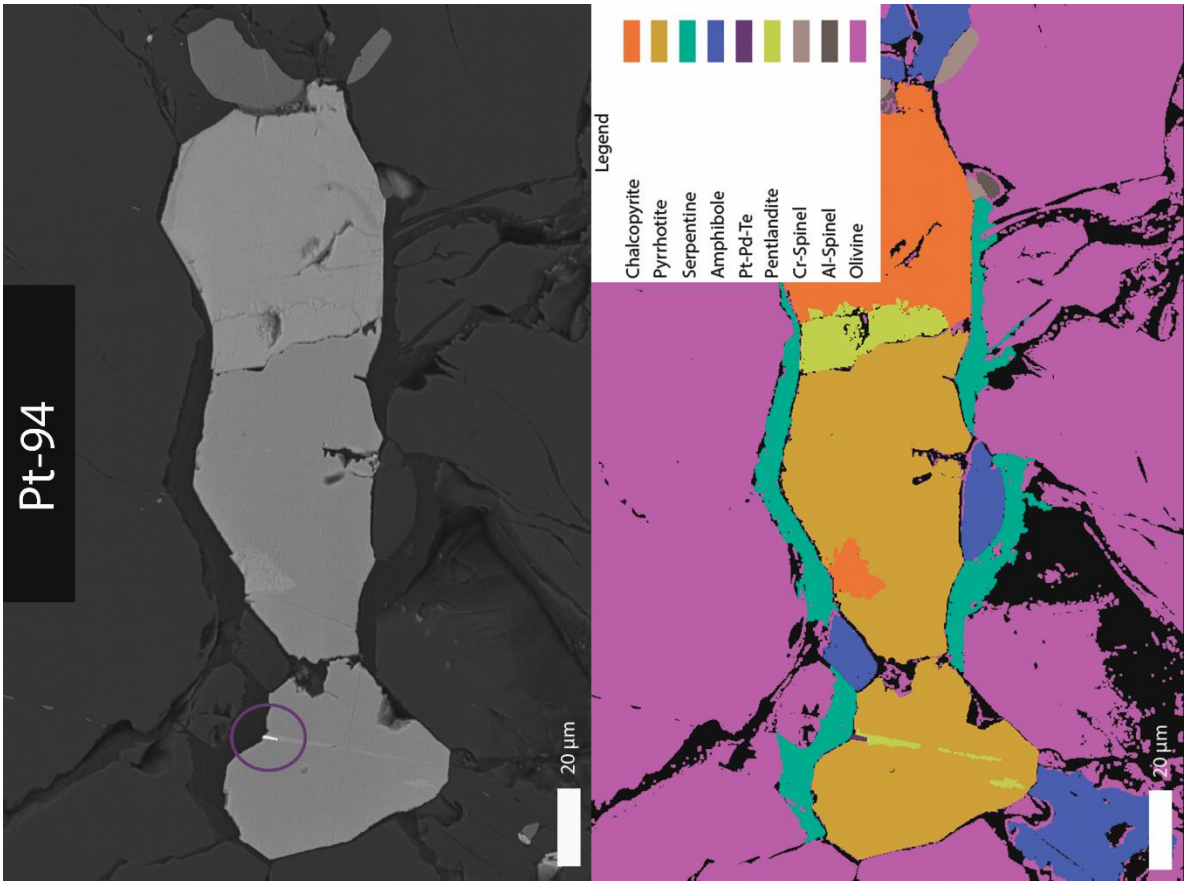

Figure B 24

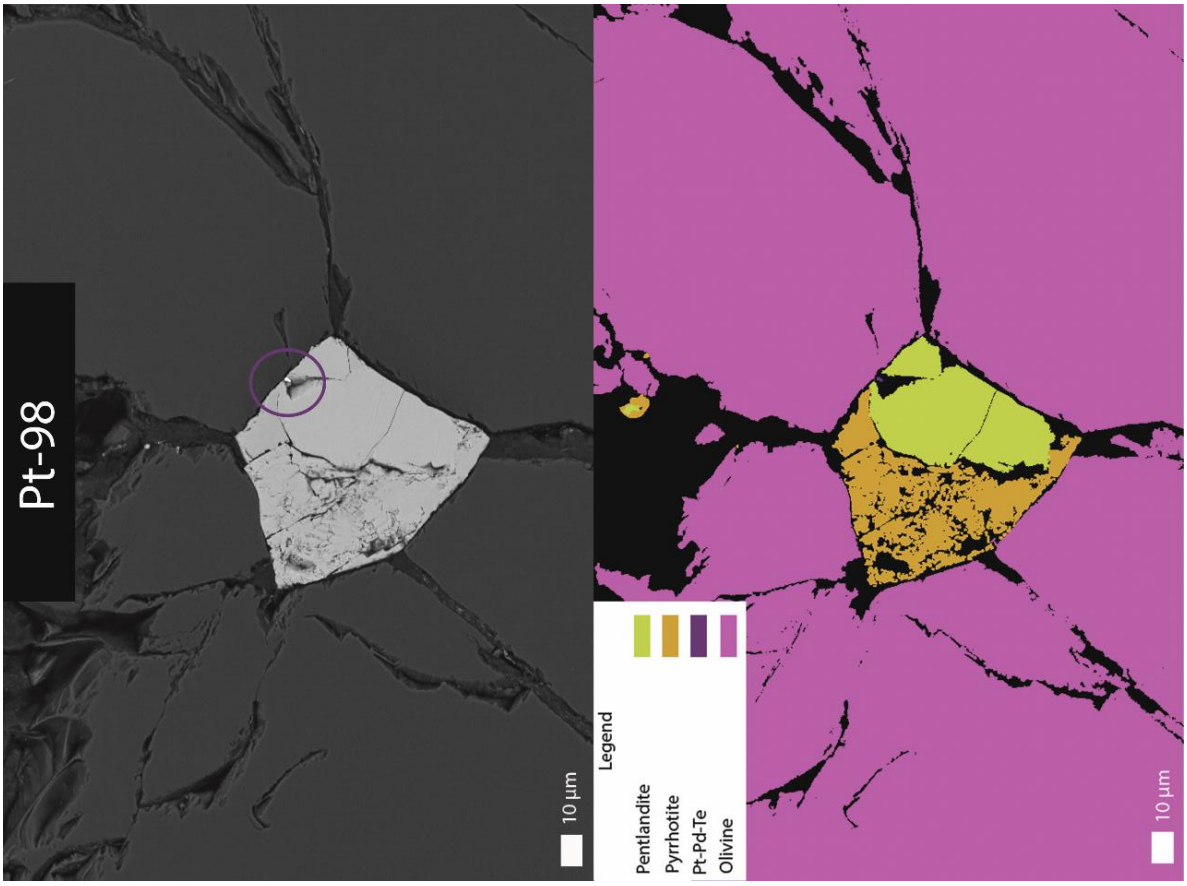

Figure B 25

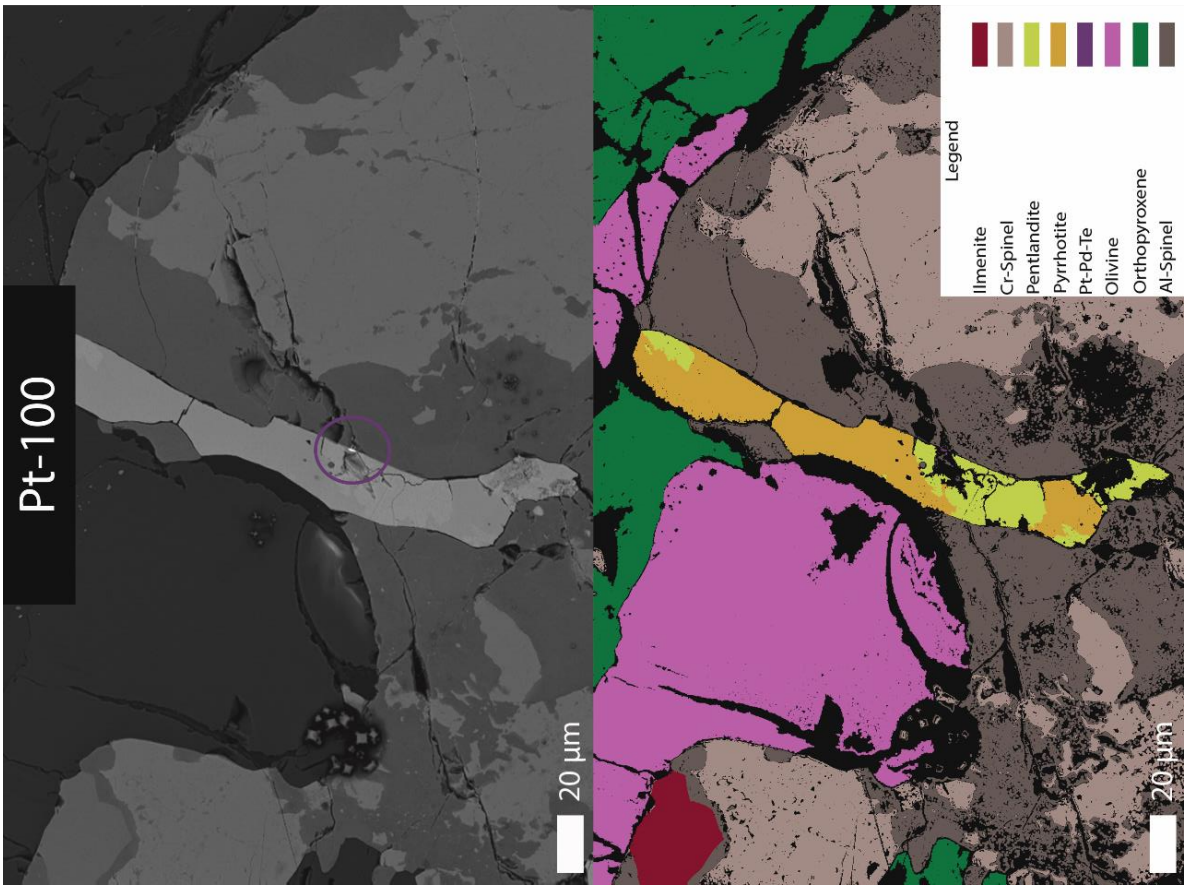

Figure B 26

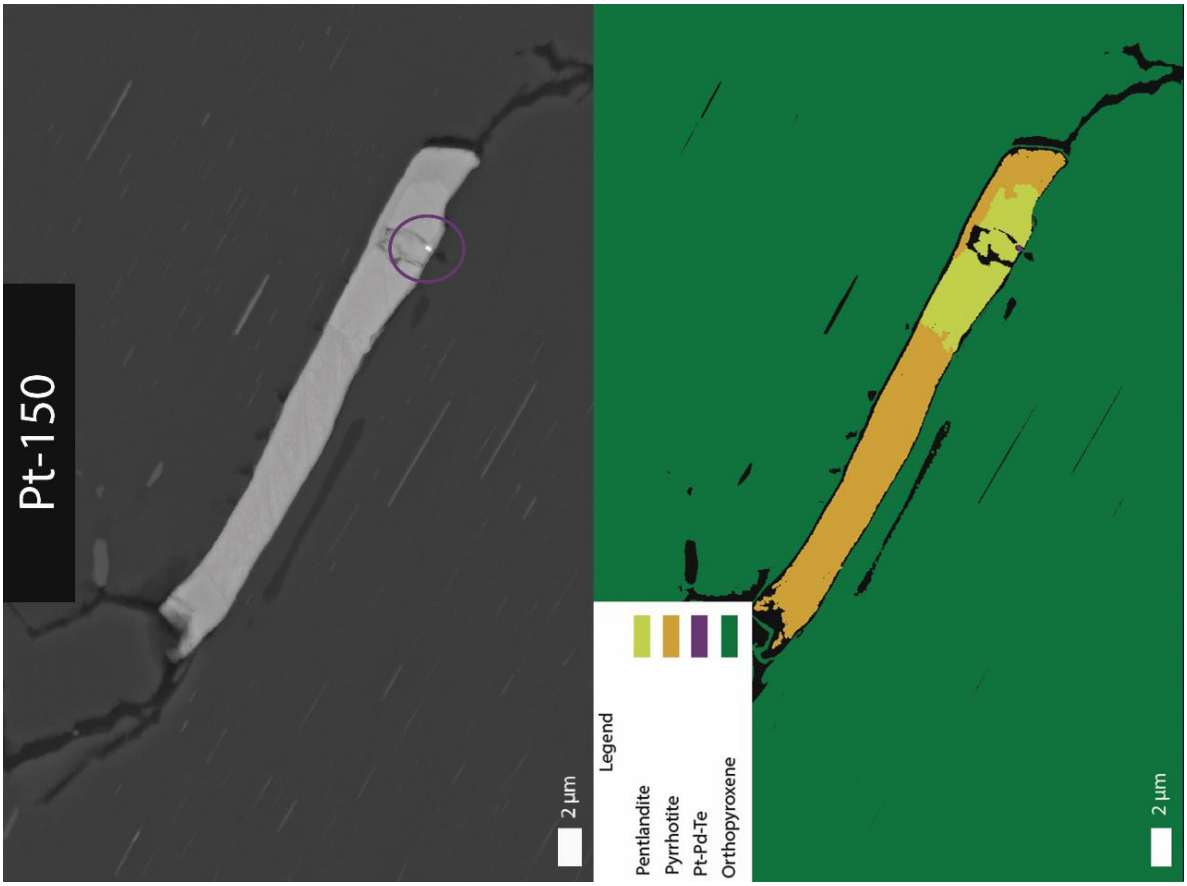

Figure B 27

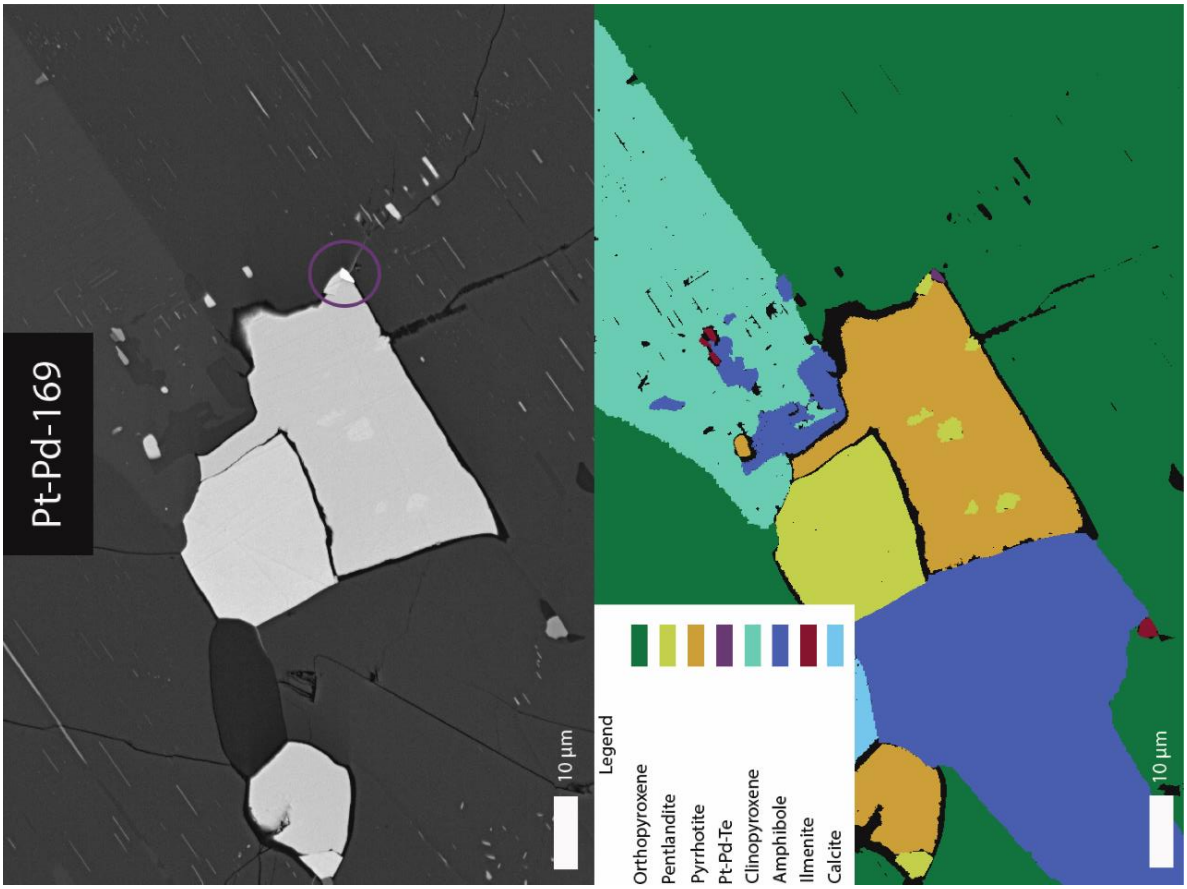

Figure B 28

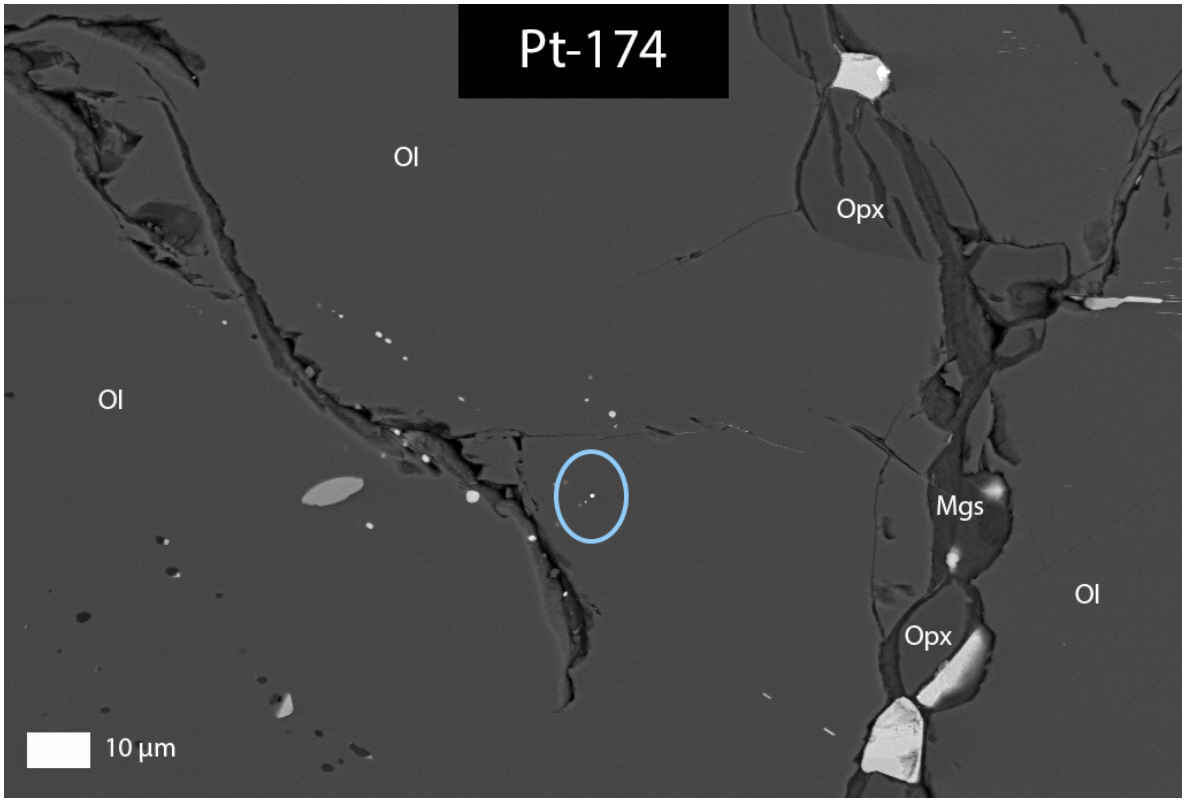

Figure B 29

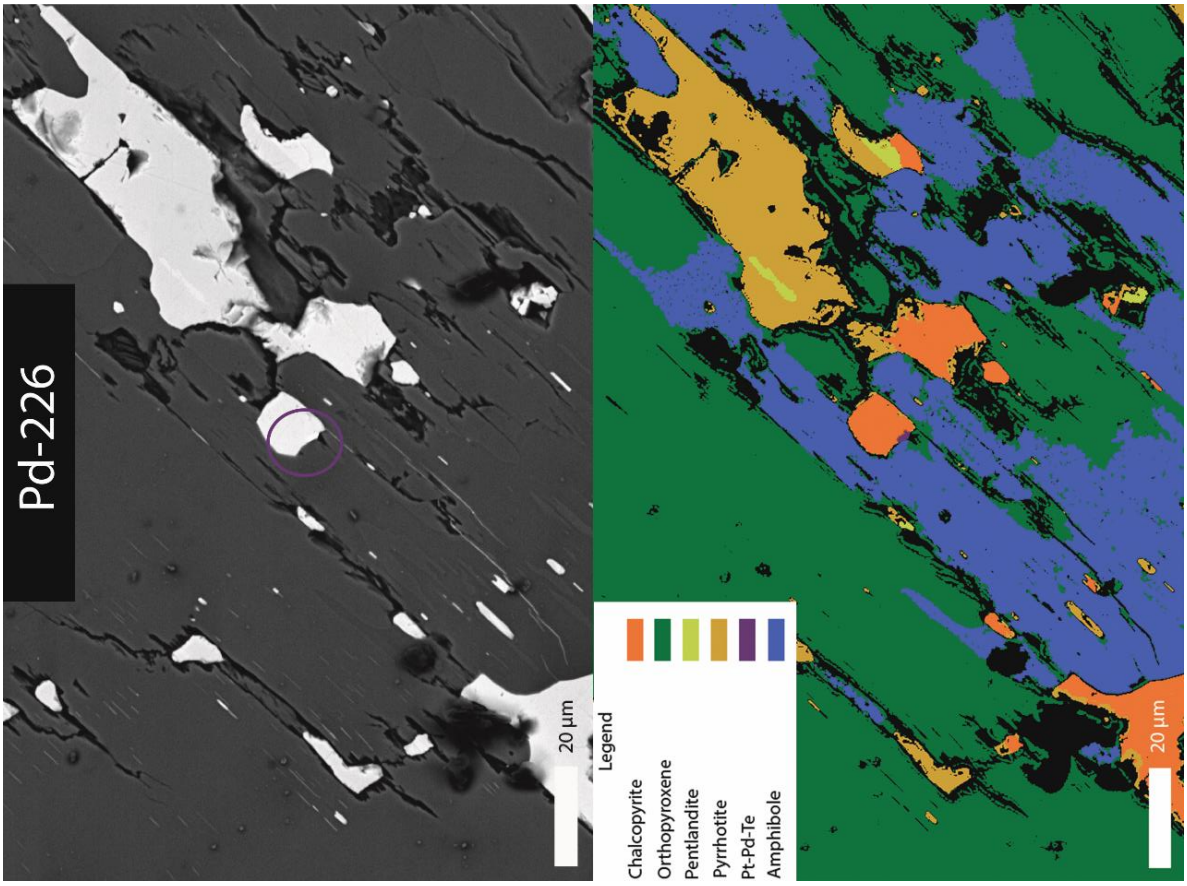

Figure B 30

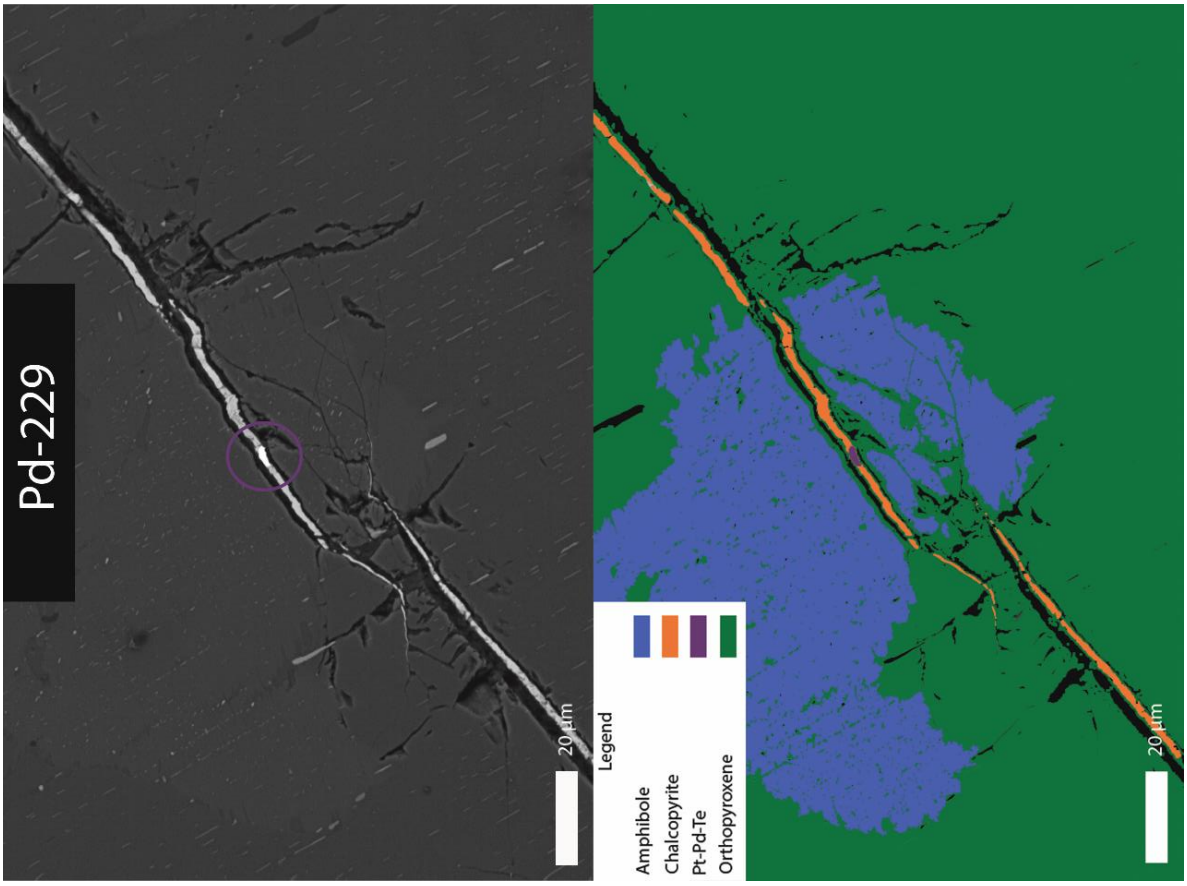

Figure B 31

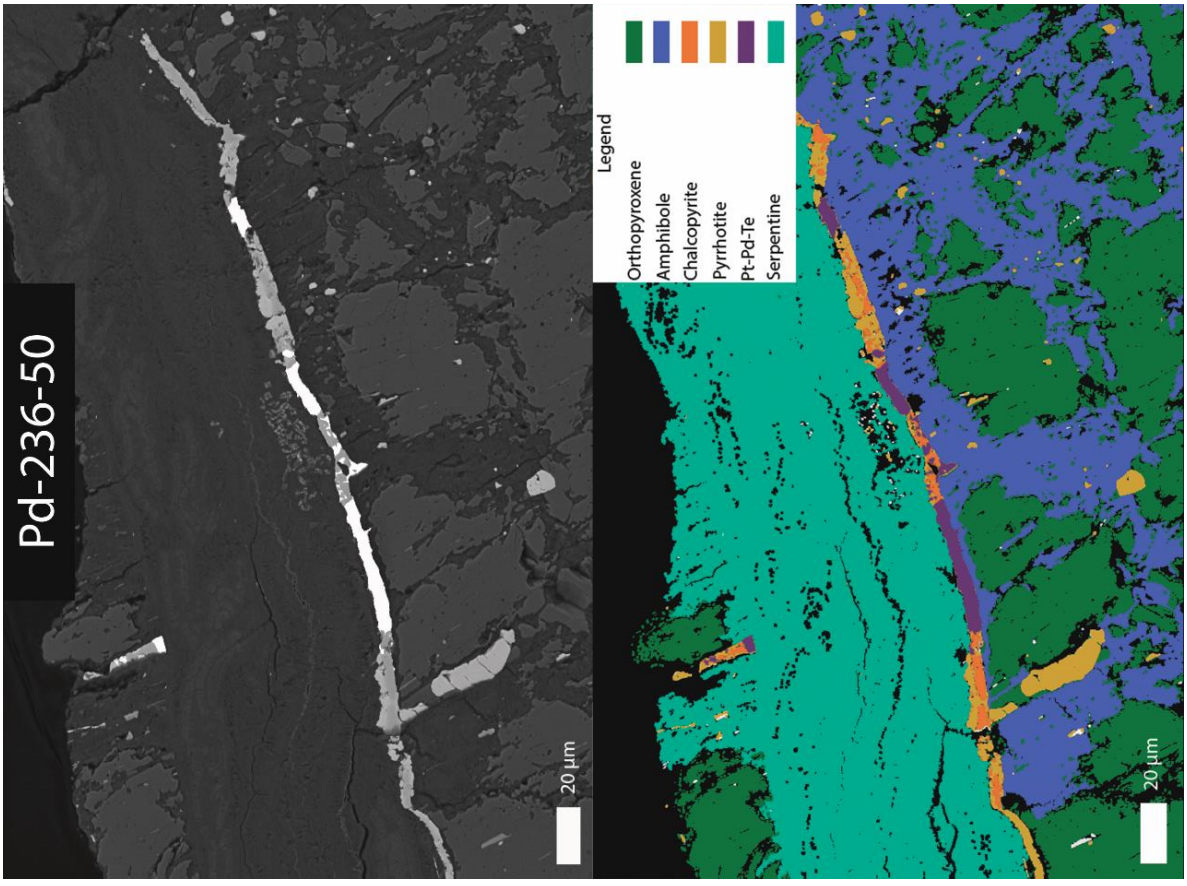

Figure B 32

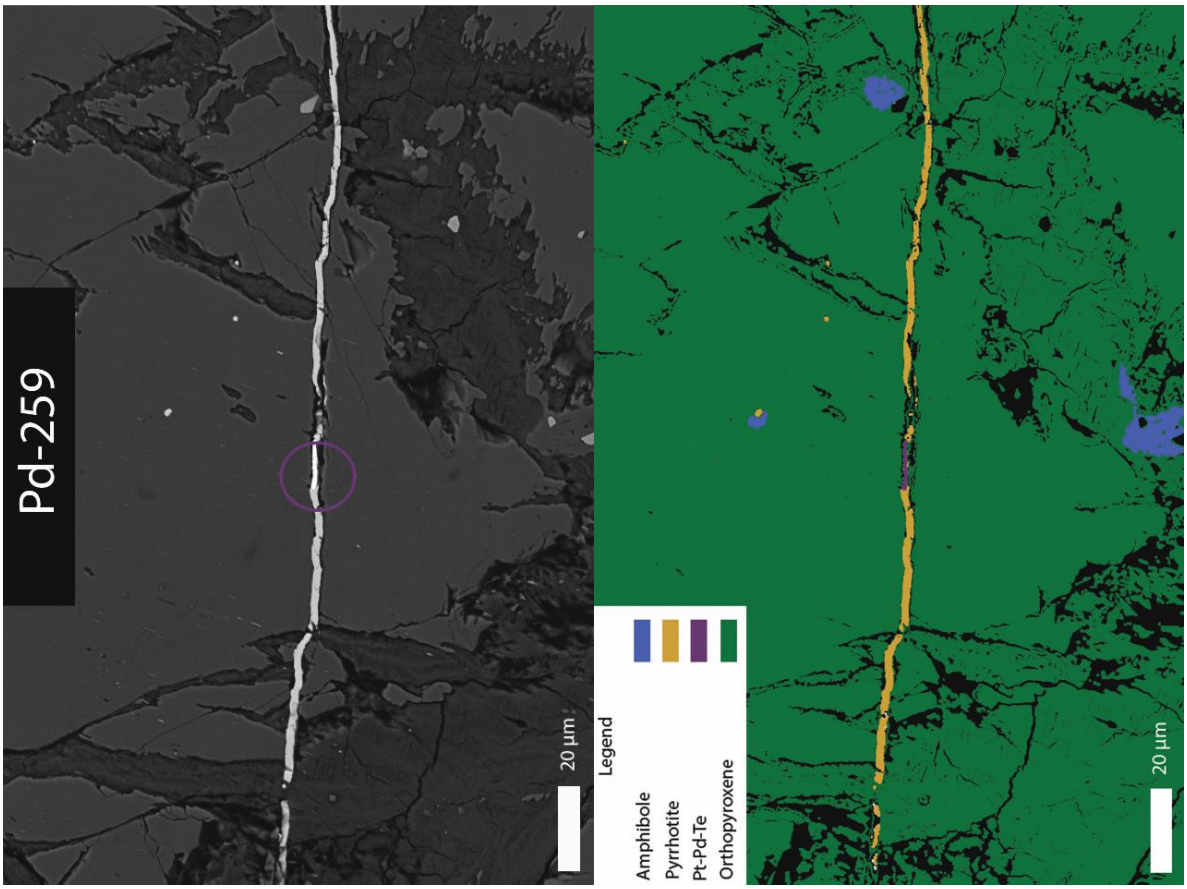

Figure B 23

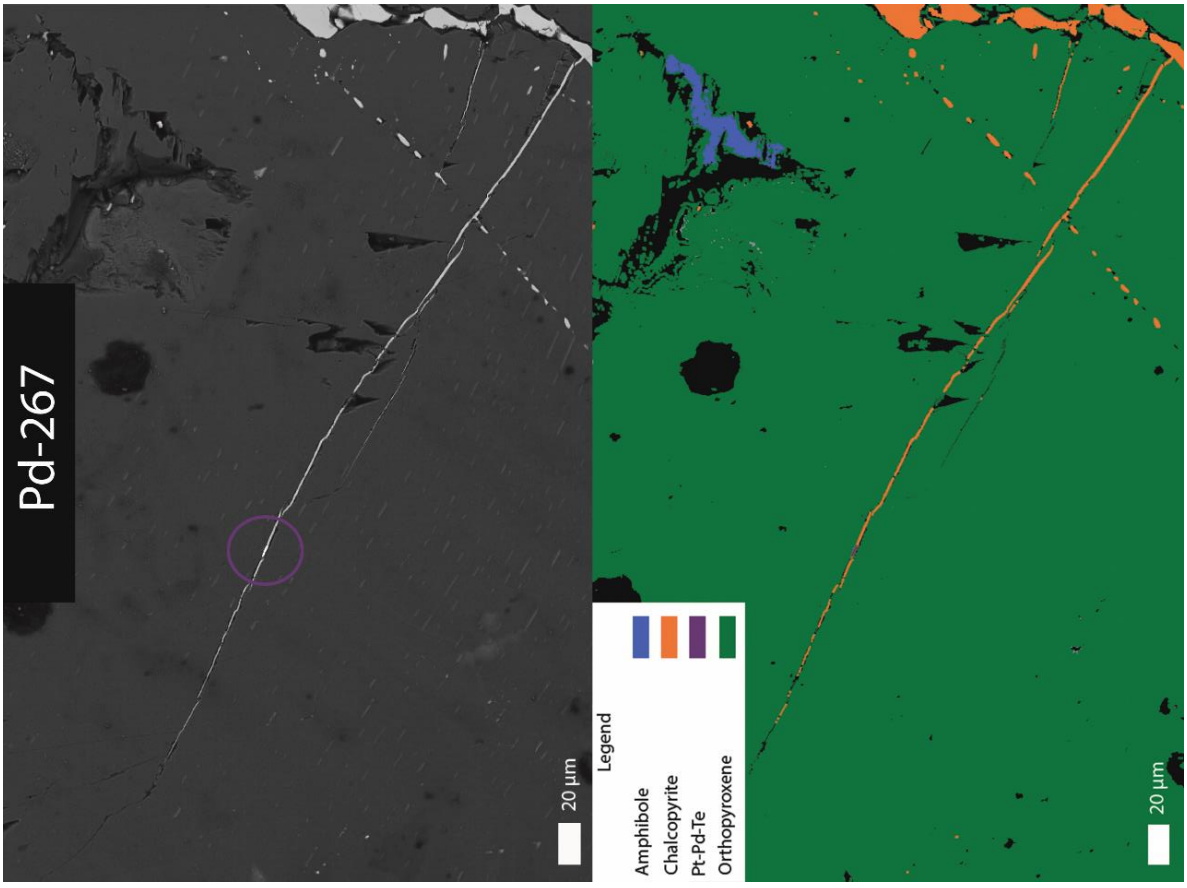

Figure B 34

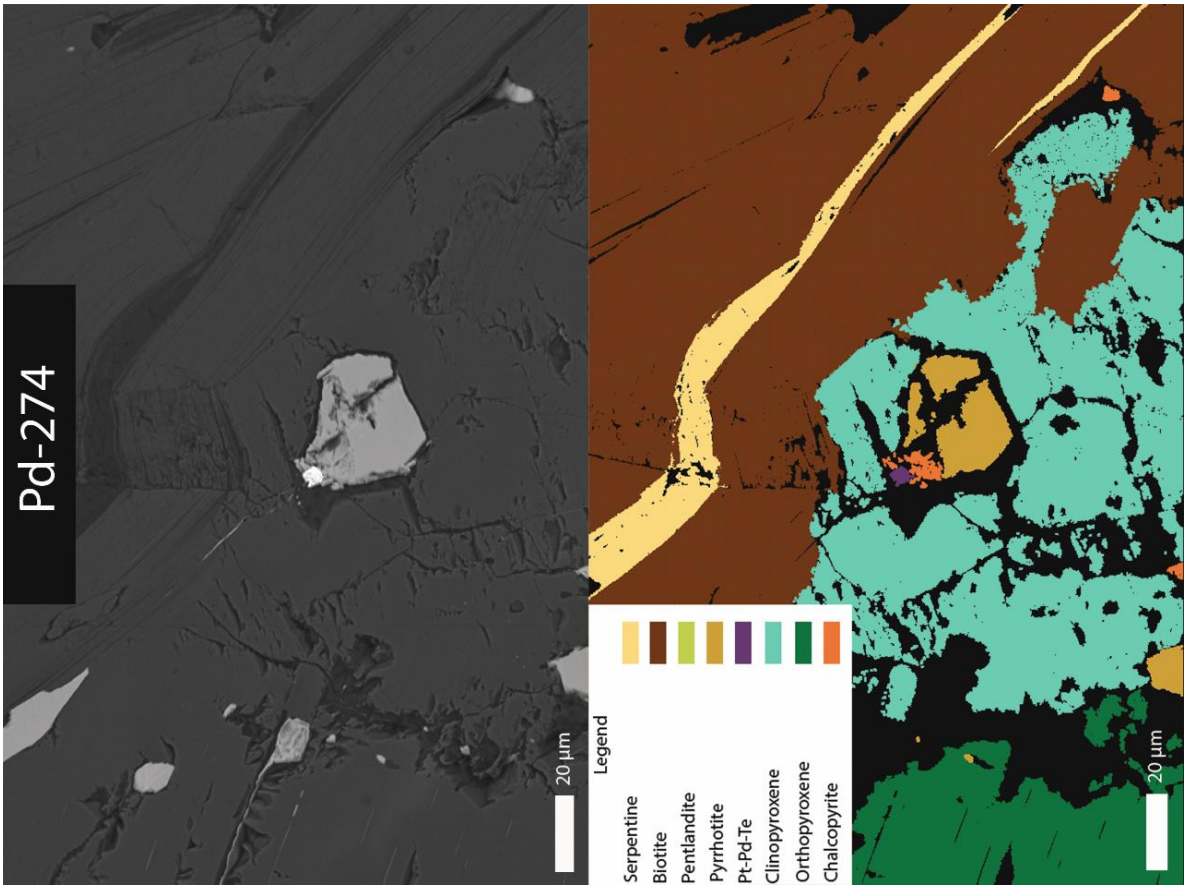

Figure B 35

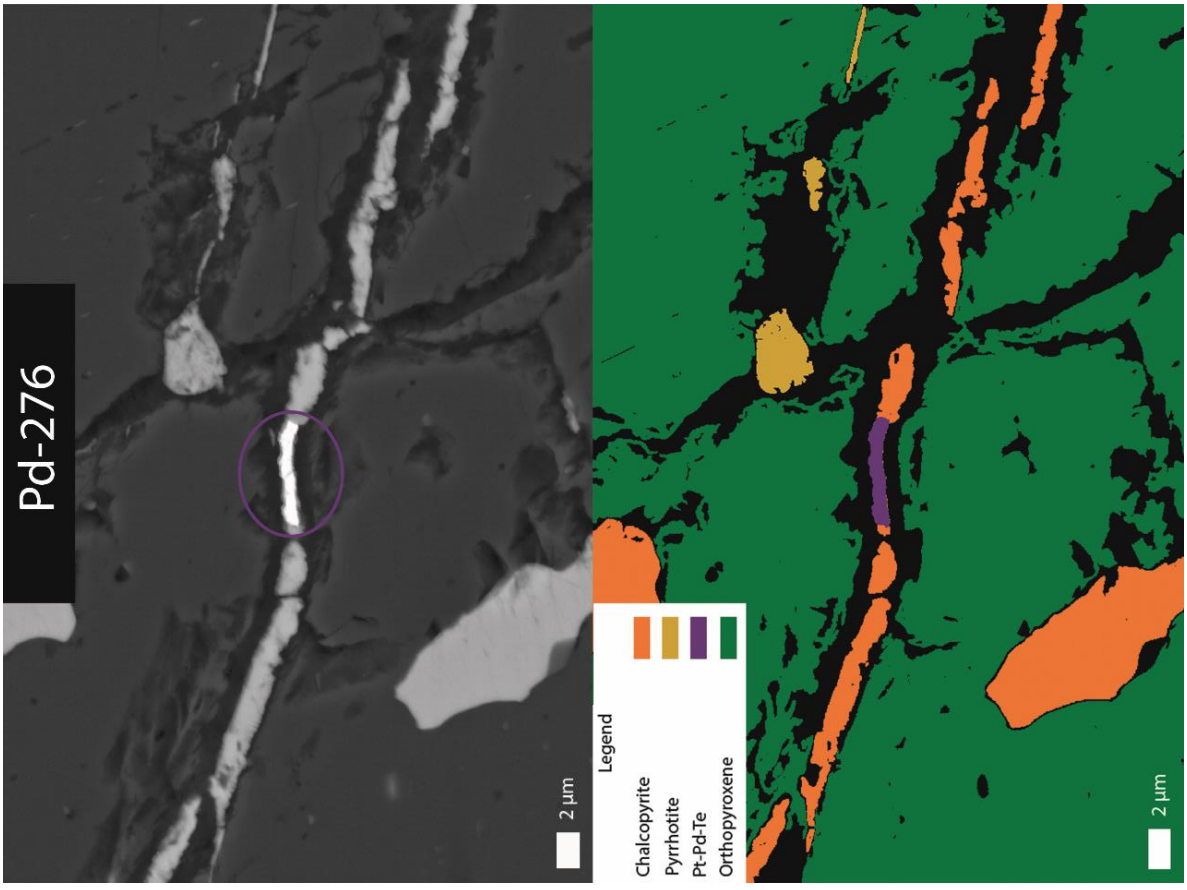

Figure B 36

Table B 3

Pd-Dominated								
Point	**Thin Section**	**L x W (µm)**	**Location (situated)**	**Host**	**Main Silicate**	**Notes**	**Link**	**EPMA**
235	110.45	6x1	In sulfide (inside)	Ccp	Amp-Cpx-Ol	In a Ccp portion of a larger sulfide. Totally enclosed by Ccp and needle shaped, oriented normal to Pn lamellae in Po.	Figure B 37	Yes
275	110.3	5x5	In sulfide (inside)	Pn	Opx	Located in the large sulfide at the end of the Pl vein. Enclosed by pentlandite in an environment of symplectic Py, Ccp and Pn.	Figure B 38	Yes
282	110.3	8x2	In sulfide (inside)	Po	Opx	a needle not following the Pn lammelas direction	Figure B 39	Yes
14	109.55	0.4-0.3	In sulfide (inside)	Ccp	Ol	In the outskirts of the “gold cluster”. Uncertain to what process this is connected to.	Figure B 40	No
20	109.55	0.5-0.2	In sulfide (inside)	Cbn	Amp-Opx-Mgs	A small observation of Pd-Sn alloy inside the main grain of Cbn in the area known as “gold cluster”	Figure B 41	No
Pd-Cluster (Figure B 42 & Figure B 43)								
4	110.45	3x2	In sulfide	Ccp	Opx-Amp	Rounded grain at the edge of the main Ccp	Figure B 44	No
10	110.45	3x1	In sulfide	Ccp	Opx-Amp	Needle shaped PGM, inside the main Ccp	Figure B 45	No

11	110.45	3x2	In sulfide	Ccp	Opx-Amp	Rounded grain inside the main Ccp	Figure B 46	No
30	110.45	3x3	In silicate	Ccp	Opx-Amp	Rounded grain that is in contact with sulfide, but not boosted by it. Located as a satellite grain outside of the main Pd hosting Ccp	Figure B 47	No
39	110.45	1x1	In sulfide	Ccp	Opx-Amp	Located at the edge of the main Ccp grain that hosts the larger PGM's	Figure B 48	No
41	110.45	20x5	In vein	Ccp-Po	Opx	Close to the Pd-cluster, but most likely not associated due to the presence of Pt. Located in a small and isolated vein	Figure B 49	No
43	110.45	3x1	In sulfide	Ccp	Opx-Amp	Rounded grain inside the main Ccp.	Figure B 54	No
47	110.45	1x1	In sulfide	Ccp	Opx-Amp	Rounded grain inside the main Ccp	Figure B 50	No
48	110.45	1x1	In sulfide	Ccp	Opx-Amp	Rounded grain inside the main Ccp	Figure B 50	No
49	110.45	1x0.5	In sulfide	Ccp	Opx-Amp	Needle shape grain located inside the main Ccp	Figure B 51	No
50	110.45	1x1	In sulfide	Ccp	Opx-Amp	Needle shape grain located at the edge of the main Ccp	Figure B 52	No
53	110.45	40x20	In sulfide	Ccp	Opx-Amp	Largest PGE grain located at the edge of the main Ccp	Figure B 53	Yes
54	110.45	5x5	In sulfide	Ccp	Opx-Amp	Rounded grain inside the main Ccp	Figure B 54	Yes

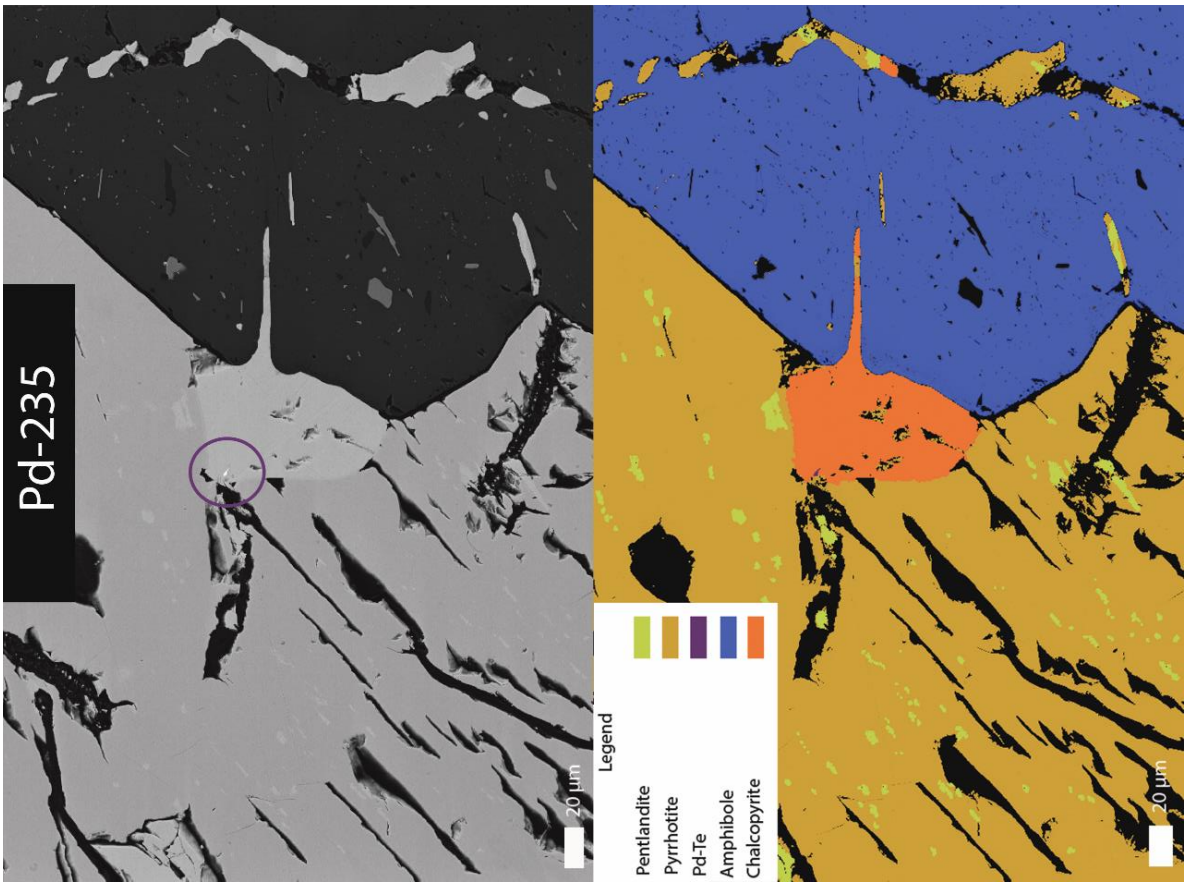

Figure B 37

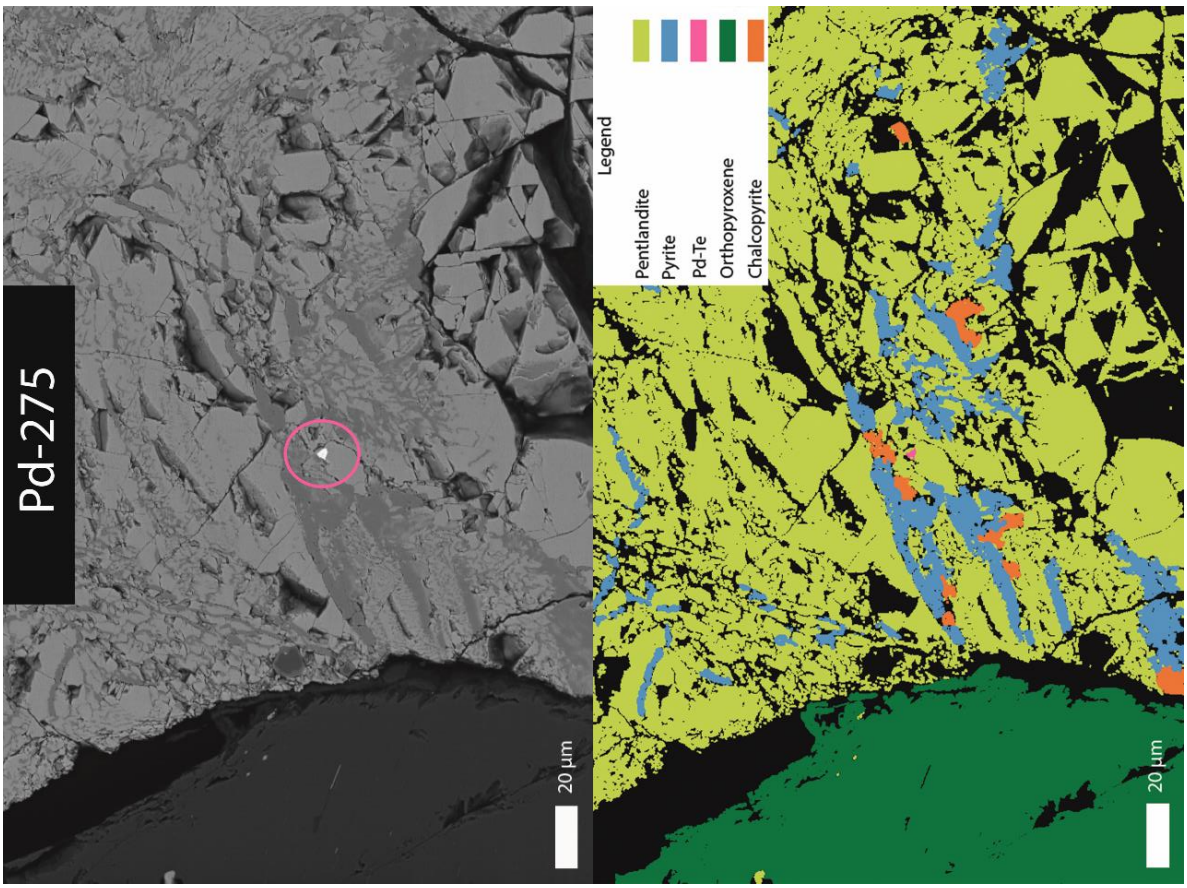

Figure B 38

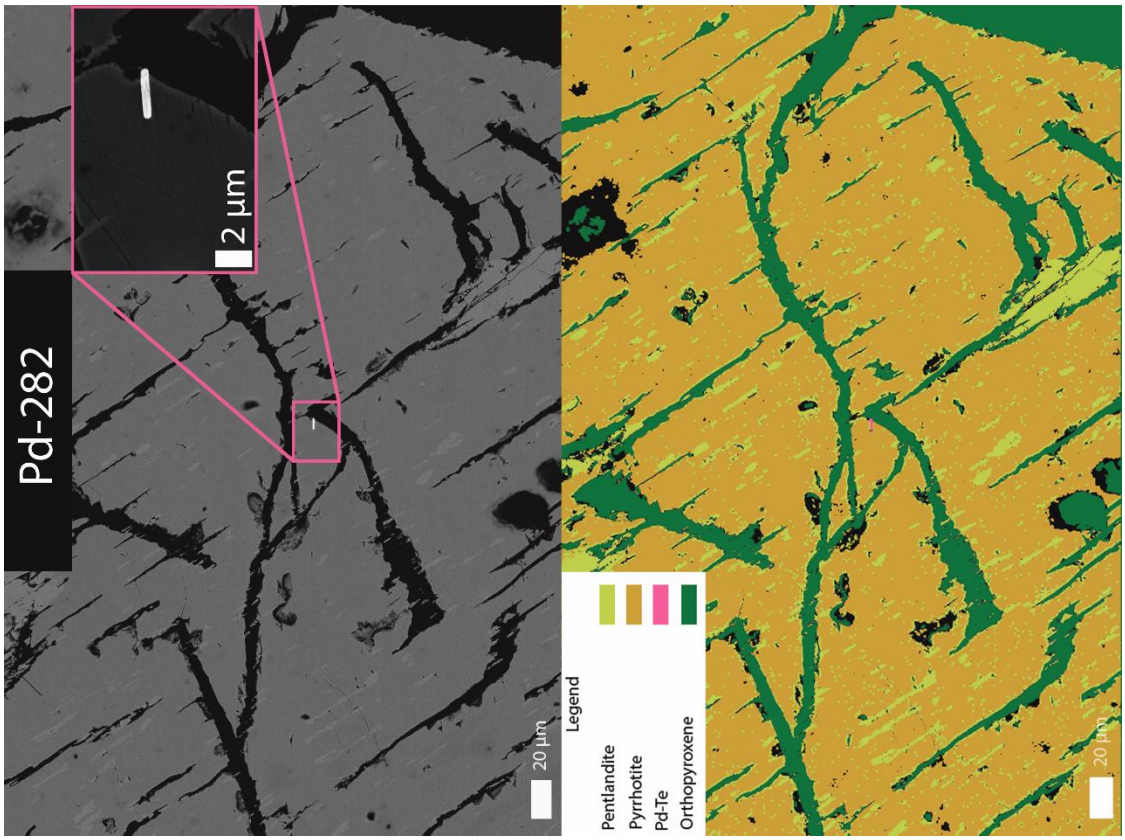

Figure B 39

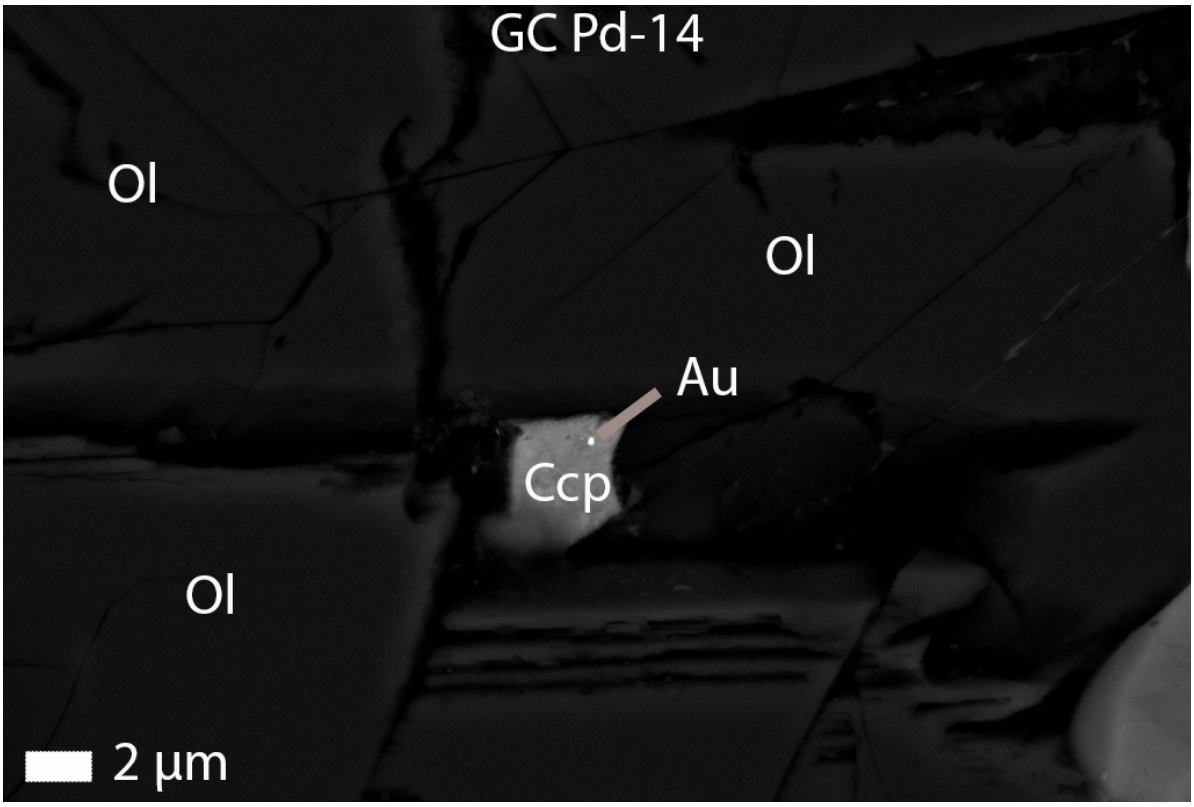

Figure B 40

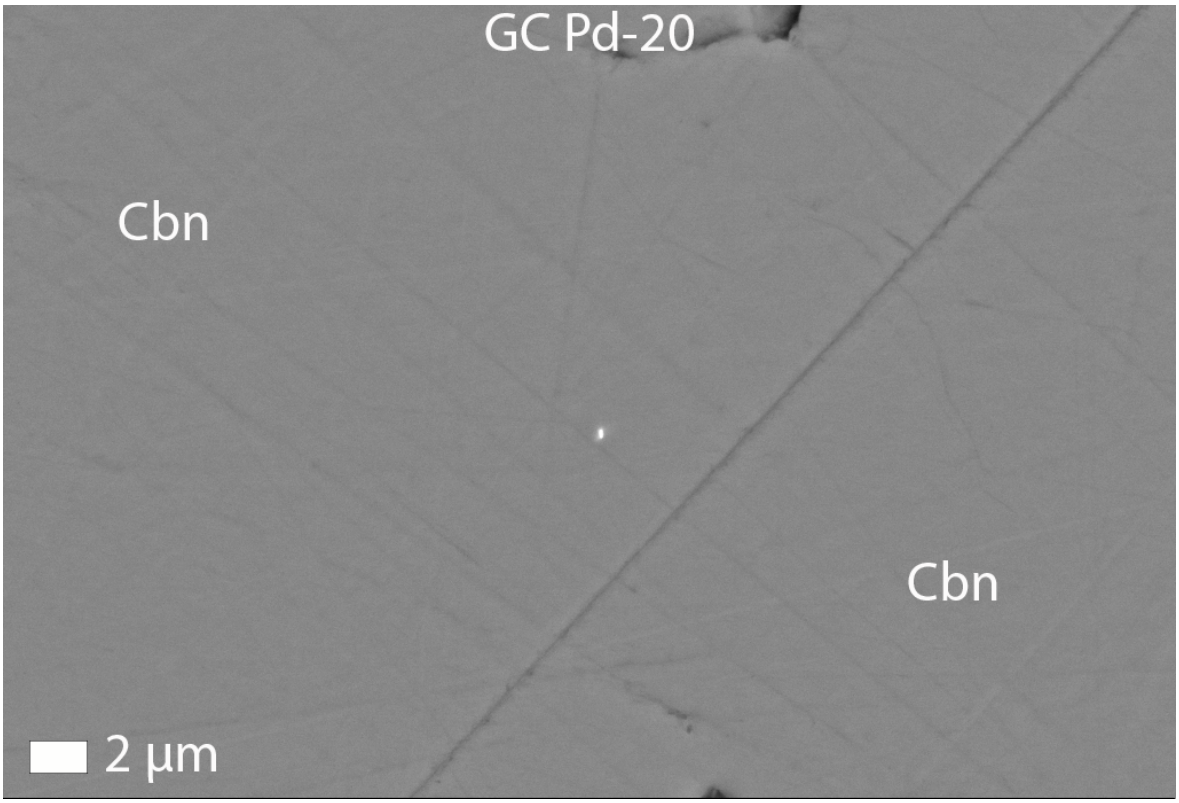

Figure B 41

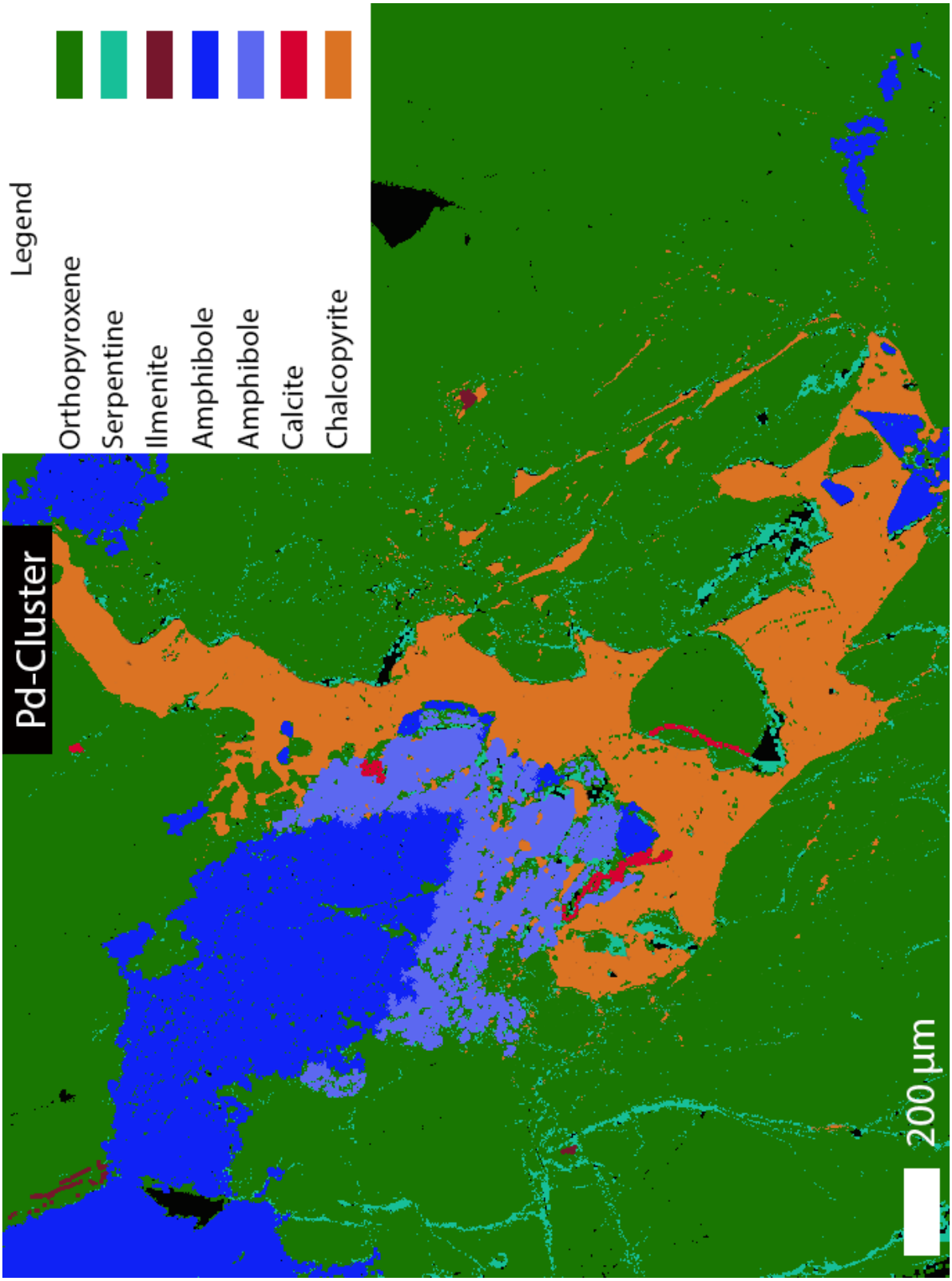
Pd-Cluster
Legend
Orthopyroxene
Serpentine
Ilmenite
Amphibole
Amphibole
Calcite
Chalcopyrite
200 µm

Figure B 42

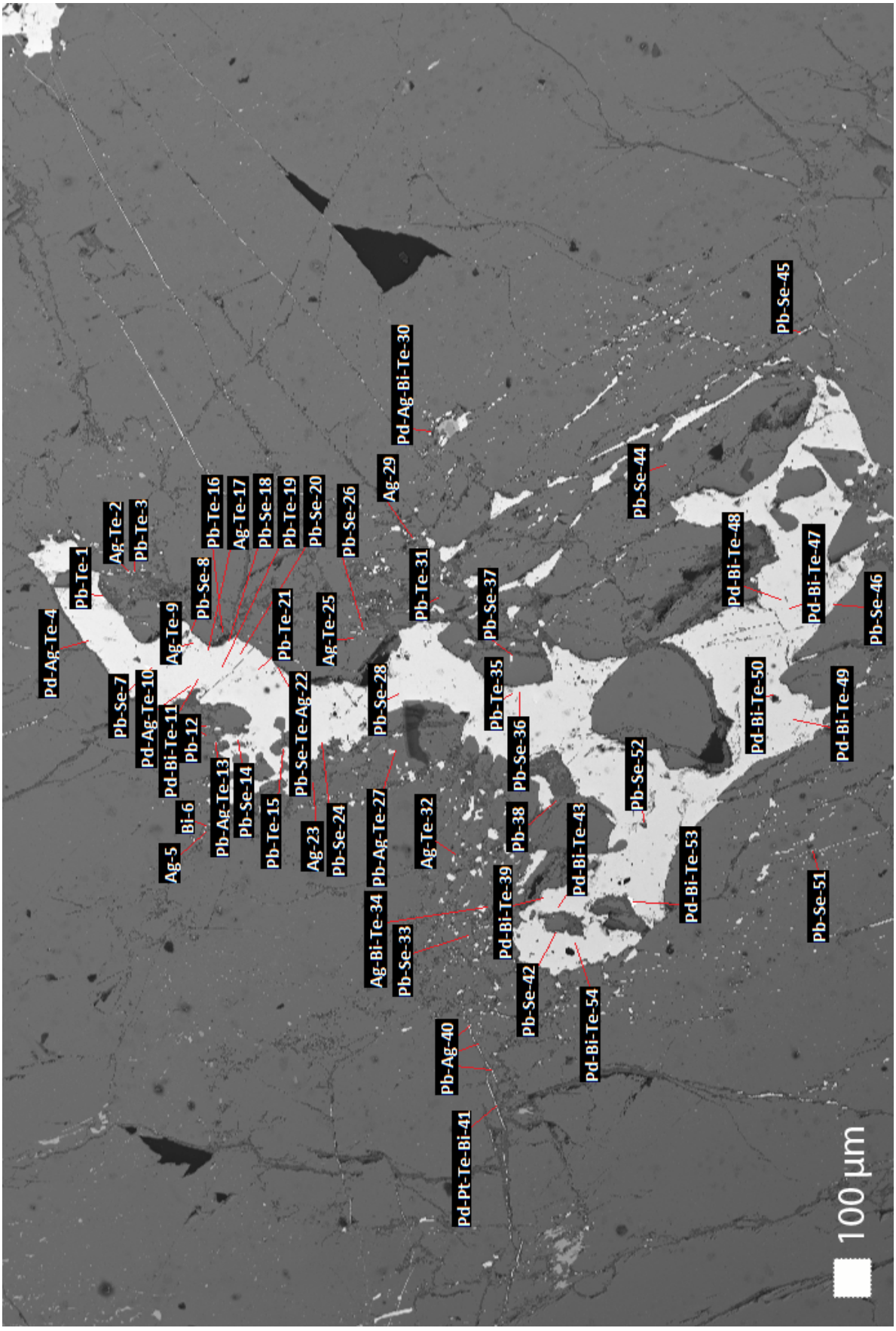
Pd-Ag-Te-4
Pb-Te-1
Ag-Te-2
Pb-Te-3
Pb-Se-7
Pd-Ag-Te-10
Pd-Bi-Te-11
Pb-12
Ag-Te-9
Pb-Se-8
Pb-Te-16
Ag-Te-17
Pb-Se-18
Pb-Te-19
Pb-Se-20
Pb-Te-21
Pb-Se-Te-Ag-22
Ag-23
Pb-Se-24
Ag-Te-25
Pb-Se-26
Pb-Ag-Te-27
Pb-Se-28
Ag-29
Pd-Ag-Bi-Te-30
Pb-Te-31
Ag-Te-32
Pb-Se-33
Ag-Bi-Te-34
Pb-Te-35
Pb-Se-36
Pb-Se-37
Pb-38
Pd-Bi-Te-39
Pb-Ag-40
Pd-Pt-Te-Bi-41
Pb-Se-42
Pd-Bi-Te-43
Pd-Bi-Te-54
Pb-Se-44
Pb-Se-45
Pd-Bi-Te-48
Pd-Bi-Te-47
Pb-Se-46
Pb-Se-52
Pd-Bi-Te-53
Pd-Bi-Te-50
Pd-Bi-Te-49
Pb-Se-51
Ag-5
Bi-6
Pb-Ag-Te-13
Pb-Se-14
Pb-Te-15
100 µm

Figure B 43

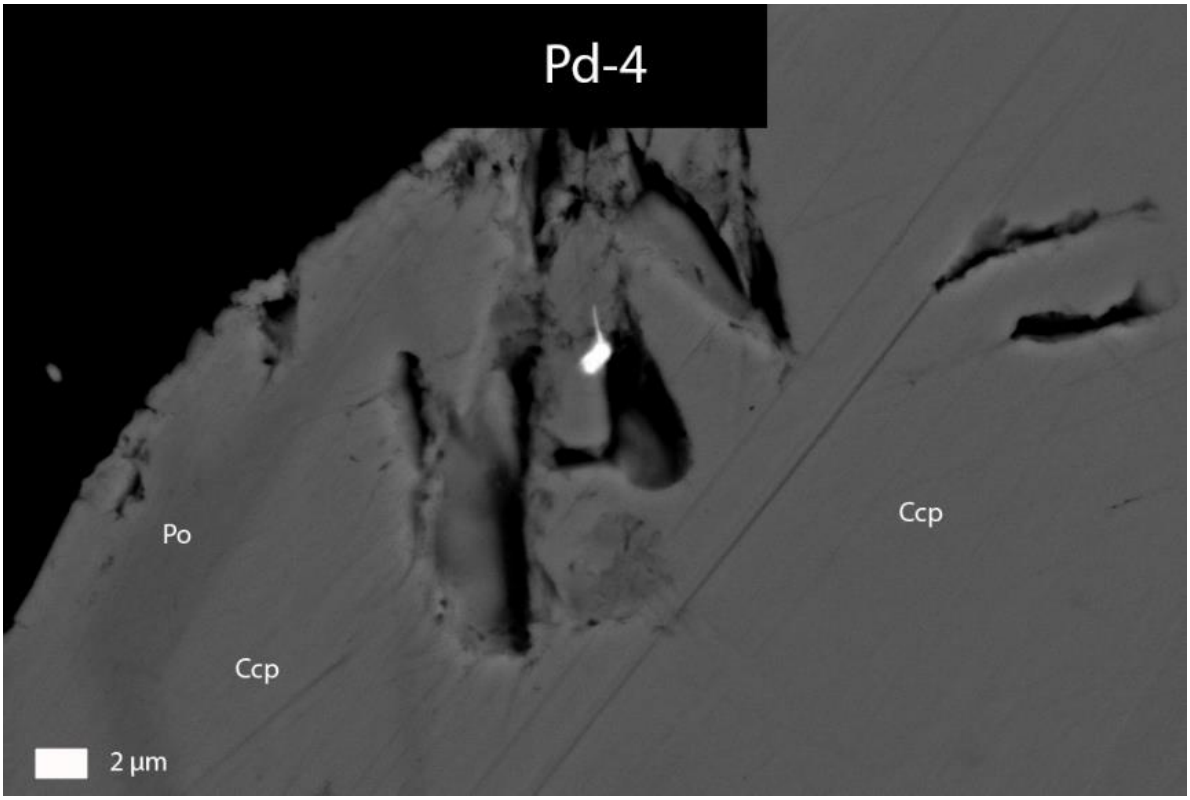

Figure B 44

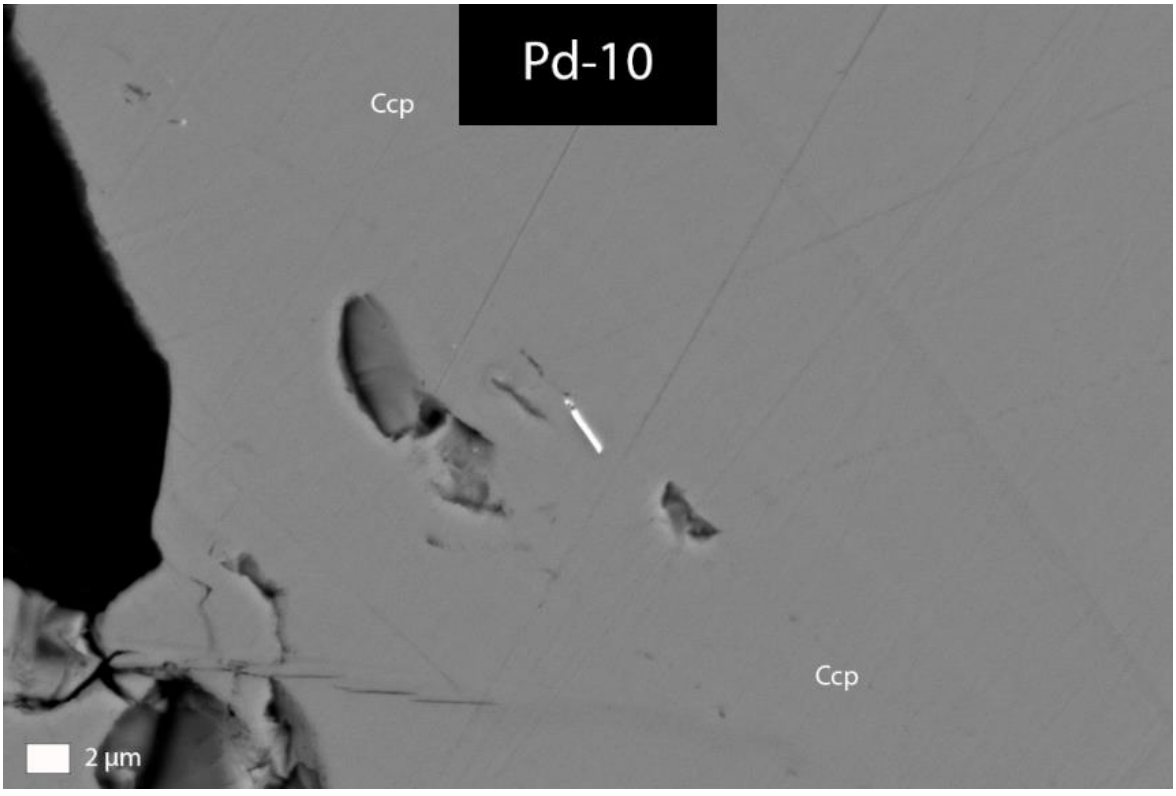

Figure B 45

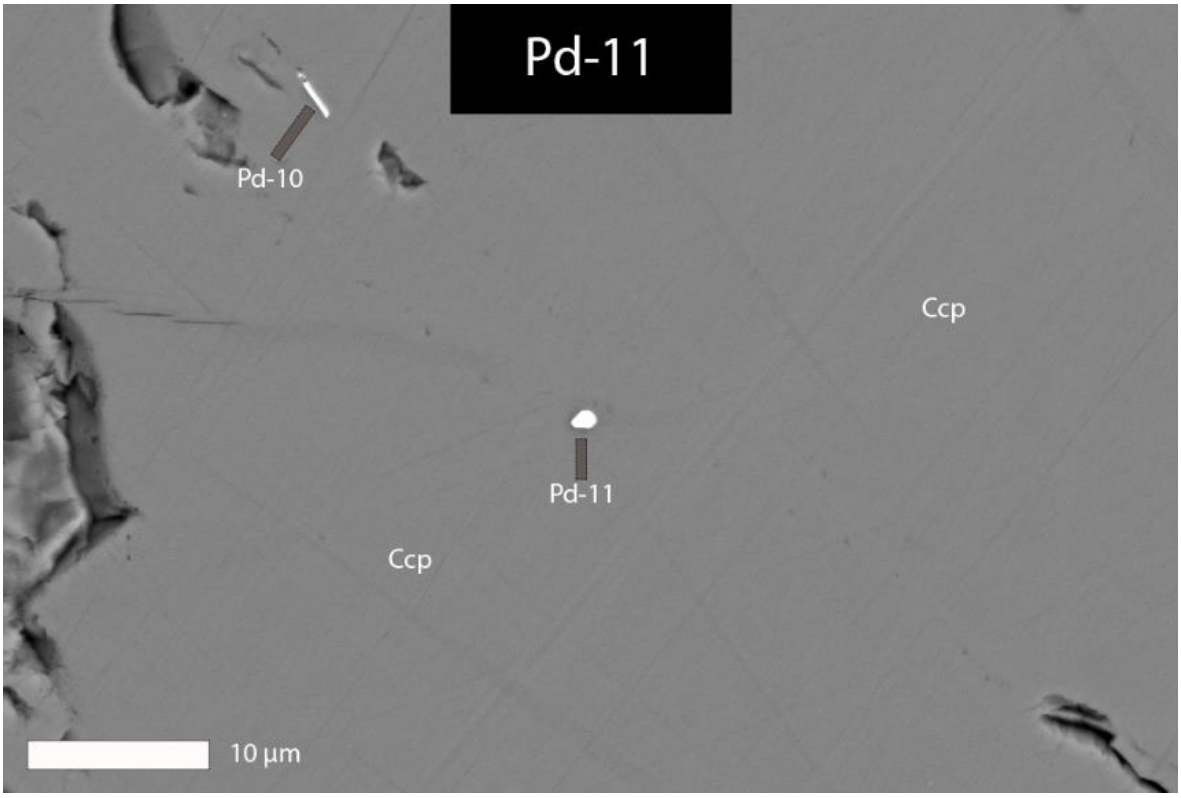

Figure B 46

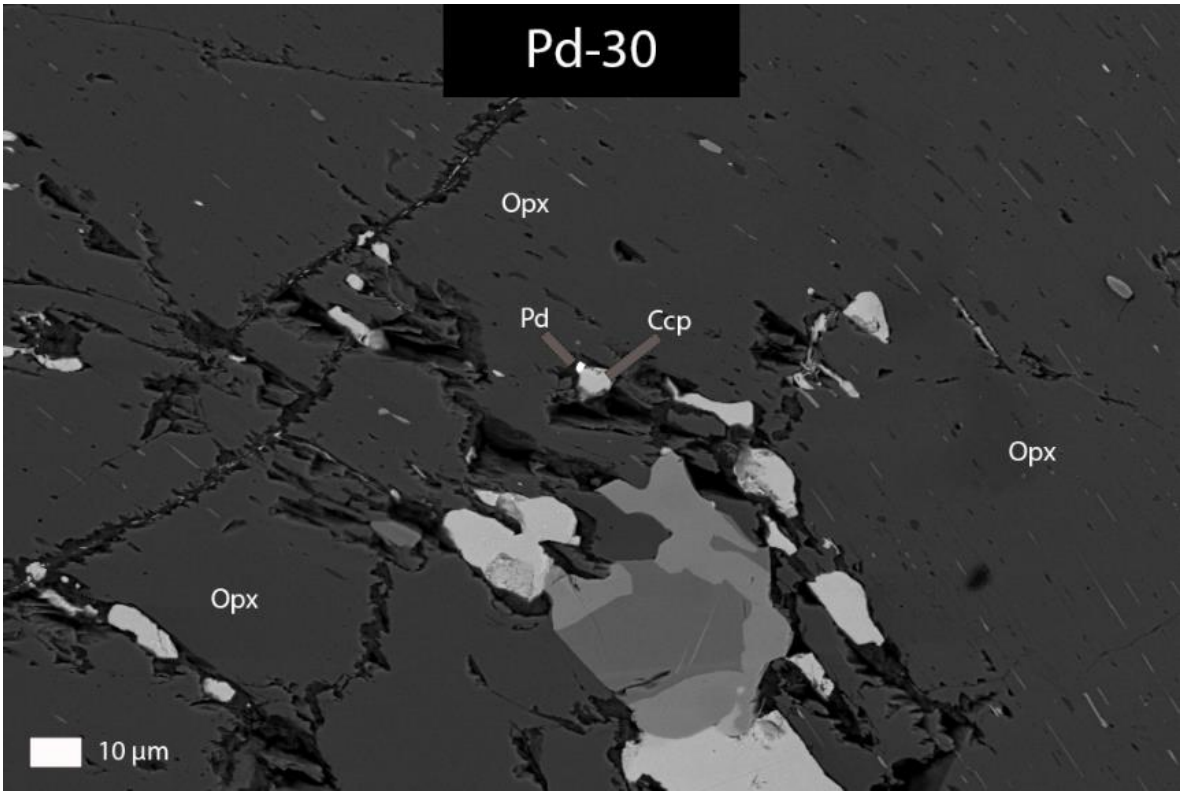

Figure B 47

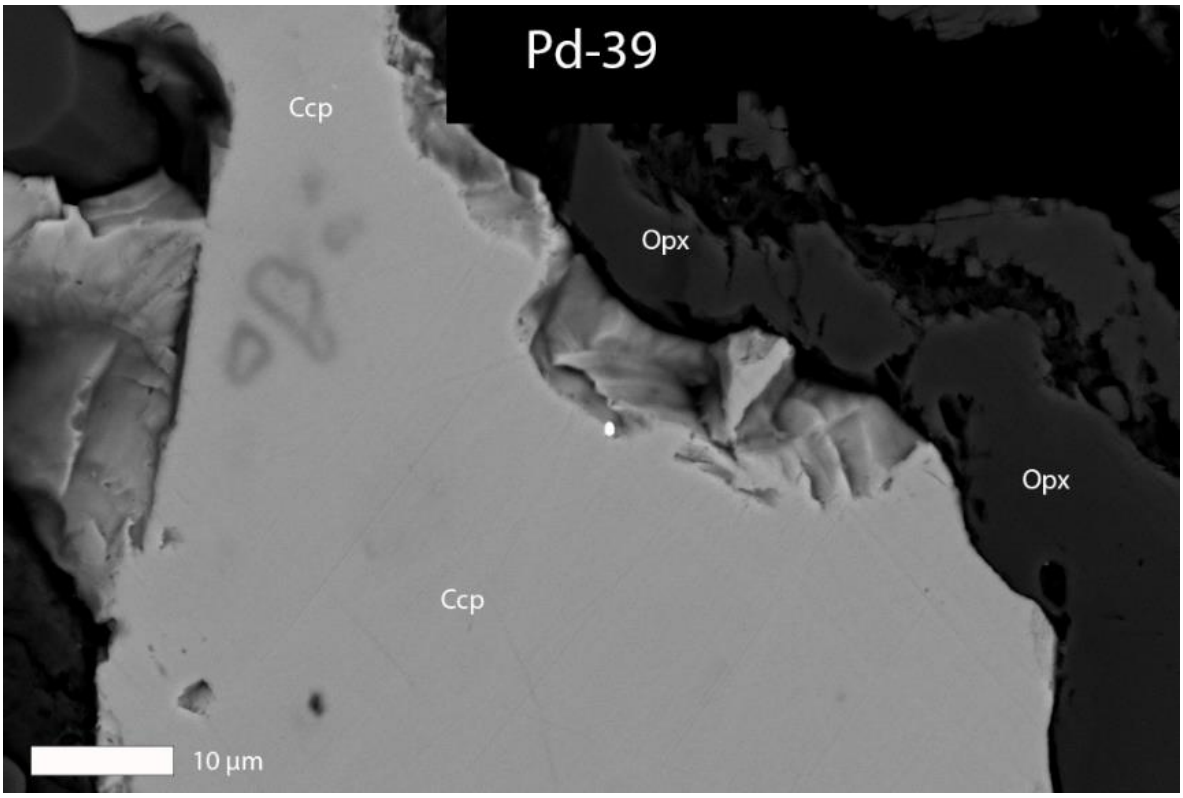

Figure B 48

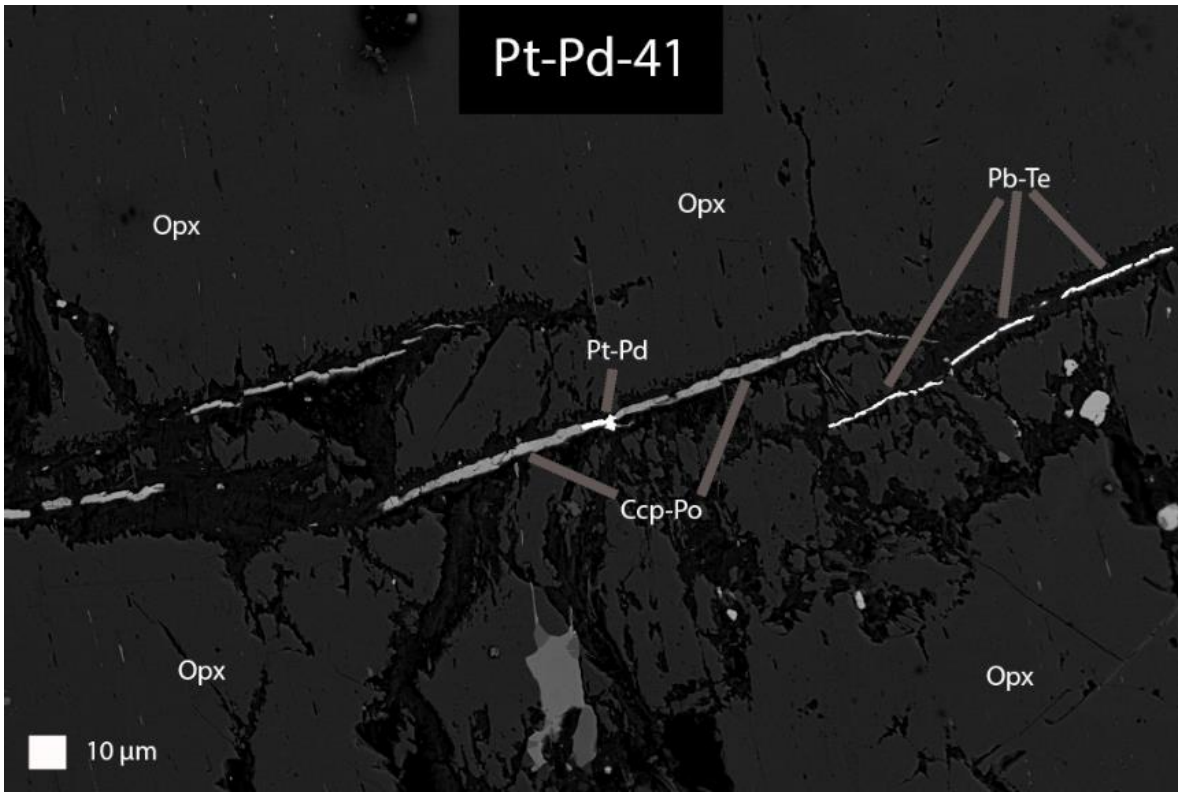

Figure B 49

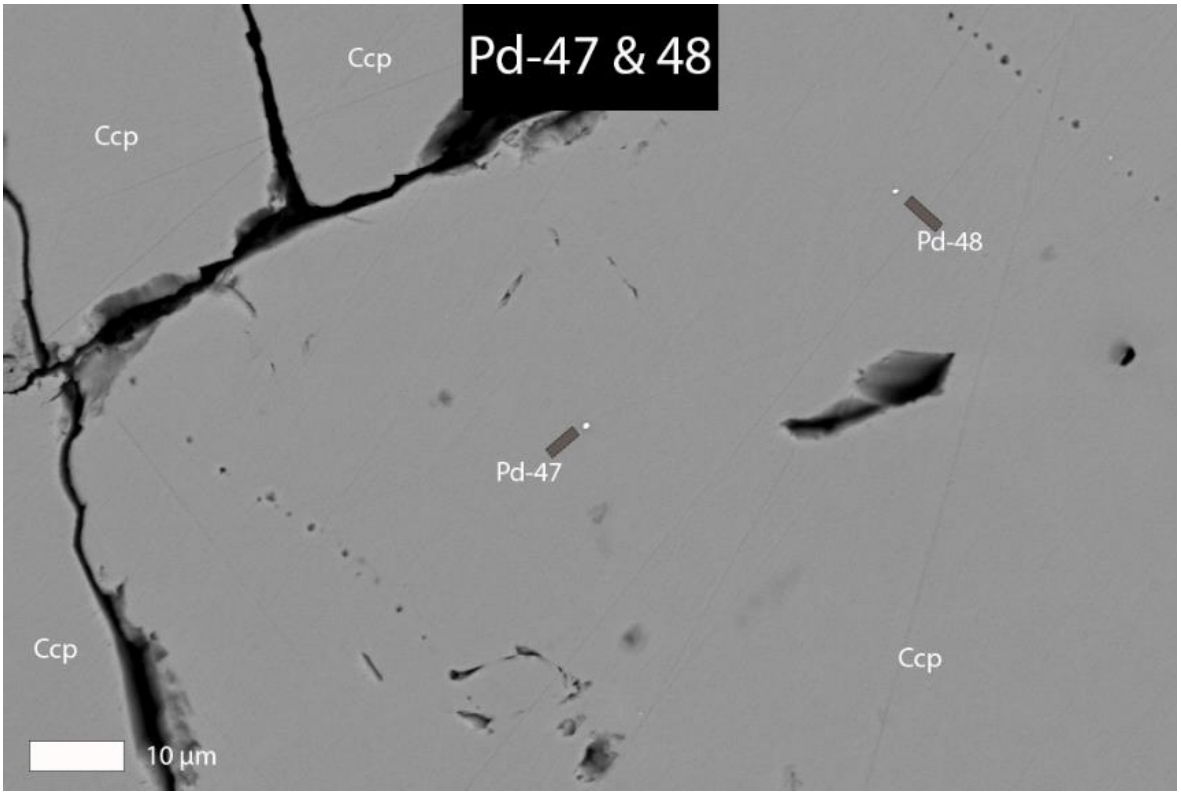

Figure B 50

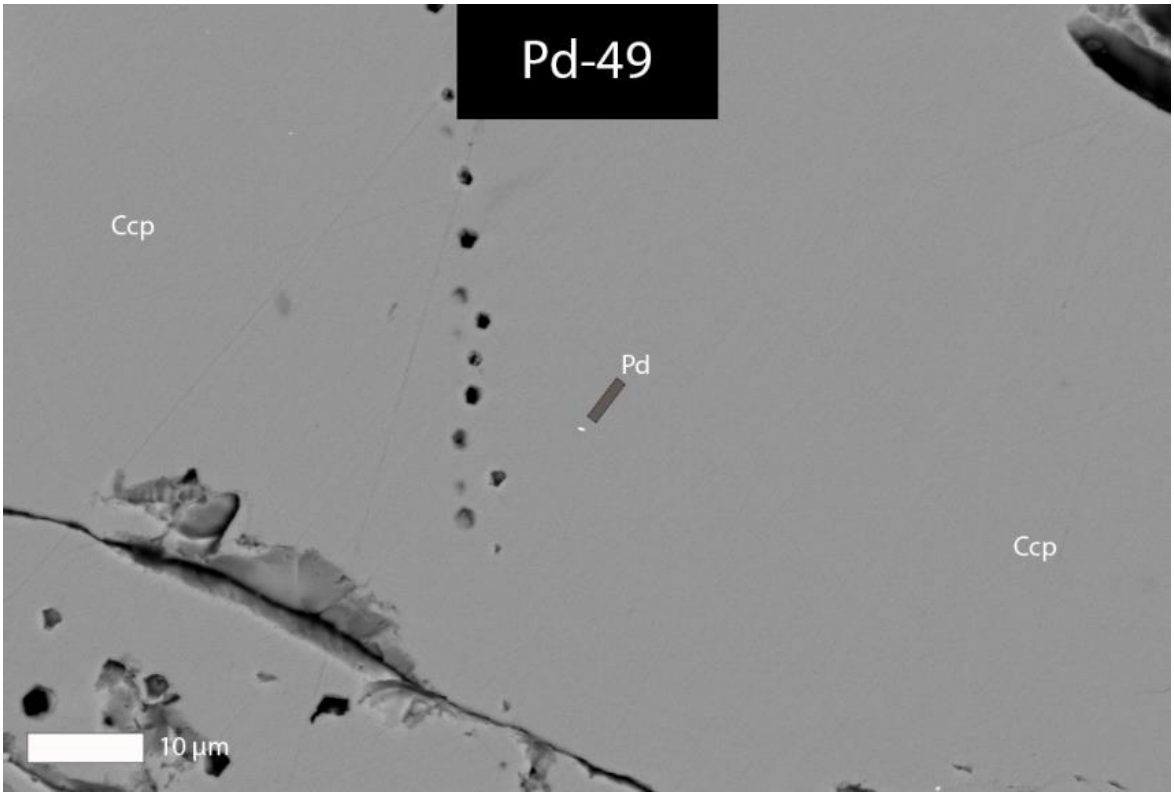

Figure B 51

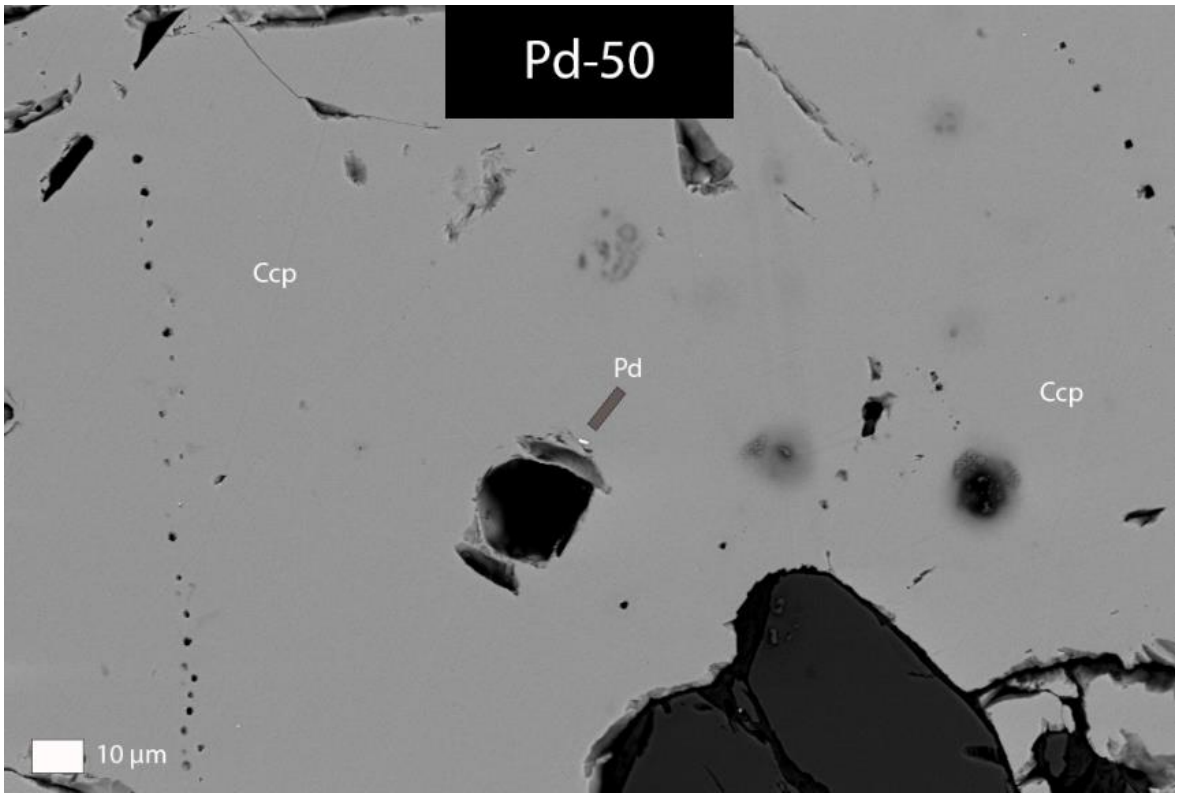

Figure B 52

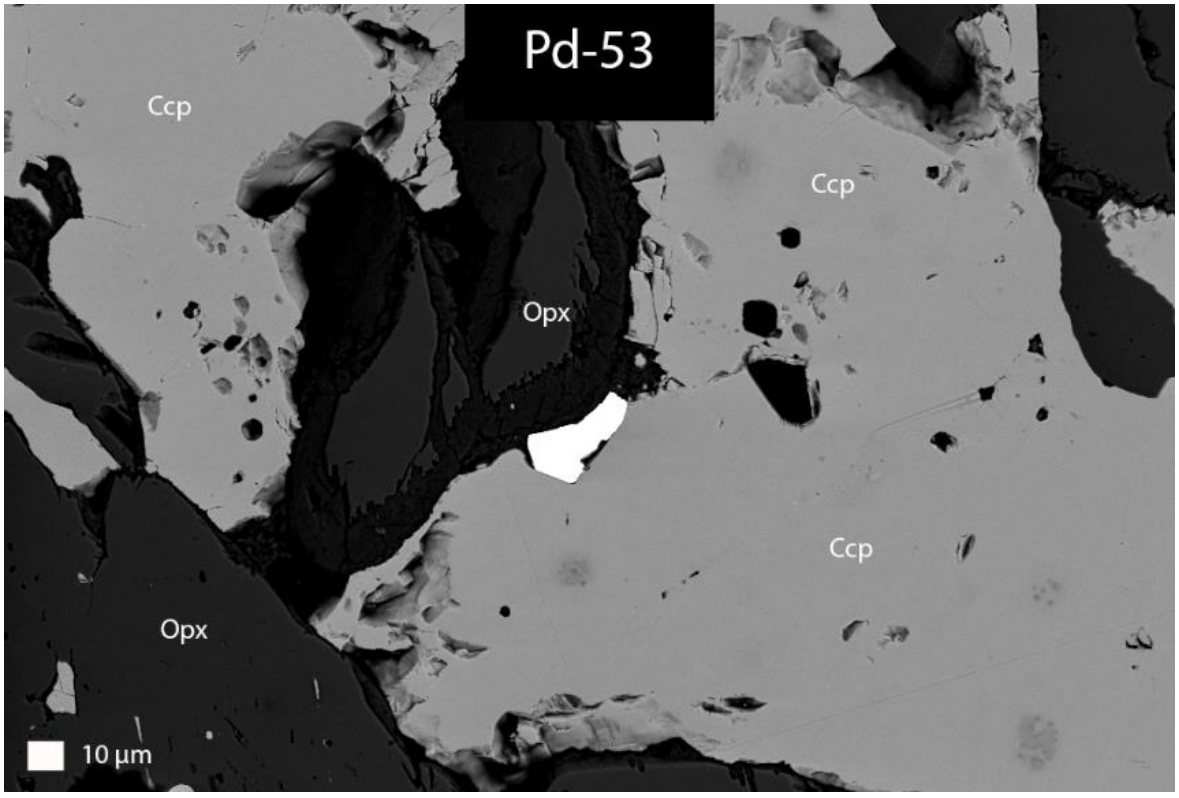

Figure B 53

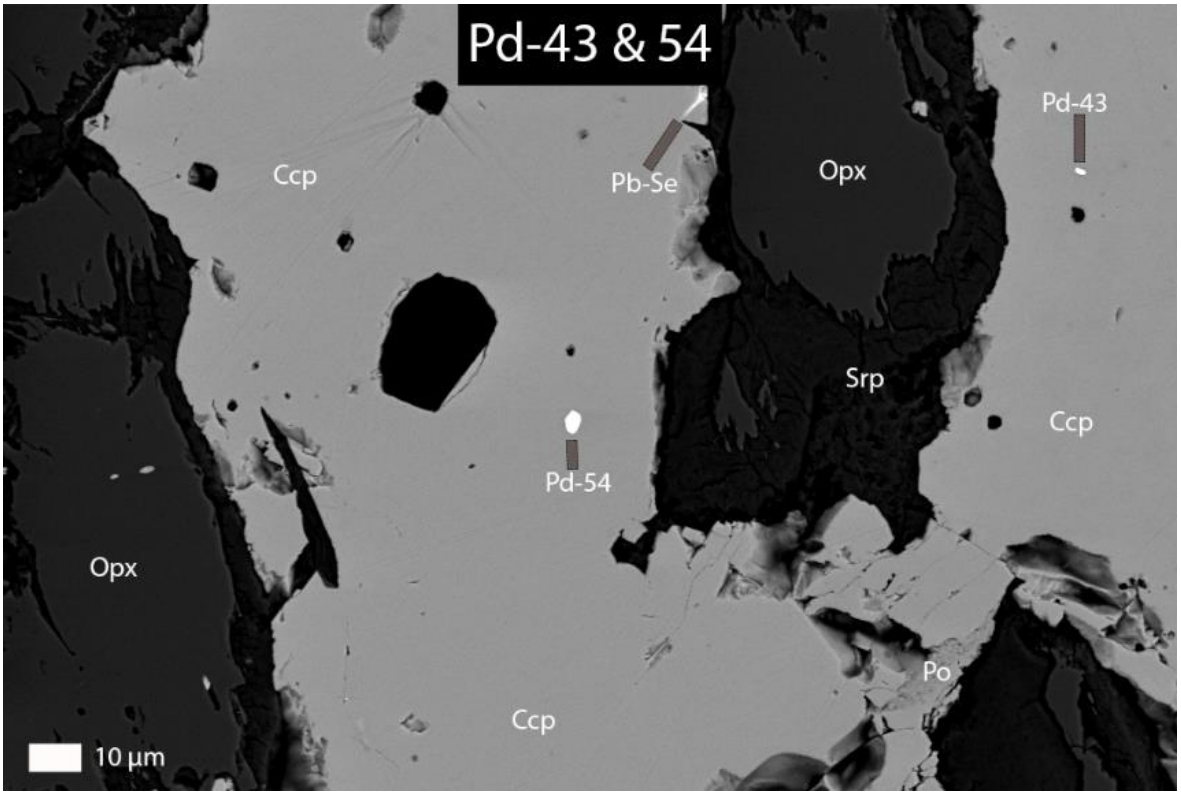

Figure B 54

Table B 4

Gold								
Point	**Thin Section**	**L x W (µm)**	**Location (situated)**	**Host**	**Main Silicate**	**Notes**	**Link**	**EPMA**
81	109.55	24x6	In silicate	Srp-Mgs	Ol	Needle shaped gold, emplaced in a Srp vein. No presence sulfides.	Figure B 55	Yes
92	109.55	2x2	In silicate	Ccp	Opx-Cpx	Forming on a line with sulfides as Ccp and Pn in a Opx with surrounding Cpx	Figure B56	Yes
132	109.4	1x1	In sulfide (inside)	Ccp	Opx-Ol	Mainly in Opx, but also in small parts in contact with Ol	Figure B 8	No
171	109.4	2x2	In silicate	Opx	Opx – Amp	In a bay created by Ccp and Po of a large sulfide. Uncertain if it is surface contamination.	Figure B57	No
277	110.3	1x1	In sulfide	Ccp	Opx	Situated in a Ccp in a Opx strongly enriched in Cpx lamellas.	Figure B58	Yes
Gold cluster (Figure B 59 & Figure B 60)								
1	109.55	0.5x0.5	In silicate	Amp	Amp-Bt	Completley round grain of pure gold located at the rim of the "gold cluster" carbonate cloth	Figure B 61	No
4	109.55	1x0.5	In sulfide (edge)	Ccp	Opx	Elongated grain with high content of Ag with Au. At the edge of a Ccp satellite grain of the larger Cbn.	Figure B 62	No
5	109.55	0.3x0.2	In sulfide (edge)	Ccp	Opx	Small grain at the edge of a satellite Ccp grain.	Figure B 62	No
8	109.55	0.1x0.1	In sulfide (edge)	Cct	Amp	Small grain at the edge of a satellite Cct grain	Figure B 63	No

9	109.55	0.1x0.1	In sulfide (edge)	Ccp	Mgs	Small grain at the edge of a satellite Ccp grain.	Figure B 64	No
10	109.55	0.1x0.1	In sulfide (edge)	Ccp	Amp	Small grain at the edge of a satellite Ccp grain.	Figure B 65	No
12	109.55	0.3x0.2	In sulfide (edge)	Ccp	Opx	Small grain at the edge of a satellite Ccp grain	Figure B 66	No
13	109.55	1x1	In sulfide (edge)	Ccp-Cct	Opx	Small grain at the edge of a satellite Ccp grain	Figure B 67	No
15	109.55	0.3x0.2	In silicate	Opx	Opx	Grain of pure gold located in Opx	Figure B 68	No
17	109.55	0.1x0.1	In sulfide (edge)	Ccp-Cct	Opx	Small grain at the edge of a satellite Ccp grain	Figure B 69	No
18	109.55	1x1	In sulfide (edge)	Ccp	Opx-Spl	Small grain at the edge of a satellite Ccp grain	Figure B 70	No
22	109.55	0.1x0.1	In sulfide (edge)	Ccp	Amp	Small grain at the edge of a satellite Ccp grain	Figure B 71	No
23	109.55	0.3x0.2	In sulfide (edge)	Ccp	Opx	Small grain at the edge of a satellite Ccp grain	Figure B 72	No
24	109.55	3x2	In sulfide (edge)	Ccp	Amp	Small grain at the edge of a satellite Ccp grain	Figure B 73	Yes
26	109.55	1x0.4	In sulfide (edge)	Ccp	Amp	Small grain at the edge of a satellite Ccp grain	Figure B 74	No
27	109.55	1x1	In sulfide (edge)	Ccp	Amp	Small grain at the edge of a satellite Ccp grain	Figure B 75	No
28	109.55	0.3x0.2	In sulfide (edge)	Ccp	Amp	Small grain at the edge of a satellite Ccp grain	Figure B 76	No

Ruthenium

Point	**Thin Section**	**L x W (µm)**	**Location (situated)**	**Host**	**Main Silicate**	**Notes**	**Link**	**EPMA**
144	109.40	2x2	In sulfide (inside)	Po	Opx-Cpx	Rounded grain of Ru-Os, occurring in pyrrhotite. The only occurrence.	Figure B 77	Yes

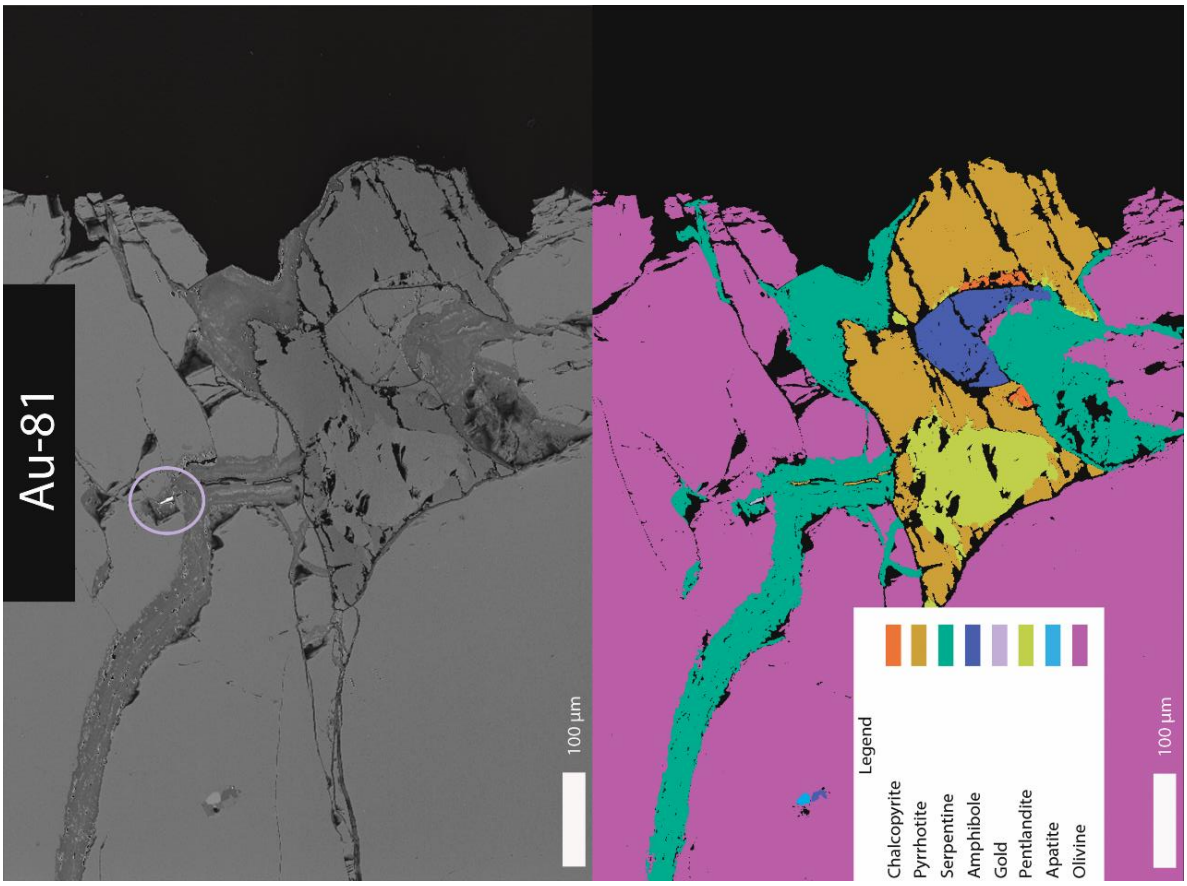

Figure B 55

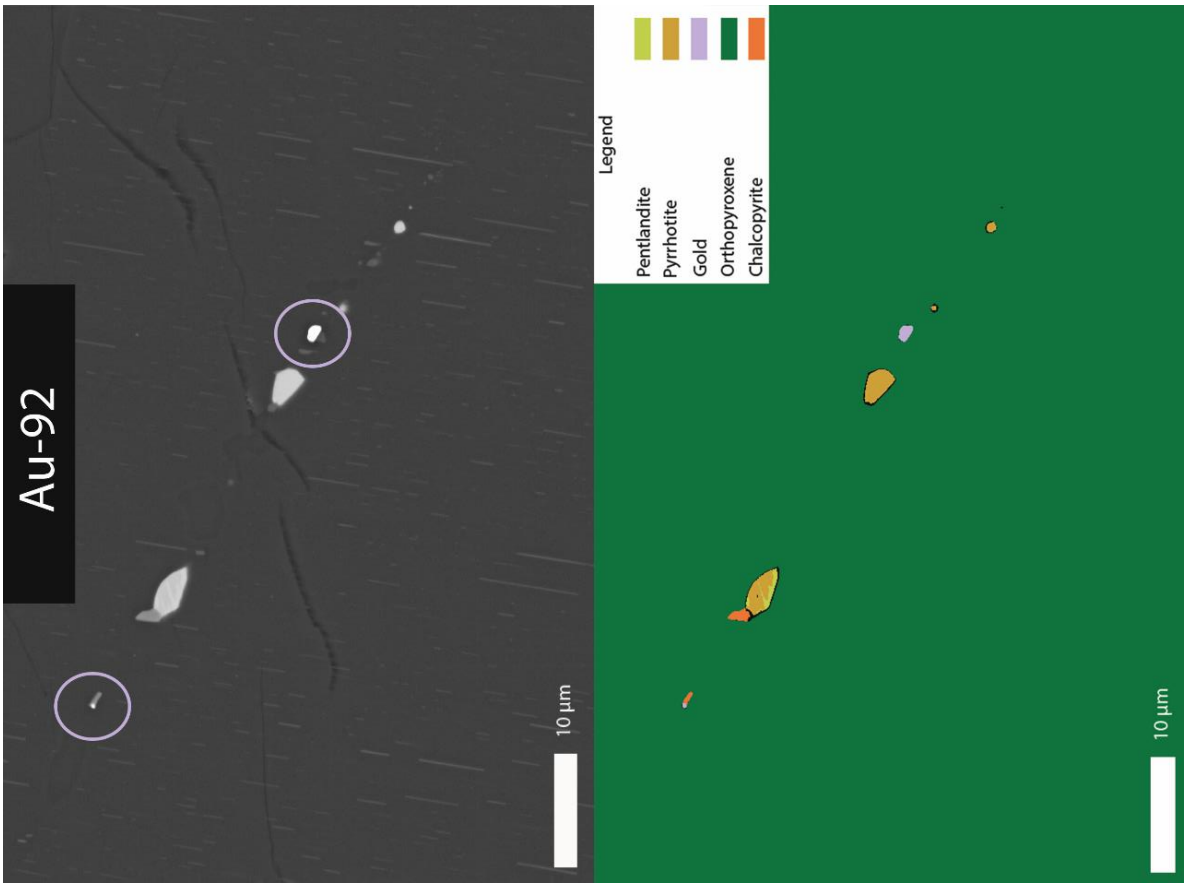

Figure B 56

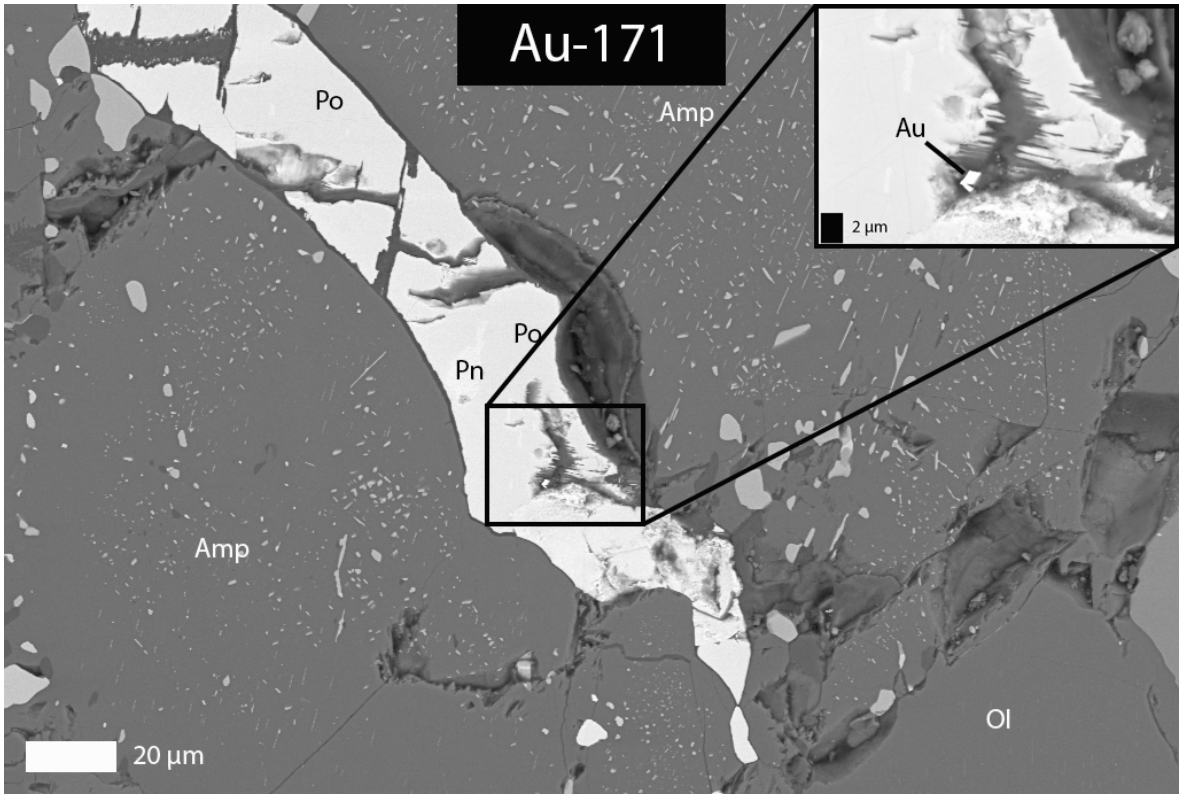

Figure B 57

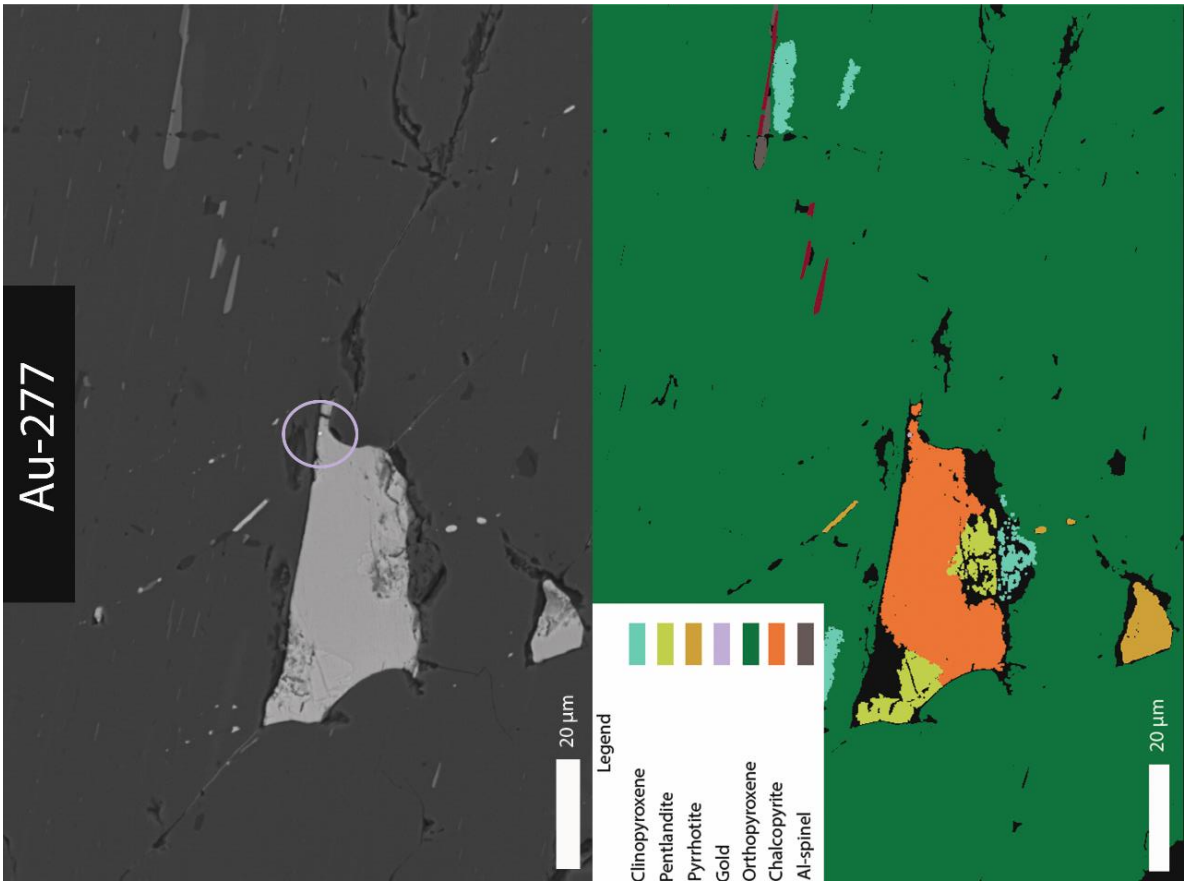

Figure B 58

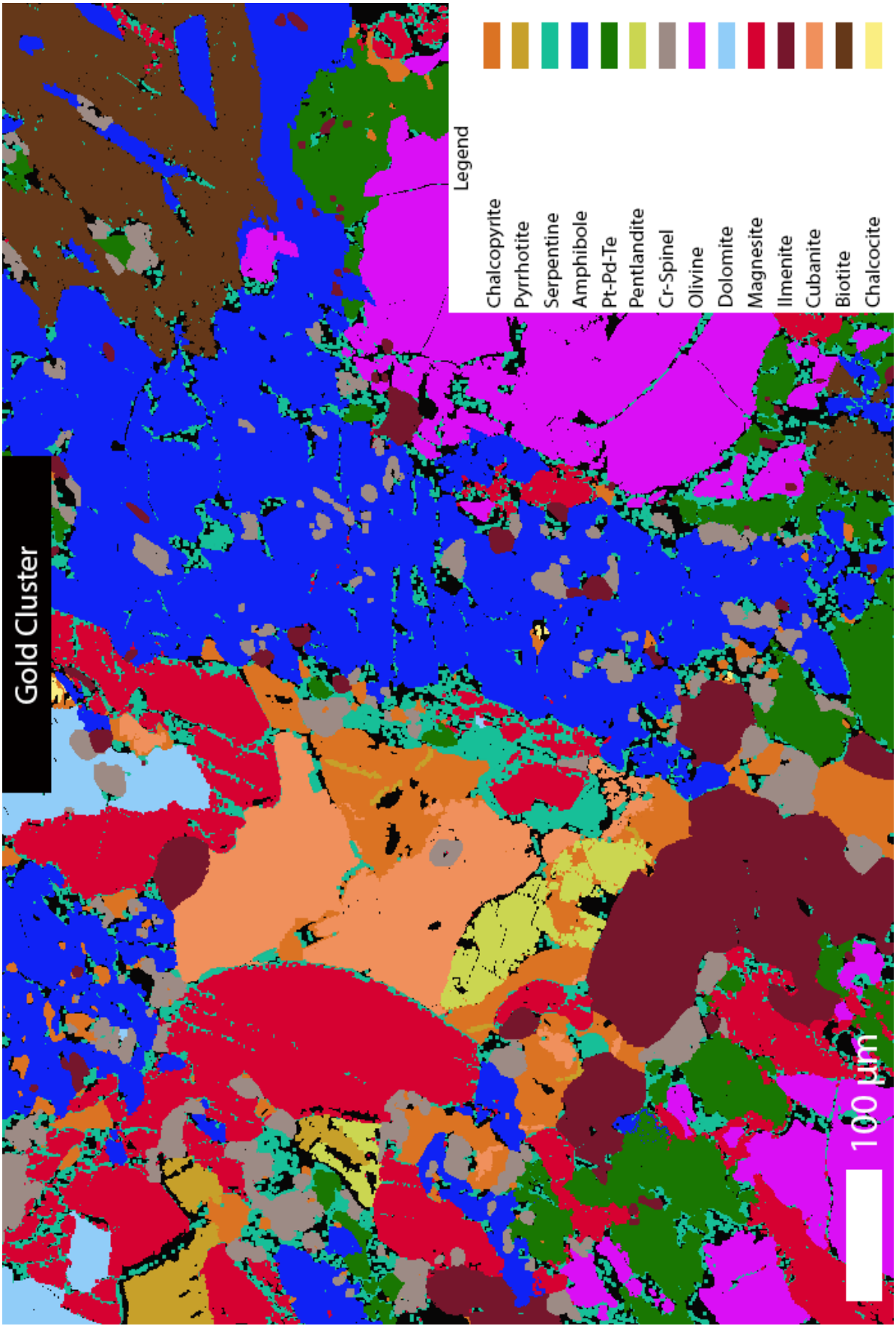
Gold Cluster
Legend
Chalcopyrite
Pyrrhotite
Serpentine
Amphibole
Pt-Pd-Te
Pentlandite
Cr-Spinel
Olivine
Dolomite
Magnesite
Ilmenite
Cubanite
Biotite
Chalcocite
100 um

Figure B 59

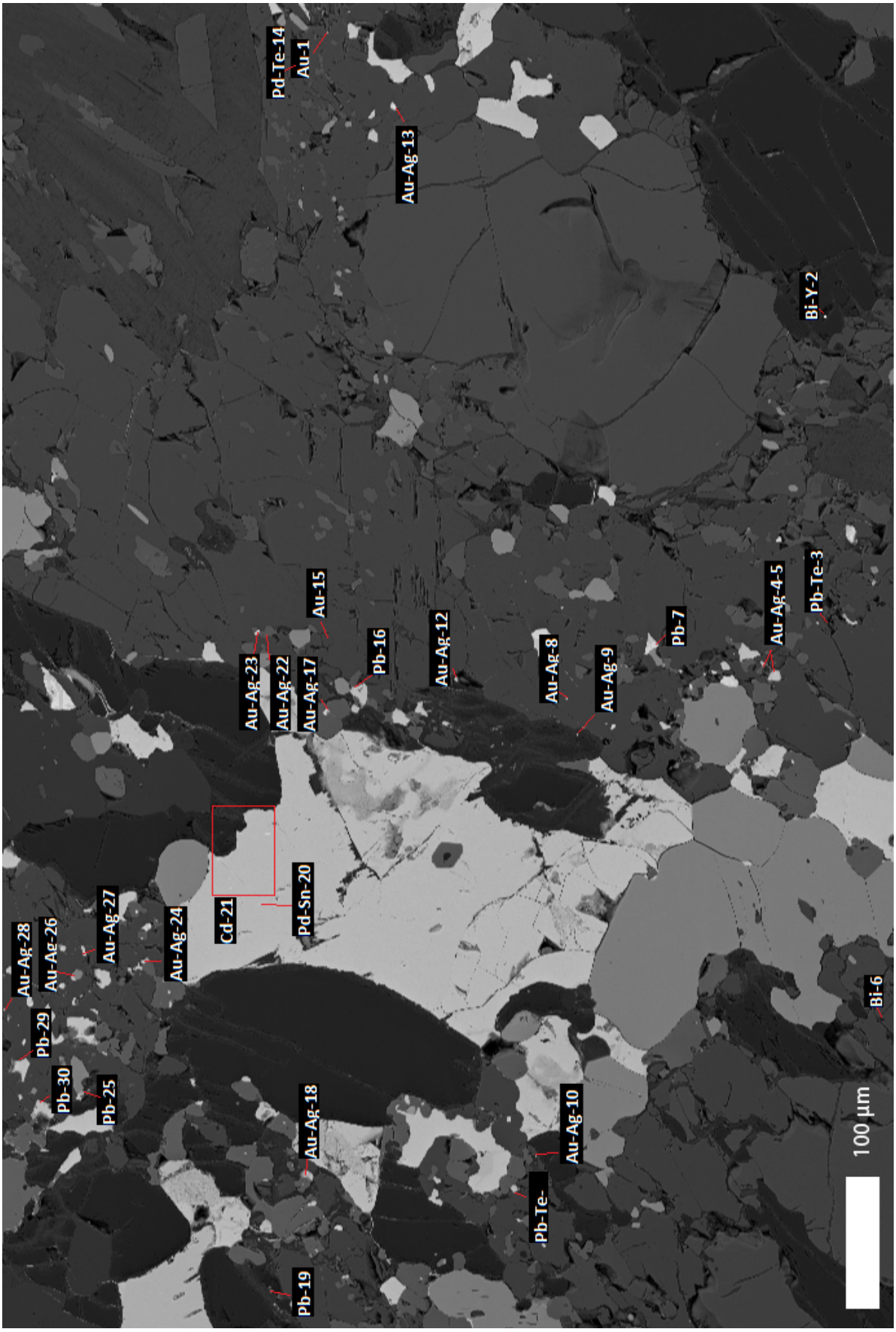
Pd-Te-14
Au-1
Au-Ag-13
Bi-Y-2
Au-15
Au-Ag-23
Au-Ag-22
Au-Ag-17
Pb-16
Au-Ag-12
Au-Ag-8
Au-Ag-9
Pb-7
Au-Ag-4-5
Pb-Te-3
Au-Ag-28
Au-Ag-26
Au-Ag-27
Au-Ag-24
Cd-21
Pd-Sn-20
Pb-29
Pb-30
Pb-25
Au-Ag-18
Au-Ag-10
Pb-Te-
Bi-6
Pb-19
100 µm

Figure B 60

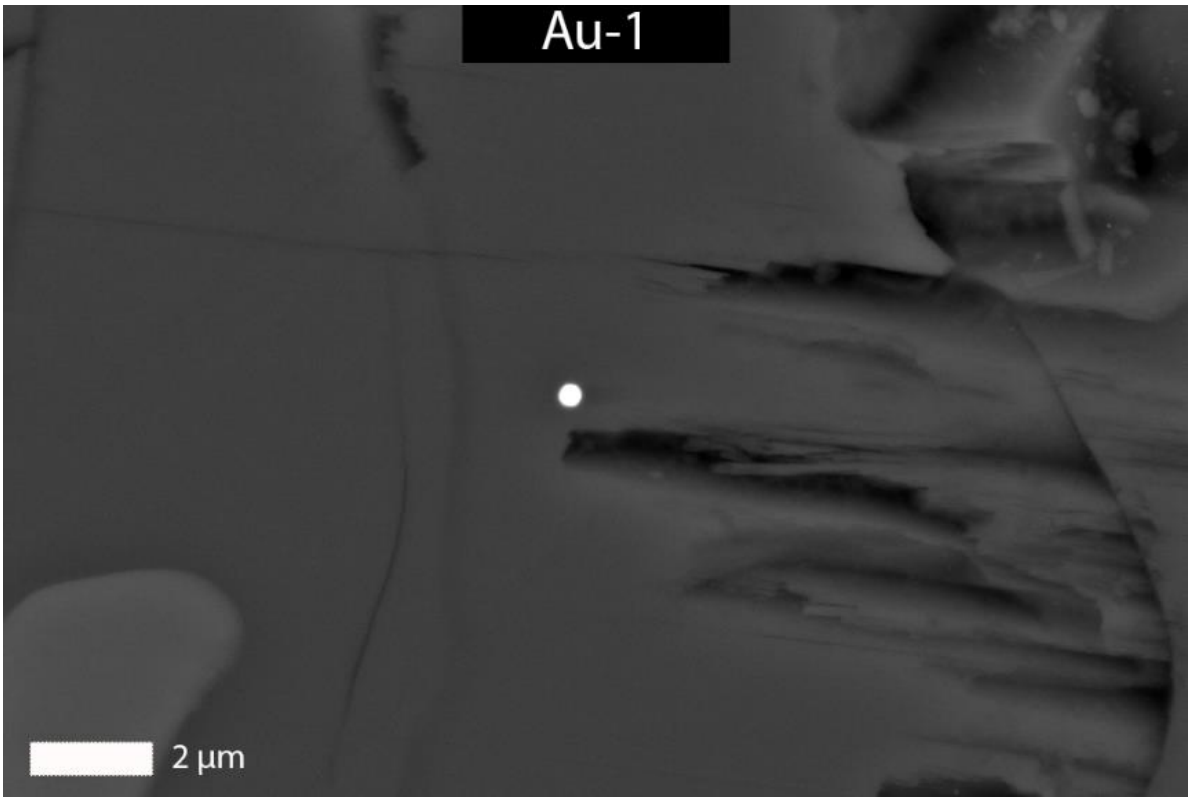

Figure B 61

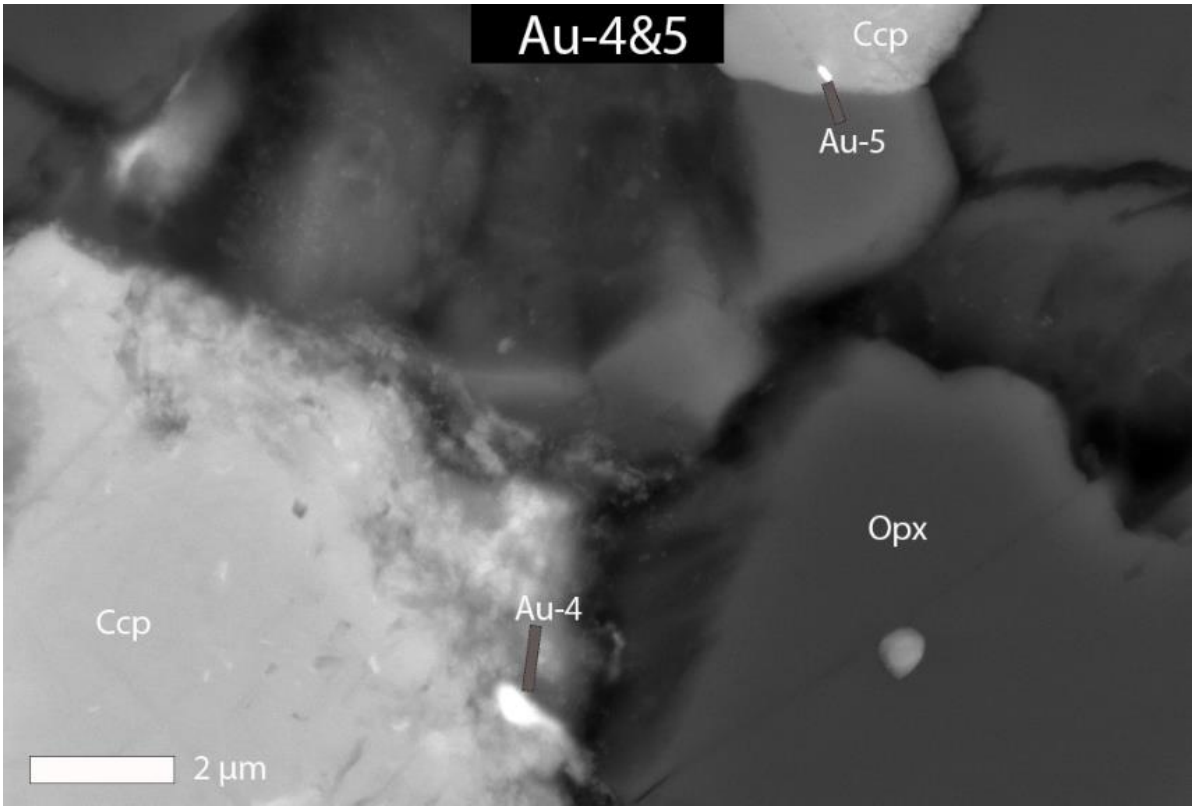

Figure B 62

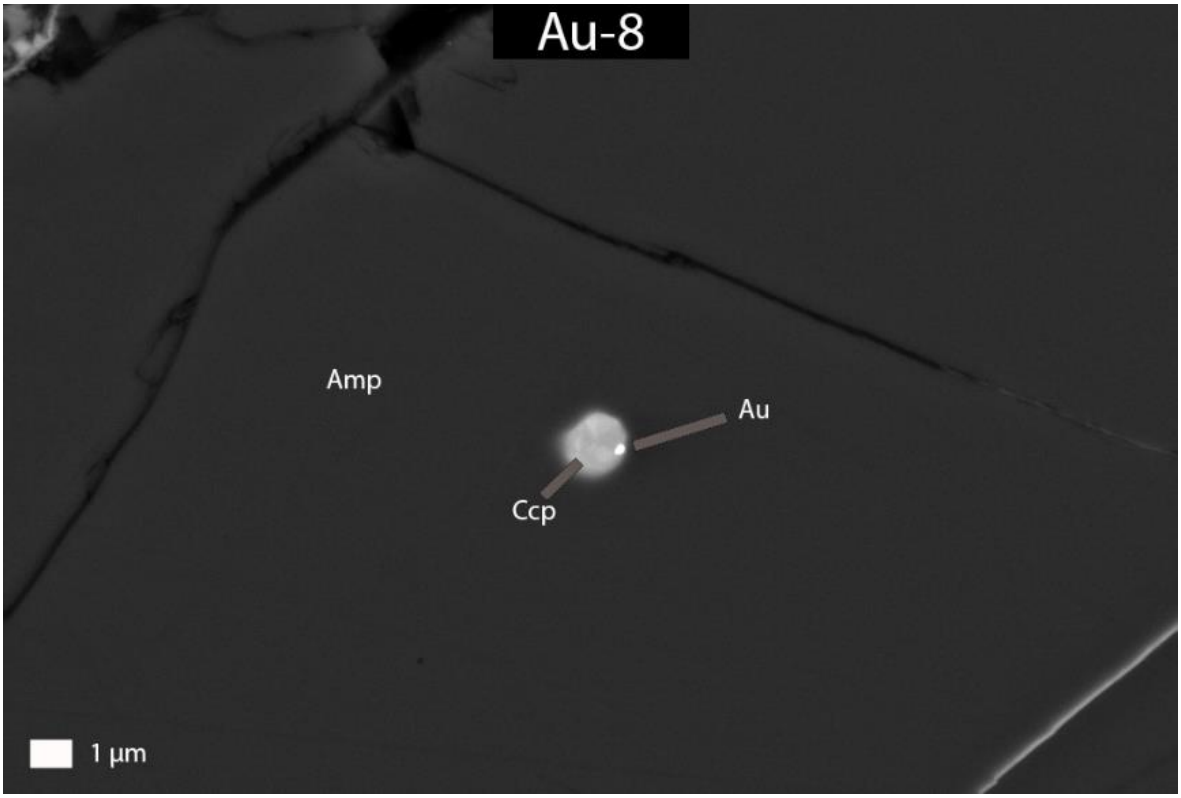

Figure B 63

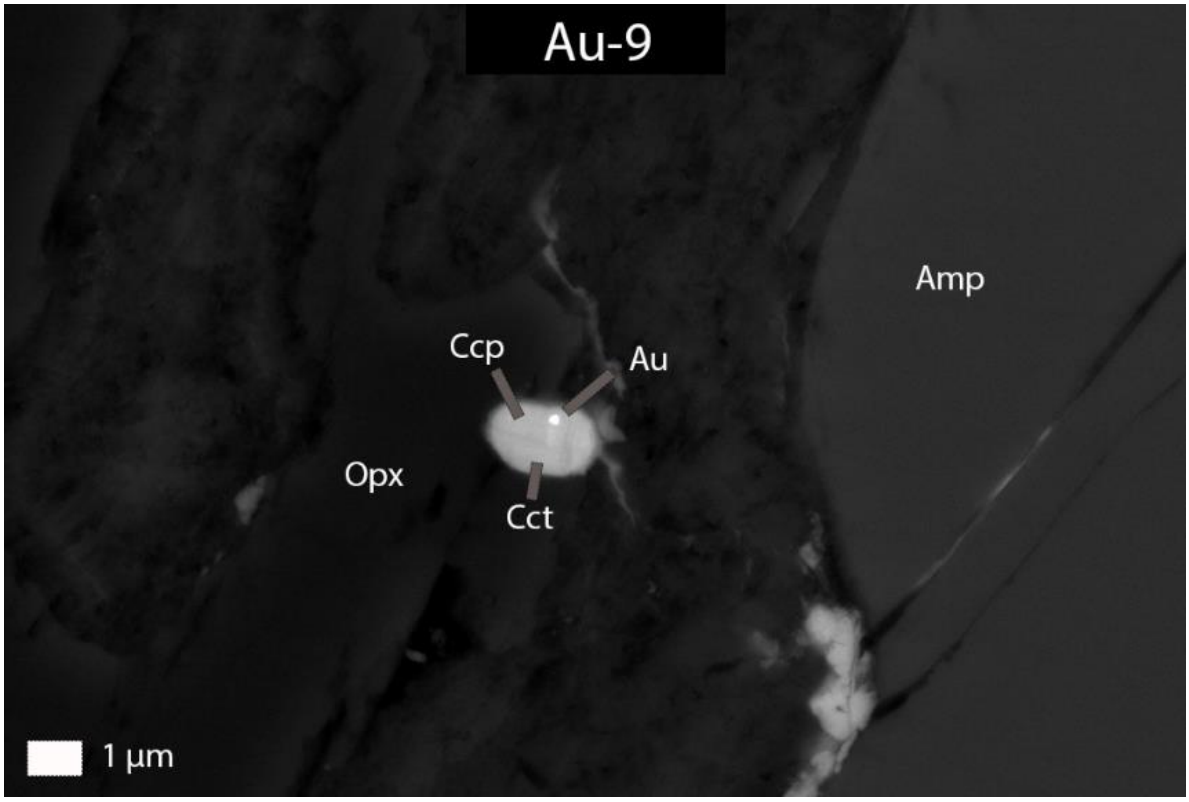

Figure B 64

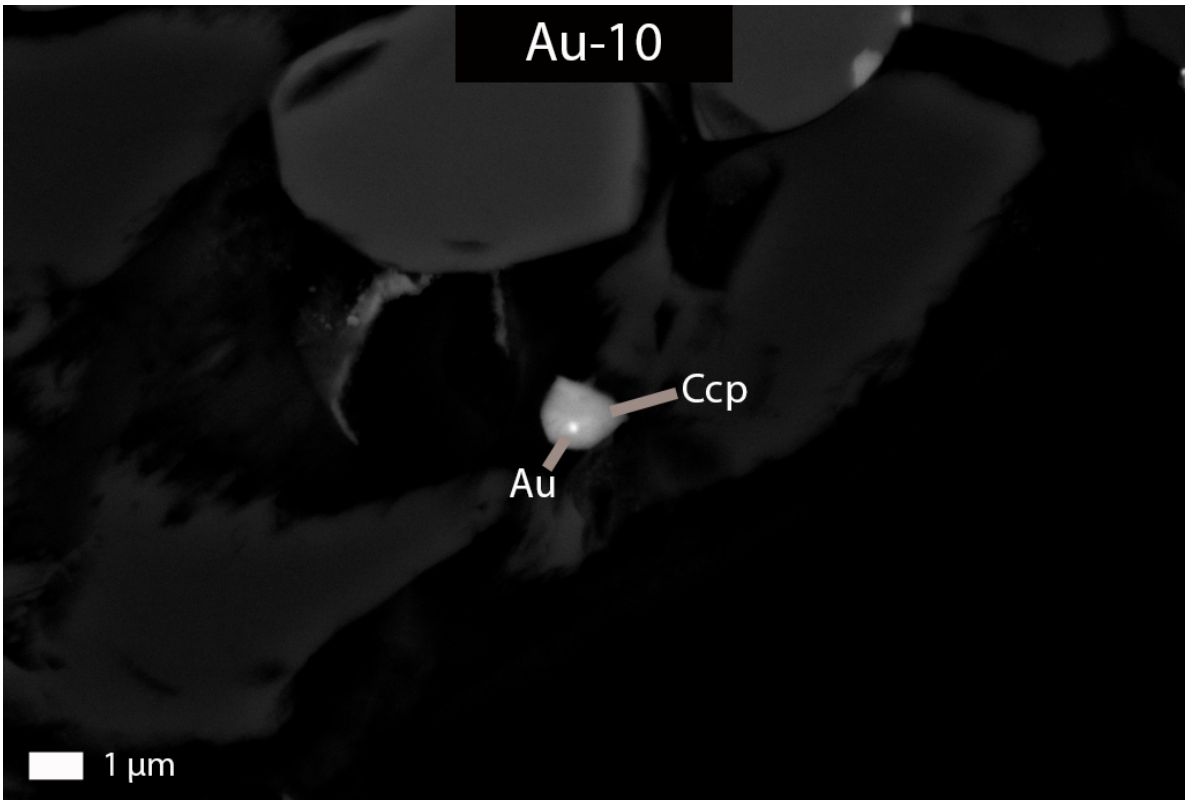

Figure B 65

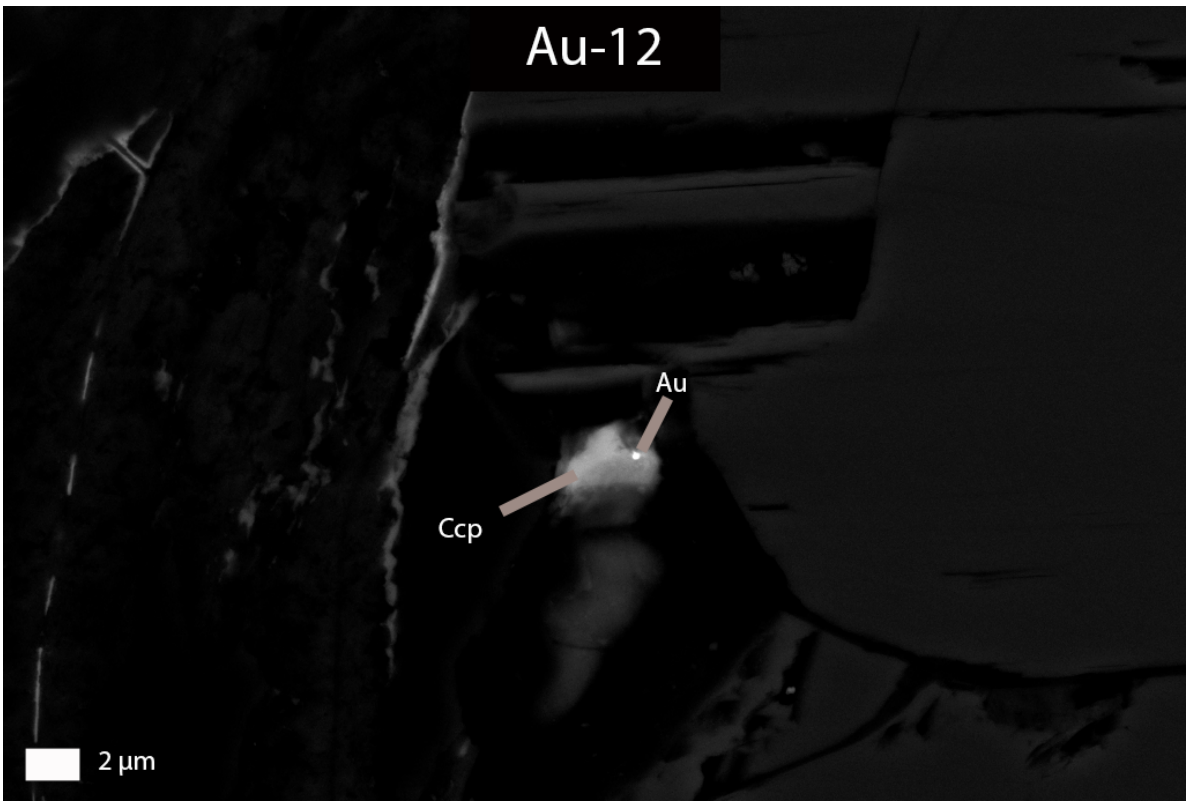

Figure B 66

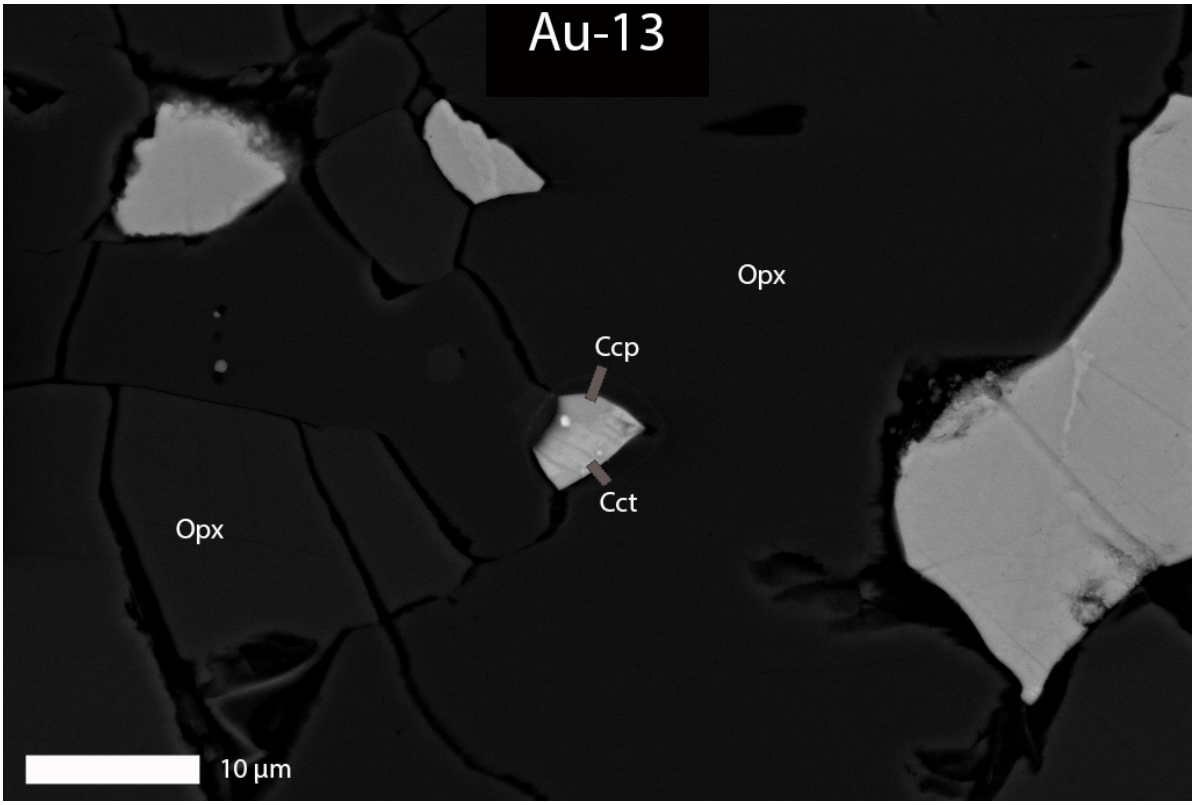

Figure B 67

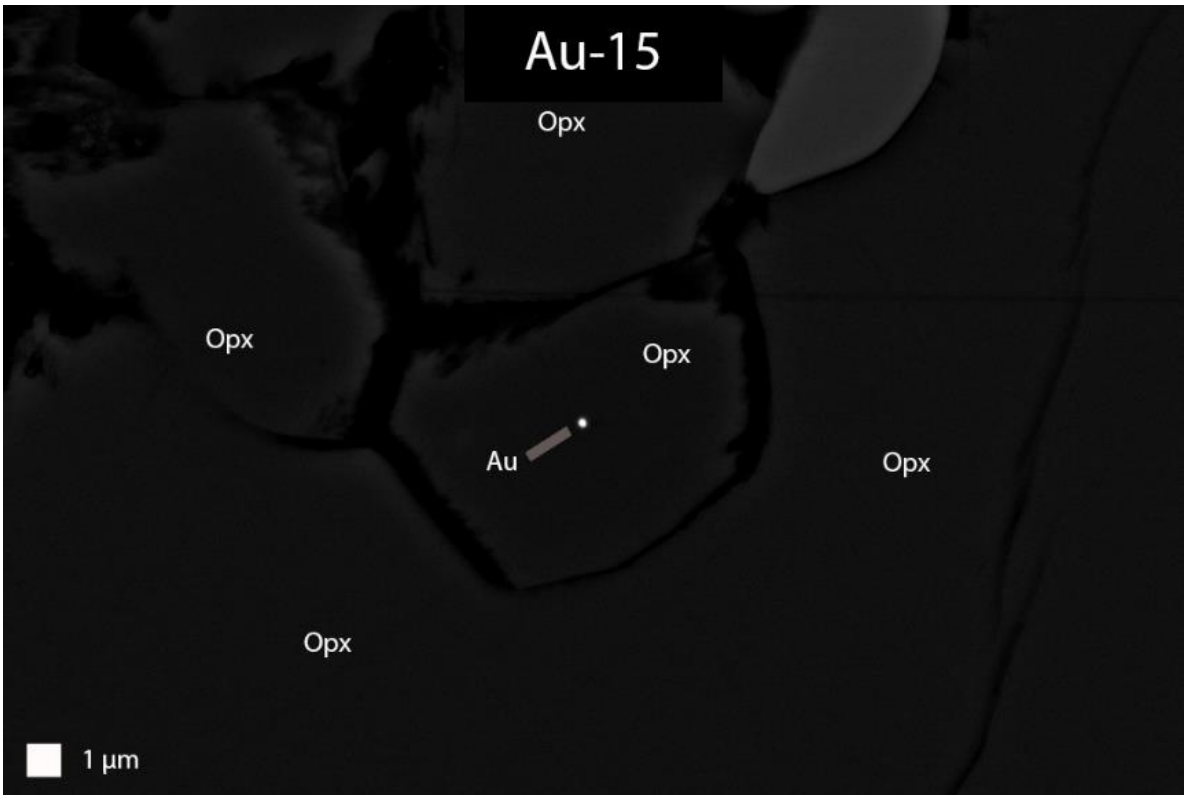

Figure B 68

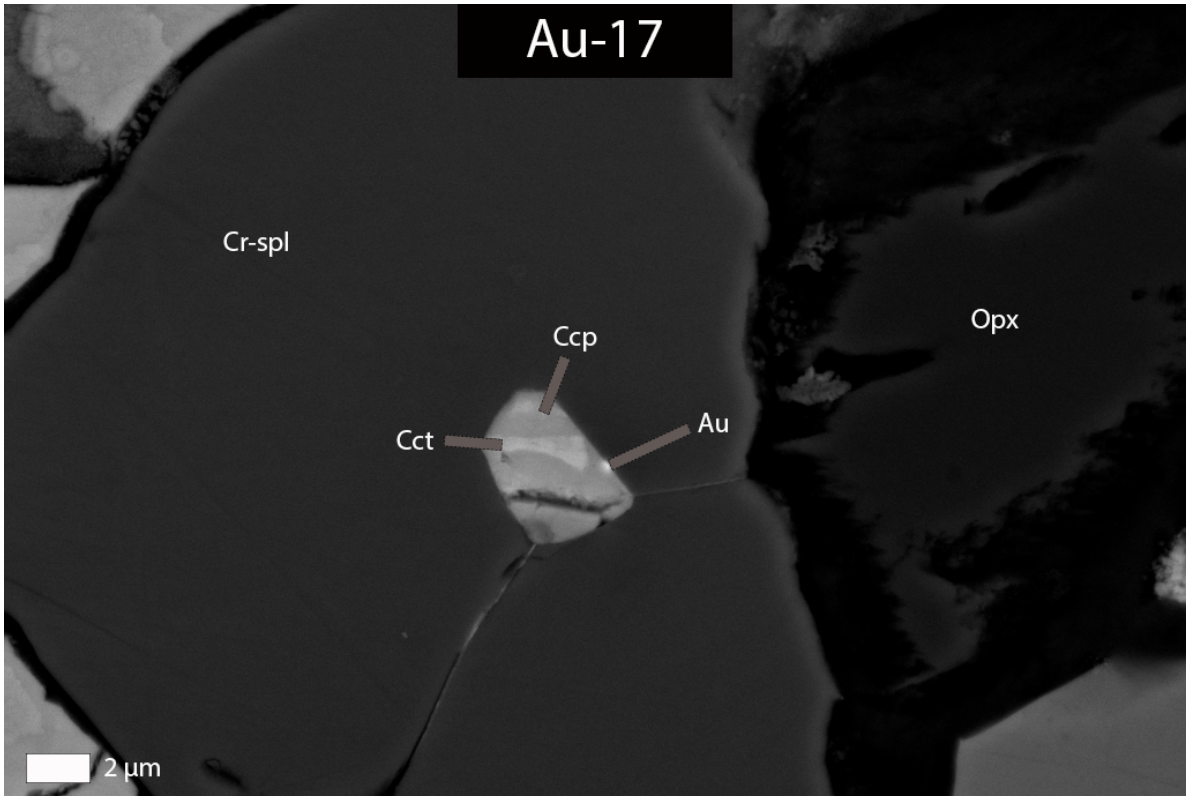

Figure B 69

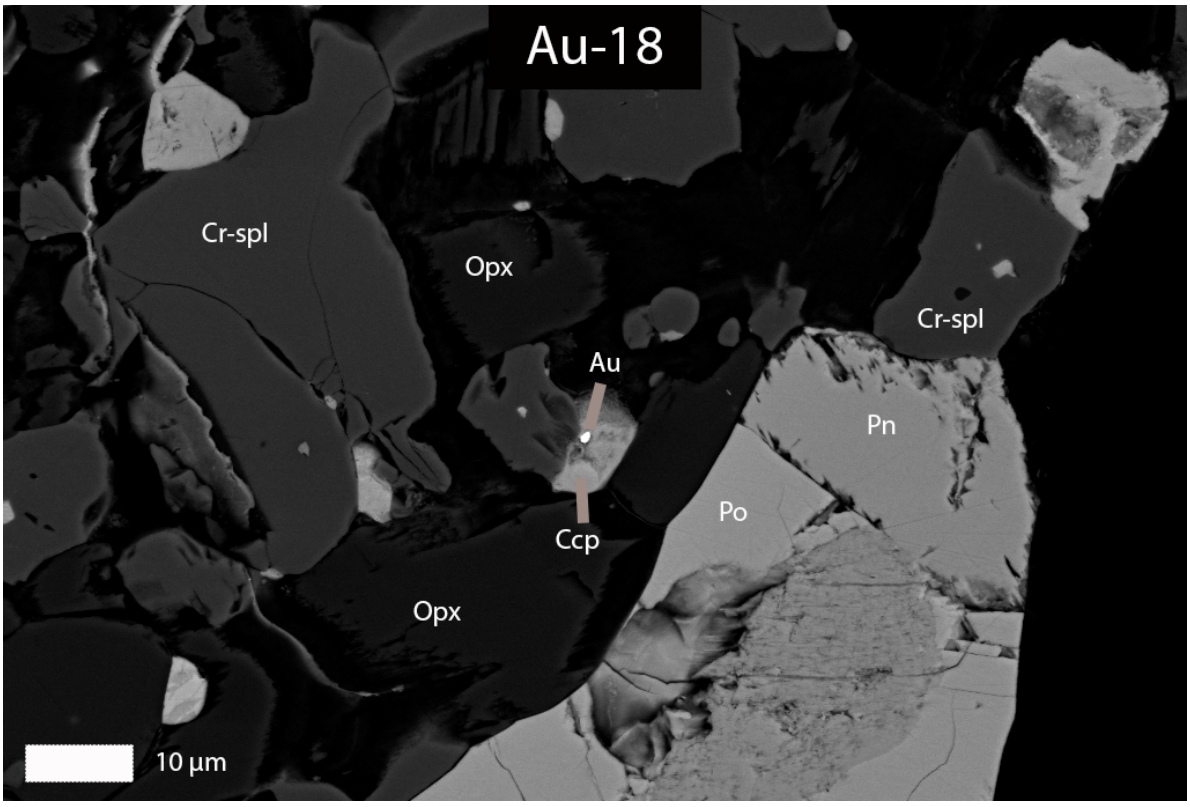

Figure B 70

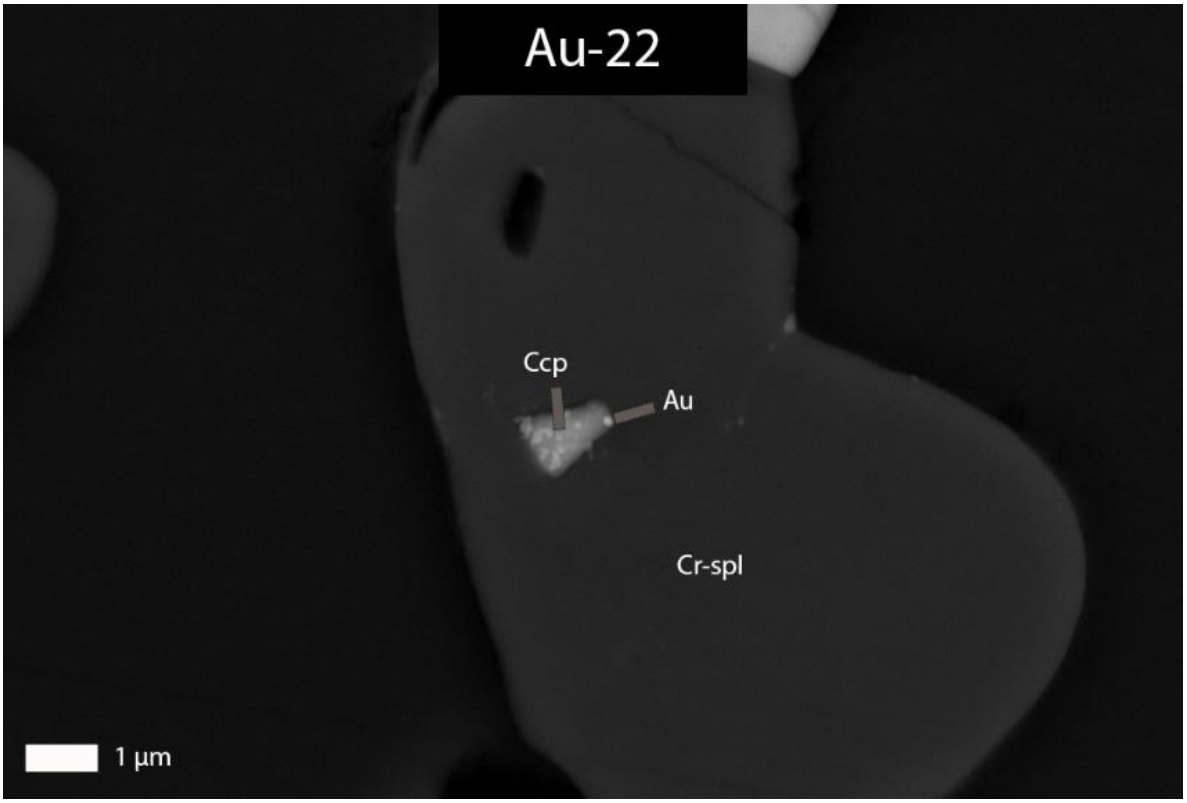

Figure B 71

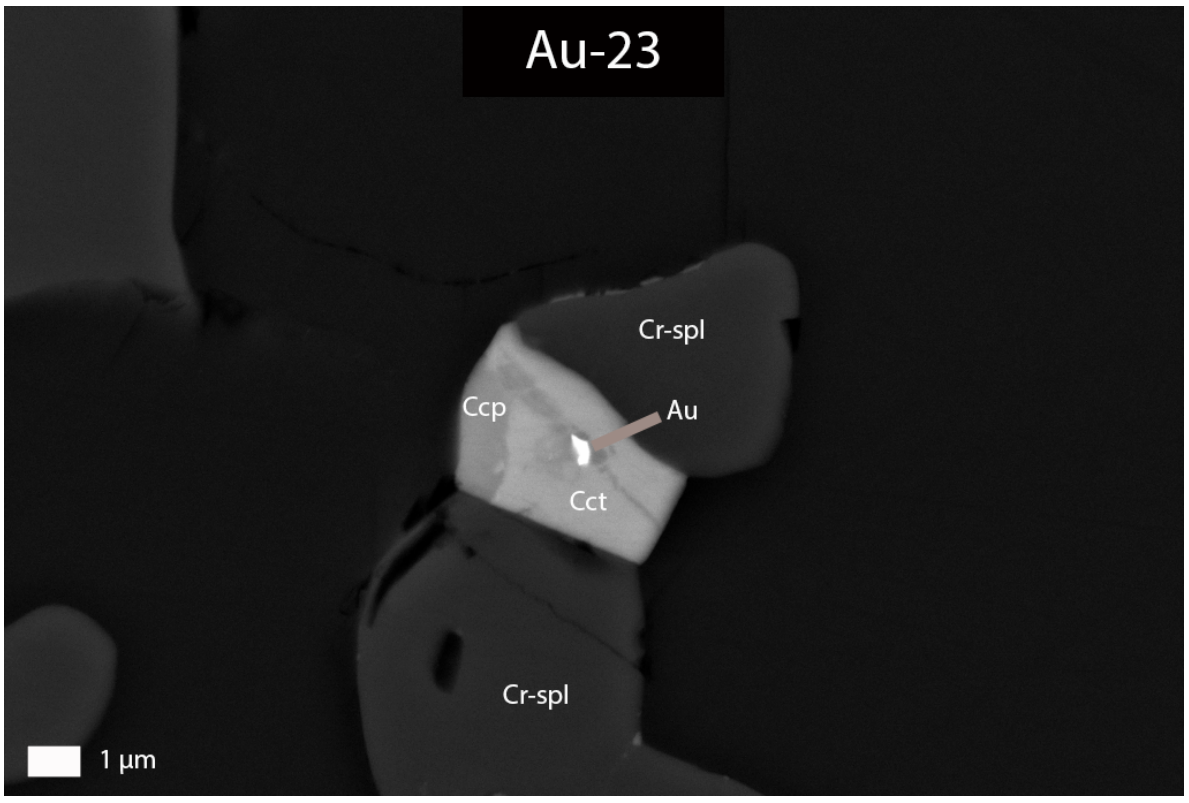

Figure B 72

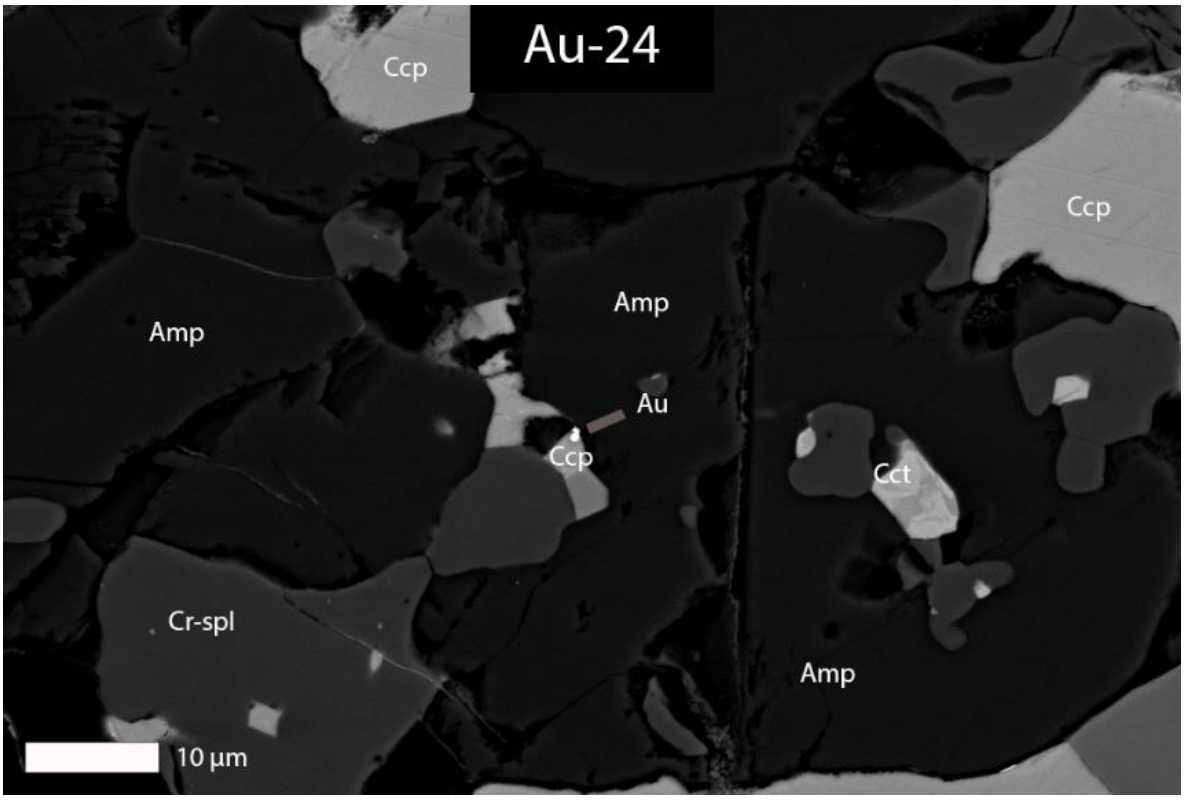

Figure B 73

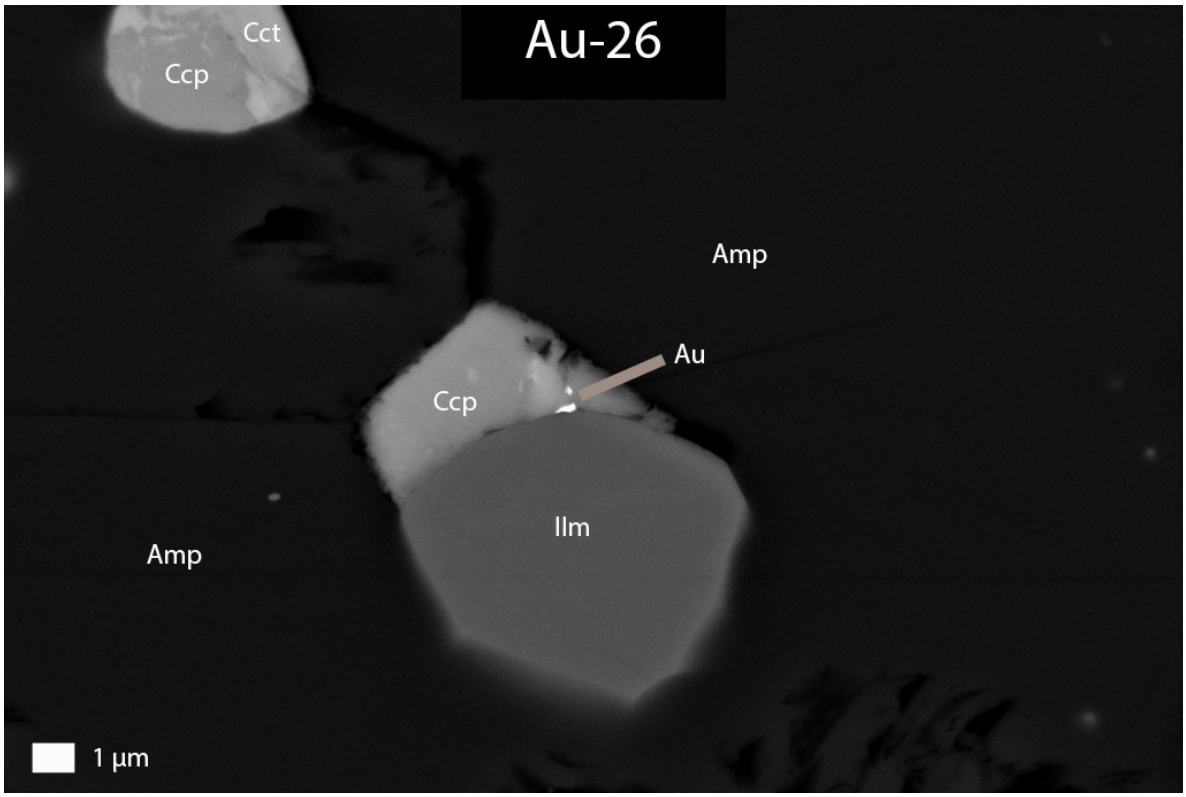

Figure B 74

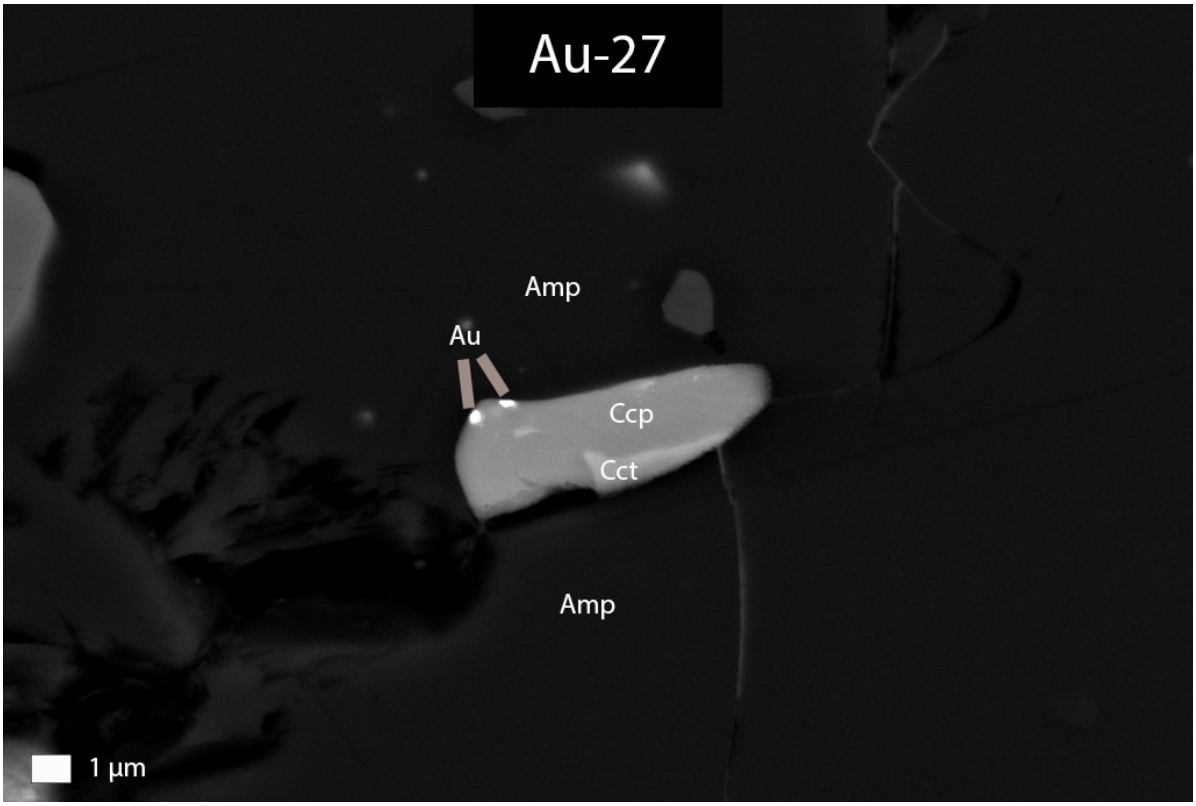

Figure B 75

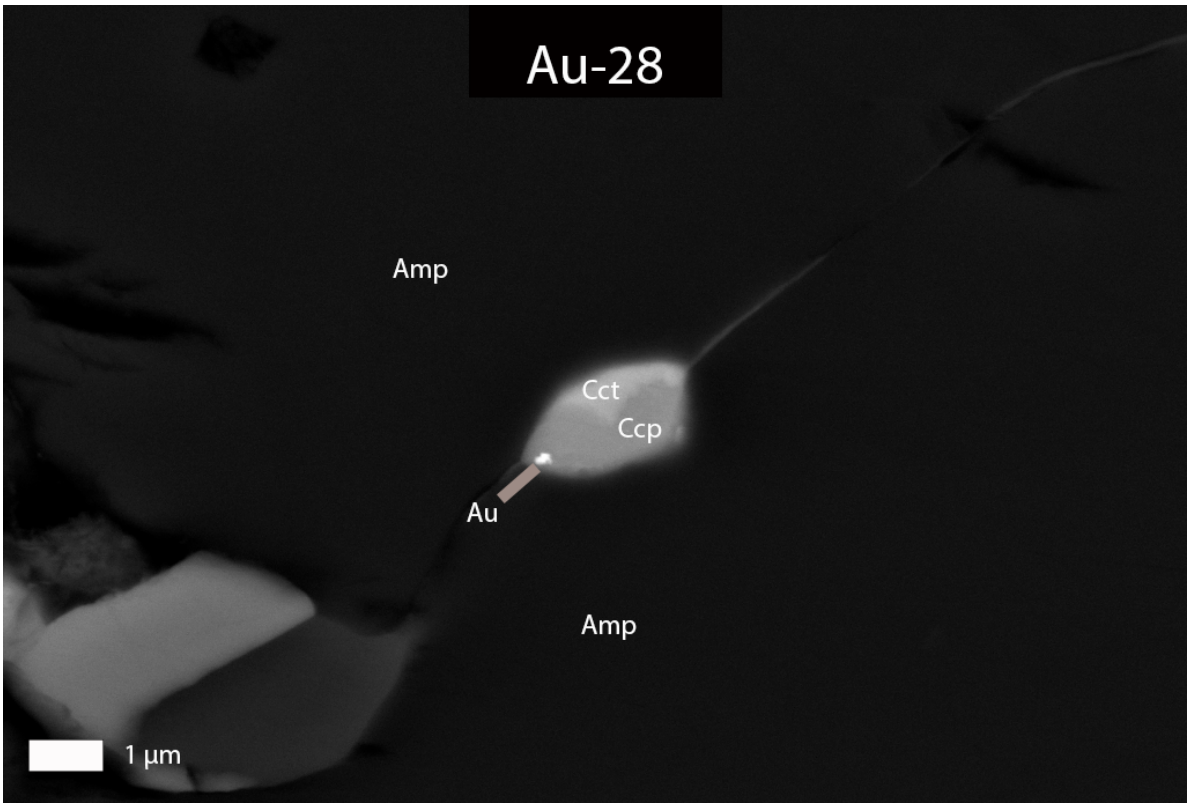

Figure B 76

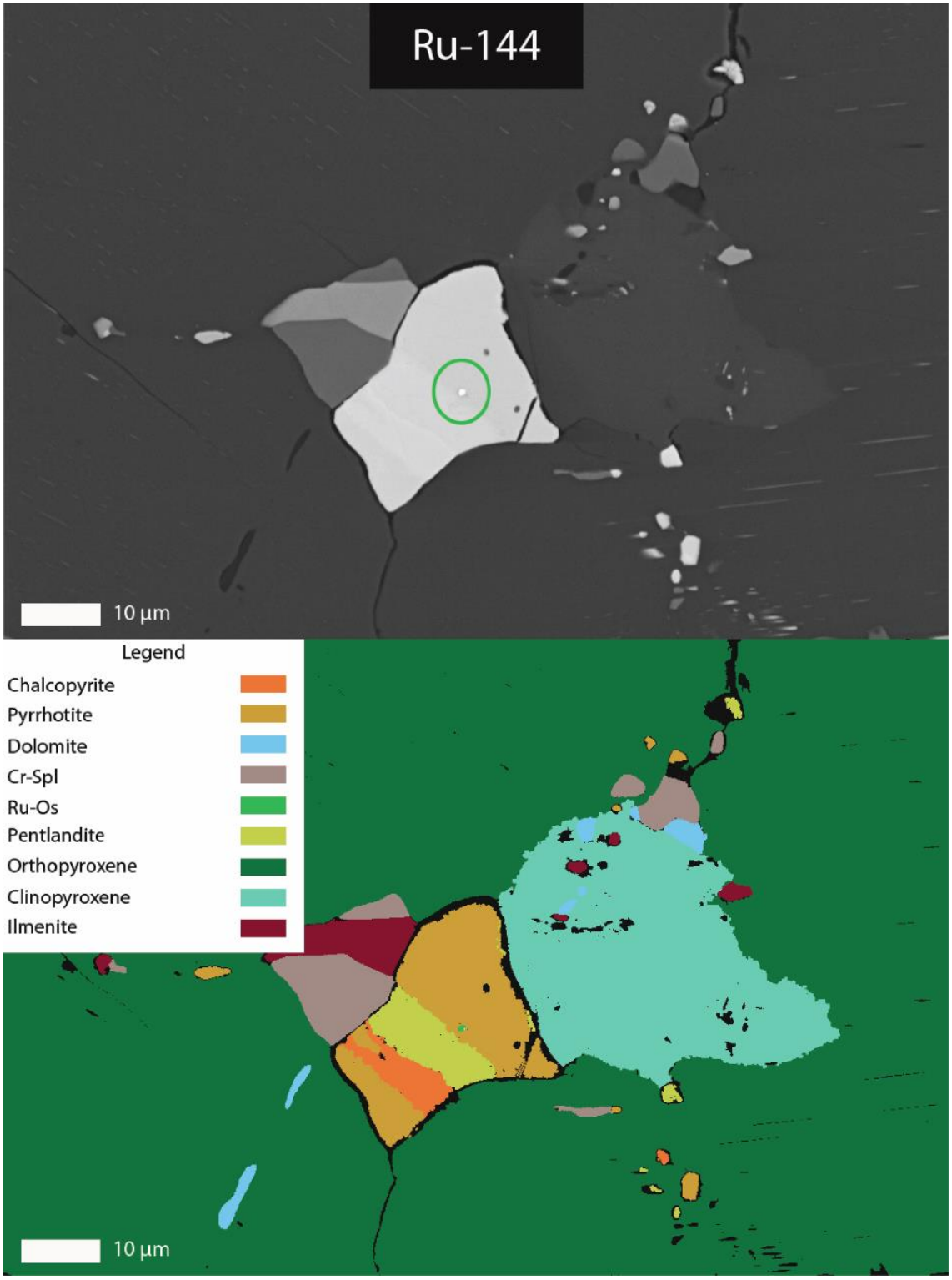
Ru-144
10 µm
Legend
Chalcopyrite
Pyrrhotite
Dolomite
Cr-Spl
Ru-Os
Pentlandite
Orthopyroxene
Clinopyroxene
Ilmenite
10 µm

Figure B 77

Appendix C

The following table show the most significant elements that were analyzed during the PGE sessions on the EPMA. Metal standards where used to calibrate for these analyzes.

Table C 1

Pt-dominant (wt%)																
Pd	**Pt**	**Se**	**Rh**	**Ir**	**Ru**	**Au**	**Ag**	**Cu**	**Te**	**Ni**	**S**	**Fe**	**Pb**	**Os**	**Bi**	**Point**
0.087	89.314	0.155	0.545	0.655	0.000	4.161	0.007	0.029	0.000	0.044	0.035	3.756	0.015	0.000	0.046	Pt-223
0.229	40.492	0.000	0.302	0.351	0.000	0.000	0.053	0.426	51.993	0.022	0.624	2.673	0.135	0.000	5.208	Pt-109-1
0.070	39.750	0.074	0.168	0.302	0.008	0.000	0.000	0.325	51.572	0.289	0.553	2.388	0.378	0.000	5.066	Pt-109-2
0.175	39.458	0.087	0.158	0.126	0.022	0.000	0.027	0.000	51.025	1.048	0.584	2.193	0.128	0.000	5.161	Pt-109-3
0.000	40.763	0.000	0.212	0.019	0.000	0.000	0.000	0.558	54.162	1.100	0.728	2.467	0.530	0.000	0.880	Pt-125
0.215	26.086	0.015	0.150	2.472	0.000	0.000	1.573	0.310	0.000	0.251	0.774	1.137	2.331	3.268	0.000	Pt-180
0.036	40.896	0.012	0.279	0.000	0.000	0.000	0.000	0.085	51.161	0.051	0.686	3.705	0.000	0.000	5.607	Pt-166-1
0.073	40.231	0.000	0.103	0.265	0.011	0.000	0.004	0.013	50.290	0.256	0.772	3.777	0.077	0.000	5.022	Pt-166-2
0.000	35.681	0.000	0.196	0.497	0.000	0.096	0.000	0.307	21.088	0.000	5.631	6.742	0.000	0.000	26.618	Pt-153
0.000	39.005							0.227	48.916	0.675	0.995	2.600			4.768	Pt-107
0.000	33.096							0.473	47.900	0.092	2.220	2.853			9.702	Pt-138
0.000	41.161	0.000	0.112	0.339	0.000	0.000	0.000	0.040	41.811	3.384	3.995	6.399	0.000	0.180	0.000	Pt-87

Pt-Pd-dominant (wt%)																
Pd	**Pt**	**Se**	**Rh**	**Ir**	**Ru**	**Au**	**Ag**	**Cu**	**Te**	**Ni**	**S**	**Fe**	**Pb**	**Os**	**Bi**	**Point**
8.736	5.974	0.074	0.398	0.225	0.110	0.000	0.568	0.206	66.619	9.769	0.595	1.756	0.000	0.000	3.657	Pd-274
6.300	18.167	0.000	0.186	0.008	0.000	0.000	0.346	0.023	62.201	5.173	0.114	0.886	0.000	0.000	2.459	Pt-236
5.717	18.749	0.079	0.155	0.632	0.000	0.244	0.411	0.050	62.296	5.272	0.048	0.731	0.000	0.000	2.320	Pt-237
7.557	3.176	0.026	0.000	0.271	0.029	0.000	2.134	0.097	69.569	12.570	0.159	1.413	0.000	0.000	1.739	Pt-238
6.315	18.935	0.018	0.159	0.292	0.003	0.000	0.424	0.034	62.043	5.122	0.108	0.698	0.000	0.000	2.505	Pt-239
7.245	15.658	0.000	0.136	0.365	0.000	0.000	0.318	0.048	64.748	5.815	0.106	1.020	0.000	0.000	3.263	Pt-240
26.881	36.616	0.026	0.170	0.203	0.000	0.000	2.096	0.022	0.000	7.691	0.447	2.836	0.152	0.000	0.000	Pt-169
5.095	1.393							0.000	66.179	14.205	2.679	7.491			4.755	Pd-282
9.863	13.902							0.000	53.734	4.645	2.404	4.772			7.930	Pd-259
5.615	23.761							2.045	49.939	1.879	2.880	3.632			6.104	Pd-226
12.793	13.771	0.035	0.100	0.165	0.000	0.000	4.469	0.127	55.133	2.876	0.225	1.603	0.000	0.000	5.851	Pd-41
Pd-dominant (wt%)																
22.337	0.656	0.000	0.035	0.000	0.095	0.000	1.326	1.135	28.799	0.000	0.311	0.861	0.000	0.532	45.918	Pd-53-1
21.785	0.773	0.077	0.020	0.000	0.000	0.000	1.106	2.403	38.601	0.888	0.066	0.054	0.000	1.476	19.342	Pd-54
22.364	0.996							0.969	28.668	0.064	0.345	0.964			45.613	Pd-53-2
26.649	1.764	0.000	0.443	0.165	0.000	0.000	1.949	0.095	66.164	3.076	1.278	2.781	0.000	0.000	2.740	Pd-275
21.592	0.103	0.020	0.265	0.699	0.000	0.104	3.152	2.871	57.430	3.000	0.053	0.131	0.000	3.495	1.930	Pd-235

Gold (wt%)																
0.000	0.000	0.082	0.000	0.000	0.000	15.150	32.598	11.925	0.000	0.050	16.473	15.188	0.000	8.483	0.060	Au-277
0.000	0.000	0.000	0.000	0.000	0.000	72.085	20.362	0.404	0.000	0.037	0.102	3.018	0.000	0.000	0.667	Au-81
0.346	0.030	0.000	0.000	0.000	0.000	95.189	2.346	1.169	0.000	0.004	0.053	2.106	0.030	0.679	0.000	Au-92
0.000	0.000	0.072	0.069	0.000	0.000	17.009	16.086	17.738	0.000	0.251	20.427	17.708	0.000	12.253	0.196	Au-24
Ruthenium (wt%)																
0.066	0.000	0.236	0.230	11.766	15.723	0.000	0.000	8.244	0.000	0.121	34.822	27.822	0.000	15.965	0.000	Ru-144

Appendix D

1. Table D 1:	List of selected elements that are above trace level and does occur at significant amount to be included in the mineral formula. Complete EPMA list for the PGM's in appendix C.
2. Table D 2:	Table D 1 values normalized
3. Table D 3:	Calculated for Mol of Elements (Normalized values / Mol weight) Pd: 106. 42 Pt: 195.085 Ag: 107.868 Te: 127.6 Ni: 58.693 Bi: 208.98
4. Table D 4:	Table D 3 values normalized to percentage Mol for each mineral
5. Table D 5:	The elements are arranged according to the known formulas for PGM's. Pd, Pt, Ag and Ni occupy the first slot in the mineral lattice. The factor indicates the amount from the complete mineral that is represented by the Pd, Pt, Ag and Ni. (Factor = 1/(Mol% Pd + Mol% Pt + Mol% Ag + Mol% Ni))
6. Table D 6:	The final amount that each element represents and from this the empirical formula can be constructed. (Mol% * Factor)

Table D 1

From EPMA							
Pd	**Pt**	**Ag**	**Te**	**Ni**	**Bi**	**Total**	**Point**
	89.314					89.3140	Pt-223
	40.492		51.993		5.208	97.6930	Pt-109-1
	39.750		51.572		5.066	96.3880	Pt-109-2
	39.458		51.025		5.161	95.6440	Pt-109-3
	40.763		54.162			94.9250	Pt-125
	26.086		0.000			26.0860	Pt-180
	40.896		51.161		5.607	97.6640	Pt-166-1
	40.231		50.290		5.022	95.5430	Pt-166-2
	35.681		21.088		26.618	83.3870	Pt-153
	39.005		48.916		4.768	92.6890	Pt-107
	33.096		47.900		9.702	90.6980	Pt-138
	41.161		41.811	3.384		86.3560	Pt-87
8.736	5.974		66.619	9.769	3.657	94.7550	Pd-274
6.300	18.167		62.201	5.173	2.459	94.3000	Pt-236
5.717	18.749		62.296	5.272	2.320	94.3540	Pt-237
7.557	3.176	2.134	69.569	12.570		95.0060	Pt-238
6.315	18.935		62.043	5.122	2.505	94.9200	Pt-239
7.245	15.658		64.748	5.815	3.263	96.7290	Pt-240
26.881	36.616	2.096		7.691		73.2840	Pt-169
5.095	1.393		66.179	14.205	4.755	91.6270	Pd-282
9.863	13.902		53.734	4.645	7.930	90.0740	Pd-259
5.615	23.761		49.939		6.104	85.4190	Pd-226-2
12.793	13.771	4.469	55.133	2.876	5.851	94.8930	Pd-41-1
22.337			28.799		45.918	97.0540	Pd-204-1
21.785			38.601		19.342	79.7280	Pd-209
22.364			28.668		45.613	96.6450	Pd-204-2
26.649			66.164	3.076		95.8890	PD-275
21.592		3.152	57.430	3.000		85.1740	Pd-235

Table D 2

Normalized						
Pd	**Pt**	**Ag**	**Te**	**Ni**	**Bi**	**Total**
	100.000					100.000
	41.448		53.221		5.331	100.000
	41.240		53.505		5.256	100.000
	41.255		53.349		5.396	100.000
	42.942		57.058			100.000
	100.000					100.000
	41.874		52.385		5.741	100.000
	42.108		52.636		5.256	100.000
	42.790		25.289		31.921	100.000
	42.082		52.774		5.144	100.000
	36.490		52.813		10.697	100.000
	47.664		48.417	3.919		100.000
9.220	6.305		70.307	10.310	3.859	100.000
6.681	19.265		65.961	5.486	2.608	100.000
6.059	19.871		66.024	5.587	2.459	100.000
7.954	3.343	2.246	73.226	13.231		100.000
6.653	19.948		65.363	5.396	2.639	100.000
7.490	16.187		66.938	6.012	3.373	100.000
36.681	49.965	2.860		10.495		100.000
5.561	1.520		72.227	15.503	5.190	100.000
10.950	15.434		59.655	5.157	8.804	100.000
6.573	27.817		58.464		7.146	100.000
13.482	14.512	4.710	58.100	3.031	6.166	100.000
23.015			29.673		47.312	100.000
27.324			48.416		24.260	100.000
23.140			29.663		47.196	100.000
27.792			69.001	3.208		100.000
25.350		3.701	67.427	3.522		100.000

Table D 3

Mol Corrections						
Pd mol	**Pt-Mol**	**Ag mol**	**Te mol**	**Ni Mol**	**Bi mol**	**Total**
	0.513		0.000			0.513
	0.212		0.417		0.026	0.655
	0.211		0.419		0.025	0.656
	0.211		0.418		0.026	0.655
	0.220		0.447			0.667
	0.513		0.000			0.513
	0.215		0.411		0.027	0.653
	0.216		0.413		0.025	0.654
	0.219		0.198		0.153	0.570
	0.216		0.414		0.025	0.654
	0.187		0.414		0.051	0.652
	0.244		0.379	0.067		0.691
0.087	0.032		0.551	0.176	0.018	0.864
0.063	0.099		0.517	0.093	0.012	0.784
0.057	0.102		0.517	0.095	0.012	0.783
0.075	0.017	0.021	0.574	0.225		0.912
0.063	0.102		0.512	0.092	0.013	0.782
0.070	0.083		0.525	0.102	0.016	0.797
0.345	0.256	0.027		0.179		0.806
0.052	0.008		0.566	0.264	0.025	0.915
0.103	0.079		0.468	0.088	0.042	0.780
0.062	0.143		0.458		0.034	0.697
0.127	0.074	0.044	0.455	0.052	0.030	0.781
0.216			0.233		0.226	0.675
0.257			0.379		0.116	0.752
0.217			0.232		0.226	0.676
0.261			0.541	0.055		0.857
0.238		0.034	0.528	0.060		0.861

Table D 4

Mol Percentage						
Pd mol %	**Pt-Mol %**	**Ag mol %**	**Te mol %**	**Ni Mol %**	**Bi mol %**	**Total**
	1.000					1
	0.324		0.637		0.039	1
	0.322		0.639		0.038	1
	0.323		0.638		0.039	1
	0.330		0.670		0.000	1
	1.000		0.000		0.000	1
	0.329		0.629		0.042	1
	0.330		0.631		0.038	1
	0.385		0.348		0.268	1
	0.330		0.632		0.038	1
	0.287		0.635		0.078	1
	0.354		0.549	0.097	0.000	1
0.100	0.037		0.638	0.203	0.021	1
0.080	0.126		0.659	0.119	0.016	1
0.073	0.130		0.661	0.122	0.015	1
0.082	0.019	0.023	0.629	0.247		1
0.080	0.131		0.655	0.118	0.016	1
0.088	0.104		0.659	0.129	0.020	1
0.428	0.318	0.033		0.222		1
0.057	0.009		0.619	0.289	0.027	1
0.132	0.101		0.600	0.113	0.054	1
0.089	0.205		0.658		0.049	1
0.162	0.095	0.056	0.583	0.066	0.038	1
0.320			0.344		0.335	1
0.341			0.504		0.154	1
0.322			0.344		0.334	1
0.305			0.631	0.064		1
0.277		0.040	0.614	0.070		1

Table D 5

Factor						
Pd mol %	**Pt-Mol %**	**Ag mol %**	**Ni Mol %**	**Te mol %**	**Bi mol %**	**Factor**
	1.000					1.000
	0.324			0.637	0.039	3.083
	0.322			0.639	0.038	3.103
	0.323			0.638	0.039	3.099
	0.330			0.670		3.031
	1.000					1.000
	0.329			0.629	0.042	3.041
	0.330			0.631	0.038	3.028
	0.385			0.348	0.268	2.600
	0.330			0.632	0.038	3.031
	0.287			0.635	0.078	3.486
	0.354		0.097	0.549		2.220
0.100	0.037		0.203	0.638	0.021	2.933
0.080	0.126		0.119	0.659	0.016	3.076
0.073	0.130		0.122	0.661	0.015	3.084
0.082	0.019	0.023	0.247	0.629		2.697
0.080	0.131		0.118	0.655	0.016	3.045
0.088	0.104		0.129	0.659	0.020	3.114
0.428	0.318	0.033	0.222			1.000
0.058	0.009		0.291	0.624	0.027	2.799
0.132	0.101		0.113	0.600	0.054	2.888
0.089	0.205			0.658	0.049	3.409
0.162	0.095	0.056	0.066	0.583	0.038	2.636
0.320				0.344	0.335	3.122
0.341				0.504	0.154	2.930
0.322				0.344	0.334	3.108
0.305			0.064	0.631		2.712
0.277		0.040	0.070	0.614		2.589

Table D 6

Element Partitions						
Pd	**Pt**	**Ag**	**Ni**	**Te**	**Bi**	**Formula**
	1.0			1.9	0.1	Pt
	1.0			2.0		Pt (Te, Bi)2,1
	1.0			2.0		Pt (Te, Bi)2,1
	1.0			1.7		Pt (Te, Bi)2,1
	1.0			2.0		Pt (Te, Bi)2
	1.0			2.1	0.1	Pt
	1.0					Pt (Te, Bi)2
	1.0			9.4	0.4	Pt (Te, Bi)2
	1.0			1.7	0.2	PtTeBi
	1.0			2.2	0.2	Pt (Te, Bi)2
	1.0			1.5	0.1	Pt (Te, Bi)2,5
	0.8		0.2			(Pt, Ni) Te
0.3	0.1		0.6			(Ni, Pd, Pt) (Te, Bi)2
0.2	0.4		0.4			(Pt, Ni, Pd) (Te)2
0.2	0.4		0.4	2.0	0.1	(Pt, Ni, Pd) (Te)2
0.2	0.1	0.1	0.7	2.0	0.1	(Ni, Pd, Pt) (Te, Bi)1,7
0.2	0.4		0.4	2.0	0.1	(Pt, Ni, Pd) (Te)2
0.3	0.3		0.4	2.0		(Ni, Pd, Pt) (Te, Bi)2,2
0.4	0.3		0.2			Pd4Pt3Ni2
0.2	0.0		0.8	1.7	0.1	(Ni, Pd) (Te, Bi)1,8
0.4	0.3		0.3	1.9	0.1	(Pd, Pt, Ni) (Te, Bi)1,9
0.3	0.7			0.9	0.7	(Pt, Pd) (Te, Bi)2,4
0.4	0.3	0.1	0.2	1.9	0.1	(Pd, Pt, Ni, Ag) (Te, Bi)1,6
1.0				2.2	0.3	PdTeBi
1.0				1.2		Pd (Te, Bi)2
1.0						PdTeBi
0.8			0.2			(Pd, Ni) Te1,7
0.7		0.1	0.2	1.1	1.0	(Pd, Ni, Ag) Te1,6

Appendix E

1. Table E 1:	Weight percent for each oxide in a mineral. (Calculations excluding sulfides) Ions is calculated from excel spreadsheet by Andy Tindle (Tindle). Weight = (Molar weight / Cations per oxide) * Ions Wt% oxide is the weight calculation normalized
2. Table E 2:	Carbonate calculations is slightly different. Since CO_2 is added after the measured composition of Mg, Ca and Fe as oxides, then the equation is balanced when CO_2 is in equal proportion. Molar Proportion = Oxides (EPMA) / Molar compound weight The results are normalized and CO_2 is added to an equal amount. Weight Oxide = Molar proportion * molar weight These results are then normalized to get the weight percent of each oxide.
3. Table E 3:	The same calculations for sulfides as done for silicates and oxides in Table E 1.
4. Table E 4:	Pixels are counted in Adobe Photoshop by implementing Figure B and measuring the amount of pixels covered by each color. Then normalized and multiplied with the density of each mineral. (Density found in the internet mineral library of Webmineral)
5. Table E 5:	Element occupation = (Cct (Normalization(Table E 4)) * Cct(Cu(Table E 5))) +…+ (Ccp (Normalization(Table E 4)) * Ccp(Cu(Table E 5))) The results are then normalized.
6. Table E 6:	The same described above is done for silicates and oxides. These results are presented to represent the carbonate cloth (gold cluster) composition. Discussed in section 6.3..

Several assumptions had to be made.

- The area on the surface was assumed to represent the volume, with a thickness of 1 µm, where the minerals have the same form and shape over this thickness.
- The sulfide and the carbonatitic portions are treated as immiscible, in order to compare with other carbonatitic compositions elsewhere in SIP.
- Several minerals had to be calculated from data collected elsewhere in the thin section. Neither ilmenite nor Cr-spinel were analyzed on the EPMA in this setting and comparisons with EDS from other areas was necessary to calculate their melt contribution.
- During the EPMA session, magnesium was not included in the oxide analyses. This resulted in magnesium being added manually during the cation calculation.
- For fluorine and chlorine in amphibole and biotite there exist uncertainties that resulted in them being excluded from the total assemblage. The uncertainty lies in what position they occupy in the crystallographic structure, but the total amount of these halogens have not been found to contribute to any significant extent

Table E 1

	Na2O	**F**	**Cl**	**Cr2O3**	**SiO2**	**Al2O3**	**K2O**	**MnO**	**MgO**	**CaO**	**FeO**	**TiO2**	**H2O**
Molar weight	61.979	18.998	35.453	151.989	88.17	101.961	94.195	70.844	40.304	56.077	71.844	79.865	17.007
Cations per oxide	2	1	1	2	1	2	2	1	1	1	1	1	2
Opx (ions)				0.003	1.994	0.065		0.007	1.551	0.002	0.376	0.002	
Weight				0.228	175.811	3.314		0.496	62.512	0.112	27.013	0.160	
Wt% oxide				0.085	65.201	1.229		0.184	23.183	0.042	10.018	0.059	
Amp (ions)	1.083	0.016	0.019	0.046	6.068	2.411	0.036	0.016	3.339	1.673	1.000	0.121	1.964
Weight	33.561	0.312	0.681	3.519	535.037	122.894	1.688	1.105	134.557	93.822	71.810	9.678	16.704
Wt% oxide	3.273	0.030	0.066	0.343	52.180	11.985	0.165	0.108	13.123	9.150	7.003	0.944	1.629
Bt (ions)	0.499	0.031	0.003	0.010	2.721	1.528	0.400	0.001	2.282	0.007	0.333	0.090	1.966
Weight	15.463	0.598	0.102	0.771	239.869	77.899	18.842	0.106	91.981	0.379	23.893	7.156	16.715
Wt% oxide	3.132	0.121	0.021	0.156	48.579	15.776	3.816	0.021	18.628	0.077	4.839	1.449	3.385
Ilm (ions)											1.000	1.000	
Weight											71.844	79.865	
Wt% oxide											47.356	52.644	
Cr-Spl				3.90		2.34			2.05		16.34	0.45	
Weight				296.00		119.38			82.52		1174.15	35.71	
Wt% oxide				17.33		6.99			4.83		68.75	2.09	

Table E 2

Carbonate				
	MgO	**CaO**	**FeO**	**CO2**
Molar weight	40.304	56.077	71.844	44.009
Wt % (Mgs)	37.129		9.582667	
Molar proportion	0.921224		0.133382	
Normalized Mol	0.873525		0.126475	1
Oxide weight	35.20654		9.086496	44.009
Wt% oxide	39.87058		10.29025	49.83917
Wt % (Dol)	18.3955	25.9575	2.8905	
Molar portion	0.456419	0.46289	0.040233	
Normalized Mol	0.475663	0.482408	0.0419294	1
Oxide weight	19.17112	27.05197	3.0123745	44.009
Wt% oxide	20.56007	29.01187	3.2306202	47.19744

Table E 3

Sulfides				
	Cu	**S**	**Fe**	**Ni**
Molar weight	63.546	32.06	55.845	58.6934
Po (ions)		0.568	0.432	
Mol portion		18.21008	24.12504	
Wt% element		43.01412	56.98588	
Pn (ions)		0.477508	0.269201	0.253291
Mol portion		15.30889	15.03354	14.86652
Wt% element		33.86252	33.25346	32.88402
Ccp (ions)	0.224	0.509	0.226	
Mol portion	14.2343	16.31854	12.62097	
Wt% element	32.96976	37.79731	29.23293	
Cct(ions)	0.553	0.324	0.122	
Mol portion	35.14094	10.38744	6.81309	
Wt% element	67.13785	19.84553	13.01662	
Cb (ions)	0.202	0.398	0.4	
Mol portion	12.83629	12.75988	22.338	
Wt% element	26.779	26.61959	46.60141	

Table E 4

Mineral	Pixels	Area (%)	Density (gm/cc)	Volumetric density	Normalized
Cct	251	0.0457	6.46	0.29523	0.083327
Po	7503	1.3661	3.95	5.396181	1.523045
Pn	9527	1.7346	5.07	8.79465	2.482247
Cb	30166	5.4925	4.03	22.13488	6.247461
Ccp	39779	7.2428	4.2	30.41989	8.585863
Ilm	47718	8.6883	4.79	41.61714	11.74623
Cr-Spl	32360	5.8920	4.2	24.74641	6.984553
Mgs	119413	21.7423	2.98	64.79214	18.28726
Dol	14726	2.6813	2.84	7.614784	2.149235
Opx	59670	10.8645	3.55	38.56904	10.88592
Amp	147016	26.7682	3.24	86.72894	24.47882
Bt	41090	7.4815	3.1	23.19275	6.54604

Table E 5

Mineral	Cu	S	Fe	Ni
Cct	67.13785	19.84553	13.01662	
Po		43.01412	56.98588	
Pn		33.86252	33.25346	32.88402
Cb	26.779	26.61959	46.60141	
Ccp	32.96976	37.79731	29.23293	
Element occupation	455.969	642.0486	712.5504	81.62624
Normalized	**24.09737**	**33.93143**	**37.65736**	**4.31384**

Table E 6

Mineral	Na2O	F	Cl	Cr2O3	SiO2	Al2O3	K2O	MnO	MgO	CaO	FeO	TiO2	H2O
Ilm											47.356	52.644	
Cr-Spl				17.333	0.000	6.991	0.000	0.000	4.832	0.000	68.753	2.091	
Mgs									39.871		10.290	0.000	
Dol									20.560	29.012	3.231	0.000	0.000
Opx	0	0	0	0.085	65.201	1.229	0.000	0.184	23.183	0.042	10.018	0.059	0.000
Amp	3.273	0.030	0.066	0.343	52.180	11.985	0.165	0.108	13.123	9.150	7.003	0.944	1.629
Bt	3.132	0.121	0.021	0.156	48.579	15.776	3.816	0.021	18.628	0.077	4.839	1.449	3.385
Oxide occupation	100.621	1.538	1.761	131.404	2305.075	458.864	29.008	4.780	1502.601	287.291	1543.758	666.207	62.037
Normalized	**1.242**			**1.621**	**28.442**	**5.662**	**0.358**	**0.059**	**18.540**	**3.545**	**19.048**	**8.220**	**0.765**

Appendix F

Table F 1

Plagioclase															
Na2O	F	Cl	Cr2O3	SiO2	Al2O3	K2O	MnO	MgO	CaO	FeO	TiO2	Comment	CO2	SO3	NiO	P2O5
5.692				55.868	28.129	0.102	0.001	0.008	10.489	0.060	0.136	1-110.3				
5.796				55.675	28.073	0.083	0.000	0.000	10.357	0.025	0.100	1-110.3				
6.055				56.292	27.682	0.165	0.000	0.006	9.749	0.004	0.049	1-110.3				
5.752				56.222	28.041	0.167	0.030	0.015	10.324	0.000	0.034	1-110.3				

Table F 2

Clinopyroxene																
Na2O	F	Cl	Cr2O3	SiO2	Al2O3	K2O	MnO	MgO	CaO	FeO	TiO2	Comment	CO2	SO3	NiO	P2O5
0.801	0.000	0.001	0.621	48.860	5.956	0.000	0.138	13.314	22.850	5.483	1.553	1-110.3				
0.397			0.312	54.802	2.926	0.000	0.123	15.726	24.299	3.855	0.311	1-109.55				
0.491			0.415	52.653	6.263	0.014	0.100	15.712	22.350	4.958	1.026	1-109.4				

Table F 3

Biotite															
Na2O	F	Cl	Cr2O3	SiO2	Al2O3	K2O	MnO	MgO	CaO	FeO	TiO2	Comment	CO2	SO3	NiO	P2O5
3.856	0.103	0.028	0.211	37.976	18.056	4.153	0.026	21.298	0.120	5.558	1.716	1-109.55				
3.283	0.173	0.019	0.145	37.492	17.909	4.546	0.023	21.169	0.055	5.473	1.588	1-109.55				
0.366	0.096	0.025	0.710	37.539	15.849	9.461	0.030	19.073	0.000	6.951	3.821	1-110.3				
0.413	0.233	0.025	0.806	37.664	15.330	9.618	0.037	17.569	0.000	9.022	4.591	1-110.3				
0.367	0.126	0.011	0.780	37.577	15.426	9.680	0.012	17.744	0.000	8.613	4.403	1-110.3				
0.335	0.209	0.030	0.835	37.614	15.154	9.265	0.033	19.988	0.000	7.284	3.914	1-110.3				

Table F 4

Olivine																
Na2O	F	Cl	Cr2O3	SiO2	Al2O3	K2O	MnO	MgO	CaO	FeO	TiO2	Comment	CO2	SO3	NiO	P2O5
0.011				39.159	0.000	0.010	0.235	41.711	0.007	19.586		1-109.55.5		0	0.254	
0.067				39.176	0.001	0.026	0.212	41.715	0.002	19.465		1-109.55.9		0	0.261	
0.019				39.265	0.003	0.003	0.222	42.353	0.017	19.681		1-109.55.14		0.042	0.219	
0.005				39.139	0.084	0.011	0.222	41.972	0.361	19.263		1-109.55.15		0.392	0.222	
0.001				39.113	0.001	0.010	0.239	42.094	0.001	19.789		1-109.55.25		0	0.207	
0.000				39.243	0.002	0.000	0.251	41.666	0.004	20.736		1-109.4.3		0.011	0.195	
0.015				39.123	0.000	0.001	0.243	41.600	0.015	20.759		1-109.4.10		0.008	0.157	
0.003				39.122	0.000	0.009	0.239	41.677	0.014	20.876		1-109.4.13		0.01	0.212	
0.018				39.251	0.000	0.008	0.236	41.777	0.008	20.876		1-109.4.17		0.023	0.143	

Table F 5

Amphibole																
Na2O	F	Cl	Cr2O3	SiO2	Al2O3	K2O	MnO	MgO	CaO	FeO	TiO2	Comment	CO2	SO3	NiO	P2O5
3.187	0.050	0.070	0.774	40.897	13.290	0.433	0.072	14.930	12.175	7.465	1.879	1-109.55				
3.185	0.006	0.000	0.668	43.408	12.597	0.030	0.066	16.079	12.287	7.577	1.093	1-109.55				
3.211	0.024	0.000	0.693	43.437	12.574	0.004	0.095	16.500	11.995	7.449	0.927	1-109.55				
3.420	0.037	0.019	0.623	43.106	12.758	0.004	0.070	16.679	12.369	7.235	0.962	1-109.55				
3.785	0.024	0.083	0.403	42.334	14.227	0.177	0.125	15.183	10.594	8.326	1.104	1-109.55				
3.950	0.048	0.074	0.408	41.699	14.097	0.212	0.130	15.830	11.031	8.225	1.127	1-109.55				
3.253	0.224	0.019	0.353	44.235	12.068	0.006	0.104	16.675	11.989	7.714	0.766	1-109.4				
2.339	0.148	0.029	0.752	46.104	9.505	0.104	0.072	17.188	12.495	6.604	0.897	1-110.45				
2.396	0.000	0.052	0.725	43.018	12.560	1.115	0.095	14.602	12.085	7.844	2.400	1-110.45				
2.693	0.159	0.045	0.430	44.393	12.500	0.255	0.074	15.538	11.984	7.093	1.532	1-110.45				
2.066	0.031	0.021	0.477	47.215	9.563	0.190	0.058	16.957	12.021	6.266	1.057	1-110.45				
1.800	0.143	0.020	0.405	48.717	7.793	0.138	0.076	17.428	13.213	5.766	0.899	1-110.45				
2.111	0.031	0.031	0.584	47.731	9.124	0.182	0.103	17.265	12.270	6.109	1.047	1-110.45				
1.766	0.106	0.012	0.480	49.157	7.882	0.123	0.074	17.988	12.257	5.881	0.921	1-110.45				
2.653	0.111	0.016	0.944	42.170	13.754	1.063	0.088	14.637	12.050	7.316	2.039	1-110.45				
0.147	0.057	0.034	0.187	47.937	2.412	0.170	0.111	27.764	0.715	7.431	0.070	1-110.45				

Table F 6

Orthopyroxene																
Na2O	F	Cl	Cr2O3	SiO2	Al2O3	K2O	MnO	MgO	CaO	FeO	TiO2	Comment	CO2	SO3	NiO	P2O5
0.056			0.073	57.174	1.392	0.009	0.278	29.601	0.111	13.287	0.000	1-109.55.10				
0.033			0.375	55.715	4.057	0.000	0.284	28.816	0.348	13.384	0.334	1-109.55.13				
0.000			0.101	57.448	1.590	0.000	0.232	29.984	0.050	12.959	0.073	1-109.55.22				
0.003			0.068	57.859	1.069	0.000	0.262	30.278	0.219	13.720	0.051	1-109.4.1				
0.000			0.071	57.729	1.258	0.000	0.263	30.138	0.188	13.625	0.024	1-109.4.2				
0.014			0.171	56.250	4.006	0.000	0.284	28.848	0.622	13.815	0.243	1-109.4.5				
0.000			0.173	55.991	4.226	0.000	0.261	28.617	0.993	13.202	0.171	1-109.4.8				
0.000			0.058	57.407	1.902	0.000	0.239	29.633	0.266	13.563	0.037	1-109.4.9				
0.000			0.023	57.673	1.101	0.023	0.239	30.218	0.156	13.393	0.021	1-109.4.14				
0.000			0.028	57.639	1.052	0.029	0.291	30.305	0.146	13.486	0.045	1-109.4.15				
0.053			0.029	57.922	1.094	0.017	0.256	30.092	0.127	13.663	0.032	1-109.4.16				
0.000			0.052	57.821	1.090	0.015	0.276	30.187	0.127	13.758	0.031	1-109.4.18				
0.042			0.289	55.586	4.188	0.008	0.236	26.219	2.734	14.156	0.249	1-110.3.9				
0.036			0.330	55.991	4.143	0.000	0.265	27.225	2.464	13.378	0.215	1-110.3.14				
0.022			0.316	56.288	3.946	0.003	0.246	27.928	1.050	13.583	0.047	1-110.45.2				
0.013			0.253	56.469	2.855	0.000	0.253	27.878	0.197	15.185	0.052	1-110.45.9				
0.028			0.076	56.862	2.245	0.000	0.268	28.273	0.255	15.258	0.092	1-110.45.10				
0.015			0.238	56.296	3.421	0.000	0.270	27.993	0.259	15.214	0.129	1-110.45.11				

Table F 7

Serpentine																
Na2O	F	Cl	Cr2O3	SiO2	Al2O3	K2O	MnO	MgO	CaO	FeO	TiO2	Comment	CO2	SO3	NiO	P2O5
0.071				31.805	0.000	0.012	0.227	33.071	0.029	16.259		1-109.55.1		6.473	0.264	
0.573				27.800	0.000	0.101	0.174	31.392	0.094	21.685		1-109.55.2		9.822	0.328	
0.047				35.866	0.106	0.018	0.196	34.318	0.053	10.227		1-109.55.3		2.647	0.182	
0.033				31.080	0.000	0.022	0.232	33.141	0.031	17.243		1-109.55.4		6.094	0.257	
0.019				40.175	0.000	0.079	0.286	34.368	0.048	6.490		1-109.55.8		1.068	0.273	
0.009				34.956	0.000	0.000	0.271	34.680	0.014	12.741		1-109.55.23		1.057	0.138	
0.000				37.896	0.000	0.000	0.282	36.364	0.032	7.585		1-109.55.24		1.165	0.257	
0.000				41.293	0.000	0.031	0.127	36.689	0.016	8.569		1-109.4.7		2.838	0.387	
0.008				37.925	0.000	0.013	0.168	35.762	0.025	9.220		1-109.4.11		0.979	0.304	
0.000				38.238	0.000	0.005	0.208	34.957	0.032	10.782		1-109.4.12		0.795	0.209	
0.014				44.870	2.330	0.351	0.052	36.043	0.037	4.603		1-110.3.7		0.01	0.01	
0.000				46.514	0.057	0.031	0.444	29.656	0.256	6.225		1-110.3.13		8.886	2.992	
0.094				44.277	6.091	0.111	0.186	28.062	0.625	9.384		1-110.45.7		0.077	0	
0.077				48.459	2.753	0.065	0.165	27.597	0.728	7.510		1-110.45.12		0.055	0	

Table F 8

Dolomite																
Na2O	F	Cl	Cr2O3	SiO2	Al2O3	K2O	MnO	MgO	CaO	FeO	TiO2	Comment	CO2	SO3	NiO	P2O5
0.026				0.000	0.005		0.156	18.241	26.302	2.568		1-109.55.1	52.701			
0.052				0.492	0.038		0.252	20.873	27.947	5.754		1-109.55.3	44.593			
0.000				0.000	0.000		0.138	17.912	26.722	2.853		1-109.55.5	52.375			
0.000				0.000	0.012		0.130	17.985	26.418	2.785		1-109.55.6	52.669			
0.016				0.000	0.016		0.166	18.302	26.189	2.788		1-109.55.7	52.522			
0.004				0.000	0.033		0.156	18.489	25.726	2.993		1-109.55.11	52.598			
0.000				0.000	0.000		0.148	18.241	26.276	2.802		1-109.55.14	52.532			
0.031				0.234	0.000		0.174	18.777	25.774	3.584		1-109.55.18	51.424			
0.017				0.178	0.003		0.158	18.562	25.915	3.772		1-109.4.2	51.395			
0.000				0.000	0.000		0.168	18.798	26.117	3.379		1-109.4.4	51.538			
0.005				0.110	0.034		0.155	18.025	26.288	3.162		1-109.4.5	52.221			
0.021				0.398	0.016		0.156	18.852	25.858	3.983		1-109.4.9	50.716			
0.023				0.000	0.000		0.161	17.631	26.753	3.555		1-110.3.1	51.876			
0.000				0.000	0.000		0.160	17.370	26.897	3.680		1-110.3.3	51.893			
0.011				0.107	0.057		0.135	17.470	26.287	3.809		1-110.3.4	52.124			

Table F 9

Magnesite																
Na2O	F	Cl	Cr2O3	SiO2	Al2O3	K2O	MnO	MgO	CaO	FeO	TiO2	Comment	CO2	SO3	NiO	P2O5
0.021				0.286	0.027		0.325	37.410	0.592	8.968		1-109.55.2	52.37			
0.000				0.000	0.000		0.367	37.649	0.345	9.177		1-109.55.4	52.463			
0.017				0.047	0.068		0.336	36.890	0.796	9.379		1-109.55.8	52.469			
0.004				0.013	0.000		0.301	37.096	0.283	9.876		1-109.55.9	52.427			
0.009				0.079	0.018		0.312	37.401	0.444	9.493		1-109.55.10	52.241			
0.000				0.036	0.000		0.310	37.709	0.308	8.915		1-109.55.12	52.722			
0.000				0.160	0.000		0.329	37.578	0.448	9.233		1-109.55.13	52.251			
0.000				0.143	0.004		0.337	37.732	0.334	9.181		1-109.55.15	52.268			
0.028				0.257	0.015		0.326	37.731	0.329	9.021		1-109.55.16	52.292			
0.025				0.453	0.006		0.309	37.471	0.613	9.011		1-109.55.17	52.113			
0.070				0.280	0.000		0.290	37.372	0.532	9.339		1-109.4.1	52.117			
0.001				0.153	0.000		0.336	37.366	0.706	9.364		1-109.4.3	52.073			
0.000				0.180	0.003		0.360	37.646	0.336	9.403		1-109.4.6	52.071			
0.010				0.088	0.000		0.341	37.654	0.376	9.512		1-109.4.7	52.017			
0.000				0.147	0.000		0.329	37.647	0.275	10.124		1-109.4.8	51.479			
0.007				0.356	0.000		0.344	37.284	0.461	9.305		1-109.4.10	52.245			

Table F 10

Calcite															
Na2O	F	Cl	Cr2O3	SiO2	Al2O3	K2O	MnO	MgO	CaO	FeO	TiO2	Comment	CO2	SO3	NiO	P2O5
0.019				0.000	0.087		0.994	0.627	48.713	0.680		1-110.45.1	48.881			
0.023				0.025	0.086		0.265	0.436	49.699	0.399		1-110.45.2	49.066			
0.040				0.529	0.041		1.165	1.076	51.682	0.926		1-110.45.3	44.54			
0.000				0.000	0.017		0.465	0.518	49.149	0.745		1-110.45.4	49.107			

Table F 11

Apatite																
Na2O	F	Cl	Cr2O3	SiO2	Al2O3	K2O	MnO	MgO	CaO	FeO	TiO2	Comment	CO2	SO3	NiO	P2O5
0.030	3.816	1.539	0.000	0.311	0.032	0.112	0.059	0.820	56.896	1.050	0.017	1-109.55.7			42.042	0.030
0.021	3.344	0.706	0.000	0.000	0.033	0.000	0.012	0.076	56.286	0.166	0.000	1-110.45.3			44.754	0.021
0.000	3.179	0.669	0.000	0.000	0.014	0.000	0.039	0.116	56.502	0.171	0.000	1-110.45.4			42.932	0.000
0.000	3.399	0.713	0.009	0.000	0.008	0.005	0.033	0.093	56.132	0.176	0.000	1-110.45.5			44.803	0.000

Table F 12

EPMA calibration standards (Silicates)						
Oxides/Mineral group	Oxides (Spinel, Ilmenite)	Amphibole, Biotite	Pyroxenes	Olivine, Serpentine	Carbonates	Plagioclase
Na_2O	Ast 34	Ast 28	Ast 28	Ast 28		Ast 28
F		Ast 23			Ast 23	
Cl		Ast 45			Ast 45	
Cr_2O_3	AST 10	Ast 17	Ast 17			
SiO_2	Ast 35	Ast 29	Ast 21	Ast 34		Ast 35
Al_2O_3	Ast 35	Ast 29	Ast 28	Ast 28		Ast 35
K_2O		Ast 41	Ast 41	Ast 41		Ast 41
MnO	AST 11	AST 11	AST 11	Ast 39	Ast 39	AST 11
MgO	Ast 34	Ast 29	Ast 21	Ast 34	Ast 22	Ast 34
CaO	Ast 35	Ast 29	Ast 21	Ast 4	Ast 22	Ast 35
FeO	AST 12	Ast 29	AST 12	Ast 34	Ast 34	Ast 34
TiO_2	Ast 40	Ast 40	Ast 40			Ast 29
NiO	AST 14			Ast 52		
SrO					Ast 13	
SO_3	Ast 36					
V_2O_3	AST 9					
CuO	AST 15					

Table F 13

Pyrrhotite									
Pd	Pt	Se	Rh	Ir	Cu	Ni	S	Fe	Comment
0.000	0.000	0.000	0.000	0.000	0.012	0.166	35.967	63.324	Pt-146-host-Po
0.000	0.021	0.000	0.046	0.206	0.126	0.910	50.673	43.728	Pd-275-sulfid-2
0.000	0.151	0.017	0.000	0.134	0.056	0.029	35.643	64.209	Pd-282-sufM
0.008	0.000	0.000	0.000	0.000	0.000	0.074	35.503	62.378	Pd-282-sufD
0.006	0.167	0.000	0.035	0.045	0.175	0.046	50.841	42.824	Pt-236-M

Table F 14

Chalcopyrite									
Pd	Pt	Se	Rh	Ir	Cu	Ni	S	Fe	Comment
0.000	0.000	0.016	0.015	0.000	34.736	0.483	33.364	27.506	Pt-153-house light
0.000	0.000	0.000	0.027	0.049	32.154	0.270	34.910	29.846	Pt-153-house dark
0.019	0.000	0.034	0.000	0.011	21.133	0.000	33.718	38.008	Pt-236-L
0.032	0.000	0.000	0.000	0.031	31.929	0.000	35.320	29.623	Pt-236-Lsuf

Table F 15

Pentlandite									
Pd	Pt	Se	Rh	Ir	Cu	Ni	S	Fe	Comment
0.000	0.000	0.049	0.063	0.415	0.000	34.147	32.194	31.202	Pt-148-matrix-1
0.027	0.000	0.000	0.000	0.471	0.000	34.559	32.336	31.226	Pt-148-matrix-2
0.000	0.005	0.020	0.039	0.143	0.163	29.381	35.417	33.293	Pt-148-def10um.1
0.000	0.091	0.011	0.000	0.000	0.036	28.442	35.735	33.681	Pt-148-def10um.2
0.008	0.000	0.000	0.000	0.280	0.031	34.200	32.708	31.130	Pt-146-host-Pn
0.000	0.073	0.013	0.000	0.188	0.022	35.156	32.174	30.515	Pd-275-sulfid-1
0.000	0.169	0.000	0.000	0.441	0.063	30.445	33.923	36.821	Pd-282-sufL
0.000	0.073	0.013	0.000	0.188	0.022	35.156	32.174	30.515	Pd-275-sulfid-1
0.000	0.169	0.000	0.000	0.441	0.063	30.445	33.923	36.821	Pd-282-sufL